Operation-Dependent Degradation of Automotive Lithium-Ion Cells

Vom Promotionsausschuss des Fachbereiches Material- und Geowissenschaften der Technischen Universität Darmstadt genehmigte kumulative Dissertation zur Erlangung des akademischen Grades Doktor-Ingenieur (Dr.-Ing.) von

M.Sc. Mathias Storch

Erstgutachter: Prof. Dr. Ralf Riedel
Zweitgutachter: Prof. Dr.-Ing. Kai Peter Birke

Darmstadt 2022

TECHNISCHE UNIVERSITÄT DARMSTADT

Mathias Storch: Operation-Dependent Degradation of Automotive Lithium-Ion Cells

Darmstadt, Technische Universität Darmstadt

Jahr der Veröffentlichung der Dissertation auf TUprints: 2022

URN: urn:nbn:de:tuda-tuprints-215544

Tag der mündlichen Prüfung: 13. Mai 2022

Erklärung zur Dissertation

Hiermit versichere ich, die vorliegende Dissertation ohne Hilfe Dritter nur mit den angegebenen Quellen und Hilfsmitteln angefertigt zu haben. Alle Stellen, die aus Quellen entnommen wurden, sind als solche kenntlich gemacht. Diese Arbeit hat in gleicher oder ähnlicher Form noch keiner Prüfungsbehörde vorgelegen.

Darmstadt, den 13.05.2022

(Mathias Storch)

The presented cumulative dissertation summarizes the essential research findings reported to the scientific community in the following peer-reviewed articles. The articles itself [1]-[5] are enclosed in the Chapter Publications.

[1] **Storch M**, Hahn SL, Stadler J, Swaminathan R, Vrankovic D, Krupp C, Riedel R (2019): Post-mortem analysis of calendar aged large-format lithium-ion cells: Investigation of the solid electrolyte interphase. In: *Journal of Power Sources* 443, S.227-243

[2] **Storch M**, Fath JP, Sieg J, Vrankovic D, Mullaliu A, Krupp C, Spier B, Passerini S, Riedel R (2021): Cycle parameter dependent degradation analysis in automotive lithium-ion cells. In: *Journal of Power Sources* 506 S. 230227

[3] **Storch M**, Fath JP, Sieg J, Vrankovic D, Krupp C, Spier B, Riedel R (2021): Temperature and Lithium Concentration Gradient Caused Inhomogeneous Plating in Large-format Lithium-ion Cells. In: *Journal of Energy Storage* 41, S.102887

[4] Hahn SL, **Storch M**, Swaminathan R, Obry B, Bandlow J, Birke KP (2018): Quantitative validation of calendar aging models for lithium-ion batteries. In: *Journal of Power Sources* 400, S.402–414

[5] Fath JP, Alsheimer L, **Storch M**, Stadler J, Bandlow J, Hahn SL, Riedel R, Wetzel T (2020): The influence of the anode overhang effect on the capacity of lithium-ion cells – a 0D-modeling approach. In: *Journal of Energy Storage* 29, S. 101344

Table of Contents

List of Abbreviations

a_x	activity
AES	Auger electron spectroscopy
BMS	battery management system
BOL	beginning of life
CC	constant current
CE	coulombic efficiency
CEI	cathode electrolyte interphase
CMC	carboxy methyl cellulose
CV	constant voltage
DEC	diethyl carbonate
DMC	dimethyl carbonate
DV	differential voltage
E	cell potential
E^0	standard potential
EC	ethylene carbonate
EDX	energy-dispersive X-ray spectroscopy
EELS	electron energy loss spectroscopy
EIS	electrochemical impedance spectroscopy
EMC	ethyl methyl carbonate
EV	electric vehicle
FIB	focused ion beam
η	viscosity
η_{ohm}	ohmic polarization
η_{act}	activation polarization
η_{con}	concentration polarization
ICP	inductively coupled plasma
LCO	$LiCoO_2$
LFP	$LiFePO_4$
LIB	lithium-ion battery
LMO	$LiMn_2O_4$
LNMO	$LiNi_{0.5}Mn_{1.5}O_4$
LTO	$Li_4Ti_5O_{12}$
NCA	$Li(Ni_{0.8}Co_{0.15}Al_{0.05})O_2$
NMC	$Li(Ni_xMn_yCo_z)O_2$
NMC111	$Li(Ni_{0.33}Mn_{0.33}Co_{0.33})O_2$
NMC442	$Li(Ni_{0.4}Mn_{0.4}Co_{0.2})O_2$
NMC532	$Li(Ni_{0.5}Mn_{0.3}Co_{0.2})O_2$
NMC622	$Li(Ni_{0.6}Mn_{0.2}Co_{0.2})O_2$
NMC811	$Li(Ni_{0.8}Mn_{0.1}Co_{0.1})O_2$
OCV	open circuit voltage
OES	optical emission spectroscopy
PC	propylene carbonate
PHEV	plug-in hybrid electric vehicle
PVDF	polyvinylidene difluoride
R	gas constant
SEI	solid electrolyte interphase
SEM	scanning-electron microscopy
SOC	state of charge
STEM	scanning transmission electron microscopy
T	temperature
TEM	transmission electron microscopy

U^0	open circuit voltage
UPS	ultraviolet photoelectron spectroscopy
VC	vinylene carbonate
XPS	X-ray photoelectron spectroscopy
XRD	X-ray diffraction
h	Planck's constant
ν	frequency of the photon
E_{kin}	kinetic energy of the electron
$E_{binding}$	binding energy
W	work function
F_B	buoyant force
ρ_{liquid}	density of the liquid
V	displaced volume
g	gravity
F_W	weight
m_C	cell mass
F_R	resulting force

Broader Context

Gradually the understanding of the basic conflict of economic growth and threat of the earth is focused by the society more and more. One of the main challenges is the hunger for energy, typically electricity or heat conversed from fossil fuels is needed. In order to protect the earth, these fossil fuels have to be replaced by renewable energies, e.g. solar, wind or water power, which directly opens the question for proper storage technologies. The lithium-ion battery is one of the answers; it has a high power and energy density and is thus the technology of choice to store energy ranging from some Wh to several kWh.

However, the lithium-ion batteries have to be optimized regarding the use of resources and time of usage to move on in the decarbonisation of the energy supply. At this point, the present thesis enters the game; the proper understanding of the battery degradation will enhance the lifetime, performance and safety of existing and future lithium-ion batteries. The optimized design and operation of the battery will lead to a reduced failure ratio und thus, resources can be preserved. Moreover, less degraded batteries are more valuable for the potential 2nd life, again saving the resources.

Furthermore, besides the improvements in technology, the economic and political constraints have to be aligned, just to mention a few keywords, raw materials supply, charging infrastructure, sustainable energy supply, and bureaucracy.

1. Introduction

The lithium-ion battery (LIB) technology is one of the key technologies to help human society with the transition from fossil energy to renewable energy in the 21st century. The success of LIB technology was pointed out and appreciated by awarding John B. Goodenough, M. Stanley Whittingham and Akira Yoshino with the Nobel prize in chemistry 2019 for their research on the development of the lithium-ion battery [6].

Public discussion in the last five to ten years started to focus more and more on the challenges of global warming which is mainly caused by the emission of greenhouse gases. In order to reduce these gases, alternatives to coal, gas and to the main energy supply for personal transport, that is oil, have to be established. While nuclear power plants raise concerns regarding public safety during operation and final deposition, wind and solar energy are promising candidates. However, they are not always accessible as their availability depends on the time of day, season and the geographical location. A variety of energy storage technologies are available for application or under research, see Figure 1. The traditional Lead-Acid, Ni-Cd and Ni-MH technologies are applied for years, but cannot achieve the required power and energy density. The sodium-ion battery is a promising candidate for stationary storage, as they are low cost and the materials are abundant. However, for personal transportation, lithium-ion batteries with their high power and energy densities are the most suitable for today's application. Even higher energy density can be achieved with solid state, lithium-sulfur and lithium-air batteries, however these technologies still lack in applicability and durability.

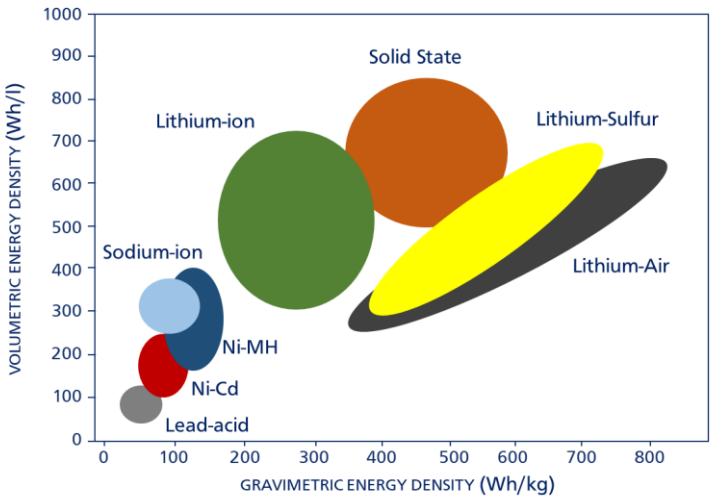

Figure 1: Volumetric versus gravimetric energy density on cell level for commercially available batteries.(Own, complemented drawings adapted from literature [7–9]).

The answer of the automobile industry to the challenge of global warming and local pollution of today's growing cities lies in the modification of its energy portfolio to partly or fully electrified vehicles models replacing the conventional combustion engines [10]. However, the application of LIBs to meet large-scale power requirements, of 10-20 kWh for plug-in hybrid electric vehicle (PHEV) and up to 120 kWh for pure electric vehicle (EV) is challenging. The battery has to fulfill several requirements such as high energy and power density, high safety, long lifetime as well as low costs. These requirements are in conflict with one another. For example, the energy density of the battery can be improved by using Ni-rich transition metal oxide cathodes, but in parallel the lifetime of the battery will suffer if no further constraints are applied [11].

For the design of a battery, typically, more than 300,000 km of total driven distance and more than 10 years of life are supposed as lifetime requirements for most conventional powered cars. The lifetime of the battery can be controlled by the composition of the used cell, the operation conditions and additional internal protecting components, e.g. battery cooling/heater. It is therefore necessary for a battery and car manufacturer to gain knowledge of the expected performance of the battery over its entire lifetime in an early development phase. Typically, the degradation of lithium-ion cells is analyzed in long-term temperature-accelerated calendar tests and cycle-life tests with condensed operation conditions, such as intensified power, or short rest phases [12–16]. However, to be able to avoid the degradation in an early state the corresponding processes inside the cells have to be known [17]. Hence it is necessary to analyze the cell components on material level in a post-mortem analysis after the aging test. With the knowledge of the degradation mechanism the quality of the cells and influences of for example new chemistries on the degradation, can be identified in an early state, which shortens development time and cost.

In this work, the aging and the predominant degradation mechanisms in large-format automotive lithium-ion cells are analyzed. The first part of the study focuses on calendar aging which is evaluated on a 50.8 Ah pouch-bag type lithium-ion cell composed of a graphite anode and a NMC111 ($Li(Ni_{0.33}Mn_{0.33}Co_{0.33})O_2$) cathode. The degradation mechanisms are examined by using scanning electron microscopy (SEM), inductively coupled plasma optical emission spectroscopy (ICP-OES), X-ray photoelectron spectroscopy (XPS) and Raman spectroscopy. For the second part of the study it is switched to a lithium-ion cell of higher energy density with a 39 Ah pouch-bag type lithium-ion cell composed of a graphite anode and a NMC622:NMC111 ($Li(Ni_{0.6}Mn_{0.2}Co_{0.2})O_2$:$Li(Ni_{0.33}Mn_{0.33}Co_{0.33})O_2$) blend cathode. In the beginning, the designed cycle aging test matrix is discussed in detail, followed by the results of the post-mortem analysis comprising SEM, ICP-OES, X-ray diffraction (XRD), XPS, focused

ion beam scanning electron microscopy (FIB-SEM), transmission electron microscopy (TEM) and three-electrode test cell measurements with materials harvested from the aged large-format cells. The last section addresses the challenge of inhomogeneous degradation arising from intensive operation or as side effects of the gas evolution.

2. Fundamentals

This section provides the fundamental information required to understand and follow the performed analysis, the results gathered and the discussion in this work. For further basic knowledge the reader is referred to common literature [7,18–20]. The theory of the lithium-ion battery comprising the electrochemical principle, the components and the cell formats are briefly discussed, followed by the potential degradation mechanism emerging during operation. The fundamentals section is completed with a detailed description of the available non-destructive and destructive physical/chemical analysis methods used for the evaluation of the LIB degradation mechanisms.

2.1. Lithium-Ion Battery

The research in the field of LIBs intensified in the 2nd half of the 20th century [21–24] and finally led to the batteries' first commercialization by Sony in 1991 [20]. Due to their high power and high energy density, the LIBs are widely used in mobile electronic applications in the majority of offices and households all over the world. An estimated ~50–60 GWh of LIBs were produced for this field of application per year in 2018-2020 [25]. Nevertheless, during the first years of applications several problems were recognized. Initially a strong capacity fade in a relatively short time of one to two years of application was observed for consumer electronic batteries in the 1990s and 2000s. In the following years more and more companies as Sanyo/Panasonic Corporation 1994 [26], Samsung SDI 1999 [27], LG Chem Ltd 1999 [28] and A123 Systems 2001 [29] started to manufacture LIBs in series resulting in a knowledge boost on the LIB properties. As shown in Figure 2 a strong increase in production capacity (blue) and drop in production cost per Wh (black) was the result.

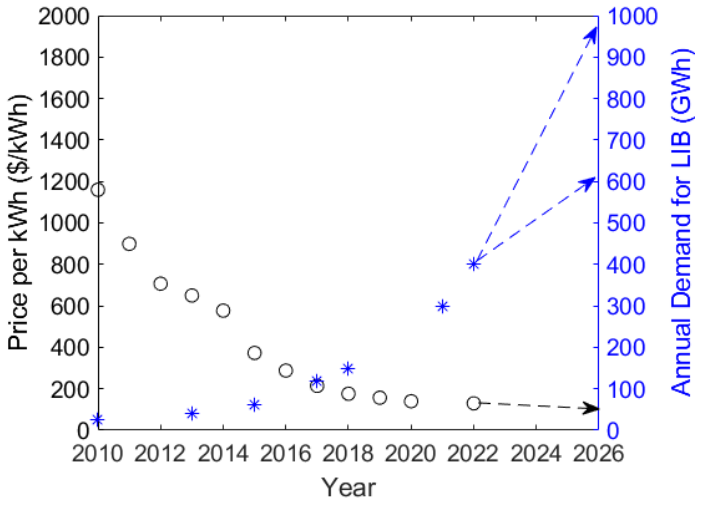

Figure 2: Lithium-ion battery market evolution: annual demand for LIBs in GWh (blue) and price per kWh (black), data until 2022 and forecast to 2026 [30,31].(Own drawing)

These developments paved the way for the first LIB-powered highway-capable vehicle, such as the Tesla Roadster in 2008 and the Tesla Model S in the following years [32]. In parallel, the Daimler AG developed and produced the Smart fortwo as an electric version and the BMW AG introduced the fully electric i3 [33,34]. However, not only electric vehicles, but also hybrid electric vehicles and plug-in hybrid electric vehicles were successful in catching people's fancy in the following years. The success of electric vehicles was boosted by political measures of financial promotion [35] and the increasing awareness of global warming and emission of harmful gases in big cities.

The smallest unit of a lithium-ion battery is an electrochemical cell consisting of two lithium-ion storage-materials as negative and positive electrodes, separated by a system composed of an electrical-insulating and ion-conductive medium. LIBs are separated into two classes, the primary lithium-ion batteries for single-use and the secondary lithium-ion batteries for multiple-use (rechargeable). Primary lithium-ion batteries are mostly used in the form of coin cells in small household appliances, such as balance, timer and radio control. Secondary lithium-ion batteries are used in cell phones, notebooks and, as discussed in this work, for electric transportation and grid storage. While primary lithium-ion batteries owe their supreme energy density to the use of metallic lithium as anode, the recharging is impeded by dendrite formation and rapid failure which can even lead to a thermal event. That's why secondary lithium-ion batteries employ intercalation compounds as both electrodes which are designed for repeated charge and discharge for several hundred to thousands of cycles. In this work, secondary LIBs consisting of graphite and a lithium transition metal oxide electrode are used for all investigations.

The working principle of a LIB is the conversion of electric energy into chemical energy (charging) and vice versa (discharging). During charging, the current applied on the external circuit forces lithium ions to move from the transition metal oxide electrode through the electrolyte to the graphite electrode; the respective electrons move through the outer circuit to the same electrode (see Figure 3 green arrows). When the external circuit is opened, the lithium ions will keep their residence and consequently the chemical energy is stored. A consumer load can be inserted into the external circuit and the lithium ions move through the electrolyte back to the initial electrode. The corresponding electrons power the consumer load and are transported to the same electrode (see Figure 3 red arrows).

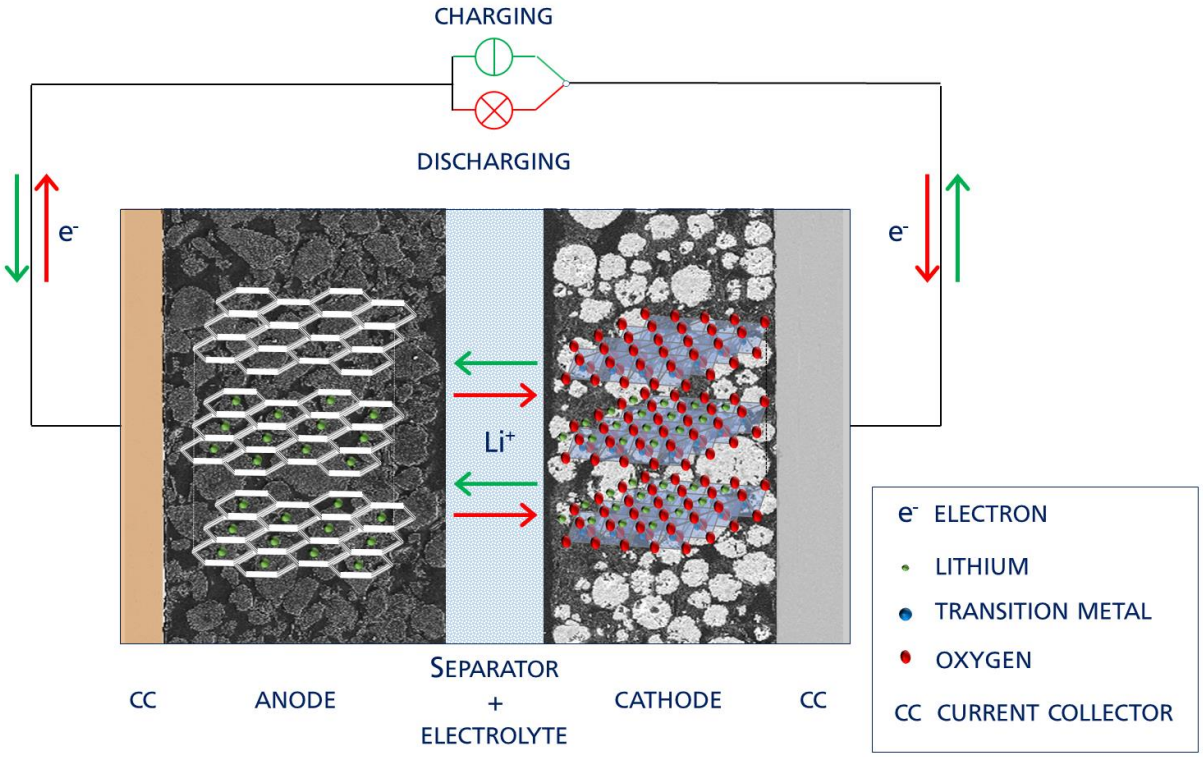

Figure 3: Schematic of a lithium-ion electrochemical cell in charging (green) and discharging modes (red). The illustrated electrodes are a state-of-the-art graphite anode and a lithium transition metal oxide cathode, each in a fully lithiated state. (Own drawing)

The reaction mechanism of a LIB is a redox reaction at both electrodes, in charge direction it is an oxidation reaction of the transition metal oxide host structure and a reduction reaction of the graphite host structure [19]. In discharge direction, the oxidation reaction takes place at the graphite and the reduction reaction is at the transition metal oxide. In this example of graphite and transition metal oxide, the following chemical reactions are valid for a discharge:

Oxidation (anode): $Li_xC_n \rightarrow xLi^+ + xe^- + nC$

Reduction (cathode): $Li_{1-x}MO_2 + xLi^+ + xe^- \rightarrow LiMO_2$

Total reaction (anode+cathode): $Li_xC_n + Li_{1-x}MO_2 \rightarrow LiMO_2 + nC$

The naming convention in electrochemistry is that the anode is defined by the oxidation reaction, whereas the cathode is the place of reduction, thus the naming would change with operation mode. To simplify, in the field of LIBs only the discharge direction is considered for denotation, where the anode (graphite) is the oxidative and the cathode (transition metal oxide) is the reductive electrode [7]. Besides the chemical reactions, the electric potential of the cell in equilibrium is described by the Nernst-equation (equation 1) and is dependent on the lithiation degrees of the electrodes and the temperature.

$$E = E^0 - RTln\left(\frac{a_{LiMO_2} \times a_{nC}}{a_{Li_xC_n} \times a_{Li_{1-x}MO_2}}\right) \qquad (1)$$

E = cell potential
E^0 = standard potential
R = gas constant
T = temperature
a_x = activity of the reactant

The cell voltage in equilibrium is called the open circuit voltage (*U^0, OCV*). A positive load leads to an increase in cell voltage and a negative load leads to decreasing cell voltage due to charge transfer between the electrodes and, therefore, a change in the electrode potentials. Additionally, three types of polarization modes occur, the ohmic (η_{ohm}), the activation (η_{act}) and the concentration (η_{con}) polarization (see equation 2). The ohmic polarization stems from the electrical conductivity of the cell's components and immediately builds up when a load is applied. It is used for the determination of the ohmic resistance. The activation polarization results from ion transfer through the double layer at the electrode/electrolyte interface where the Li^+ ions picking up/stripping their solvation shell. The concentration polarization results from a concentration gradient of Li^+ ions in the electrolyte and the electrode depending on the ion diffusion.

$$U = U^0 - \eta_{ohm} - \eta_{act} - \eta_{con} \qquad (2)$$

The higher the applied load, the stronger is the effect of these polarizations. Therefore, the OCV is used to characterize lithium-ion batteries without the influence of polarization effects. The OCV depends solely on the electrode potentials which again depend on the degree of lithiation. The minimum OCV and the maximum OCV of a lithium-ion cell are typical defined to protect the cell from overdischarge and overcharge which may result in cell failure. The amount of charge transferred between the minimum OCV and the maximum OCV is used for the calculation of the state of charge (SOC), which is the actual amount of charge divided by the maximum possible charge stored in between the OCV limits. The OCV varies as shown in the OCV-SOC graph of a commercial graphite/NMC111 LIB in Figure 4. In general, the OCV-SOC curve is measured by stepwise charging or discharging of the cell with a sufficient rest period (~2 h) for relaxation of the cell voltage after each load step. The influence of the electrode material and the respective potential on the appearance of the OCV-SOC curve is discussed in section 2.4.1. Additionally, the OCV-SOC is characteristic of a cell at beginning of life (BOL) and changes due to degradation effects.

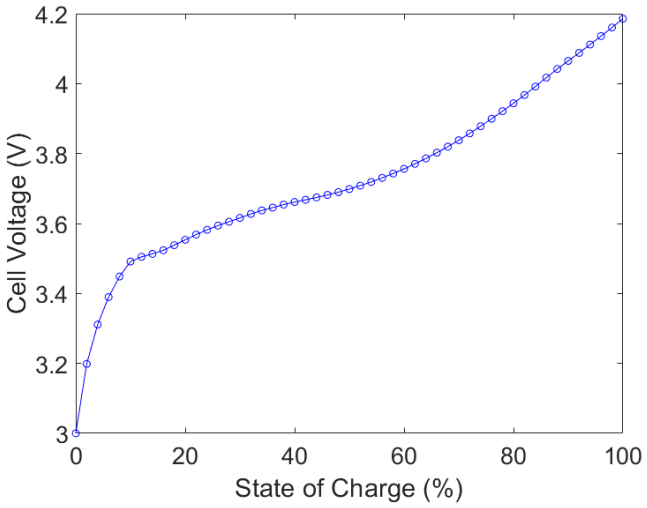

Figure 4: Open circuit voltage versus state of charge graph of a graphite/NMC111 lithium-ion cell.

2.2. Components and Materials of Lithium-Ion Batteries

First, the typical anode materials and their properties and advantages/disadvantages are discussed. Subsequently, the sections on the typical cathode materials and electrolytes used in LIBs follow. For more detailed and basic description it is referred to literature [36–40].

For most of the components in the interior of today's commercially available LIBs the materials offer a quite balanced mix of properties rather than possessing outstanding properties in one direction. The reason for this is that one outstanding property often brings along large drawbacks in terms of deterioration of the overall performance. Nevertheless, a lot of effort is made on the optimization of the cell properties and to develop tailored lithium-ion cells for special applications, for example extremely long life and safety features for aerospace, high power density for high-power consumer electronics and high energy density for automotive applications. These requirements necessitate a careful selection of materials. A general overview of available and practical state-of-the-art materials is given in Figure 5.

An appropriate anode material should combine a highly reversible lithiation and delithiation process with a high specific capacity, a potential close to the potential of Li/Li^+, a high electrical conductivity and good ionic conductivity. Additionally, it should be inert to chemical reaction with the remaining components, it should have small volume changes during lithiation/delithiation and for commercial reasons it should be low-cost and highly abundant.

Despite offering a perfect potential and great specific capacity (3800 $mAh \cdot g^{-1}$ [7]) metallic lithium is not a proper anode material for secondary lithium-ion batteries using liquid electrolytes. The main disadvantages are the formation of dendrites on the surface of the

lithium electrode and the high volume change when the cell is being charged [41]. These dendrites are a safety problem as penetration of the separator can lead to short circuit and fatal battery failure [7]. A solution for the replacement of lithium as negative electrode and lithium source was presented by Auborn and Barberio [42] in 1987, applying $LiCoO_2$ (LCO) as positive electrode, with a metal oxide negative electrode (MoO_2,WO_2). In parallel the intercalation of lithium into carbons, namely petroleum coke and graphite was investigated [43–45] leading to the application of Sony's first commercial graphite/LCO lithium-ion cell [20].

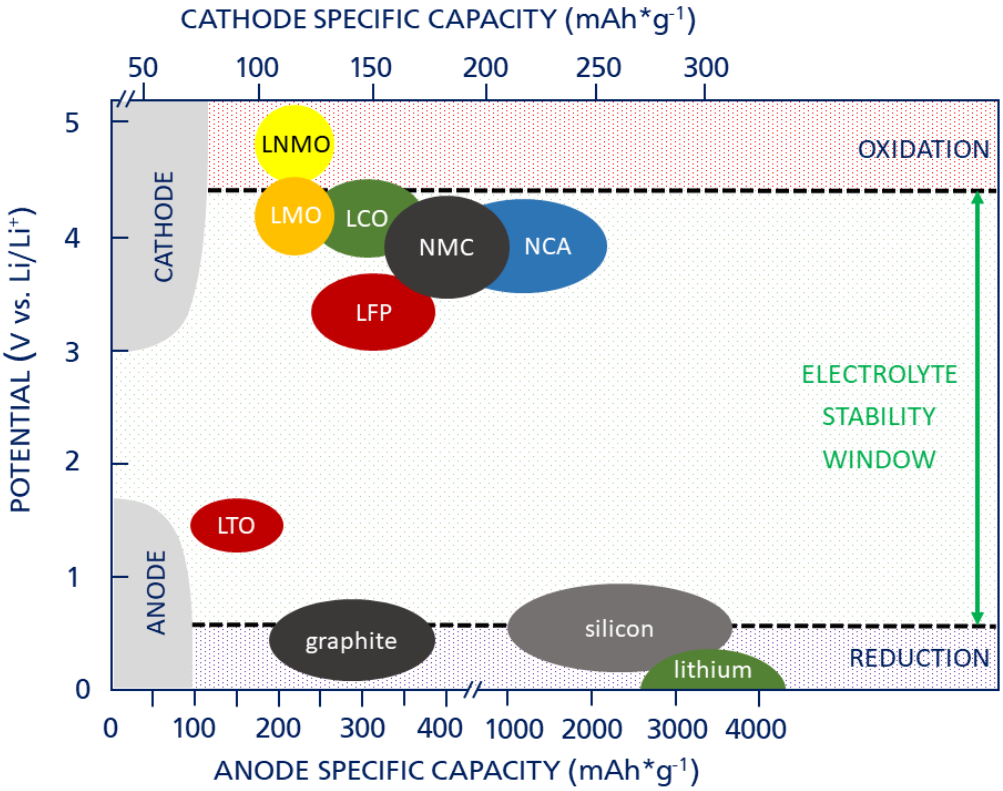

Figure 5: Electrode potential versus Li/Li^+ of the most prominent materials. The materials are sorted according to their specific capacity. The electrolyte stability window and the oxidation and reduction potential regions of state-of-the-art carbonate-based $LiPF_6$ electrolytes are marked. (Own drawing according to [7,40,46])

Since then, graphite has been established as the most common anode material in LIBs that are commercially available. Graphite has the advantage of combining good electrochemical properties without any outstanding drawbacks. Graphite belongs to the class of lithium-intercalation compounds where lithium ions intercalate in between the graphene sheets (see Figure 3). The maximum amount of lithium intercalating into the graphite is reached at a stoichiometry of LiC_6 which equals a theoretical specific capacity of 372 $mAh \cdot g^{-1}$. Depending on the degree of lithiation, several phases can form (see Figure 6) which are named by the number of graphene layers between the occupied interspaces. For example in stage III three graphene layers, and thus two empty interspaces, are in between the occupied ones. These

different stages can be observed visually due to the different colors of the lithiated graphite; i.e. empty graphite appears grey and changes to blue, to reddish and, in a fully lithiathed state, to gold.

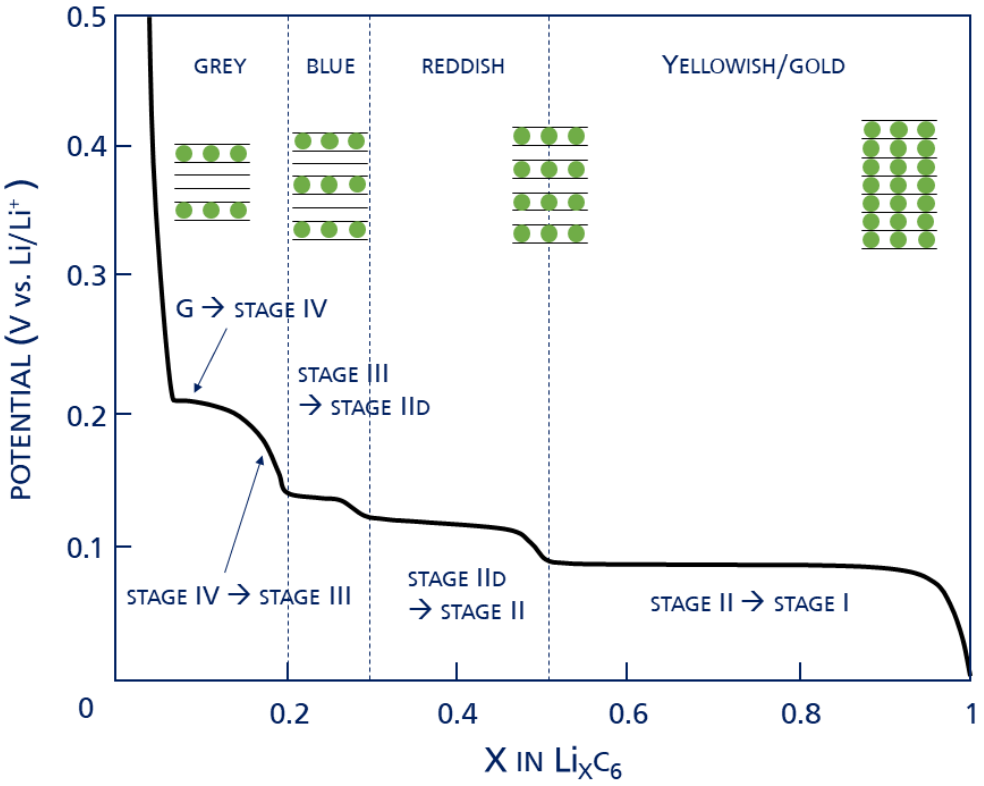

Figure 6: Graphite potential versus degree of lithiation, including the staging process and the corresponding schematic occupation of the graphite lattice. (Own drawing complemented and adapted from [7,47])

Advantageous properties of graphite are its highly reversible lithiation and delithiation process, the good electrical conductivity and a relatively flat potential curve close to the potential of Li/Li^+, which accomplishes good energy density. However, the potential of lithiated graphite is outside the electrolyte's stability window and thus, the electrolyte solvents decompose at the interface graphite/electrolyte to form the solid electrolyte interphase (SEI). The SEI is necessary for the operation due to its passivating effect for the electrolyte decomposition and stripping of the solvation shell from the Li^+ ions during intercalation. At the same time the growth of the SEI is a degradation mechanism of the LIB, which is discussed in section 2.3.2. As a result, the cycle efficiency of graphite electrodes is very high, which again enables LIBs to last for several thousands of cycles.

For the use-case of graphite in a lithium-ion cell, two additional features are of interest. The low volumetric change from empty to fully lithiated state of only ~10% and the low voltage hysteresis in charge and discharge direction keep the control by and the integration into the battery management system (BMS) quite simple. On top of its superior electrochemical

performance, graphite is a highly abundant and low-cost material, which strengthens its position for commercial use.

A promising, but still not widely used material for the negative electrode in high energy LIBs is silicon. In contrast to graphite, lithium does not intercalate into silicon, but forms an alloy which results in a high theoretical specific capacity of ~4200 $mAh \cdot g^{-1}$ [7]. The alloying potential versus Li/Li^+ of ~0.16 V [7] is in the range of graphite, but it has a strong hysteresis between charge and discharge, thus complicating the BMS function. Similar to graphite, the electrolyte decomposes under formation of the SEI on the silicon surface. However, the high volumetric changes during cycling of 200–400% [7] restrict its use in large-scale commercial LIBs for long-life applications. The high volume change results in particle grinding which leads to exposure of fresh silicon surface to the electrolyte and severe decomposition of electrolyte and surface deposits [48]. A lot of studies focus on overcoming these problems, one possible solution can be the nanosizing of silicon to enable reversible cycling without cracking [48]. However, up to now only a few producers are known to use this method and overall only a small amount of silicon is used in the cells [49].

The third state–of-the-art anode material, lithium titanate (LTO), is the most stable negative electrode material. The reason for its high stability is also its drawback for high-power and high-energy applications. The comparatively high potential of ~1.55 V vs. Li/Li^+ lowers its full cell potential compared to graphite. But due to this higher potential, the common electrolytes are stable and do not form an SEI, which drastically reduces the degradation. While LTO is not used for high energy and power application as in the automotive sector, it is a commonly used material where extreme lifetime and safety requirements have to be met, for example in space application. [20]

Similar to the anode material, a material suitable for use as cathode in LIB should be lithiathed and delithiated reversibly. It should have a high electronic and ionic conductivity, the volume change during cycling should be small and the crystal structure should be stable in each state of delithiation. Additionally, it should be low-cost and environmentally friendly. In contrast to the anode, the cathode should have a potential quite different from Li/Li^+ (+4 V) in order to increase the energy and power density. However, the potential is limited by the type of electrolyte used and its stability window (cf. Figure 5).

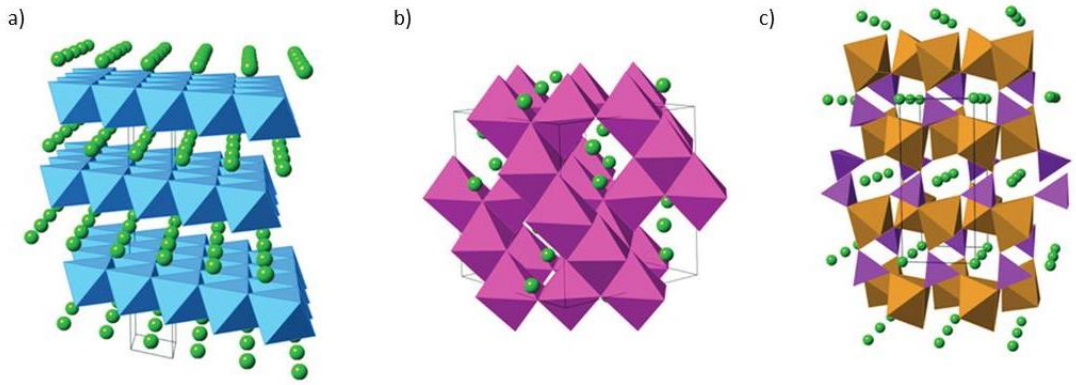

Figure 7: Crystal structures of the three most-prominent types of cathode materials for lithium-ion batteries. a) The layered-type, b) the spinel-type and c) the olivine–type structures. Modified graphic (reproduced with permission from [50] Copyright 2014, Royal Society of Chemistry[1]

The state-of-the-art cathode materials for LIBs are divided into three types according to their structure; the layered-type LCO, $LiNi_{1-y}Co_yO_2$, $Li(Ni_xMn_yCo_z)O_2$ with $x+y+z=1$ (NMC) and $Li(Ni_{0.8}Co_{0.15}Al_{0.05})O_2$ (NCA), the spinel-type $Li_2Mn_2O_4$ (LMO), and the olivine-type $LiFePO_4$ (LFP)(cf. Figure 7). Since its market introduction in the 1990s the layered-type transition metal oxide is the material of choice for high-power and high-energy applications. LCO was developed by Goodenough *et al.* [51] in 1980. Its outstanding properties are the high nominal voltage of 3.8 to 4.3 V vs. Li/Li^+ in the lithiation range of 1 to 0.5, fast delithiation/lithiation and low self-discharge. However, LCO has some disadvantages: the long-term stability of LCO-based cells is poor, the thermal stability is low, the costs of cobalt are high and it is a toxic element. To improve the properties of the layered oxides with one transition metal several transition metals are added, the two most prominent representatives are NMC and NCA. In NCA, cobalt improves structural stability because nickel tends to mix with the lithium ions, which is known as cation mixing. Aluminum improves the thermal stability and the electrochemical performance. In NMC, cobalt again acts as a structure stabilizer while the two main advantages of the manganese are low-cost and non-toxicity. However, the manganese ions tend to undergo disproportionation and dissolve in the electrolyte; and as a result, the Mn ions reach the anode surface and act as catalyzers for the SEI growth, which will be discussed in detail in section 2.3.2. In 2001, the most frequently used NMC composition NMC111 was first synthesized by Ohzuku and Makimura [52]. Since then studies on the transition metal compositions NMC111, NMC442 (40% nickel, 40% manganese, 20% cobalt), NMC532 (50%, 30%, 20%), NMC622 (60%, 20%, 20%) and NMC811 (80%, 10%, 10%) were published [53–61]. The nickel content in these materials has been found to be the limiting factor for the degree of lithiation until the structure is still stable. Therefore, the more nickel

is used, the higher can be the degree of delithiation, which enhances the usable capacity and energy density.

Apart from the layered-type transition metal oxide materials, the olivine-type structured materials with their most prominent representative LFP are often used. LFP is known for its outstanding thermal and cycle stability resulting in highly safe LIBs. Since no cobalt and nickel are needed for LFP, it is a low-cost and non-toxic cathode material. However, its potential of ~3.4 V vs. Li/Li^+ and the ionic conductivity are comparably low, thus limiting energy and power density. Moreover, its potential versus degree of lithiation is extremely flat on a wide range of lithiation and a strong charge/discharge hysteresis complicates the state of charge estimation in applications [39]. The last type of cathode material mentioned here, is the spinel-type LMO, the advantage is, similar to LFP, the low-cost and non-toxicity. However, the challenges are the manganese dissolution (cf. section 2.3.4), a high self-discharge rate and bad high current capability, which omit its use for automotive batteries [39,40].

The important feature of a suitable electrolyte for lithium-ion batteries is its high lithium ion conductivity which is provided by low viscosity (η) solvents. The properties should remain reasonably constant in the range of -20 °C to 60 °C and a good thermal as well as chemical stability in the range of typical operation conditions of LIBs in automotive application is required. The solvents have to dissolve the salts properly; also, a high dielectric constant of the solvents is required and no toxic/hazardous substances should be used. The state-of-the-art electrolyte in commercial lithium-ion batteries fulfilling these requirements is based on organic carbonates with 1 $Mol \cdot l^{-1}$ $LiPF_6$ dissolved as conducting salt. The use of an aqueous electrolyte is inhibited by the high cell voltage of ~3.7 V (cf. Figure 5) as it exceeds the electrolysis voltage of water at 1.23 V. Thus, in the past 40 years different mixtures of cyclic carbonates (ethylene carbonate EC, propylene carbonate PC) and linear carbonates (di methyl carbonate DMC, ethyl methyl carbonate EMC, di ethyl carbonate DEC), as shown in Figure 8a, have proven their applicability. The cyclic carbonates with their high dielectric constant enable the solvation of the salt while the linear carbonates improve the ion conductivity due to their low viscosity. A mixture of these carbonates enables low temperature usage of the electrolyte since EC in pure form is not liquid at or below room temperature with its melting temperature of 36.4 °C [20].

The commonly used conducting salt is $LiPF_6$. Even though $LiPF_6$ is not outstanding in any of the important properties of a conducting salt in carbonate solution because it has lower ion conductivity than $LiAsF_6$, a low thermal stability at <80 °C compared to >100 °C for most of the other available salts, and it suffers from hydrolysis when H_2O contamination is present

(see Figure 8b). However, $LiPF_6$ has no eliminating feature that impedes commercial use; rather it has a quite balanced mixture of properties. Some candidates besides the $LiPF_6$ are often used. However, each of them has at least one elimination criterion. $LiClO_4$ and $LiAsF_6$ were used in the early years of LIB research due to their high ionic conductivity and thermal/chemical stability. Nevertheless, $LiClO_4$ is a potential explosive and $LiAsF_6$ is highly toxic and these properties impede their commercial use. $LiBF_4$ has proven its potential in cycle stability, due to its stronger B-F bond compared to P-F. It is less subject to hydrolysis and thermal degradation. Additionally, the formed SEI is less ion-resistive than the SEI formed with $LiPF_6$. However, the ionic conductivity of $LiBF_4$ is significantly lower than that of $LiPF_6$, thus impeding its commercial use in high-power applications [38].

In addition to the solvents and the conducting salt, a variety of chemicals is used as additives to improve certain properties. Vinylene carbonate (VC) is the most prominent additive forming a thermally more stable SEI [62]. With 1,3-propane sultone the formation of gas during operation at high temperatures ~55 °C is significantly reduced [63]. Different types of sulfites have been reported to improve the Li^+ diffusion of the SEI [64]. Additionally, additives can be used as fire-retardants, salt stabilizers, cathode protection agents, Al corrosion inhibitors and many more functions as reported in literature [64].

a)

	EC	PC	DMC	EMC	DEC
	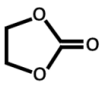	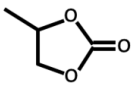	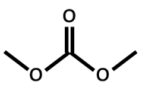	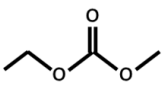	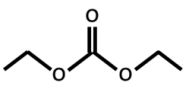
Viscosity (cP)	89.78	64.92	3.107	2.958	2.805
Dielectric constant	1.90 (40 °C)	2.53	0.59 (20 °C)	0.65	0.75
$T_{melting}$ (°C)	36.4	-48.8	4.6	-53	-74.3
$T_{boiling}$ (°C)	248	242	91	110	126

b)

	$LiPF_6$	$LiClO_4$	$LiAsF_6$	$LiBF_4$
	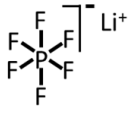	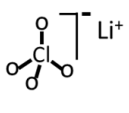	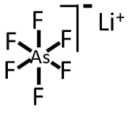	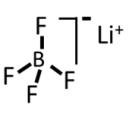
$T_{decompose}$ (°C)	~80	>100	>100	>100
Ionic conductivity (mS·cm^{-1}) in EC/DMC	10.7	8.4	11.1	4.9

Figure 8: Characteristic information on common solvents and conducting salts of carbonate-based electrolytes in lithium-ion batteries, adapted from [37].

The production of LIBs starts with the electrode production. Therefore, state-of-the-art graphite electrodes are produced by mixing graphite with a binder (Na-carboxy methyl cellulose, CMC or polyvinylidene difluoride, PVDF) dissolved in an appropriate solvent (slurry). This slurry is then coated on both sides of a thin copper foil (thickness $\sim 10\,\mu$m). During drying, a porous system emerges which enables electrolyte to penetrate the entire depth of the electrode and thus enables lithium ions to access the graphite particles. Cathode electrodes using NMC are manufactured by the same procedure. PVDF is used as binder material and the aluminum current collector thickness is thicker ($\sim$15-20 μm). Depending on the desired type of format and the type of electrode configuration, the electrodes can be cut and stacked separated by single separator sheets or z-folded using a continuous separator band. Another method is the production of a so-called jelly-roll, in which continuous bands of the electrodes and two separators are wound. As shown in Figure 9, three types of cell housings are common, the pouch-bag type (Figure 9a), the prismatic hard case type (Figure 9b) and the cylindrical hard case type (Figure 9c).

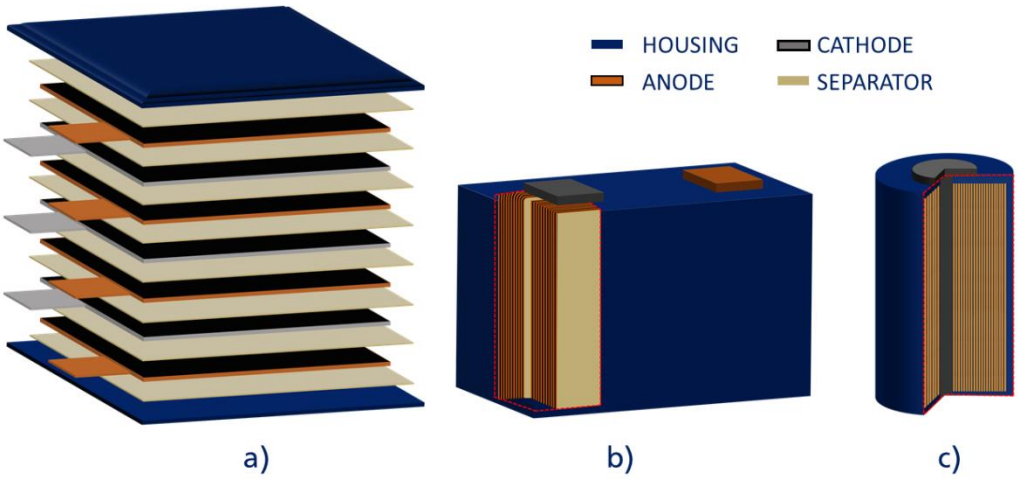

Figure 9: The three types of lithium-ion cell formats: a) expand of a pouch cell, the electrodes are stacked, b) prismatic hard case lithium-ion cell, cut open to see the wound electrodes, c) cylindrical cell, cut open and the wound jelly-roll can be seen. (Own drawing)

The differences between the types lie in their material of casing, pouch foil and metal hardcase container. In the pouch-bag type typically a stacked or z-folded electrode stack is applied, while hard case cells have a jelly-roll implemented. Typically, the anode electrode is larger than the cathode by at least 1 mm in all dimensions, in order to prevent the cell from lithium plating at the edge (cf. section 2.3.5). The electrode current collectors are joined to a single tab by laser welding. Nickel is used as anode tab and aluminum is used as cathode tab. Before sealing the housing, the air-sensitive electrolyte is added by a dosing needle. The last

step of cell production is the formation. A specified cycling procedure at varying temperatures is applied to the cell in order to form a good quality SEI. Gas evolving during this step is removed from the cell before the final sealing. A more comprehensive description of the cell production process is presented in literature [65].

2.3. Lithium-Ion Battery Degradation Mechanism

In the following section, the degradation mechanism of state-of-the-art LIBs will be discussed. The focus is the mechanisms, which are investigated in this study, lithium plating, the formation and growth of the solid electrolyte interphase, gas evolution, as well as the degradation mechanisms of the cathode. The section will be completed with a short discussion of inhomogeneous degradation and the interplay of different mechanisms.

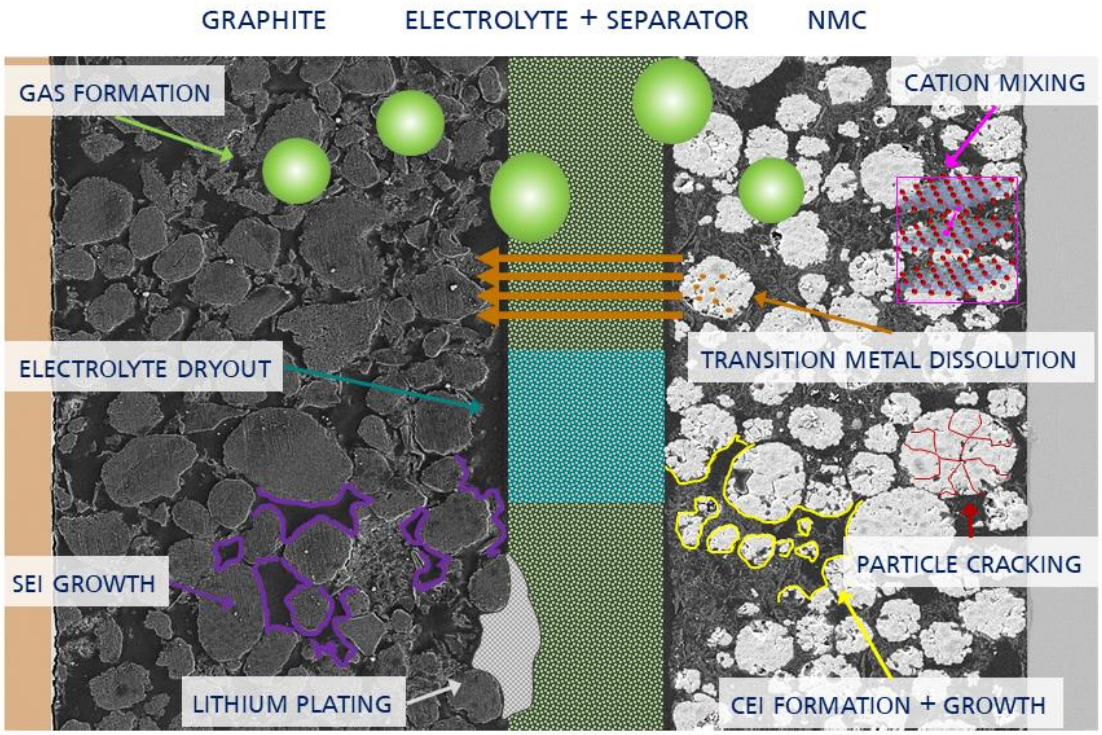

Figure 10: Overview of the main aging mechanisms in automotive lithium-ion cells. (Own drawing)

Many studies [66–71] dealing with degradation mechanisms in lithium-ion cells have been published in the past few years and more than 20 mechanisms have been observed to date [70]. Numerous studies have been conducted using all possible types and combinations of materials, cell designs, quality grades of materials and operation conditions. Furthermore some mechanisms are observed on lab-scale cells and are monitored for a few formation cycles only [67,68,72]. Additionally, the majority of tests on the degradation of large-format lithium-ion cells are accelerated by intense conditions, which may not regularly occur in later

applications. Cycle tests at T∼0 °C or T∼40 °C, combined with high currents [12,14,15,73,74], and calendar aging tests at high storage SOC and at temperatures ranging between 40 °C and 60 °C [75–78] are typically performed. As a result, differing degradation mechanisms are predominant. Today's knowledge on the major degradation mechanisms is illustrated in Figure 10 and the following subsections.

2.3.1. Dendritic Lithium Growth – Lithium Plating

The most prominent degradation mechanism of LIBs is the formation of metallic lithium on the anode surface. According to Legrand et al. [79] the deposition of metallic lithium is thermodynamically favored when the anode potential drops below the equilibrium potential of the reaction 3 during the charging process.

$$Li^+ + e^- \rightarrow Li^0 \qquad (3)$$

Which means that the anode potential becomes lower than 0 V vs. Li/Li^+. Lithium plating can typically be observed when the lithium metal (0 V vs. Li/Li^+) or graphite (stage I ∼0.08 V vs. Li/Li^+) are used as anode. In principle the deposition of metallic lithium is a reversible reaction with the deposition during the charging process and the so-called stripping during the discharge process. However, the potential of the metallic lithium deposits is outside the stability window of the electrolyte. Hence, irreversible reactions of the metallic lithium with the electrolyte occur and the active lithium inventory is reduced.

For the graphite electrode, lithium plating is either charge transfer limited, lithium ions reach the electrode surface faster than they are transferred into the electrode or solid diffusion limited, the lithium ions enter the graphite particle without sufficient diffusion into the bulk particle as presented in Figure 11 [79]. The operation parameter leading to lithium plating due to charge transfer limitation is a high charge current [12,80,81] as too many lithium ions are transported to the graphite surface. The potential becomes low and metallic lithium deposits on the surface [82,83]. The operation parameters leading to lithium plating due to solid diffusion limitation are either a high SOC or low temperature, both slowing down the diffusion of lithium ions in the graphite particles [12,81,84–86].

When lithium is plated on the electrode, the surface of the lithium reacts with the electrolyte forming a SEI. Therefore, a part of the lithium is irreversibly lost from the active lithium inventory to the inactive SEI. Fortunately, lithium plating is partly reversible, as long as the metallic lithium is electrical connected, lithium ions can dissolve in the following discharge and further contribute to the cell function. In the worst case the plated lithium cannot be

stripped off and reacts with the electrolyte under the formation of electrical insulated islands [67]. This irreversible loss of lithium diminishes the amount of active lithium, which is available for the charge/discharge process, resulting in a decrease of capacity.

Besides the loss of cell performance, lithium plating is a safety-critical degradation mechanism. The metallic lithium tends to exhibit dendritic growth, which may result in electrical short circuiting by puncture of the separators, potentially followed by a thermal runaway [67]. Thus, the operation conditions have to be limited in order to avoid lithium plating.

Many studies evaluated the suitability of various fast charging protocols avoiding lithium plating [12,74,79,84,87]. One method of preventing lithium plating is the multi-step constant current charging procedure by Liu and Luo [88] reducing the constant current stepwise with increasing SOC. The method by Sieg et al. [89] prevents lithium plating and, at the same time optimizes the charging time. The maximum possible charge current without violation of the plating limit is determined on three-electrode test cell level by regulating the current in a way that the anode potential is kept closely above 0 V vs. Li/Li^+ until the maximum cell voltage is reached. Then a constant voltage step is performed until the cell is completely charged. After repeating this measurement at different temperatures, the resulting charge current map can be easily transferred to the large-format pouch/hardcase cell, which enables shorter charging time without degradation by lithium plating [89].

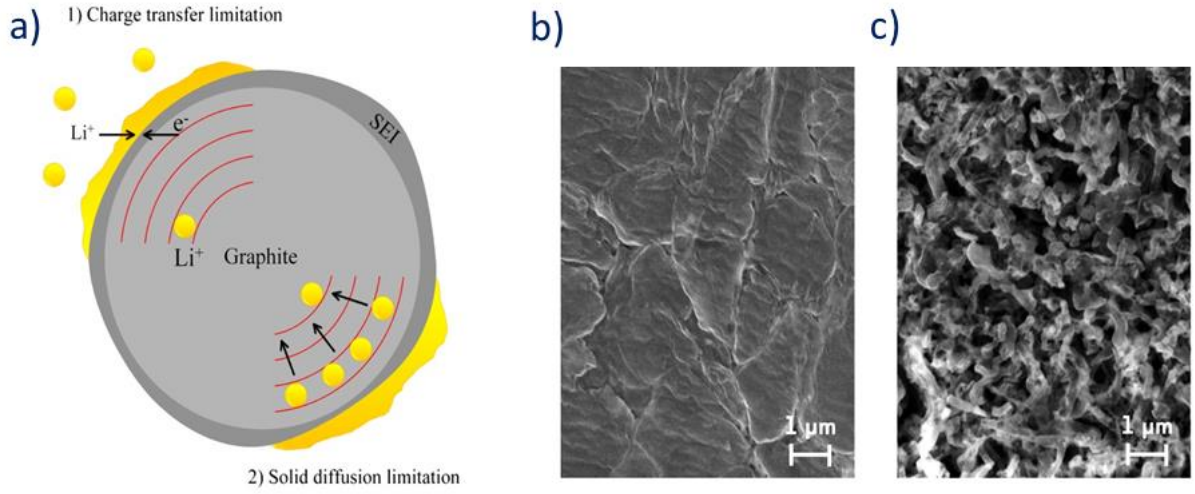

Figure 11: a) Schematic of a graphite particle and the two cases of limitations leading to lithium plating (reproduced from [79] Copyright 2014, with permission from Elsevier[2]). b) SEM image of a dense plated lithium metal layer and c) dendritic grown lithium metal each on a graphite anode (reproduced from [90] Copyright 2016, with permission from Elsevier[3]).

However, on the level of commercial LIBs, most methods for preventing the cells from lithium plating do not explicitly consider the effect of inhomogeneous conditions, i.e. a current density gradient, a temperature gradient and a pressure gradient [77,90–93]. Thus, section 3.3 is dedicated to inhomogeneous cell conditions leading to inhomogeneous distribution of lithium plating and the degradation which may not occur in the homogenous case.

2.3.2. The Solid Electrolyte Interphase

The SEI is a lithium ion permeable and electrical-insulating surface film on the negative electrode (e.g. metallic lithium, graphite) and a decomposition product of the electrolyte, arising at the electrode/electrolyte interface [94]. It is a passivating layer protecting the electrode surface from contact with the electrolyte and further decomposition. By peeling of the solvation shell of the Li ions before entering the active material it protects graphite from solvent co-intercalation and exfoliation.

The SEI forms when the electrode potential is located outside the electrolytes stability window, which can be the case for pristine material — lithium metal 0 V vs. Li/Li^+ — or when the electrode is lithiated. The onset point of the SEI formation is at around ~0.7-0.8 V vs. Li/Li^+ [45,95,96], whereas the potential of pristine graphite is higher, in typical usage the graphite potential ranges between ~0.8 V and ~0.08 V (cf. Figure 6) when it is once charged and used in cell voltages of 2.5 V to 4.2 V [95]. This implies that during operation graphite constantly has the potential to form additional SEI. Therefore, the SEI is also a crucial constituent of a stable long-life lithium-ion battery, as it prevents the direct contact of electrolyte and the anode interface. Thus, slowing down further electrolyte decomposition to a minimum and preventing the graphite from solvent co-intercalation [97]. But on the other hand, the SEI formation irreversibly consumes electrolyte and active lithium and, therefore, restricts the cell lifetime due to deterioration of the resistance and capacity [98–101]. Thus, ideally, a thin and stable passivating SEI should form in the initial cell formation procedure and only minor SEI growth, during the operation.

Typical SEI formation reactions include the carbonates from the electrolyte, and intercalated lithium and electrons [96,102,103]:

$$2C_3H_4O_3 + 2Li^+ + 2e^- \rightarrow (CH_2OCO_2Li)_2 + C_2H_4 \qquad (4)$$

$$C_3H_4O_3 + 2Li^+ + 2e^- \rightarrow Li_2CO_3 + C_2H_4 \qquad (5)$$

The main constituents of the SEI using $LiPF_6$/carbonate-based electrolytes have been identified to be lithium alkyl carbonates ($ROCO_2Li$), especially lithium ethylene dicarbonate ($(CH_2OCO_2Li)_2$) and lithium carbonate (Li_2CO_3) and additionally lithium fluoride (LiF) [104–108]. LiF forms according to equations 6-8 due to the decomposition of the conducting salt [109]:

$$LiPF_6 \rightleftharpoons LiF + PF_5 \qquad (6)$$

$$PF_5 + Li_2CO_3 \rightarrow 2LiF + POF_3 + CO_2 \qquad (7)$$

$$PF_5^- + ne^- + nLi^+ \rightarrow LiF + Li_xPF_y \qquad (8)$$

However, impurities, i.e. water or hydrofluoric acid can further react with the constituents of the SEI:

$$2ROCO_2Li + H_2O \rightarrow 2ROH + Li_2CO_3 + CO_2 \qquad (9)$$

The thickness of the SEI is assumed to be in the range of several nanometers to several hundreds of nanometers [106,110–116]. Moreover, it depends on the electrolyte components and the formation procedure, which is the first cycles of a cell subsequent to the production process and are crucial to control the initial SEI formation. Furthermore, the structure of the SEI is identified as a compact inorganic inner layer in the vicinity of the graphite particles of up to 10 nm and a porous organic outer layer on the electrolyte side (cf. Figure 12a) with thickness of up to several hundred nanometers [109,112,117–120]. Tang and Newman [119] assume that solely the outer porous system grows in thickness and the inner layer forms immediately, staying constant during aging.

However, three different general growth theories (cf. Figure 12 b-d) explaining the increase in SEI thickness during operation are commonly discussed in literature:

- **e^- tunneling** through the SEI to reach and react with the electrolyte molecules [94,121]
- **solvent diffusion** through the SEI reaching the anode surface and forming new SEI at the interface electrode/SEI [122]
- **SEI crack formation** due to reversible graphite expansion (~10%) followed by SEI growth on excavated surface [109,123–125]

Li et al. [121] describe the SEI growth as an electron tunneling from the graphite through the inner compact layer to the outer porous layer where the SEI building reaction of the solvent

molecules and the electrons take place (cf. Figure 12b). This formation route can only be valid in case of a very thin inner compact layer in order to allow electron tunneling (a few nanometers). Ploehn et al. [122] adapted the model of Peled [94] so that the solvent molecules diffuse through the SEI and are reduced at the interface graphite/SEI (cf. Figure 12c). The passivating effect is explained by a slowdown of the solvent diffusion through the SEI. Aurbach [109] explained the SEI growth as an dissolution and precipitation process of the initial formed SEI. The initial SEI undergoes a breakdown process and bare electrode surface is exposed to the electrolyte solution. Deshpande et al. [123] complements these SEI growth mechanism by a mechanical part, the volume expansion of graphite during the lithium intercalation causes mechanical stress on the SEI, which leads to crack formation (cf. Figure 12d). Bare graphite surface is exposed to the electrolyte solution and forms new SEI. This mechanism is repeated for each charge and discharge cycle and thus, the ideal passivating effect of the SEI is weakened during operation. In the real system most probably none of these SEI growth models will appear solely, but rather a combination of electron tunneling, solvent diffusion and crack formation will lead to the growth of the SEI.

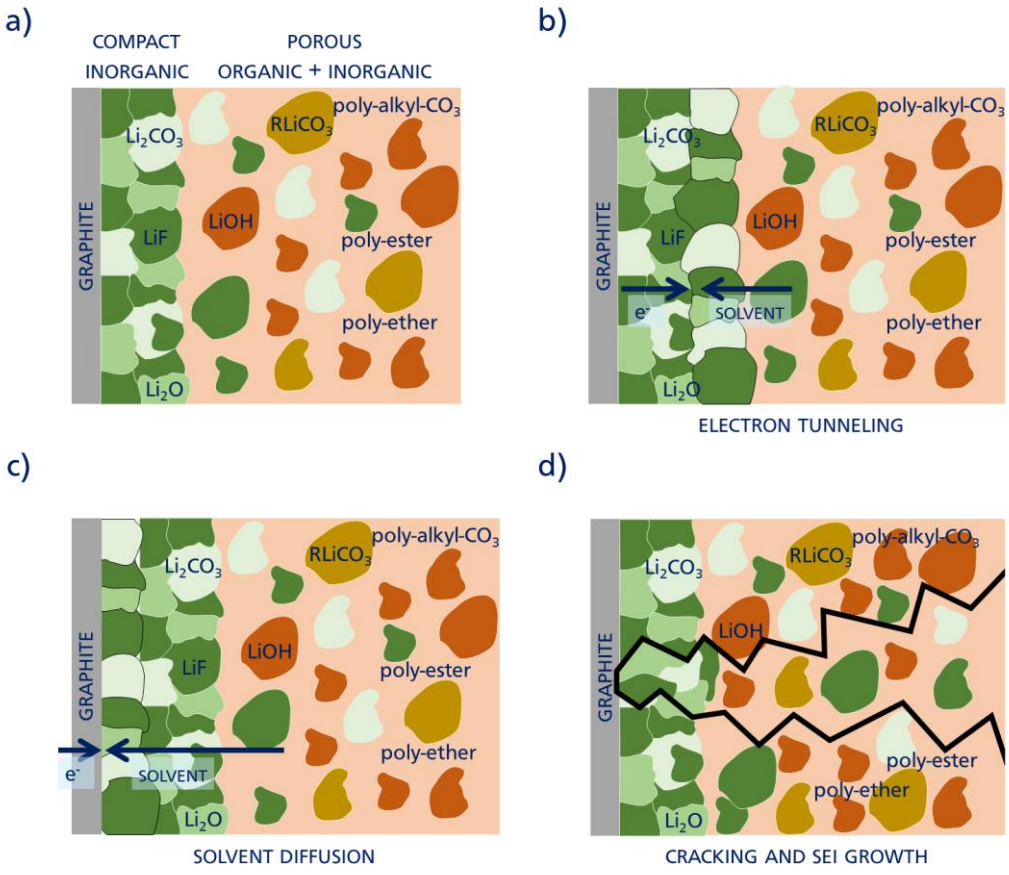

Figure 12: Schematic of the SEI structure and constituents as reported in the literature, own drawings adapted from [109,119,126–129].

Independent from the growth mechanism of the SEI, the increase in thickness and amount comes along with degradation of the LIB. On one hand side the SEI formation consumes lithium from the active lithium inventory resulting in capacity degradation. On the other side, it consumes solvent and salt of the electrolyte which results in performance degradation. Additionally, the growing SEI possibly clogs the porous network of the graphite electrode, again resulting in an increase of the resistance. This pore clogging in turn can provoke lithium plating due to the reduced active graphite surface and thus, locally increased current densities. Another factor for the quality and the growth of the SEI is the presence of impurities from the cell components, e.g. traces of water stemming from the electrolyte or impurities resulting from degradation of the cell components, e.g. manganese incorporation into the SEI and catalytic acceleration of the SEI growth (section 2.3.4). In terms of the operation conditions, two parameters influence the growth of the SEI mostly, the SOC of the cells, which correlates with the graphite potential/graphite stage and the temperature, which is assumed to accelerate the SEI growth in an Arrhenius-like behavior [130,131].

On the level of large-scale lithium-ion cells, only a few studies have been conducted to date, evaluating SEI formation [100] and growth [118] as a result of calendar aging for six months at 60% SOC and 100% SOC with and without subsequent cycling. They observed the main components of the inner and outer SEI [100] and a thickening effect at high SOC aging and additional cycling [118]. Therefore, analyzing the SEI resulting from long-term aging tests with a wide range of operation conditions is performed in this study.

2.3.3. Electrolyte Decomposition — Gas Evolution

The mechanism of gas formation cannot completely be separated from the above mentioned growth of the SEI. According to the equations 4 and 5, ethylene gas can form as decomposition product from ethylene carbonate at the anode [96,102,132]. Similarly, the rest of the electrolyte solvents and additives, i.e. DMC, VC can decompose under formation of gases [133]. This decomposition is driven by the anode electrode potential being outside the electrolyte stability window (cf. Figure 5). Therefore, the solvent reduction on the anode happens to a great extent during the formation of the cell, but also during normal operation, as the SEI may breakdown or gets damaged (cf. section 2.3.2). With increasing SOC, that is, decreasing anode potential, this process is enhanced and, consequently the amount of gas formed at high SOC increases as well. Besides the reductive decomposition of the electrolyte on the anode, the electrolyte can react with oxygen released from the cathode in an oxidation reaction under formation of CO_2, CO, H_2O and H_2 or by an electrochemical reaction at high cell voltages [134–139].

Additionally, many studies have observed an increase in the amount of gas formed during operation at high temperatures above 40 °C [103,140–143]. $LiPF_6$ is stable for temperatures beyond 60 °C [144]. However, according to equation 6, it is in equilibrium with LiF and PF_5 [145]. PF_5 further reacts according to equation 7 and 8, therefore it is removed from the equilibrium [103,145–147]. The thermal enhanced decomposition of the electrolyte is one of the reasons for the typical operation temperature limit of 60 °C.

Besides the importance of the operation conditions for gas evolution, the production quality is crucial. Already, low amounts of impurities, i.e. H_2O, HF can dramatically influence the electrolyte decomposition concomitant with the formation of gas [132,148].

However, independent of the origin of the gas formed inside the cell, the challenge is that typically lithium-ion cells are sealed tight in order to protect the cell interior from the outside. In the same time gas from the inside cannot be release from the cell. To a certain amount the evolution of gas is already included in the cell design, e.g. gas pockets on the edges of pouch-bag cells or free volume in hardcase cells (cf. Figure 9). Another challenge is that the gas can be trapped inside the porous network of the electrodes or inside the electrode stack/jelly roll, henceforth, the dried out areas are electrochemically inactive. Nevertheless, the volume which a cell can withstand is limited and in case of too much overpressure, the cell case will open, release the gas and ambient air can penetrate the cell.

2.3.4. Cathode Degradation Mechanism

Besides the degradation reactions on the anode and the decomposition of the electrolyte, different types of cathode degradation mechanisms can occur. The cathode active material can crack, transition metal ions can dissolve into the electrolyte, cation mixing in the crystal structure of the transition metal oxides can occur and, similar to the SEI on the anode, a cathode electrolyte interphase (CEI) can form.

The state-of-the-art transition metal oxide cathodes, i.e. NMC532, NMC622, and NMC 811 are produced as large secondary particles ($\sim 5\,\mu m$–$10\,\mu m$) formed out of many primary particles ($<0.2\,\mu m$–$1\,\mu m$) [149,150]. Electrochemical cycling of these materials results in volume expansion of 1–4% [39,151,152] depending on the composition of the transition metal oxide. This is the reason for the formation of cracks in the secondary particles, so called intergranular cracking [56,153]. Sun et al. [150] identified lattice expansion due to the diffusion of Li^+ ions as one of the critical processes. Thus, Liu et al. [149] propose to reduce the sizes of the primary and secondary particles; adjusting the voltage range during operation, or apply a coating on the secondary particles to mitigate the mechanical stress. Another

option to avoid the cathode particle cracking was recently discussed by Harlow et al. [60], they studied the degradation of single crystal NMC532/graphite cells. Even after ~5000 cycles no significant cracking of the single crystal cathode and excellent capacity retention of the cell. They concluded that these new single crystal NMC532 containing cells enable far more lifetime, e.g. an electric car can be powered for more than 1.6 million kilometers or more than 20 years of usage in grid storage. Liu et al. [61] extended this study to more nickel containing NMC622 and NMC811, again no cracking of the single crystals was observed.

As presented in Figure 7a, the typically used NMC materials have a layered structure containing a layer of lithium and a layer of the transition metal oxide. When the lithium ions leave the material, empty sites remain in the crystal structure. Nickel ions, which are similar in ionic radius, i.e. Li^{+}=0.76 Å and Ni^{2+}=0.69 Å [154], may occupy these empty sites or interchange with the lithium ions. As a consequence, the diffusion of the lithium ions and the lithium sites for intercalation during the discharge process are blocked. This effect has been found to depend on the chemical composition of the active material, for example, NMC containing less nickel is less prone to cation mixing [59]. Additionally, cation mixing depends on the degree of delithiation and thus amplifies at high cathode potentials during electrochemical cycling [155].

Similar to the SEI on the anode side, the CEI forms on the surface of the cathode side. The major difference is the lower thickness of the CEI with ~1 nm–5 nm compared to that of the SEI counting up to hundreds of nanometer which complicates its detection and degradation analysis. However, the main constituents are similar, that is, LiF, Li_2CO_3, and R_2CO_3, resulting from the decomposition of the conducting salt and the electrolyte solvents [156]. Qian et al. [156] highlighted the major impact of the selection of additive on the constituents and the structure of the CEI. Besides the appearances, many questions on the properties of the CEI still remain open [156–158]. The investigations on the CEI are complicated since its composition and properties change with the electrode potential [159].

Transition metal dissolution is another degradation mechanism regarding the cathode active material. The disproportionation reaction of Mn(III), the phase transformation mechanism and a chemical lithiation and protonation mechanism can lead to dissolution of manganese ions into the electrolyte [160]. However, in the currently used NMC cathodes transition metal dissolution occurs and not only manganese ions but also nickel and cobalt can dissolve and incorporate into the SEI on the graphite surface [161,162]. The manganese ions incorporated into the SEI catalyze the decomposition of the electrolyte. Thus, the capacity fading of the LIB

accelerates [163,164]. As the driving force for the transition metal dissolution, the increase in temperature and upper cut-off voltage has been identified [160].

2.3.5. Inhomogeneity and Reversible Effects

In order to perform realistic lifetime tests, the operating conditions have to be chosen carefully. The material characteristics, the mechanical constraints and temperature control have to be managed properly as described in the following. Otherwise, degradation effects, which would not occur in the application, may distort the test results. Some examples from literature are lithium plating caused by inhomogeneous pressure [91,93], or temperature [165–168] and current density [90,169]. Also, electrolyte dry-out and gas accumulation inside the electrode stack or jelly-roll [74,77] can provoke lithium plating. Therefore, a more profound understanding of the rise and the effects of these gradients and defects is necessary to decide on an ideal test setup and operating conditions.

Reversible effects may also occur in a test setup leading to a misinterpretation of the test results. One of them is called the overhang effect and it was observed first by Gyenes et al. [170] when measuring the Coulombic Efficiency (CE). They observed the dependency of the CE on the storage SOC of the cell, prior to the cycle phase. A storage at SOC 100% results in CE larger than unity even ~100 h after storage. In commercially available LIBs, the anode dimensions are typically designed larger than those of the cathode to avoid lithium plating at the edges of the anode. In stacked, pouch-bag type LIBs, the anode overhang amounts to 1-2 mm in lateral direction and two complete layers on top and bottom of the cell. This anode overhang area equals ~5% of total capacity. Together with the observation of incremental coloring of the anode edge area, which represents different graphite stages (cf. Figure 6), Gyenes et al. [170] concluded that the anode overhang acts as a reservoir for lithium ions. When held at high SOC, lithium is stored in the overhang and the overhang empties when held at low SOC. Later, Wilhelm et al. [171] confirmed the CE measurements and complemented the findings through a post-mortem study and storage SOC-dependent evolution of the cell capacity. Thus, the anode overhang effect has to be considered when interpreting capacity retention of long-term aging tests. Hüfner et al. [172] studied the overhang effect for four different lithium ion cells with different lengths of the anode overhang, showing the correlation of time to get the lithium out of the overhang with the size of the overhang. The short overhang area (~3 mm) can be emptied in ~13 h, while the long overhang area is partly filled even after hundreds of hours. To avoid misinterpretation of the aging test results, modeling of the effect and correction of the capacity retention or the preconditioning of the batteries prior to the aging test can improve the validity of aging tests.

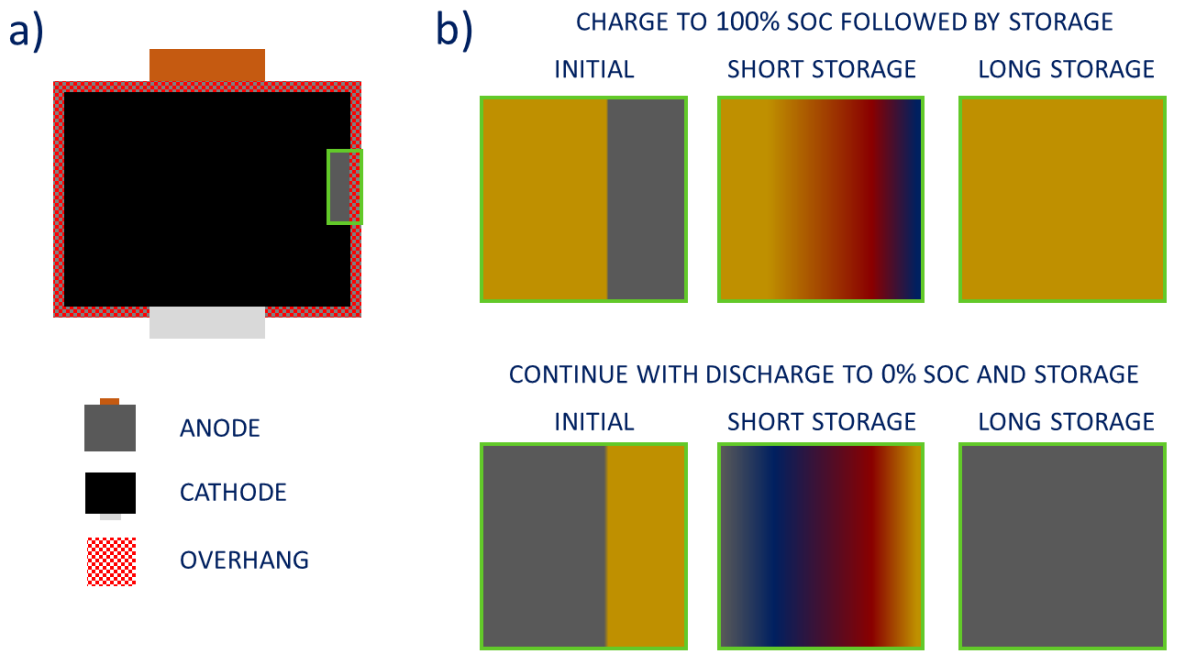

Figure 13: a) Schematic of the anode overhang area resulting from oversized anode dimensions; the green rectangle cuts through the cathode and b) illustration of the procedure of lithium transport from active anode area to the overhang area from charging the cell to 100% SOC, followed by short/long storage. Below: the overhang emptying due to subsequent discharge to 0% SOC and short/long storage. Coloring of the graphite represents the intercalation stages, according to Figure 6. (Own drawing)

2.4. Non-Destructive Cell Analysis

In this section, the non-destructive methods to analyze the degradation of lithium-ion cells are explained. The electrical testing results, namely capacity retention, resistance and differential voltage (DV) analysis are addressed in detail. The second part of the section contains the non-destructive methods to determine the volume and geometrical data prior to the aging test and afterwards.

2.4.1. Electrical Testing of Lithium-Ion Cells

In regular intervals, the condition of the tested cell is monitored in a check-up test. The check-up can take up to several days depending on the steps included and the depth of information to be gathered. Therefore, a decision on including detailed steps depends on the question of resources, testing time and budget as well as the deterioration of the aging test by the check-up, itself. In total, the check-up, shown in Figure 14, lasts ~67 hours, which is extremely long for regular aging tests. However, this strongly improves the database for the analysis of the degradation mechanism. Typically, a check-up contains at least one cycle, with constant current applied, between the upper and the lower voltage limit to measure the capacity, and a pulse test at a constant SOC to measure the resistance.

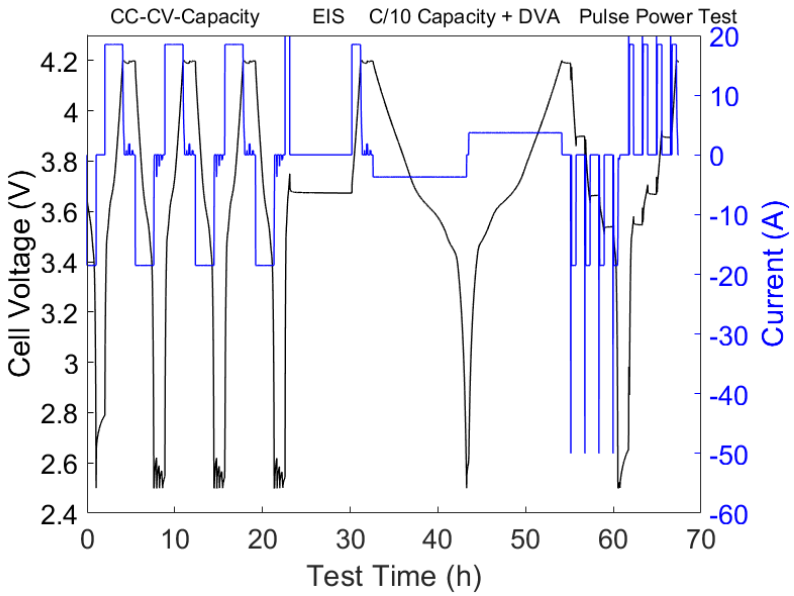

Figure 14: Exemplary current (blue) and voltage (black) profile of one check-up test used in this study.

However, the capacity measurement can be performed in various modes by applying different voltage limits and different charge and discharge rates depending on the required information. The capacity is determined by counting the amount of charge inserted into or drawn from the cell. This can be realized by integrating the current over time. Typically, the capacity is given in Ah and can be scaled to the nominal and/or begin of test capacity to determine the capacity retention. The quality of the collected data can be improved by applying low current rates at the cost of test time. Increasing the current rate raises the influence of the resistance effect and the resulting overpotential. Thus, the degradation effects distort the measured capacity. An exemplary current and voltage profile for one check-up used in this study is depicted in Figure 14. This check-up starts with an initial discharge to the lower voltage limit of 2.5 V, followed by three cycles in constant current-constant voltage (CC-CV) mode applying a current of 18.5 A (~0.5C). The CV-phase is separated into three steps each having a smaller cut-off current (C/10, C/20, C/50) separated by breaks of 15 minutes. These three cycles result in three capacity values, of which the last one is used for capacity determination. Afterwards, the cell is charged up to 3.75 V to set the state of charge for the following electrochemical impedance spectroscopy (EIS) measurement. At the end of a seven hour rest step, after the cell is completely relaxed, the EIS measurement is performed. Then the cell is charged to the upper cut-off voltage, which is 4.2 V to prepare the C/10 discharge and charge cycle. This cycle enables a further analysis of the differential voltage and the change in the quasi-open circuit voltage. The last part of the check-up is a pulse test in discharge and charge direction in steps of 25% SOC in order to determine the internal resistance of the test object. A short current pulse of 50 A for 30 s is applied. The internal

resistance can be calculated from the voltage signal using a method established in literature [7,173], clearing the voltage signal from SOC drift and measurement impact (see Figure 15). With the determined initial voltage drop and the pulse current, the ohmic resistance is calculated by Ohm's law equation 10. The higher the applied current, the higher is the voltage drop and the better is the determination of the resistance. However, the current limit of the cell listed in the operation window as provided by the cell supplier, should not be exceeded.

$$R = \frac{\Delta U}{I} \qquad (10)$$

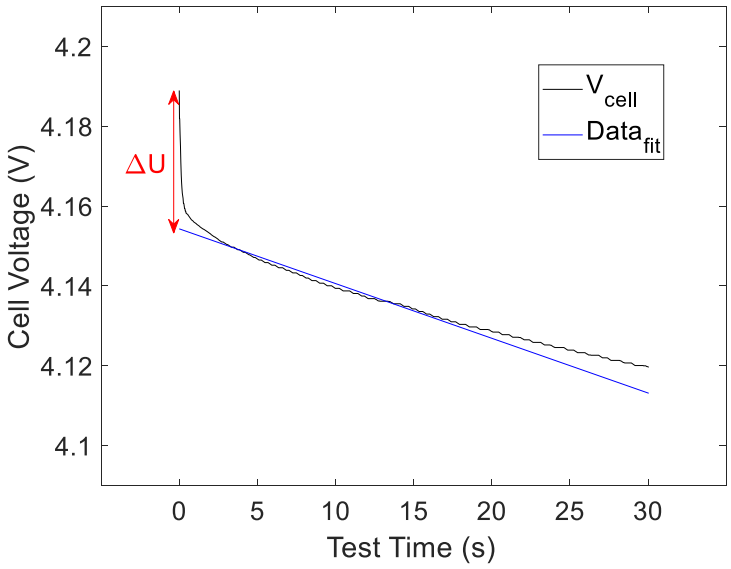

Figure 15: Exemplary voltage signal for a 30 s discharge pulse at SOC 100% with $I_{discharge}$=50 A and resistance evaluation adapted from literature [7,173]. A linear fit determines the initial voltage drop when the pulse starts. Using this voltage drop and the pulse current, the ohmic resistance is calculated by Ohm's law.

Using the low current cycling data collected during the check-up, the DV analysis can be performed. Therefore, the voltage vs. charge-throughput data set (see Figure 16) with a small current rate applied is required. In the ideal case, a highly resolved OCV curve is used for the DV analysis, this enables the high resolution of the DV curve and aging dependent differences can be identified more reliable. However, to record a highly resolved OCV is very time consuming. Thus, in the scientific community it is accepted to record a quasi-OCV curve applying a current rate < C/10 [174–176]. At a current rate of C/10 still the resistance effect on the cell voltage is noticeable, the smaller the current rate, the better is the resolution of the data. Basically, DV analysis is the derivation of the potential/voltage to charge (dV/dQ), depending on the cell configuration either the characteristic curve of one electrode (half-cell potential, electrode vs. lithium reference) or the superposition of two electrodes (full cell voltage, electrode A vs. electrode B, see equation 11 [174]) is investigated.

$$\left(\frac{dV}{dQ}\right)_{cell} = \left(\frac{dV}{dQ}\right)_{electrode\ A} - \left(\frac{dV}{dQ}\right)_{electrode\ B} \qquad (11)$$

In the differential voltage the peaks describe phase transitions [174]. They can be accessed, divided into anode and cathode affiliations, even though the data originate from full cell measurements [177]. The graphite transitions *GIII* and *GII* (see Figure 6 and Figure 16) show up as peaks in DV. By the distance of the graphite peaks, information on the change in anode active material can be obtained; and by the distance from the second peak GII to the end of the graph (*E*), the amount of active lithium can be evaluated. Furthermore, the height and the shape of the peaks offer information on the degree of homogeneity of the lithium distribution of the cell [169,178–181]. The degradation of the cathode can be identified by the areas between the graphite peaks [177].

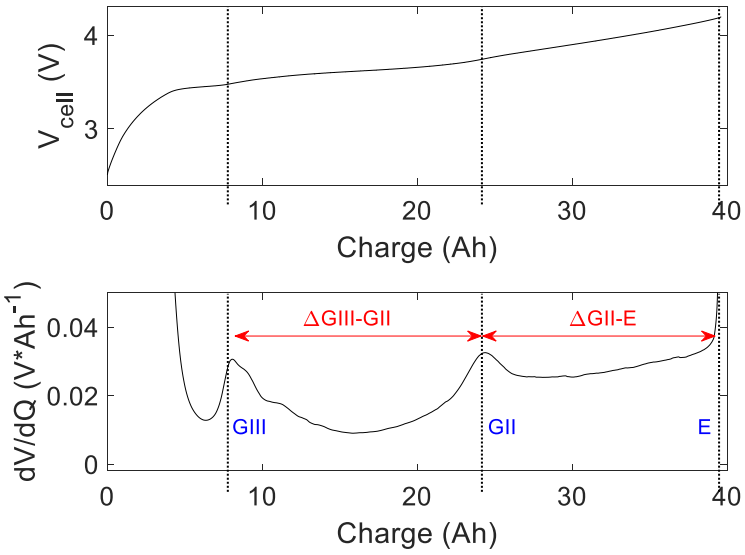

Figure 16: C/10 cell potential and dV/dQ vs. charge. The C/10 graph is derived to obtain the dV/dQ. The resulting peaks represent the points of one phase graphite, either stage III (GIII) or stage II (GII) [47]. The end of the graph represents the fully charged state (E). The change in charge difference between GIII and GII allows determination of the anode active material loss and the change in charge difference between GII and E allows determination of the change in active lithium.

2.4.2. Lithium-Ion Cell Volume Determination

In the following the method for the analysis of the cell volume of large-format LIBs is described. It is derived from the setup for small-scale cells to determine their in-situ volume as presented by Aiken et al. [182]. A schematic of the measurement setup is shown in Figure 17. The underlying principle is known as Archimedes principle for a body in liquid. In the specific, present case the body is represented by the cell and the liquid, that is water, is de-ionized to

prevent an electrical short-circuit of the cell. Two forces are acting on the cell: the weight (equation 12) and the buoyancy force (equation 13). With a force gauge, the resulting force (equation 14) is measured. Inserting equations 12 and 13 into equation 14 followed by rearrangement to the volume, results in equation 15. The volume can be calculated with the mass of the cell m_C measured prior to the experiment, the known density of the liquid ρ_{liquid} and the measured resulting force F_R.

For degradation analysis, the volume change of a cell can be calculated by subtraction of the volume prior to the aging experiment and afterwards. The volume change results mainly from gas built up inside the gas-tight cell.

$$F_W = m_C * g \qquad (12)$$

$$F_B = \rho_{liquid} * V * g \qquad (13)$$

$$F_R = F_W - F_B \qquad (14)$$

$$V = \frac{F_R/g - m_C}{\rho_{liquid}} \qquad (15)$$

F_B = *buoyant force*
ρ_{liquid} = *density of the liquid*
V = *displaced volume*
g = *gravity*
F_W = *weight*
m_C = *cell mass*
F_R = *resulting force*

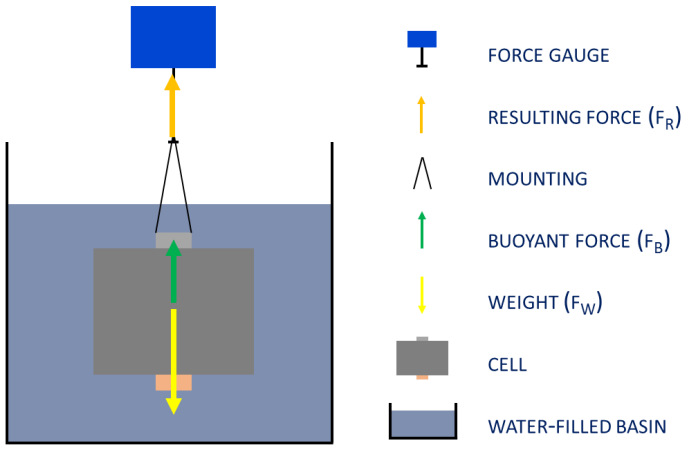

Figure 17: Schematic of the measurement setup for cell volume determination. The acting forces are marked with green and yellow arrows. The force measured with the force gauge is used for the calculation of the volume. (Own drawing)

2.5. Post-Mortem Analysis

In this section, the materials preparation during post-mortem analysis and the following destructive methods to analyze the degradation of lithium-ion batteries are explained. Post-mortem analysis is illustrated, followed by the imaging methods SEM combined with energy-dispersive X-ray spectroscopy (EDX) and FIB preparation for TEM. Then the elemental composition analysis via ICP-OES and surface sensitive XPS in combination with argon-ion etching for depth-profiling are explained. Structure analysis is performed by using XRD and Raman spectroscopy.

The segmentation of a lithium-ion cell is known as post-mortem analysis. It is called post-mortem since it is a destructive method. In the following the working routine, partly adapted from literature [183] and applied in this thesis, is explained and illustrated in the schematic seen in Figure 18. For safety reasons, post-mortem analysis is commonly performed on discharged cells and in inert atmosphere. Also the handling under inert atmosphere allows for proper analysis of the materials gathered from the cell. The discharged cell is transferred into an argon-filled glovebox with water and oxygen contents < 0.1 ppm. Pouch bag cells can easily be cut-open by electrical insulating ceramic scissors or a knife. During the opening process, it is important to prevent the cells from shorting through contact of the electrodes, contact of the current collectors or any bypass through additional non-insulating, metallic tools or particles.

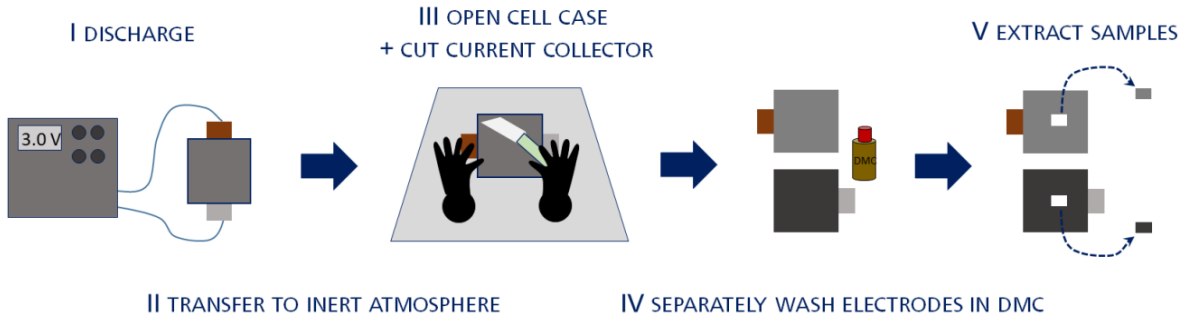

Figure 18: Schematic of the typical post-mortem analysis routine. The lithium-ion cell is discharged and transferred into an argon atmosphere, followed by the cell opening with a ceramic knife. The electrodes from the stack or jelly roll are separated and washed in dimethyl carbonate, to remove residual conducting salt. The electrodes are cut and extracted for further physicochemical analysis. (Own drawing)

The extracted electrodes were placed in a bath of dimethyl carbonate, one of the electrolyte solvents, to remove any electrolyte leftovers, especially to prevent residues of conducting salt. Two separate baths, one for the anode and one for the cathode need to be prepared to prevent cross-contamination. After a drying process the electrodes are prepared for further analysis or packed for storage. Due to personal and environmental protection, all remaining

materials need to be disposed separately (to prevent short-circuits) and professionally as they contain heavy metal (Cobalt, Nickel) and likely traces of hydrogen fluoride [184]).

2.5.1. Selection of Physicochemical Methods

The electrode material gathered from the post-mortem analysis has to be analyzed physicochemical in order to evaluate the presence of the degradation mechanisms and to evaluate their characteristics. A comprehensive overview of possible methods, their advantages and disadvantages is given by Waldmann et al. [183] and Birkl et al. [71]. In Figure 19 several methods are depicted and assigned to the suitable degradation mechanism. However, the plurality of the methods requires a careful selection and combination.

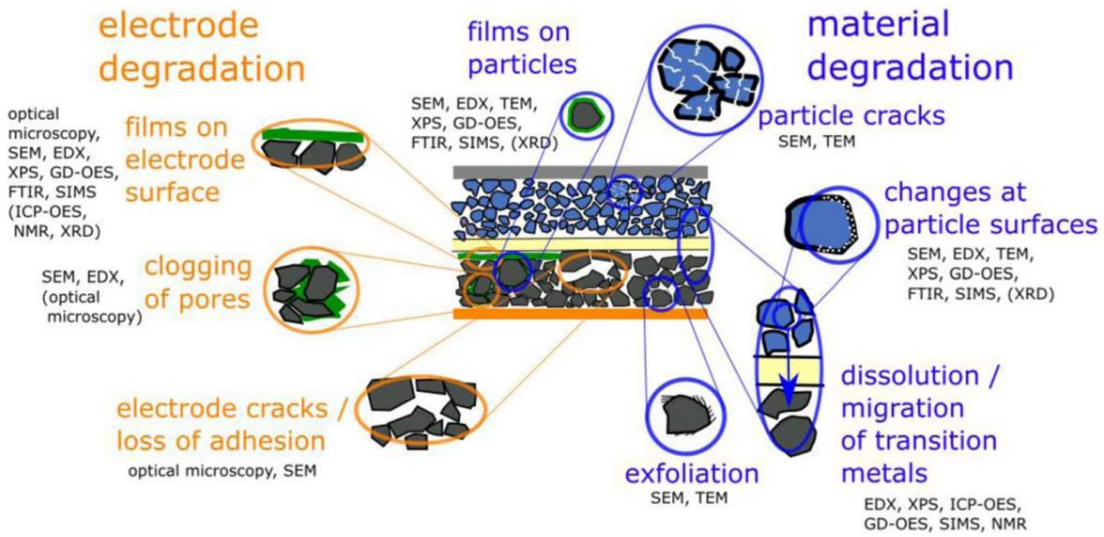

Figure 19: Summary of the degradation mechanism and the corresponding suitable physicochemical method. Methods in brackets have limited access to the mechanism and the methods can be used for the mechanisms occurring on anode and cathode side. Reproduced from Waldmann et al. [183], Copyright 2016, with permission of The Electrochemical Society.[4]

In this study, SEM is used for the optical inspection of the electrode surfaces. It enables a first qualitative identification of the degradation mechanisms like particle cracking, surface film formation, pore clogging, loss of electrode cohesion and exfoliation. For the evaluation of the composition of surface deposits SEM-EDX is used, even though it cannot measure lithium (low energy of characteristic radiation) the corresponding fluor, phosphorous, carbon and sulfur containing reaction products can be identified. Complementary ICP-OES is used to determine the elemental composition of the electrode volume comprising the active material, the binder phase and all possible surface deposits like SEI and lithium plating. FIB-SEM and scanning transmission electron microscopy (STEM) are used for cross-section imaging of the electrode surface. Here, the advantage is that the samples can be prepared in inert atmosphere and with

low energy impact by applying cryo-FIB. STEM then enables imaging the sample in nanometer scale and by the addition of an electron energy loss spectrometer (EELS) an elemental mapping of the imaging area is possible. The degradation of the cathode active material is analyzed using XRD, the crystal structure and defects as a result of repeated cycling can be evaluated. In order to get three-dimensional information on the composition of the electrode and the surface films XPS depth-profiling is applied. The XPS spectra are recorded with stepwise sputtering of the sample with argon ions which results in depth profiles of the investigated elements. Additionally, the XPS spectra can be evaluated in terms of the atomic binding of each species, e.g. the identification of the more-organic and more-inorganic layer of the SEI is possible. A detailed discussion of XPS depth-profiling follows in section 2.5.2. Nevertheless, a single method of the mentioned ones calls for the further complementary methods in order to get a holistic view on the process and degradation arising during the operation of LIBs.

2.5.2. X-ray Photoelectron Spectroscopy

In the following section, the basic working principle of a photoelectron spectroscopy, including the setup as well as advantages and disadvantages, are discussed. In general, electron spectroscopy comprises two methods distinguished by photon energy, namely ultraviolet photoelectron spectroscopy (UPS) using low photon energy from ultraviolet radiation (<100 eV) and X-ray photoelectron spectroscopy (XPS) using X-rays (Al-Kα~1486 eV or Mg-Kα~1254 eV). The latter is discussed in detail. The photons, upon reaching the surface atoms, transfer their energy to the core level electrons that leave the atom as photoelectrons. The kinetic energy of the electrons offers information about the chemical element and the chemical state.

XPS uses photoelectric effect, which was discovered by H. Hertz and his co-worker P. Lenard in 1902 [185,186] and explained by A. Einstein in 1905 [186,187]. In the following years, H. Robinson established a device for electron spectroscopy, but the resolution of its signals was low and the method was hardly used. It took around 50 years until Kai Siegbahn made several modifications to the known setup, which resulted in the first high-resolution, double-focusing spectrometer and the problems of low resolution were overcome [188]. In the following years, the group around Siegbahn improved the setup further and measured binding energies of several elements, setting up a still used database [188]. Due to the great importance of these studies, Kai Siegbahn was honored with a Nobel prize in physics in 1981 [188].

Today's spectrometer comprises a source of primary monochromatic radiation, typically Al-Kα or Mg-Kα, a sample holder for sample mounting and an electron energy filter and detector to

determine the electrons' kinetic energy. All these components are attached to a vacuum chamber (see Figure 20a) that operates in ultra-high vacuum. A computer accumulates, processes, and visualizes the data as shown in Figure 20c.

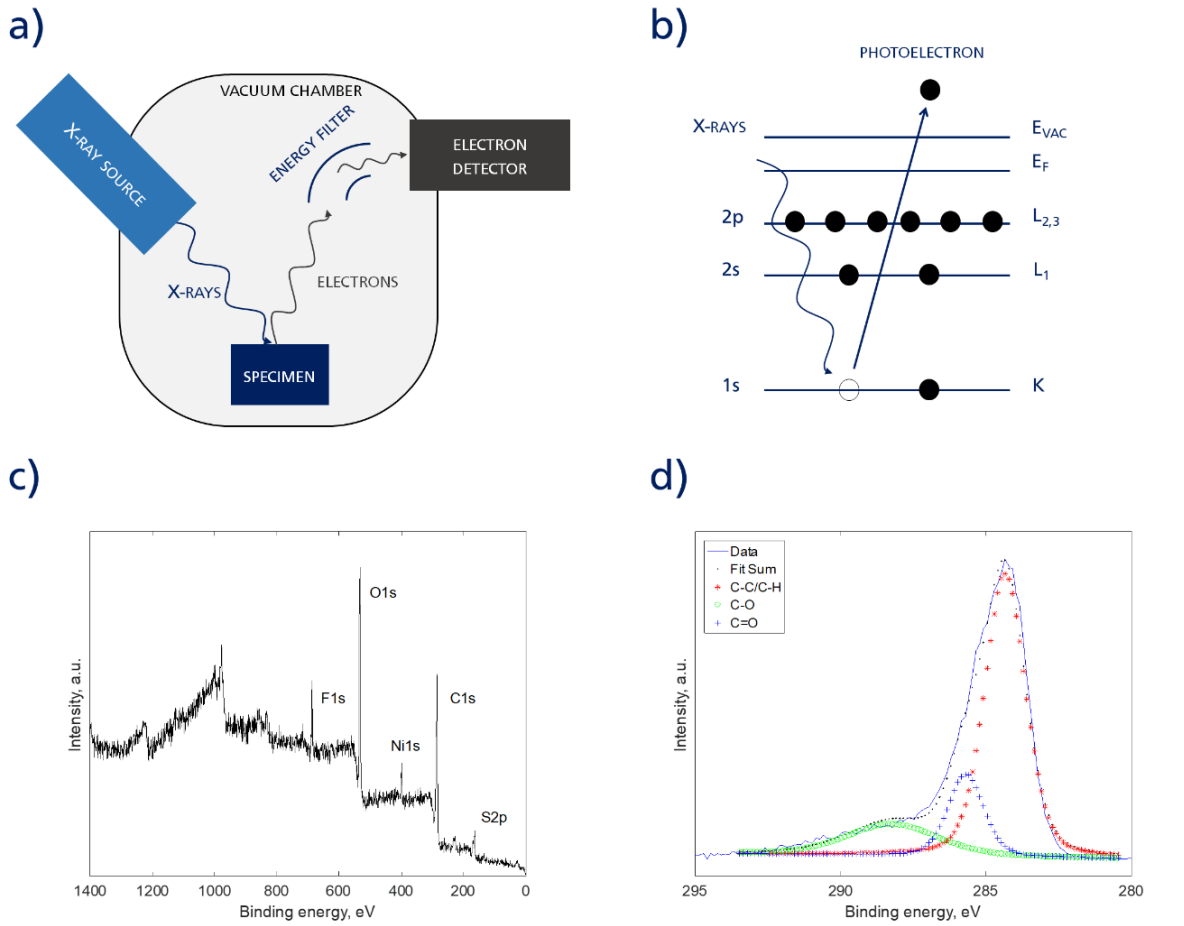

Figure 20: a) Schematic setup of a typical X-ray photoelectron spectroscope, b) schematic of the photoelectric effect with spectroscopic notation left and chemist notation right. a) and b) are own drawings adapted from van der Heide [186]. c) Example of an intensity versus binding energy graph measured with used anode of a lithium-ion battery. A certain region of binding energy belongs to each chemical element; and depending on the chemical state, the peak shifts to lower or higher binding energy. d) Example of peak deconvolution to identify the chemical state of one element, in this case carbon. (Own drawing)

The physics behind the method is based on the photoelectric effect, which is energy transfer from a photon to an electron of an atom with the result of electron release leaving a valence hole (see Figure 20b). Using equation 16 and the measured kinetic energy of the electron E_{kin}, the Planck constant h, the frequency of the photon ν and the work function of the spectrometer W, the binding energy $E_{binding}$ can be calculated.

$$E_{binding} = h\nu - E_{kin} - W \qquad (16)$$

h= Planck's constant
ν= frequency of the photon
E_{kin}= kinetic energy of the electron
$E_{binding}$= binding energy
W= work function of the spectrometer

Depending on the binding of the atom, a shift to lower or higher energy can be observed and the oxidation state of the atom is identified. An additional effect is the release of an Auger electron, which results from a series of processes occurring in the excited atom. An electron from a higher energy level falls into the valence hole and releases energy, which is transferred to an additional electron. This electron of higher energy is emitted and can be measured in the Auger electron spectroscopy (AES).

The high surface sensitivity (3-10 nm [186]) of the XPS is the base for depth-profiling. Depth-profiling can be achieved by recording a surface survey spectrum of the material. In a second step, the surface can be etched by using an ion sputter gun, for example, with argon ions, removing the top surface atoms. Then the next survey spectrum is recorded, again followed by etching. Step by step, the element concentration is determined by this alternation of spectra recording and etching (see Figure 21). Some aspects of the XPS depth-profiling via argon ion etching need to be discussed, especially first the influence of energy impact of the ions on the chemical state of the present atoms. In the first XPS spectrum, the original oxidation states can be evaluated; but when the etching process takes place, organic materials can be modified. The second is the etching rate on flat surfaces, which is usually the case for samples analyzed in XPS. The sputter depth can be measured after the XPS via atomic force microscopy. Then the total sputter depth is divided by the total sputter time and an etching rate results. More complex will be the measurement and calculation when several layers of materials are etched. Each layer may have a different etching rate. Therefore, in literature, often the etching parameter and the etching time are given or for depth calculation they are referred to a calibration material, for example SiO_2. Another aspect is the possible redepositing of atoms on the sample surface after etching.

The analysis of electrode materials of state-of-the-art large-format lithium-ion batteries is not as straightforward as, for example, the analysis of artificially grown thin layers on a flat substrate. The typical electrodes are produced from powders pressed on metal foils and thus the surface is very rough. Nevertheless, literature and own measurements have shown that an analysis of the electrodes surface is still possible and reasonable results can be obtained [113,115,118].

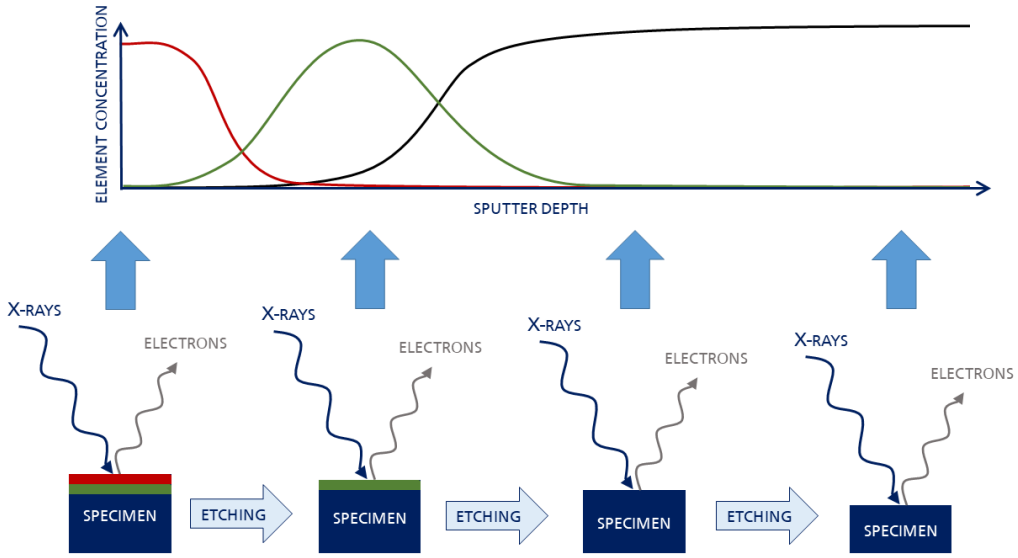

Figure 21: Schematic of the XPS depth-profiling process by argon ion etching on an idealized flat surface. (Own drawing)

3. Cumulative Part of the Thesis

The cumulative part of this thesis comprises the scientific work and findings reported in the publications [1–5]. The degradation mechanism of automotive, large-format lithium-ion cells are discussed in the context of the underlying operation conditions. The discussion starts with section 3.1 picking up the results of calendar degradation through storage of the cells at elevated temperature and state of charge published in [1,4]. Section 3.2 continues with the degradation mechanism during cycle operation. The operation parameters temperature, upper cut-off voltage, depth of discharge and discharge current are evaluated separately and the major degradation mechanisms are assigned. The content of this section is published in [2,5]. Section 3.3 completes the thesis with consideration of the effect of inhomogeneity caused by the large format of the present lithium-ion cells. The formation of current density gradient arising from temperature gradient and inhomogeneous distributed gas inside the electrode stack are examined in [1,3].

3.1. Calendar Aging – Storage Test and Post-Mortem Analysis

The content of this section is published in the following publications:

[1] **Storch M**, Hahn SL, Stadler J, Swaminathan R, Vrankovic D, Krupp C, Riedel R (2019): Post-mortem analysis of calendar aged large-format lithium-ion cells: Investigation of the solid electrolyte interphase.
In: *Journal of Power Sources* 443, S.227-243

[4] Hahn SL, **Storch M**, Swaminathan R, Obry B, Bandlow J, Birke KP (2018): Quantitative validation of calendar aging models for lithium-ion batteries.
In: *Journal of Power Sources* 400, S.402–414

In this section, the battery degradation occurring in calendar aging mode is presented, starting with an extensive, temperature-accelerated test matrix on large-format automotive lithium-ion cells. The present lithium-ion cell has a nominal capacity of 50.8 Ah and a graphite/NMC111 chemistry. As operation parameter, during calendar aging mode the storage conditions state of charge and temperature are varied. Since the capacity fading and resistance increase show that the degradation accelerates with increase in state of charge, the underlying mechanisms are addressed in an extensive post-mortem study. The major innovation in this study is the application of XPS depth-profiling for the determination of the growth of the SEI to a large set of degraded graphite electrodes. In combination with SEM and elemental analysis via ICP-OES, a useful set of methods to quantify the growth of the SEI and to identify additional degradation phenomena is established.

3.1.1. Discussion

A major challenge regarding the lifetime of lithium-ion batteries is the calendar degradation. Due to chemical instability of the electrolyte, several processes lead to a decrease in performance throughout storage. The parameters affecting the degradation in rest mode are known to be the cell temperature and the state of charge. However, the progress rate strongly depends on the composition of the electrolyte and the active materials of both electrodes. Therefore an extended lifetime test using 50.8 Ah pouch-bag type lithium-ion cells consisting of a graphite/PVDF/conductive agent composite anode material coated on a copper foil and a NMC111/PVDF/conductive agent composite cathode on an aluminum foil were performed prior to the experimental work of this thesis. The aging test had a duration of 280 storage days, interrupted regularly by check-up tests to monitor the capacity retention, the resistance and characteristic cell voltage recording for DV analysis.

For one set of cells the SOC was varied between 0% and 100% and the temperature was controlled at 50 °C, for the second set of cells the temperature was varied in steps of 2.5 K between 40 °C and 60 °C and the SOC was set to 85%. The capacity fade and resistance trend validate the common picture of temperature and SOC as accelerating factors of calendar degradation. In order to analyze the underlying degradation mechanism, all aged cells are characterized by volume and finally one cell for each set point is selected for post-mortem analysis. For this purpose, the cells are discharged to 3 V in CC-CV mode to ensure the same condition for all cells, eliminating the influence of actual SOC at beginning of post-mortem analysis. The capacity retention of the cells tested at varying temperature show a typical Arrhenius-like behavior up to temperatures of 52.5 °C. Higher temperature results in increasing cell volume pointing towards accelerated gas formation due to thermal decomposition of the electrolyte. The capacity fade and resistance trend of the storage SOC series in contrast exhibits a more conspicuous development. The cell volume measurements show a strong gas formation starting at SOC 85% and higher. The capacity retention is showing a plateau ranging from 22.5% to 85% followed by a steep decrease at higher storage SOC. Hence, the electrodes harvested from the storage SOC series were further evaluated to identify the underlying degradation mechanisms, as presented in publication [1].

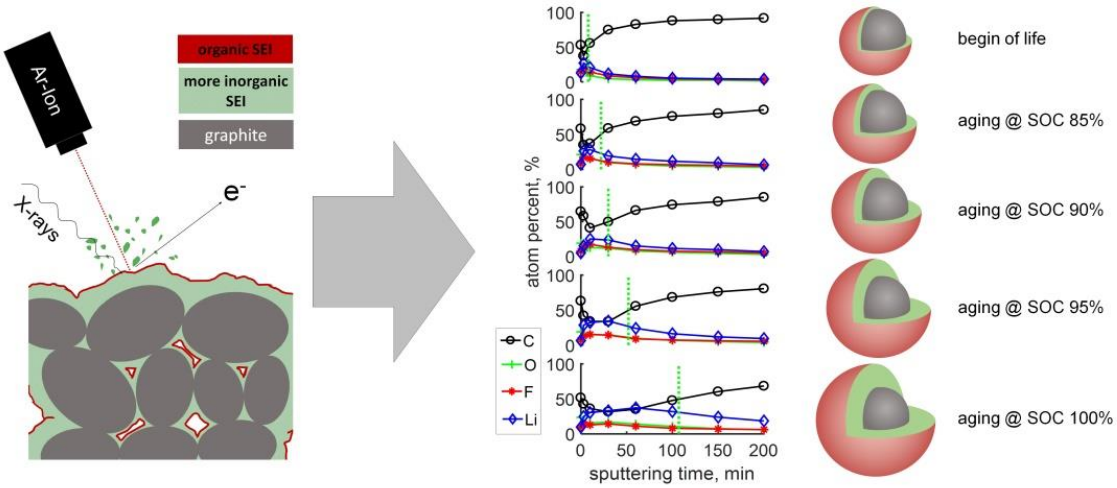

Figure 22: Schematic showing the principal of XPS depth-profiling, the depth profiles of C, O, F and Li and the resulting trend in the SEI thickness. The trends are shown for the beginning of life material and after aging at 50 °C and SOC 85% to 100%. Storage of the cells at the given conditions results in an increase of the estimated SEI thickness from a few nanometers to more than 100 nm. No sharp limit of the SEI can be given due to the rough surface profile featuring the graphite particle's curvatures. The study confirmed the two layers of the SEI with partial more organic outer SEI and more inorganic inner SEI close to the graphite particle. Reproduced from [1], Copyright 2019, with permission from Elsevier.[5]

Figure 22 shows the summary of the obtained results on the evolution of the SEI thickness published in [1]. On the base of XPS depth-profiling the thickness evolution of the SEI due to aging at different storage SOC in combination with a storage temperature of 50 °C is estimated. The sample materials are transferred to the XPS chamber without contact to ambient air, which as the experimental results showed, is crucial for gathering high quality data representing the degradation phenomena. Already a short exposure to air of ~10 min can distort the sensitive SEI. First, a surface spectrum is recorded, followed by argon-ion sputtering and a succeeding XPS spectrum. This is repeated for in total seven sputter steps and eight surface spectra. From the spectra the atomic concentration of each present element is evaluated, the depth profiles of the four major elements of the SEI for each sample are shown in Figure 23. Taking the sputter rate into account the elemental concentration in dependence of the sample depth is estimated. SEM imaging, ICP-OES and Raman spectroscopy results further support the findings of XPS depth-profiling. The estimated SEI thickness match well with the capacity retention of the respective cells in the calendar aging test, see Table 1, which proves the growth of the SEI as the major degradation mechanism of the calendar aging. With a higher storage SOC the SEI growth is fortified and again, the amount of irreversible lost active lithium increases. Hence, both capacity and resistance of the

cell deteriorate. However, the growth of the SEI is not the only degradation mechanism observed in this study. With higher storage temperature and storage SOC more gas is formed, which leads to drying out of the electrodes. Thereupon, continuing the calendar aging with check-up tests results in storage atypical degradation via lithium plating, as it is discussed in 3.3.

Table 1: Capacity retention and estimated SEI thickness

Storage SOC	**S22.5**	**S85**	**S90**	**S95**	**S100**
Capacity retention	91.48%	91.35%	86.86%	78.70%	73.65%
Estimated SEI thickness(nm)	9	22	30	52	107

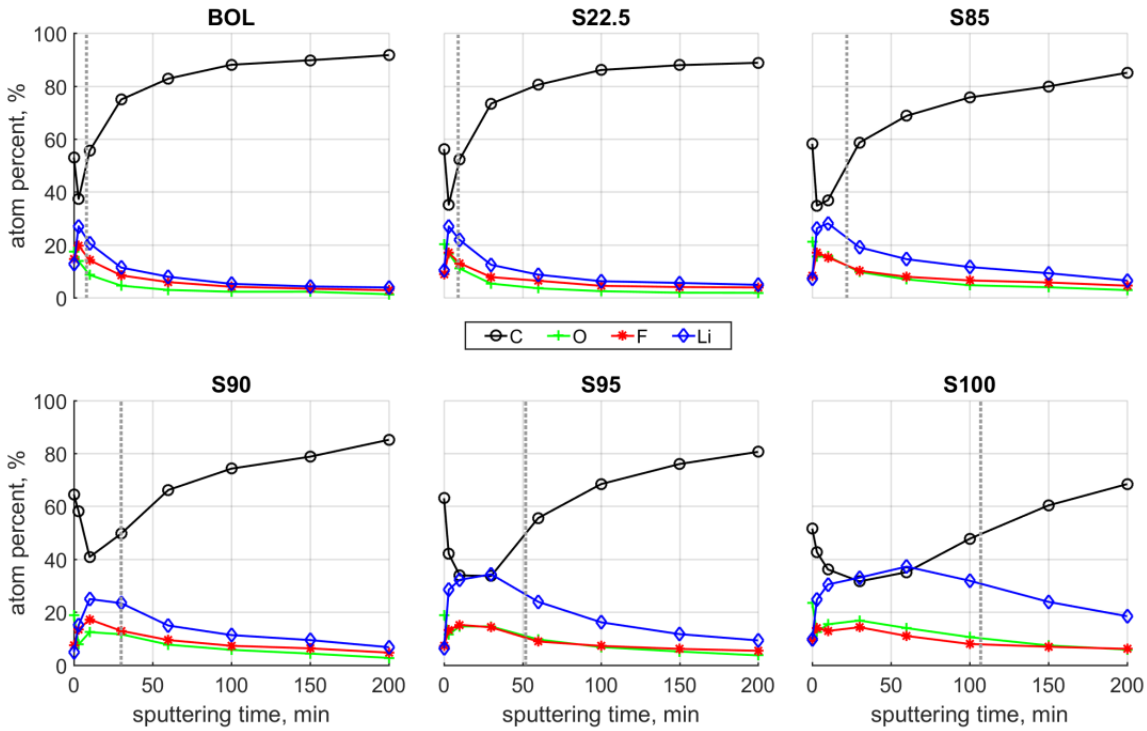

Figure 23: Depth profiles of the carbon, oxygen, fluorine and lithium concentrations versus sputtering time for anodes at beginning of life and SOC of S22.5, S85, S90, S95 and S100. Sputter depth can be calculated from sputter time and an etching rate of 1 nm min^{-1} on SiO_2. The depth profiles indicate a SOC dependent growth of the SEI during calendar aging to thicknesses of up to 107 nm (dotted line Reproduced from [1], Copyright 2019, with permission from Elsevier.[5]

Besides the SEI thickness estimation, the XPS analysis reveals information on the nature and molecular constitution of the SEI. As a result of the combination of the depth profiles, the core level spectra of C1s, O1s and F1s for 3 steps of sputter time and the depth profile of the Li/C

ratio depicted in Figure 24, two layers of the SEI are identified. LiF and other mainly inorganic constituents dominate the layer near to the graphite's surface, while the nature of the SEI changes to mainly organic constituents far from the particles surface. These findings confirm the SEI characterization presented in literature and provide extensive data on a consistent set of calendar aged lithium-ion cells.

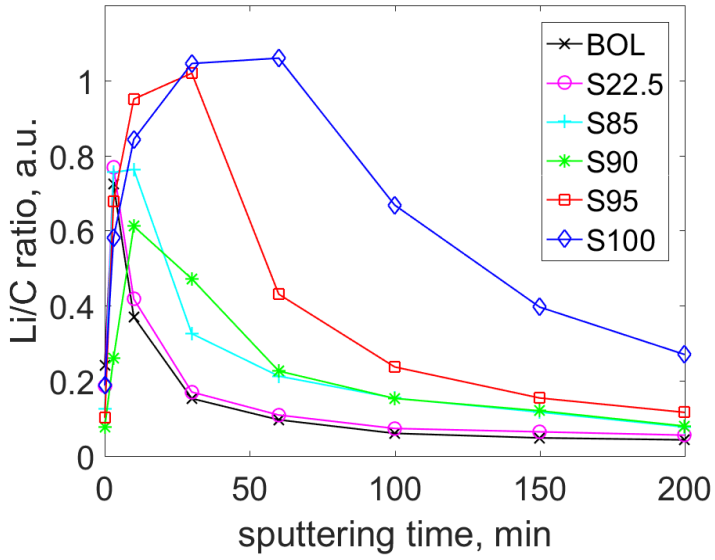

Figure 24: Lithium/carbon ratio depth profiles of the anode samples BOL, S22.5, S85, S90, S95 and S100. After the low Li/C ratio in the beginning shows the organic SEI part, a more inorganic SEI follows represented by the ratio of ~1. Reproduced from [1], Copyright 2019, with permission from Elsevier.[5]

At this point, a critical review of XPS depth-profiling as SEI probing method is required. Several comments of experts in the field of XPS research criticized the applicability of the analysis method due to its surface geometry dependence. Typically, XPS is used for the analysis of smooth flat surfaces, for example in thin film materials grown with chemical vapor or pulsed laser deposition [189]. Since the used electrodes are composed of spherical particles, the surface is not flat and the angle between surface and detector varies. However, this can be compared with angle-resolved XPS, which is applied for ultra-thin films or sensitive samples, e.g. polymers [190]. The surface of the graphite electrode is rough, hence throughout the XPS analysis several angles between the sample and the XPS provide means. Additionally, concerns on the tempering effect as a result of the sputter process, which may limits the validity due to energy input into the SEI, appeared. This limits the expressiveness of the constitution, but not the elemental composition.

Nevertheless, in the past twenty years, many studies have proven that reasonable information, compared to other analysis methods, on the surface constitution of graphite-powder based electrodes for lithium-ion cells can be obtained from XPS depth-profiling

[106,112,113,117,191,192]. Yoshida et al. [115] set a criterion for the estimation of the SEI thickness from XPS depth profiles of a few different aged electrodes. The mentioned studies from the early 2020s have two challenges, the cells and electrodes were produce in a lab and only a small variety of aged states was available. To the best of the author's knowledge, no comparable extensive study estimating the SEI thickness from measurement results and in dependence of the complete range of SOC is published so far. Nevertheless, XPS depth-profiling as an alone standing analysis method of the degradation of lithium-ion cells is insufficient without complementary analysis methods, i.e. SEM, Raman spectroscopy, ICP-OES.

In this extensive calendar aging study of automotive lithium-ion cells, the SEI growth and electrolyte decomposition are identified as the two major degradation mechanisms. Both mechanisms intensify with increase in the storage SOC (≙ decrease in anode potential). A correlation between the anode potential and the resulting SEI thickness is found, the lower the anode potential, the more SEI is grown; the effect of the anode potential plateaus can be seen in the SEI thickness evolution from SOC22.5 to SOC85 and higher. The maximum estimated SEI thickness resulting from the XPS depth-profiling, namely ~100 nm confirms the thickness resulting from SEI modelling reported in literature. The elemental compositions of the two layers of the SEI are evaluated and match well with the findings reported in literature. In addition, gas-assisted lithium plating in series with the gas enclosure in the electrode stack arises during the check-up tests. The study points the attention to the required test setup and test procedure for future aging tests with minimized external effects, e.g. mechanical constraints and temperature distribution.

3.1.2. Statement of Personal Contribution

[1] **Storch M**, Hahn SL, Stadler J, Swaminathan R, Vrankovic D, Krupp C, Riedel R (2019): Post-mortem analysis of calendar aged large-format lithium-ion cells: Investigation of the solid electrolyte interphase.
In: *Journal of Power Sources* 443, S.227-243

The data and results presented in section 3.1 are based on an extensive calendar aging test performed by BatterieIngenieure GmbH (Aachen, Germany) and designed and supervised by R. Swaminathan (Mercedes-Benz AG). Subsequent to the completion of the aging test, the cells were transferred to my responsibility. According to the electrical data, I planned the further handling and selection of analysis methods.

The post-mortem analysis, the evaluation and selection of characterization methods was initiated and most of the experimental work was done by myself. M.Sc. Naqeeb Tahasildar (co-supervision – laboratory part) and M.Sc. Jochen Stadler assisted the experimental work as part of their master thesis and intern studies under my supervision. The operation of materials characterization via SEM was performed by Mr. Samtleben and Dr. Nagel (Matworks GmbH, Aalen, Germany), ICP-OES was performed by SGS Fresenius Institut (Dresden, Germany) and XPS was carried out by Dr. Diemant and Dr. Bansmann from Ulm University (Ulm, Germany). Raman measurements were performed by myself in the laboratories of Disperse Solids group of Professor Ralf Riedel. Data evaluation, interpretation and presentation as well as literature research was performed by myself. The manuscript was written by myself, the co-authors revised and approved the manuscript. The financial funding of the work was provided by Deutsche Accumotive GmbH (Kamenz, Germany).

[4] Hahn SL, **Storch M**, Swaminathan R, Obry B, Bandlow J, Birke KP (2018): Quantitative validation of calendar aging models for lithium-ion batteries.
In: *Journal of Power Sources* 400, S.402–414

Pouch cell characterization comprising a final check-up, cell volume measurements, cell opening in the glove box system and sample preparation for various materials characterization was performed by myself. The operation of materials characterization via ICP-OES was performed by SGS Fresenius Institut (Dresden, Germany). Further personal contribution to this publication was the preparation of three-electrode cells from gathered electrodes of the pouch cells and subsequent data treatment. Besides experimental work, my personal contribution is limited to scientific discussions and proof reading, the manuscript was mainly written by Severin Hahn. The financial funding of the work was provided by Deutsche Accumotive GmbH (Kamenz, Germany).

3.2. Cycle Aging – Correlation of Operation Parameters and Degradation Mechanism

The content of this section is published in the following publications:

[2] **Storch M**, Fath JP, Sieg J, Vrankovic D, Mullaliu A, Krupp C, Spier B, Passerini S, Riedel R (2021): Cycle parameter dependent degradation analysis in automotive lithium-ion cells. In: *Journal of Power Sources* 506 S. 230227

[5] Fath JP, Alsheimer L, **Storch M**, Stadler J, Bandlow J, Hahn SL, Riedel R, Wetzel T (2020): The influence of the anode overhang effect on the capacity of lithium-ion cells – a 0D-modeling approach.
In: *Journal of Energy Storage* 29, S. 101344

In this section, the battery degradation occurring in cycle aging mode is presented. A test matrix evaluating the degradation of large-format automotive lithium-ion cells is performed followed by extensive post-mortem analysis of the degraded cells. The study has been performed on a lithium-ion cell with a capacity of 39 Ah and a graphite/NMC622:NMC111 (9:1) chemistry. One unique feature of the study is the variation of four operation parameters, however only one parameter is varied at-a-time. One-factor-at-a-time enables the identification of the predominant degradation mechanism with respect to the operation parameter temperature, upper cut-off voltage, depth of discharge and discharge current. The capacity retention and the resistance trends give a first glance on the degradation, the degradation is more pronounced when the temperature is high, the upper cut-off voltage is high and the depth of discharge is large. Surprisingly, no correlation between discharge current and the degradation is found in this study.

3.2.1. Discussion

In contrast to the calendar degradation, the cycle degradation mode occurs during intended usage of the lithium-ion battery. Hence, it is crucial to know how the cycle degradation mechanisms are related to the operation conditions. Amongst others, the most prominent operation parameters to be controlled are the cycle temperature, the cut-off voltages (correlating with the SOC), the depth of discharge and the applied charge and discharge currents. These parameters later determine the performance and the lifetime of the battery in the application. Therefore, the subject of the present publications [2,5] is a cycle parameter study planned and performed in order to evaluate the effect of these parameters separated from each other. The major degradation mechanisms resulting from each operation parameter should be identified. For this reason, a specially designed test setup for pressure control was

manufactured. In order to prevent the cells from excessive lithium plating the maximum possible charge current was evaluated by the method of Sieg et al. [89] prior to the test.

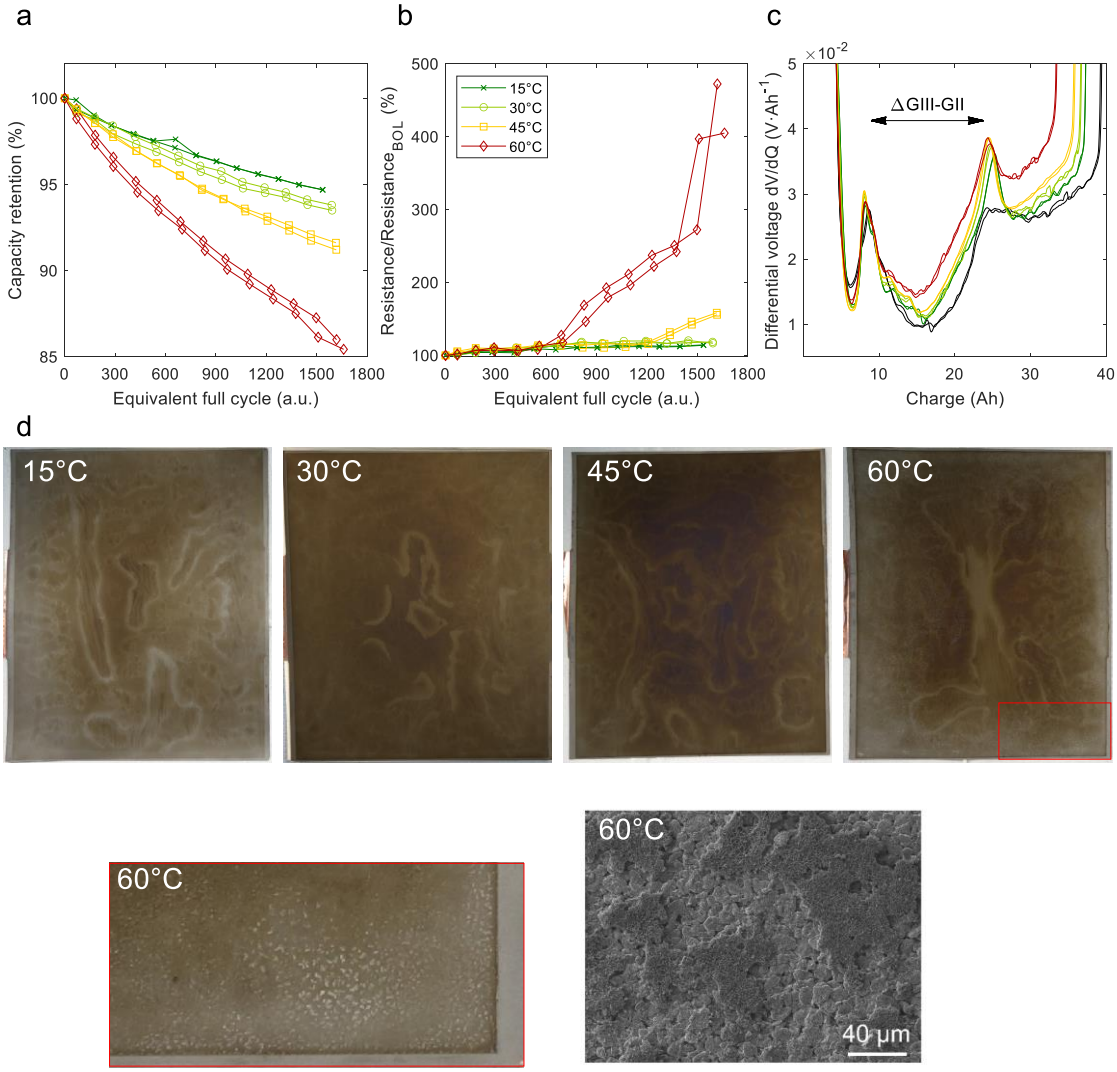

Figure 25: Overview of the results from cycling under varying **temperature**. A) C/10 discharge capacity retention versus equivalent full cycle, showing a lower capacity retention with increase in cycle temperature. B) 50 A discharge pulse resistance at 50% SOC versus equivalent full cycle, where we see a strong increase for the cell cycled at 60 °C starting at around cycle 600 and around cycle 1200 for the cell cycled at 45 °C. C) differential voltage graphs versus charge of the beginning of life cell (black) and the aged cells, minor change in the peak positions (ΔGIII-GII), but a broadening of the peaks is found. D) Photographs of a representative anode electrode extracted from the pouch-bag type cell. The anode of the cell cycled at 60 °C is magnified and a SEM image shows the deposited material on top of the graphite particles. Reproduced from [2], Copyright 2021, with permission from Elsevier.[6]

Figure 25 summarizes the findings from electrical testing and post-mortem analysis of the cells cycled at **different temperature**, namely: 15 °C, 30 °C, 45 °C and 60 °C. The capacity degradation and resistance increase with increase of the cycle temperature. The strongest

degradation is observed for the cell cycled at 60 °C. The underlying mechanisms of the increased degradation are the intensified growth of the solid electrolyte interphase, cathode degradation, the formation of gas and gas-assisted lithium plating following from enclosed gas in between the electrode stack, see data in Table 2. The huge increase in the resistance of the cell cycled at 60 °C correlates well with the amount of gas formed, a cell volume increase of 12.8% is determined and accompanied with gas-assisted plating as discussed in section 3.3 in detail. The anode active material degradation is rather low as the difference in the peak positions of the graphite stages (ΔGIII-GII) demonstrates in DV analysis. The SEI thickness is measured with XPS depth-profiling and estimated from the sputter time and the concentrations of the SEI constituents Li, F, O and C. With an increase in cycle temperature the SEI grows in thickness between 14 nm for the cell cycled at 15 °C and up to 51 nm for the cell cycled at 60 °C. The cathode degradation has been analyzed with three-electrode cell test followed by ICP-OES of the delithiated cathodes to determine $Li_{cathode,delithiated}$. Here, the increase of ~11% for the cathodes aged at 60 °C indicates partially insulated particles and trapped lithium inside.

Table 2: Overview of the data from cycling under various **temperatures** in comparison to BOL.

sample	capacity ($\%_{BOL}$)	resistance ($\%_{BOL}$)	Δcell volume (%)	SEI estimation (nm)	$capacity_{cathode}$ ($\%_{BOL}$)	ΔGIII-GII (Ah)	$Li_{cathode,delithiated}$ ($\%_{BOL}$)
BOL	100.0	100	0	7	100.0	16.91	100
15 °C	94.7	114	0.7	14	99.1	17.03	98.02
30 °C	93.7	118	1.5	24	93.4	16.72	-
45 °C	91.4	157	2.7	22	92.7	16.42	-
60 °C	85.7	439	12.8	51	86.8	16.30	110.93

- not measured

Another varied operation parameter is the **upper cut-off voltage**, which is correlated to the mean/maximum SOC of the cell. The electrical data and post-mortem results of the cells cycled up to an upper cut-off voltage of 3.55 V, 3.7 V, 3.85 V and 4.2 V are presented in Figure 26 and Table 3. The capacity retention of the sample cycled at 3.55 V shows the lowest decrease, while the two medium upper cut-off voltages result in stronger and similar decrease. The lowest capacity retention is observed for the highest cut-off voltage of 4.2 V. The resistance changes accordingly. The estimated SEI thickness is similar for the low and medium cut-off voltages and drastically increases for the cell cycled up to 4.2 V. The photographs of the anode electrodes show minor differences between the low and medium cut-off voltages, but a strong blue coloring of the anode gathered from the cell cycled with the highest cut-off voltage of 4.2 V is found (cf. Figure 26d). This blue coloring of the anode has been observed

in previous studies, and was wrongly assigned to the lithiation stage of the graphite (cf. Figure 6) [90,193]. XPS depth-profiling and STEM/EELS mapping indicate manganese incorporated into the topmost SEI (cf. Figure 26e) resulting in the blue color. The elemental mapping by EELS illustrates the Li, F and O containing SEI on the graphite surface facing the electrolyte and inside the porous network. Additionally, the enrichment of manganese in the top-most SEI proves the dissolution from the cathode and incorporation at the anode side. Concerning the cathode, the lowest degradation is found for the cell cycled up to 3.55 V, the medium and high cut-off voltages lead to slightly stronger but inconspicuous cathode degradation.

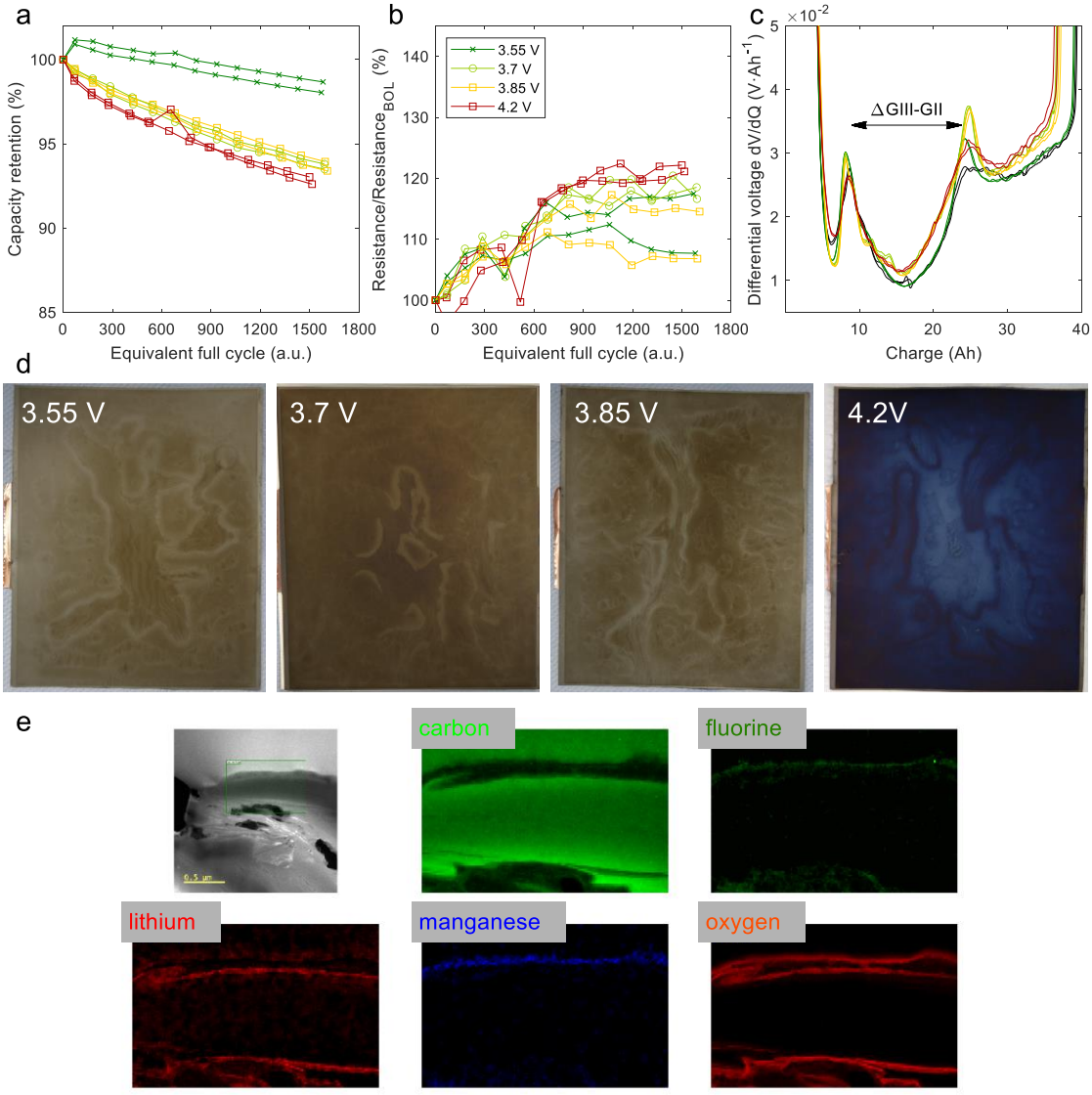

Figure 26: Overview of the results from cycling under varying **upper cut-off voltages**. A) C/10 discharge capacity retention versus equivalent full cycle, the lowest cut-off voltage results in the highest capacity retention, while an increase leads to less capacity retention. B) 50 A discharge pulse resistance at 50% SOC versus equivalent full cycle the degradation of the cells cannot be distinquished regarding the resistance evolution. C) differential voltage graphs versus charge of the beginning of life cell (black) and the aged cells, showing minor changes in the graphite

stage peak positions but a broadening of the peaks is found. D) photographs of a representative anode electrode extracted from each pouch-bag type cell, a strong blue coloring of the cell cycled up to 4.2 V is found. E) STEM/EELS elemental mapping of the surface of the anode extracted from the cell cycled up to 4.2 V indicating the deposition of manganese into the SEI. Reproduced from [2], Copyright 2021, with permission from Elsevier.[6]

Table 3: Overview of the data from cycling with various **upper cut-off voltages** in comparison to BOL.

sample	capacity ($\%_{BOL}$)	resistance ($\%_{BOL}$)	SEI estimation (nm)	Mn_{anode} (mg/cm^2)	$capacity_{cathode}$ ($\%_{BOL}$)	ΔGIII-GII (Ah)	$Li_{cathode,\ delithiated}$ ($\%_{BOL}$)
BOL	100.0	100	7	0.003	100.0	16.91	100
3.55 V	98.4	113	20	0.012	98.8	16.15	99.53
3.7 V	93.7	118	24	0.017	93.4	16.72	-
3.85 V	93.7	111	24	0.024	95.5	16.82	-
4.2 V	92.8	121	45	0.027	94.1	16.64	100.69

- not measured

The third varied operation parameter is the **depth of discharge**, the electrical data and the main findings of the post-mortem analysis of the cells cycled with DOD 20% and DOD80% are shown in Figure 27 and Table 4. The capacity degradation of the cell cycled with DOD 80% is stronger than that of the cell cycled with DOD 20%. An interesting feature is found in the first 100 equivalent full cycles of the capacity retention graph of the cell cycled with DOD 80%, instead of a typical decrease, the capacity is increasing which can be attributed to the anode overhang effect and is discussed below. Similar to the capacity retention the resistance increase is worse for the cell cycled with DOD 80%. The anode degradation is slightly stronger for the large DOD compared to the smaller one, but still relatively low as seen in the differences of ΔGIII-GII. The estimated SEI thickness with ~6 nm is in the range of the beginning of life SEI. However, the predominant degradation mechanism in the DOD 80% cycled cell is the mechanical degradation of the cathode material, namely, inter-granular cracking as shown in the FIB-SEM image in Figure 27 and the three-electrode cell data listed in Table 4.

Table 4: Overview of the data from cycling at **DOD 20% and DOD 80%** in comparison to BOL.

sample	capacity ($\%_{BOL}$)	resistance ($\%_{BOL}$)	SEI estimation (nm)	Mn_{anode} (mg/cm^2)	$capacity_{cathode}$ ($\%_{BOL}$)	ΔGIII-GII (Ah)	$Li_{cathode,\ delithiated}$ ($\%_{BOL}$)
BOL	100.0	100	7	0.003	100.0	16.91	100
DOD 20%	93.7	118	24	0.017	93.4	16.72	-
DOD 80%	87.6	129	6	0.015	78.8	15.95	113.84

- not measured

In contrast to our expectations and literature, varying the DOD reveals no significant impact on the growth of the SEI. Instead, the major degradation mechanism in the high DOD cycled cell is the instability of the cathode. Particle cracking of the cathode results in the loss of electrical contact and therefore loss of active material in terms of inactivation of particles or particle fractions. The variation of the discharge current has no significant effect on the degradation of the present cell combined with the present boundary conditions, i.e. low DOD, good thermal link of the test setup and a low and constant pressure.

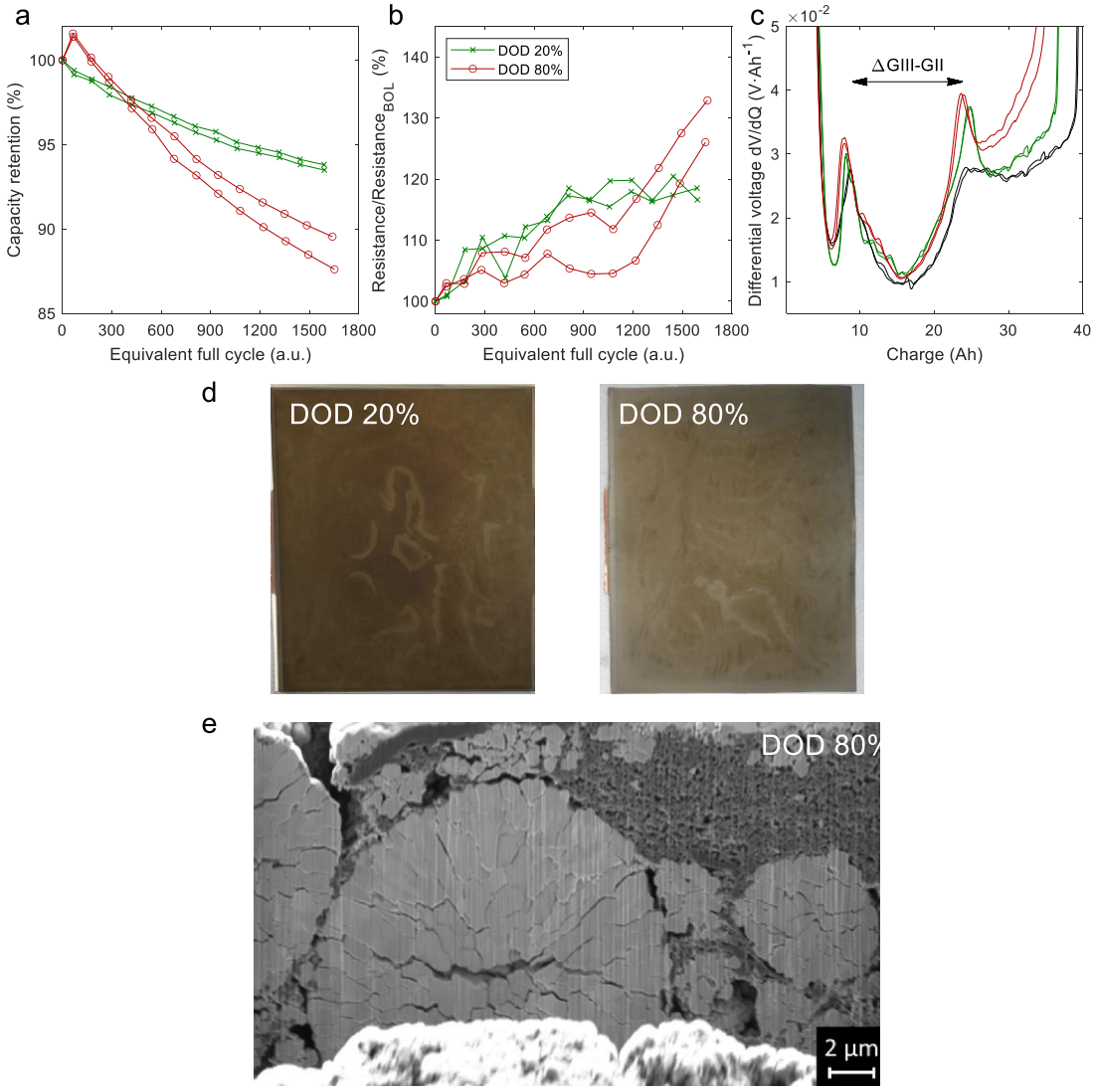

Figure 27: Overview of the results from cycling with **DOD 20% and DOD 80%**. A) C/10 discharge capacity retention versus equivalent full cycle, the DOD 80% cycling leads to less capacity retention than cycling at DOD 20%. B) 50 A discharge pulse resistance at 50% SOC versus equivalent full cycle, showing a stronger increase in the cell cycled with higher DOD. C) differential voltage graphs versus charge of the beginning of life cell (black) and the aged cells, the graphite stage peaks distance decreases (ΔGIII-GII) indicating degradation of the anode material. D) Photographs of a representative anode electrode extracted from the pouch-bag type cell. E) Cross-section FIB-SEM image of the cathode of the cell cycled with DOD 80% indicating the inter-granular cracking. Reproduced from [2], Copyright 2021, with permission from Elsevier.[6]

In addition to the observed degradation mechanism the study shows the anode overhang effect (cf. section 2.3.5). Due to the oversizing of the anode, a part of the anode is not taking part in the electrochemical cycling in the same extent as the rest of the anode. In fact, the anode overhang influences the available capacity including the cell history, i.e. the storage SOC and the mean SOC during electrochemical cycling. The resulting reversible capacity changes were observed in the DOD 80% and the 3.55 V samples as strong capacity recovery effect. The capacity retention graphs of 3.55 V (Figure 26a) and DOD 80% (Figure 27a) show an increase in capacity of around 1-2% from check-up test number 1 to check-up test number 2. This is due to an interruption of the cycle test for approximately 60 days in which the cells rest at the conditions of the end of the cycle phase. The cells 3.55 V and DOD 80% were kept at low SOC ~0-10% while the rest of the cells were kept in the SOC range of 30-80% during this period. The low SOC promotes the positive overhang effect, the diffusion of lithium from the anode overhang area to the active anode area. The subsequently measured capacity of the cells thus increases. In contrast, at high SOC the overhang effect is reversed and the lithium ions can diffuse into the anode overhang area, resulting in a decrease of the cell's capacity. This explains why the mentioned graphs of 3.55 V and DOD 80% show the overshoot in the capacity retention in the beginning of the cycle test matrix.

In order to avoid misinterpretation of the measured capacity, the anode overhang effect was further investigated. In our publication [5] we established a 0D-modeling approach for the description of the capacity change due to lithium transport into and out of the anode overhang area and depending on the lateral dimensions of the overhang. Three-electrode cell tests were performed in order to investigate the overhang extent and the corresponding lithium transport. It has been found that filling the anode overhang with lithium ions is much slower than emptying it, which is most likely potential driven. The graphite potential is steep at low SOC and flat at high SOC resulting in large and small potential differences for the same delta SOC, respectively (cf. Figure 6).

Another factor is the size of the overhang ranging from 1 mm due to oversized anode to several centimeters on the top and bottom electrode layer of the electrode stack in the large-format pouch-bag type cell. Charging from low SOC to high SOC (filling the overhang with lithium ions, see Figure 28 day 1 to day 20) results in a capacity decrease and the discharging from high SOC to low SOC (emptying the overhang, see Figure 28 day 20 to day 40) increases the capacity. In the aging test of the large-format LIBs the overshot in capacity is clearly visible (cf. Figure 26 and Figure 27). Instead, the reversible capacity decrease due to the overhang effect cannot be separated from the irreversible aging effects. Therefore, the 0D-model was developed; the correction of the capacity retention graphs is possible and enhances

the quality of the data used for the lifetime prediction of the LIB. More detailed information on this modeling approach and the correction of the data is given elsewhere [194]. Another option is the correction of the test procedure in order to avoid the overhang effect to influence the capacity evaluation. Experiments on this test procedure modulation are currently under progress.

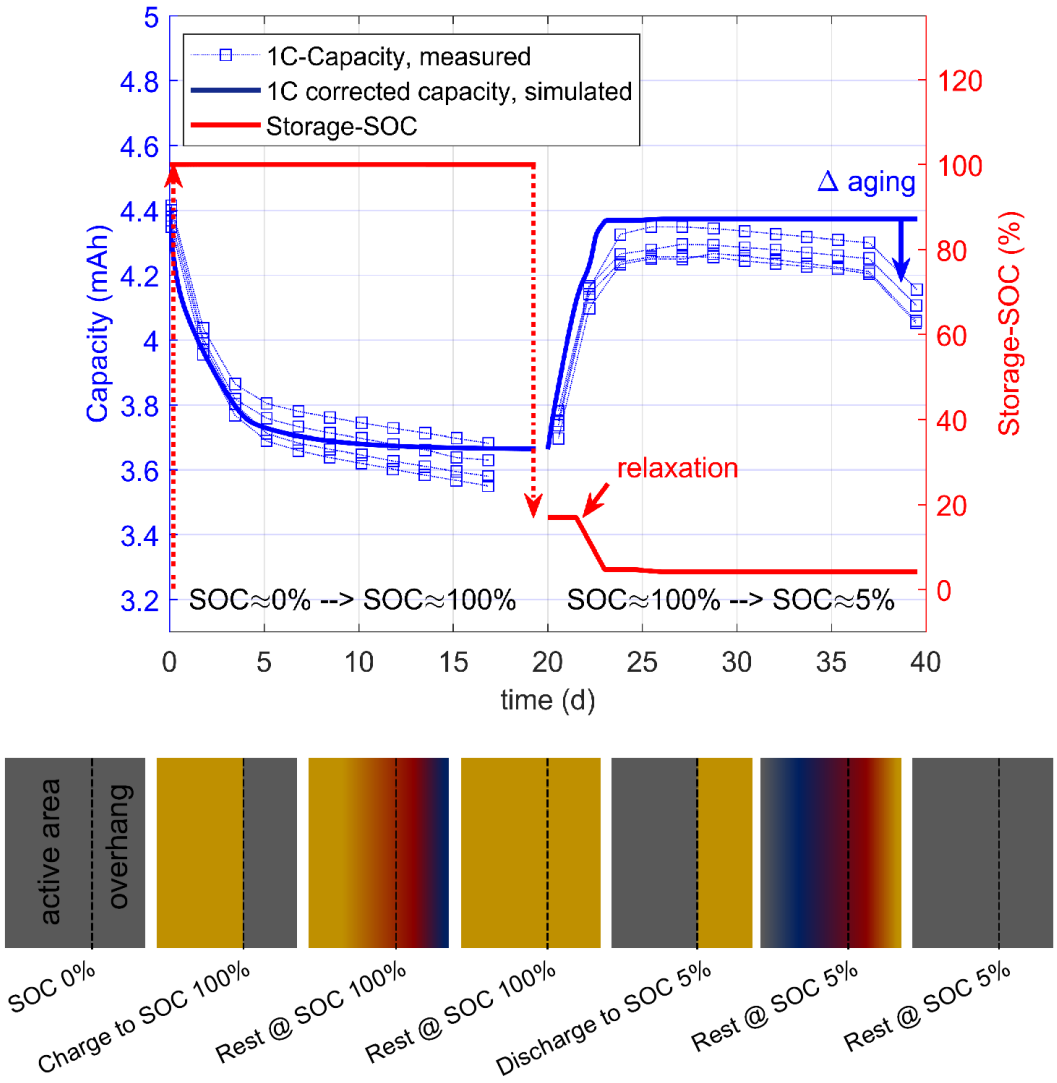

Figure 28: Overhang measurement and simulation data. 1C capacities of cells with 0.5 mm anode overhang initial state is SOC 0%, charged to SOC 100% and stored for 20 days, then the cell is discharged to SOC 5% and stored for another 20 days. Below the graphite the degree of lithiation of the anode active area and the overhang area is visualized according to the typical colors of lithiated graphite. Reproduced from [5], Copyright 2020, with permission from Elsevier.[9]

The present study proves that the design of the aging test is an important part of the separated evaluation of the lithium-ion cell degradation mechanisms. The medium operation conditions (e.g. upper cut-off voltage of 3.7 V, charge current of 18.5 A and discharge current

of 37 A), apart from the one parameter of interest, enable the evaluation of the correlation between the operation parameter and the resulting degradation mechanism. Additionally, no superposed degradation mechanism hinders the identification of the less pronounced ones, e.g. excessive lithium plating as a follow of too high charge current, superposes the formed SEI. Nevertheless, the aging test showed that the design of the test setup can be optimized further, the temperature sensors which should contact the cell surface through the aluminum plates had a thermal coupling with the plates and thus, not the cell temperature but rather the aluminum temperature was recorded. The temperature sensors have to be thermally decoupled from the aluminum plates by some low thermal conductive material, e.g. heat shrink tubes. Additionally, the check-up tests are designed to gather as much information as possible, however, the evaluation of the eight pulse tests for resistance at different SOCs has shown , that, one pulse test is sufficient for the evaluation of the cell degradation.

In summary, the experiments performed in this section reveal the most prominent degradation mechanisms of the present large-format automotive lithium-ion cells based on a graphite/Ni-rich NMC chemistry combined with a carbonate based $LiPF_6$ electrolyte. The evaluation of the electrical data requires a profound knowledge and many years of experience in the field of lithium-ion batteries in order to avoid misinterpretation, e.g. by the anode overhang effect. Although a huge data set can be gathered during the cycle test, the evaluation of the degradation mechanism can be hardly done without further post-mortem analysis. In this cycle study, the major degradation mechanisms of lithium ion cells are successfully identified and the following correlations are found:

Growth of the SEI – intensifies with increase in temperature and upper cut-off voltage

Formation of gas – results as product of the SEI growth and high temperature electrolyte decomposition

Mechanical degradation of the cathode material – predominant at large depth of discharge

Transition metal dissolution – intensifies with increase in mean SOC/upper cut-off voltage

These major degradation mechanisms are valid for a wide range of operation conditions as shown by the design of experiment. However, all these mechanisms have in common, that active lithium is irreversibly inactivated, i.e. bound in the SEI, deposited on the anode as plated lithium or lost to insulated active material. Additionally, the overhang effect reversibly superposes these effects and further complicates the evaluation of the degradation of the cell.

3.2.2. Statement of Personal Contribution

[2] **Storch M**, Fath JP, Sieg J, Vrankovic D, Mullaliu A, Krupp C, Spier B, Passerini S, Riedel R (2021): Cycle parameter dependent degradation analysis in automotive lithium-ion cells. In: Journal of Power Sources 506 S. 230227

The cycle aging test was initiated by myself. The detailed development of the test setup, the selection of the cell type and the choice of operation parameter was a collaboration of M.Sc. Johannes Fath and myself. Together, we set up and supervised the cycle test, which was performed at BatterieIngenieure GmbH (Aachen, Germany). The end-of-test characterization and the disassembly of the cells from the test equipment was again our responsibility. The gathered data was evaluated and illustrated by myself.

The post-mortem analysis was performed by myself with assistance from my college M.Sc. Johannes Fath and the students B.Sc. Florian Dominik Klein and M.Sc. Iris Dienwiebel, who spent a research period at Daimler AG under my supervision. The post-mortem analysis, the evaluation and selection of characterization methods was initiated and most of the experimental work was done by myself. Further personal contribution to this publication was the execution of the volume measurements, the three-electrode test cell measurements and the SEM imaging. External institutes performed several analysis, however, sample gathering and preparation was done by myself. The operation of materials characterization via ICP-OES was performed by SGS Fresenius Institut (Dresden, Germany). XPS was carried out by Dr. Diemant and Dr. Bansmann from Ulm University (Ulm, Germany). FIB-SEM and (S)TEM measurements were performed by Tarek Lutz and co-workers from NMI Naturwissenschaftliches und Medizinisches Institut an der Universität Tübingen (Reutlingen, Germany). Data evaluation, interpretation and presentation as well as literature research was performed by myself.

XRD was performed by Dr. Dragoljub Vrankovic in the laboratories of materials science department of technical university of Darmstadt and evaluated by Rietveld-refinement from Dr. Angelo Mullaliu from Helmholtz Institute (Ulm, Germany) and Karlsruhe Institute of Technology (Karlsruhe, Germany). The manuscript was mainly written by myself, Dr. Angelo Mullaliu wrote the section on XRD evaluation. The co-authors revised and approved the manuscript. The financial funding of the work was provided by Deutsche Accumotive GmbH (Kamenz, Germany) and Daimler AG (Stuttgart, Germany).

[5] Fath JP, Alsheimer L, **Storch M**, Stadler J, Bandlow J, Hahn SL, Riedel R, Wetzel T (2020): The influence of the anode overhang effect on the capacity of lithium-ion cells – a 0D-modeling approach.
In: *Journal of Energy Storage* 29, S. 101344

The idea for this publication was a collaboration of M.Sc. Johannes Fath and myself. Further I contributed to the scientific pre-work and the cycle aging test discussed in [2], which focused our attention to the challenge of the overhang effect. The electrical testing, post-mortem analysis and the preparation of materials for three-electrode testing were performed by myself and M.Sc. Lennart Alsheimer. The manuscript data evaluation, modelling and preparation of the manuscript was performed by M.Sc. Johannes Fath. I further contributed with proof reading and revising the manuscript. Financial funding of the work was provided by Deutsche Accumotive GmbH (Kamenz, Germany) and Daimler AG (Stuttgart, Germany).

3.3. Cycle Aging – Inhomogeneous Lithium Plating

The content of this section is published in the following publications:

[1] **Storch M**, Hahn SL, Stadler J, Swaminathan R, Vrankovic D, Krupp C, Riedel R (2019): Post-mortem analysis of calendar aged large-format lithium-ion cells: Investigation of the solid electrolyte interphase.
In: *Journal of Power Sources* 443, S.227-243

[3] **Storch M**, Fath JP, Sieg J, Vrankovic D, Krupp C, Spier B, Riedel R (2021): Temperature and Lithium Concentration Gradient Caused Inhomogeneous Plating in Large-format Lithium-ion Cells.
In: *Journal of Energy Storage* 41, S.102887

In this section, inhomogeneous lithium plating occurring as unwanted degradation mechanism in calendar and cycle aging mode is presented. Even, when a charge current is applied, for which the C rate is harmless on material level, lithium plating appears due to inhomogeneous distribution of the current density, thermal gradients, pressure gradients and gradients in the lithium distribution. In this study, inhomogeneous degradation has been observed in the calendar aged LIBs as well as in the cycle aged LIBs. However, the capacity degrading step of lithium plating occurs in cycle mode in both cases. In the following, the processes causing the observed degradation will be discussed. Both examples show that testing of large-format LIBs is not straightforward. A lot of parameters have to be controlled and their influence has to be kept low, e.g. the mechanical constraints, the ambient temperature and the degree of parameter acceleration.

3.3.1. Discussion

The calendar and cycle aging tests presented in the sections 3.1 and 3.2 result in representative and expected degradation for both aging modes. Though, in some cases unexpected degradation marks could be found.

Lithium plating in calendar aged cells

We start with the discussion of the calendar aging [1], the first fact to mention is that lithium plating is a degradation mechanism resulting from charge currents (cf. section 2.3.1) and is thus not expected in calendar aging mode. However, in most calendar aging tests regular check-up tests are performed, applying charge and discharge currents. As we identified, the inhomogeneous degradation of the calendar aged large-format 50.8 Ah LIBs (cf. section 3.1) results from several parameters, the high ambient temperature, the high storage SOC and the

cell mechanical constraints. The observed locations of the surface deposits, later identified as plated lithium, are randomly distributed (see Figure 29a).

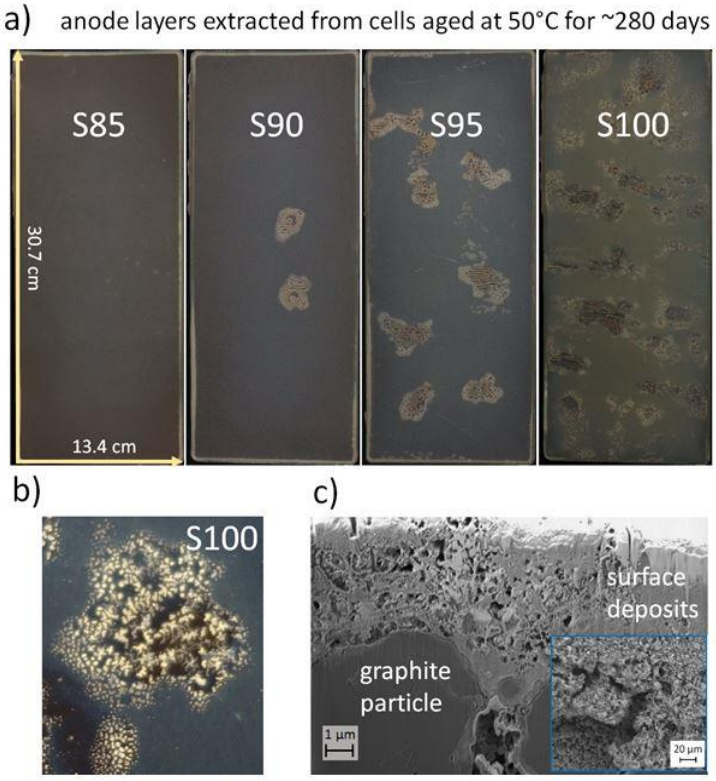

Figure 29: Optical investigation of the aged electrodes, a) optical micrographs of surface deposits emerging on anode sheets of the samples S85, S90, S95 and S10**0**, b) magnified optical micrograph of S100 surface deposit, c) FIB-SEM cross-section of surface deposits on graphite particles with 7500x magnification and the corresponding SEM top view micrograph. The surface deposits are several microns thick on top of the graphite particles and the surface deposits occur in increasing amount as storage SOC is increased. Reproduced from [1], Copyright 2019, with permission from Elsevier.[5]

Due to the increased temperature of 50 °C, two degradation mechanisms were intensified, the growth of the SEI accompanied with the formation of gas and the decomposition of the electrolyte into gaseous products (cf. 2.3.3). We found that the cell volume increase measured prior to the post-mortem analysis correlates well with the area covered with surface deposits, which was identified by image analysis of the electrodes (see Figure 30). The surface deposits were identified as lithium plating by a combination of FIB-SEM (see Figure 29 c), SEM-EDX (see Table 5) and comparable findings in literature [77]. Even though lithium cannot be measured using SEM-EDX, the available results show a strong increase in oxygen, phosphor and sulfur concentration. When metallic lithium is deposited, its potential is out of the electrolytes stability window and therefore it immediately reacts with the electrolyte. This explains the strong increase in the three elements stemming from electrolyte solvent and additives.

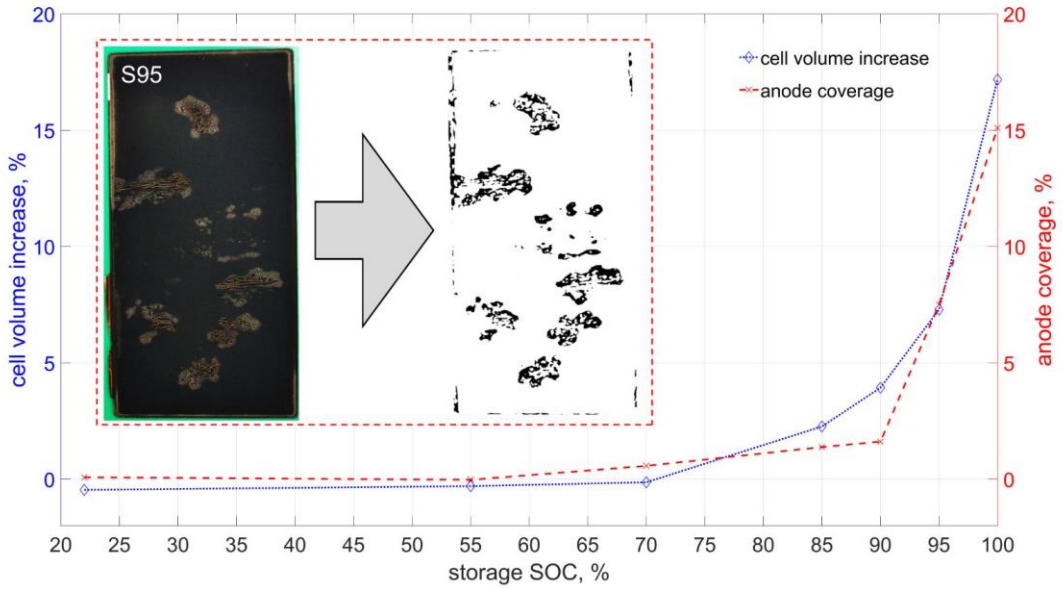

Figure 30: Cell volume increase determined according to Archimedes principle and anode coverage determined via image analysis versus the storage SOC during aging experiment. The cell volume increase data has been previously published in [4]. Inset a) shows a binary image from image analysis separating the inconspicuous and the covered electrode area. A correlation between cell volume increase and fraction of anode surface covered with lithium-plating deposits is shown. Reproduced from [1], Copyright 2019, with permission from Elsevier.[5]

Table 5: Element concentrations in the S100 anode and corresponding deposits determined via SEM-EDX analysis. The deposits possess strong increase of oxygen, phosphor and sulfur and decrease of carbon. It should be noted that lithium is not measureable in EDX due to its low atomic mass.

sample	carbon at%	oxygen at%	fluorine at%	phosphor at%	sulfur at%
S100	87.4%	7.6%	4.0%	0.6%	0.4%
S100-deposit	30.5%	57.5%	3.4%	6.3%	2.3%

The reason for the observed lithium plating is that gas formed at high SOC and temperature and gets trapped in the electrode stack. The low pressure on the cells is not high enough to push the gas bubbles out of the electrode stack into the gas pockets. The gas bubbles partially inactivated the electrode, which diminishes the effective active area of the cell. The remaining active area is reduced and therefore, the effective currents on the area near to the gas bubbles increases. The cells were “constrained” in between to aluminum plates ensuring contact between the cell and both plates when maximum thickness is reached at SOC 100% and no constraints when the cell shrinks during discharge or at lower SOC. The test setup was based on the assumption that the pressure on the cell does not have an influence on calendar aging, which is proven wrong by this study.

Since solely during the check-up test charge currents sufficiently high to allow lithium plating were applied, the monitoring part of the calendar aging test turned into one additional factor for the overall observed degradation. As a reference, a fresh cell without gas was cycled the same amount of check-up tests in a row without the calendar aging phase, here, no surface deposits, i.e. lithium plating, could be observed.

As a lessons learned, for further testing a spring loaded test setup is adopted in the cycle aging test, i.e. the exclusively designed mechanical setup (see Figure 31). A combination of 30 mm aluminum plates, six cylinder screws M6x110 - assembled with springs 0D12370 [3] was developed to ensure a pressure during one cycle and for the whole aging test of ~29 kPa. This pressure should press the eventually evolving gas out of the stack and therefore prevents gas-assisted lithium plating.

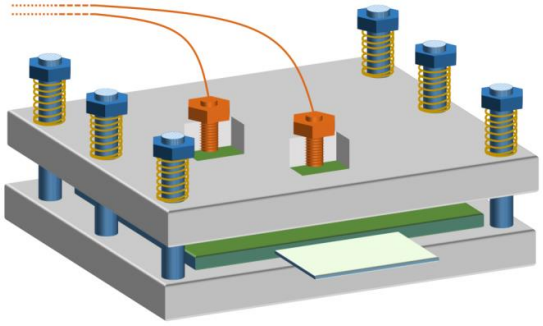

Figure 31: Schematic of the mechanical setup designed for the cycle aging matrix. The setup comprises two 30 mm thick aluminum plates kept together by six cylinder screws assembled with springs. The orange cable and screws represent two screw-in temperature sensors for evaluation of the cell surface temperature. Reproduced from [3], Copyright 2021, with permission from Elsevier.[7]

As presented in section 3.2 and Figure 26b for the test point T60 with an ambient temperature of 60 °C during electrochemical cycling a large amount of gas evolved, so that not the complete amount of gas could be pushed into the gas pockets. Beginning from the edge of the electrode stack and several centimeters in lateral direction, gas-assisted lithium plating is observed. However, the mention cells at 60 °C are the only cells with gas-assisted plating and the 60 °C are the edge of the allowed operation conditions for this cell.

Stress test at low temperature

Besides the gas-assisted lithium plating a second type of inhomogeneous degradation is observed in the cycle aged cells. The cycle test includes one test point in addition to the presented once (cf. section 3.2), the parameter combination for the evaluation of the effect of high discharge current at low ambient temperature. Therefore, two cells were cycled at 0 °C

with a discharge current of 111 A. The same measurement was performed at 30 °C (sample C3 of [2]) with all other cycle parameter being identical. Prior to the test, the maximum charge current allowed on material level has been identified by a method of Sieg et al. [89]. Therefore, even at the low ambient temperature no lithium plating was expected with the applied charge current of 18.5 A. However, The capacity retention of the cells cycled at 0 °C is significantly lower than the capacity retention of the cells cycled at 30 °C [3].

The visual inspection of the cells cycled at 0 °C showed an elliptical-like bump in the cell center amounting to around 0.7 mm in height. The post-mortem analysis of the cells revealed the deposition of a thick lithium-rich layer in the center of the anodes and a little increase of the cathode thickness (see Figure 27).

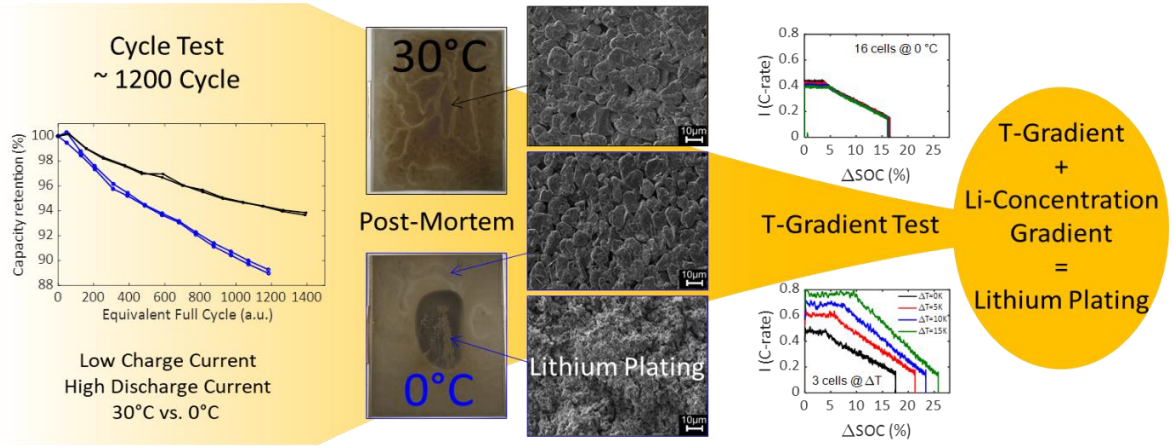

Figure 32: Overview of the main findings of inhomogeneous degradation in low temperature and high discharge current cycling of large-format LIBs. Apart from the temperature, two identical long-term aging tests have been performed. The capacity fading is stronger for the low temperature cells. Post-mortem analysis reveals a strong lithium plating pattern in the lateral electrode center. Further analysis of the temperature gradient using a parallel connection of three-electrode test cells revealed that a temperature gradient up to 15 K cannot lead to lithium plating without superposition of an additional effect. We identified the lithium concentration increase in the cell center as effect leading to lithium plating. Reproduced from [3], Copyright 2021, with permission from Elsevier.[7]

The first assumption was that a thermal gradient caused by the high discharge current leads to these two regions of different degradation. Therefore, we set up a testing method using in total 19 three-electrode cells and two temperature chambers. The three-electrode cells were connected in parallel with 16 cells in one temperature chamber and 3 cells in the other one. These cells then represent the area ratio of the conspicuous center area versus the outer are of the anode in the original tested pouch-bag cell. If the 3 cells reach an anode potential below 0 V vs. Li/Li^+ the assumption could be proven right.

However, neither the anode potentials of the three-electrode cells cycled at 0°C nor the anode potentials of the cells cycled at 5 °C, 10 °C and 15 °C drop below 0 V vs. Li/Li^+. The anode

potentials of the warmer cells are even higher due to the faster diffusion of the lithium ions inside the graphite particles at elevated temperatures. Instead, the current distribution is affected by the temperature. The effective current on the 3 cells in the warmer chamber increases with an increase in temperature, which is concomitant with the increased ΔSOC shown in Figure 32. The ΔSOC is present in the pouch cell between the inner warmer area (green) and the outer colder area (red), as shown in the developed schematics in Figure 33:

a) A delta in state of charge between the outer and the center area in the end of the high current discharge results from thermal gradient.

b) During the rest period, the lithium-ion flow from outer to center area of the anode takes place due to potential gradient (ΔSOC). The flow of lithium in the cathode in opposite direction is weaker due to the lower potential gradient.

c) The shift in the center anode potential to lower values (higher degree of lithiation) results in violation of the lithium plating limit in the following charging process. This step is irreversibly forming plated lithium, which acts as an amplification of the process, since it takes lithium from the center area.

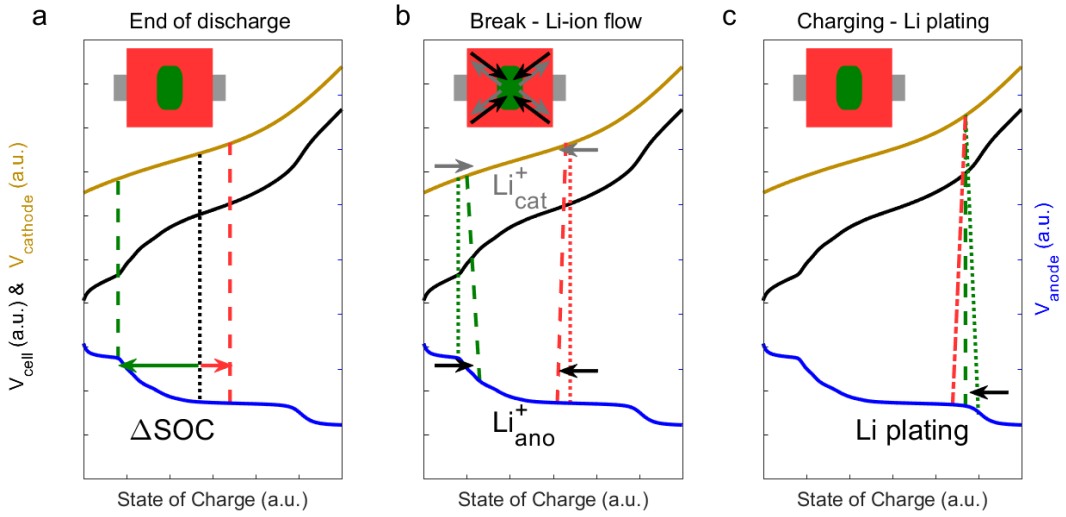

Figure 33: Schematic evolution of the potentials of the cell during the aging test. The solid lines represent the electrode potentials and the cell voltage (black=cell voltage, blue=anode potential, and yellow=cathode potential). The dotted lines represent the expected potentials caused by operation, while the potentials caused by inhomogeneity effects are dashed lines. Electrode center area and corresponding potential changes are colored green and electrode outer area and corresponding potential changes are colored red. Reproduced from [3], Copyright 2021, with permission from Elsevier.[7]

Both, the calendar and the cycle aging study demonstrated that the operation of lithium-ion cells is prone to inhomogeneous degradation. Even with optimized testing equipment and

procedure, temperature-, current density- and lithium concentration-gradients can induce local degradation, i.e. lithium plating. In order to optimize the lifetime of LIBs, effort has to be spend on the optimization of the constraints of the later application. Additionally, to avoid inhomogeneous degradation, the operation parameter of the cells should become milder with ongoing usage. Cell internal possibilities to overcome the problem of inhomogeneous degradation could be the optimization of the cell components, e.g. the electrolyte amount and additives as well as the dimensions of the cell.

3.3.2. Statement of Personal Contribution

[1] **Storch M**, Hahn SL, Stadler J, Swaminathan R, Vrankovic D, Krupp C, Riedel R (2019): Post-mortem analysis of calendar aged large-format lithium-ion cells: Investigation of the solid electrolyte interphase.
In: *Journal of Power Sources* 443, S.227-243

The post-mortem analysis, the evaluation and selection of characterization methods was initiated and most of the experimental work was done by myself. M.Sc. Naqeeb Tahasildar (co-supervision – laboratory part) and M.Sc. Jochen Stadler assisted the experimental work during their master thesis and intern studies under my supervision. The operation of materials characterization via SEM was performed by Mr. Samtleben and Dr. Nagel (Matworks GmbH, Aalen, Germany), ICP-OES was performed by SGS Fresenius Institut (Dresden, Germany) and XPS was carried out by Dr. Diemant and Dr. Bansmann from Ulm University (Ulm, Germany). Raman measurements were performed by myself in the laboratories of disperse solids group of Professor Ralf Riedel. Data evaluation, interpretation and presentation as well as literature research was performed by myself. The manuscript was written by myself, the co-authors revised and approved the manuscript. The financial funding of the work was provided by Deutsche Accumotive GmbH (Kamenz, Germany).

[3] **Storch M**, Fath JP, Sieg J, Vrankovic D, Krupp C, Spier B, Riedel R (2021): Temperature and Lithium Concentration Gradient Caused Inhomogeneous Plating in Large-format Lithium-ion Cells.
In: *Journal of Energy Storage* 41, S.102887

The cycle aging test was initiated by myself. The detailed development of the test setup, the selection of the cell type and the choice of operation parameter was a collaboration of M.Sc. Johannes Fath and myself. We together set up and supervised the cycle test, which was performed at BatterieIngenieure GmbH (Aachen, Germany). The end of test characterization

and the disassembly of the cells from the test equipment was again our task. The gathered data was evaluated and illustrated by myself.

The post-mortem analysis, the evaluation and selection of characterization methods was initiated and most of the experimental work was done by myself. Further personal contribution to this publication was the execution of the three-electrode test cell measurements and the SEM imaging. M.Sc. Johannes Sieg set up the three-electrode cell test equipment and helped me with test procedure and data evaluation. The operation of materials characterization via ICP-OES was performed by SGS Fresenius Institut (Dresden, Germany). Data evaluation, interpretation and presentation as well as literature research was performed by myself under assistance of the co-authors. The manuscript was written by myself, the co-authors revised and approved the publication. The financial funding of the work was provided by Deutsche Accumotive GmbH (Kamenz, Germany) and Daimler AG (Stuttgart, Germany).

4. Summary and Outlook

This PhD thesis represents a first milestone in the evaluation of the calendar and cycle degradation mechanisms in long-term application of automotive lithium-ion cells. Within this work the detailed analysis of the degradation mechanisms in function of battery operating conditions has been performed for the first time. It has been shown that the temperature, the state of charge and the depth of discharge are the most crucial parameters. Furthermore a unique approach consisting in a statistical analysis of long-term aged cells by means of XPS depth-profiling has been applied to determine the composition and growth of the solid electrolyte interphase for a large number of different long-term aged cell materials. The evolution of gas is identified as the second major degradation mechanism at high state of charge and especially at high temperature storage/operation. Furthermore, the profound analysis of cells at high state of charge operation using STEM-EELS revealed the intensified dissolution of transition metal from the cathode material. Contrary to literature reports, the major degradation during battery operation under a high depth of discharge is attributed to the cathode particle cracking instead of the accelerated growth of the SEI. In addition, inhomogeneous degradation resulting from enclosed gas, temperature and lithium-concentration gradients is identified as major cause for accelerated loss of cell performance. The identified correlations between operation of the lithium-ion cells, the corresponding electrical data and the data gathered from post-mortem analysis enable a lifetime optimized design of the operation strategy in the application, conceivable enhancement of lifetime >15 years and >300.000 km.

A calendar aging test of 54 cells for ~280 days and a cycle aging test of 31 cells for ~1500 cycles provide a base for the profound analysis of the calendar and operational degradation of the automotive battery cells. The main findings on the degradation mechanisms revealed by post-mortem analysis are illustrated in Figure 34.

In the calendar aging study the storage conditions state of charge and temperature fortify the degradation of the lithium-ion cells. The two major degradation mechanisms, the growth of the solid electrolyte interphase and the decomposition of the electrolyte are identified. The SEI growth is found to accelerate with the increase of the storage SOC, which correlates with the graphite stage/potential. Furthermore, the solid electrolyte interphase is confirmed to consist of an inner mainly inorganic and an outer mainly organic system with a maximum estimated SEI thickness of ~100 nm. In addition, the performance of the lithium-ion cells suffer from the gas evolution in a direct manner, namely resistance increase, and an indirect manner, the found gas-assisted lithium plating. During the check-up tests of the calendar

aging test lithium plating occurred due to elevated current density on the edges of the enclosed gas bubbles.

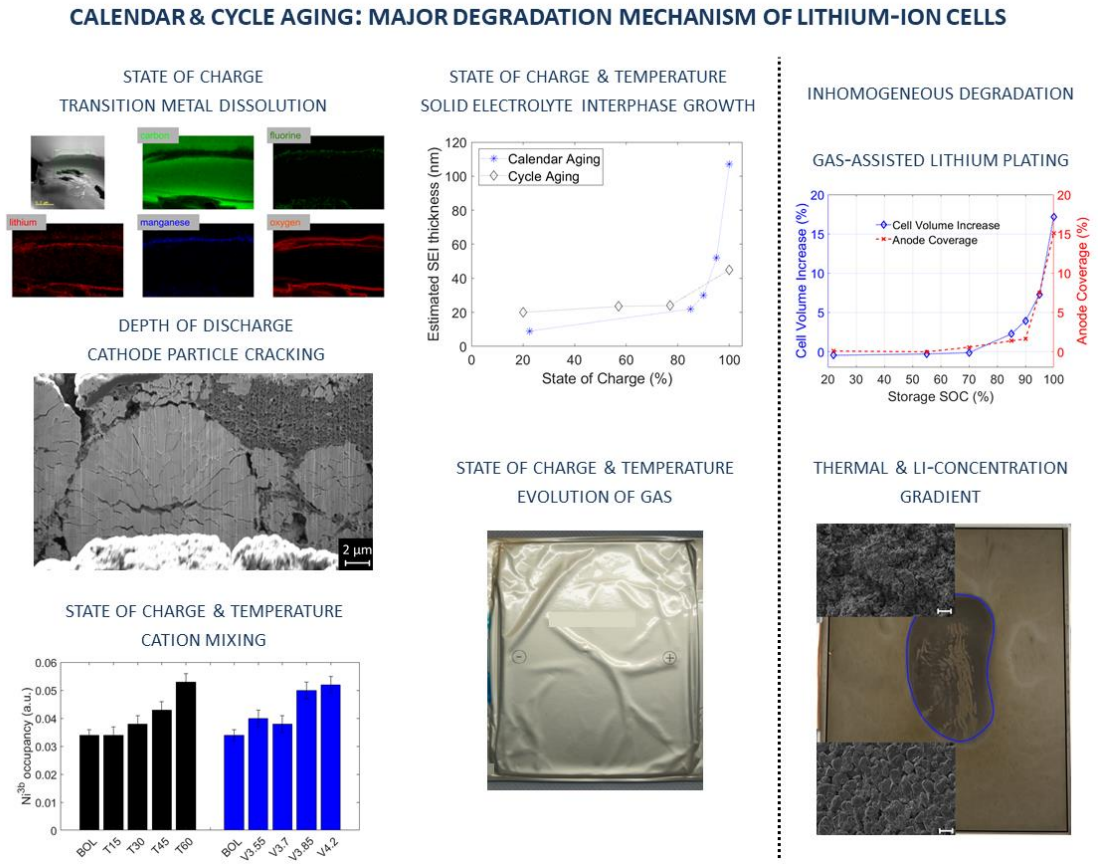

Figure 34: Overview of the major degradation mechanisms found in long-term aged automotive lithium-ion cells. Besides the typical degradation, inhomogeneous degradation resulting from enclosed gas, temperature and lithium-concentration gradients is identified.

The cycle aging study revealed the temperature, the upper cut-off voltage/state of charge and the depth of discharge resulting in accelerated degradation of the automotive lithium-ion cells under operation. The major degradation mechanisms fortified by the operation temperature are the growth of the solid electrolyte interphase, the formation of gas and cation mixing in the cathode active material. Under variation of the state of charge, the predominant degradation mechanisms are found to be the growth of the solid electrolyte interphase, the dissolution of manganese and incorporation in the SEI as well as the cation mixing in the cathode active material. The operation with different depth of discharge disclosed the mechanical degradation of the cathode active material together with the partial electrical insulation of the fragmented particles as the major degradation mechanism. In addition, the cycle aging study revealed a disturbing factor, namely, the anode overhang effect. This effect is analyzed in detail and a 0D-model on the lithium diffusion in and out of the anode overhang is established.

Further, both studies on the calendar and cycle aging point the attention to the test setup and test procedure. The external effects, e.g. mechanical constraints and temperature distribution and testing procedure have to be known and controlled in order to avoid inhomogeneous degradation which might not occur under operation in the application. In the calendar aging study gas-assisted lithium plating is found as causality of the formed gas during storage and the current applied during the check-up. In the cycle study a temperature gradient and a local lithium-concentration gradient resulting from intense operation cause heavy lithium plating even though the applied current on the cell is inconspicuous on material level. However, most of the presented degradation mechanisms have in common, that active lithium is irreversibly inactivated, i.e. bound in the SEI, deposited on the anode as plated lithium or lost to insulated active material and thus result in performance degradation.

This PhD work has provided a fundament for a holistic model on the degradation of lithium-ion cells. It enables the optimization of lithium-ion cell testing procedures in terms of time and extent. The correlation of the findings from post-mortem analysis and electrical data allows for prediction of degradation mechanism already in the early state of testing new generations of lithium-ion cells. Nevertheless, many questions and challenges regarding the degradation of large-format lithium-ion cells remain open, i.e. changing of or additional degradation due to new chemistry and material morphology changes, the effect of the cell installation in the application and homogeneity-optimized usage of the cells. These open questions are currently addressed in several following PhD studies. Those works focus on the extension and quantification of the degradation mechanism and parameterization of the lifetime models using the methodology developed in the present work.

References

[1] M. Storch, S.L. Hahn, J. Stadler, R. Swaminathan, D. Vrankovic, C. Krupp, R. Riedel, *Journal of Power Sources* **443** (2019) 227243.

[2] M. Storch, J.P. Fath, J. Sieg, D. Vrankovic, A. Mullaliu, C. Krupp, B. Spier, S. Passerini, R. Riedel, *Journal of Power Sources* **506** (2021) 230227.

[3] M. Storch, J.P. Fath, J. Sieg, D. Vrankovic, C. Krupp, B. Spier, R. Riedel, *Journal of Energy Storage* **41** (2021) 102887.

[4] S.L. Hahn, M. Storch, R. Swaminathan, B. Obry, J. Bandlow, K.P. Birke, *Journal of Power Sources* **400** (2018) 402.

[5] J.P. Fath, L. Alsheimer, M. Storch, J. Stadler, J. Bandlow, S. Hahn, R. Riedel, T. Wetzel, *Journal of Energy Storage* **29** (2020) 101344.

[6] NobelPrize.org, 2019, https://www.nobelprize.org/prizes/chemistry/2019/summary/, accessed 2 September 2020.

[7] J.-K. Park, Principles and Applications of Lithium Secondary Batteries, Wiley-VCH Verlag GmbH & Co. KGaA, Weinheim, Germany, 2012.

[8] T. Placke, R. Kloepsch, S. Dühnen, M. Winter, *J Solid State Electrochem* **21** (2017) 1939.

[9] K.M. Abraham, *ACS Energy Lett.* **5** (2020) 3544.

[10] M. Wietschel, M. Kühnbach, D. Rüdiger, 2019, www.isi.fraunhofer.de/content/dam/isi/dokumente/sustainability-innovation/2019/WP02-2019_Treibhausgasemissionsbilanz_von_Fahrzeugen.pdf, accessed 5 November 2021.

[11] L. de Biasi, A.O. Kondrakov, H. Geßwein, T. Brezesinski, P. Hartmann, J. Janek, *J. Phys. Chem. C* **121** (2017) 26163.

[12] M. Ecker, P. Shafiei Sabet, D.U. Sauer, *Applied Energy* **206** (2017) 934.

[13] Y. Preger, H.M. Barkholtz, A. Fresquez, D.L. Campbell, B.W. Juba, J. Romàn-Kustas, S.R. Ferreira, B. Chalamala, *J. Electrochem. Soc.* **167** (2020) 120532.

[14] A.S. Mussa, A. Liivat, F. Marzano, M. Klett, B. Philippe, C. Tengstedt, G. Lindbergh, K. Edström, R.W. Lindström, P. Svens, *Journal of Power Sources* **422** (2019) 175.

[15] T. Waldmann, M. Wilka, M. Kasper, M. Fleischhammer, M. Wohlfahrt-Mehrens, *Journal of Power Sources* **262** (2014) 129.

[16] T.S. Bryden, A. Holland, G. Hilton, B. Dimitrov, C.P. de León Albarrán, A. Cruden, *Energy Procedia* **151** (2018) 194.

[17] C. Pastor-Fernández, T.F. Yu, W.D. Widanage, J. Marco, *Renewable and Sustainable Energy Reviews* **109** (2019) 138.

[18] P.W. Atkins, C.A. Trapp, J. de Paula, M.P. Cady, C. Giunta, A. Höpfner, Physikalische Chemie, VCH, Weinheim, 1987.

[19] C.H. Hamann, W. Vielstich, Elektrochemie, Wiley-VCH-Verlag GmbJ &Co. KGaA, Weinheim, 2005.

[20] R. Korthauer (Ed.), Handbuch Lithium-Ionen-Batterien, Springer Berlin Heidelberg, Berlin, Heidelberg, s.l., 2013.

[21] J.O. Besenhard, G. Eichinger, *Journal of Electroanalytical Chemistry and Interfacial Electrochemistry* **68** (1976) 1.

[22] G. Eichinger, J.O. Besenhard, *Journal of Electroanalytical Chemistry and Interfacial Electrochemistry* **72** (1976) 1.

[23] W.R. McKinnon, R.R. Haering, in: R.E. White, J.O. Bockris, B.E. Conway (Eds.), Springer US, Boston, MA, 1983, pp. 235–304.

[24] S.M. Whittingham, INTERCALATION CHEMISTRY, Elsevier Science, Oxford, 1982.

[25] A. Thielmann, C. Neef, C. Fenske, M. Wietschel, 2018, https://www.isi.fraunhofer.de/content/dam/isi/dokumente/cct/lib/Energiespeicher-Monitoring_2018.pdf, accessed 16 August 2020.

[26] Panasonic Corporation, https://www.panasonic.com/global/consumer/battery/about_us/history.html, accessed 16 August 2020.

[27] L. Samsung SDI Co., https://www.samsungsdi.com/about-sdi/history/1990s.html, accessed 16 August 2020.
[28] LG Chem Ltd, https://www.lgchem.com/company/company-information/company-history, accessed 16 August 2020.
[29] A123 Systems LLC, http://www.a123systems.com/about/, accessed 16 August 2020.
[30] Jochen Mähliß, 2020, https://www.vde.com/resource/blob/1954528/be19b6edcad2be323ce8cc6485151cd8/download---praesentation-maehliss-data.pdf, accessed 8 October 2021.
[31] N. Lebedeva, D. Tarvydas, I. Tsiropoulos, Li-ion batteries for mobility and stationary storage applications: Scenarios for costs and market growth, Publications Office of the European Union, Luxembourg, 2018.
[32] Tesla Germany GmbH, https://www.tesla.com/de_DE/about, accessed 16 August 2020.
[33] Katrin Pudenz, 2013, https://www.springerprofessional.de/automobil---motoren/batterie/born-electric-bmw-i3-weltpremiere-in-new-york-london-und-peking/6562128?redirect=1, accessed 8 October 2021.
[34] Marcus Zacher, 2018, https://generationstrom.com/2018/12/20/die-geschichte-des-elektro-smarts/, accessed 8 October 2021.
[35] Bundesministerium für Wirtschaft und Energie, Bekanntmachung Richtlinie zur Förderung des Absatzes von elektrisch betriebenen Fahrzeugen (Umweltbonus): 794740, 2016.
[36] J.M. Tarascon, D. Guyomard, *Solid State Ionics* **69** (1994) 293.
[37] K. Xu, *Chem. Rev.* **104** (2004) 4303.
[38] T.R. Jow, K. Xu, O. Borodin, M. Ue (Eds.), Electrolytes for Lithium and Lithium-Ion Batteries, Springer New York, New York, NY, 2014.
[39] M.S. Whittingham, *Chem. Rev.* **104** (2004) 4271.
[40] N. Nitta, F. Wu, J.T. Lee, G. Yushin, *Materials Today* **18** (2015) 252.
[41] H. Ye, Y. Zhang, Y.-X. Yin, F.-F. Cao, Y.-G. Guo, *ACS central science* **6** (2020) 661.
[42] J.J. Auborn, Y.L. Barberio, *J. Electrochem. Soc.* **134** (1987) 638.
[43] D. Guerard, A. Herold, *Carbon* **13** (1975) 337.
[44] D. Billaud, E. McRae, J.F. Mareche, A. Herold, *Synthetic Metals* **3** (1981) 21.
[45] R. Fong, *J. Electrochem. Soc.* **137** (1990) 2009.
[46] J.B. Goodenough, Y. Kim, *Chem. Mater.* **22** (2010) 587.
[47] D. Billaud, F. Henry, *Solid State Communications* **124** (2002) 299.
[48] X. Zuo, J. Zhu, P. Müller-Buschbaum, Y.-J. Cheng, *Nano Energy* **31** (2017) 113.
[49] Christian Ruoff, 2020, https://chargedevs.com/features/enevate-says-its-silicon-dominant-anode-technology-is-ready-for-ev-production/, accessed 16 August 2020.
[50] M.S. Islam, C.A.J. Fisher, *Chemical Society reviews* **43** (2014) 185.
[51] K. Mizushima, P.C. Jones, P.J. Wiseman, J.B. Goodenough, *Materials Research Bulletin* **15** (1980) 783.
[52] T. Ohzuku, Y. Makimura, *Chem. Lett.* **30** (2001) 642.
[53] S.-C. Yin, Y.-H. Rho, I. Swainson, L.F. Nazar, *Chem. Mater.* **18** (2006) 1901.
[54] M. Kerlau, M. Marcinek, V. Srinivasan, R.M. Kostecki, *Electrochimica Acta* **52** (2007) 5422.
[55] W.J. Lee, K. Prasanna, Y.N. Jo, K.J. Kim, H.S. Kim, C.W. Lee, *Physical chemistry chemical physics PCCP* **16** (2014) 17062.
[56] M. Börner, F. Horsthemke, F. Kollmer, S. Haseloff, A. Friesen, P. Niehoff, S. Nowak, M. Winter, F.M. Schappacher, *Journal of Power Sources* **335** (2016) 45.
[57] R. Jung, F. Linsenmann, R. Thomas, J. Wandt, S. Solchenbach, F. Maglia, C. Stinner, M. Tromp, H.A. Gasteiger, *J. Electrochem. Soc.* **166** (2019) A378-A389.
[58] K.-S. Lee, S.-T. Myung, J. Prakash, H. Yashiro, Y.-K. Sun, *Electrochimica Acta* **53** (2008) 3065.

[59] O. Dolotko, A. Senyshyn, M.J. Mühlbauer, K. Nikolowski, H. Ehrenberg, *Journal of Power Sources* **255** (2014) 197.
[60] J.E. Harlow, X. Ma, J. Li, E. Logan, Y. Liu, N. Zhang, L. Ma, S.L. Glazier, M.M.E. Cormier, M. Genovese, S. Buteau, A. Cameron, J.E. Stark, J.R. Dahn, *J. Electrochem. Soc.* **166** (2019) A3031-A3044.
[61] Y. Liu, J. Harlow, J.R. Dahn, *J. Electrochem. Soc.* **167** (2020) 20512.
[62] H. Ota, Y. Sakata, A. Inoue, S. Yamaguchi, *J. Electrochem. Soc.* **151** (2004) A1659.
[63] B. Zhang, M. Metzger, S. Solchenbach, M. Payne, S. Meini, H.A. Gasteiger, A. Garsuch, B.L. Lucht, *J. Phys. Chem. C* **119** (2015) 11337.
[64] S.S. Zhang, *Journal of Power Sources* **162** (2006) 1379.
[65] H.H. Heimes, A. Kampker, C. Lienemann, M. Locke, C. Offermanns, S. Michaelis, E. Rahimzei, Lithium-ion battery cell production process, PEM der RWTH Aachen University; DVMA, Aachen, Frankfurt am Main, 2018.
[66] M. Broussely, P. Biensan, F. Bonhomme, P. Blanchard, S. Herreyre, K. Nechev, R.J. Staniewicz, *Journal of Power Sources* **146** (2005) 90.
[67] J. Vetter, P. Novák, M.R. Wagner, C. Veit, K.-C. Möller, J.O. Besenhard, M. Winter, M. Wohlfahrt-Mehrens, C. Vogler, A. Hammouche, *Journal of Power Sources* **147** (2005) 269.
[68] P. Verma, P. Maire, P. Novák, *Electrochimica Acta* **55** (2010) 6332.
[69] V.A. Agubra, J. Fergus, *Journal of Power Sources* **268** (2014) 153.
[70] C. Schlasza, P. Ostertag, D. Chrenko, R. Kriesten, D. Bouquain, *2014 IEEE Transportation Electrification Conference and Expo (ITEC)* (2014) 1.
[71] C.R. Birkl, M.R. Roberts, E. McTurk, P.G. Bruce, D.A. Howey, *Journal of Power Sources* **341** (2017) 373.
[72] V. Agubra, J. Fergus, *Materials (Basel, Switzerland)* **6** (2013) 1310.
[73] J.C. Burns, D.A. Stevens, J.R. Dahn, *Journal of the Electrochemical Society* **162** (2015) A959-A964.
[74] N. Ghanbari, T. Waldmann, M. Kasper, P. Axmann, M. Wohlfahrt-Mehrens, *The Journal of Physical Chemistry C* **120** (2016) 22225.
[75] B. Stiaszny, J.C. Ziegler, E.E. Krauß, M. Zhang, J.P. Schmidt, E. Ivers-Tiffée, *Journal of Power Sources* **258** (2014) 61.
[76] Z. Mao, M. Farkhondeh, M. Pritzker, M. Fowler, Z. Chen, *J. Electrochem. Soc.* **164** (2017) A3469-A3483.
[77] B.P. Matadi, S. Geniès, A. Delaille, T. Waldmann, M. Kasper, M. Wohlfahrt-Mehrens, F. Aguesse, E. Bekaert, I. Jiménez-Gordon, L. Daniel, X. Fleury, M. Bardet, J.-F. Martin, Y. Bultel, *Journal of the Electrochemical Society* **164** (2017) A1089-A1097.
[78] M. Ecker, N. Nieto, S. Käbitz, J. Schmalstieg, H. Blanke, A. Warnecke, D.U. Sauer, *Journal of Power Sources* **248** (2014) 839.
[79] N. Legrand, B. Knosp, P. Desprez, F. Lapicque, S. Raël, *Journal of Power Sources* **245** (2014) 208.
[80] A. Matasso, D. Wong, D. Wetz, F. Liu, *Journal of the Electrochemical Society* **162** (2015) A885-A891.
[81] T. Waldmann, M. Kasper, M. Wohlfahrt-Mehrens, *Electrochimica Acta* **178** (2015) 525.
[82] K. Jalkanen, J. Karppinen, L. Skogström, T. Laurila, M. Nisula, K. Vuorilehto, *Applied Energy* **154** (2015) 160.
[83] M. Lewerenz, A. Warnecke, D.U. Sauer, *Journal of Power Sources* **369** (2017) 122.
[84] M. Petzl, M.A. Danzer, *Journal of Power Sources* **254** (2014) 80.
[85] R.V. Bugga, M.C. Smart, *ECS Transactions* **25** (2009) 241.
[86] T. Waldmann, B.-I. Hogg, M. Kasper, S. Grolleau, C.G. Couceiro, K. Trad, B.P. Matadi, M. Wohlfahrt-Mehrens, *J. Electrochem. Soc.* **163** (2016) A1232-A1238.
[87] T. Waldmann, B.-I. Hogg, M. Wohlfahrt-Mehrens, *Journal of Power Sources* **384** (2018) 107.
[88] Y.-H. Liu, Y.-F. Luo, *IEEE Trans. Ind. Electron.* **57** (2010) 3963.

[89] J. Sieg, J. Bandlow, T. Mitsch, D. Dragicevic, T. Materna, B. Spier, H. Witzenhausen, M. Ecker, D.U. Sauer, *Journal of Power Sources* **427** (2019) 260.
[90] D. Burow, K. Sergeeva, S. Calles, K. Schorb, A. Börger, C. Roth, P. Heitjans, *Journal of Power Sources* **307** (2016) 806.
[91] J. Cannarella, C.B. Arnold, *J. Electrochem. Soc.* **162** (2015) A1365-A1373.
[92] F.B. Spingler, M. Naumann, A. Jossen, *Journal of the Electrochemical Society* **167** (2020) 40526.
[93] V. Müller, R.-G. Scurtu, M. Memm, M.A. Danzer, M. Wohlfahrt-Mehrens, *Journal of Power Sources* **440** (2019) 227148.
[94] E. Peled, *J. Electrochem. Soc.* **126** (1979) 2047.
[95] E. Peled, *J. Electrochem. Soc.* **145** (1998) 3482.
[96] R. Imhof, *J. Electrochem. Soc.* **145** (1998) 1081.
[97] L.J. Hardwick, H. Buqa, M. Holzapfel, W. Scheifele, F. Krumeich, P. Novák, *Electrochimica Acta* **52** (2007) 4884.
[98] R. Kostecki, J. Lei, F. McLarnon, J. Shim, K. Striebel, *J. Electrochem. Soc.* **153** (2006) A669-A672.
[99] A. J. Smith, J. C. Burns, D. Xiong, J. R. Dahn, *J. Electrochem. Soc.* **158** (2011) A1136-A1142.
[100] F. German, A. Hintennach, A. LaCroix, D. Thiemig, S. Oswald, F. Scheiba, M.J. Hoffmann, H. Ehrenberg, *Journal of Power Sources* **264** (2014) 100.
[101] P. Keil, S.F. Schuster, J. Wilhelm, J. Travi, A. Hauser, R.C. Karl, A. Jossen, *J. Electrochem. Soc.* **163** (2016) A1872-A1880.
[102] M. Lanz, P. Novák, *Journal of Power Sources* **102** (2001) 277.
[103] J. Self, C.P. Aiken, R. Petibon, J.R. Dahn, *J. Electrochem. Soc.* **162** (2015) A796-A802.
[104] C.R. Yang, Y.Y. Wang, C.C. Wan, *Journal of Power Sources* **72** (1998) 66.
[105] D. Aurbach, B. Markovsky, M. Levi, E. Levi, A. Schechter, M. Moshkovich, Y. Cohen, *Journal of Power Sources* **81-82** (1999) 95.
[106] A.M. Andersson, K. Edström, *J. Electrochem. Soc.* **148** (2001) A1100-A1109.
[107] D. Aurbach, *Journal of Power Sources* **119-121** (2003) 497.
[108] M. Nie, B.L. Lucht, *J. Electrochem. Soc.* **161** (2014) A1001-A1006.
[109] D. Aurbach, *Journal of Power Sources* **89** (2000) 206.
[110] D. Aurbach, *J. Electrochem. Soc.* **143** (1996) 3809.
[111] A. Schechter, D. Aurbach, H. Cohen, *Langmuir* **15** (1999) 3334.
[112] A. Andersson, A. Henningson, H. Siegbahn, U. Jansson, K. Edström, *Journal of Power Sources* **119-121** (2003) 522.
[113] V. Eshkenazi, E. Peled, L. Burstein, D. Golodnitsky, *Solid State Ionics* **170** (2004) 83.
[114] K. Edström, M. Herstedt, D.P. Abraham, *Journal of Power Sources* **153** (2006) 380.
[115] T. Yoshida, M. Takahashi, S. Morikawa, C. Ihara, H. Katsukawa, T. Shiratsuchi, J. Yamaki, *J. Electrochem. Soc.* **153** (2006) A576.
[116] L. El Ouatani, R. Dedryvère, J.-B. Ledeuil, C. Siret, P. Biensan, J. Desbrières, D. Gonbeau, *Journal of Power Sources* **189** (2009) 72.
[117] D. Bar-Tow, *J. Electrochem. Soc.* **146** (1999) 824.
[118] M. Lu, H. Cheng, Y. Yang, *Electrochimica Acta* **53** (2008) 3539.
[119] M. Tang, J. Newman, *J. Electrochem. Soc.* **158** (2011) A530-A536.
[120] J.T. Lee, N. Nitta, J. Benson, A. Magasinski, T.F. Fuller, G. Yushin, *Carbon* **52** (2013) 388.
[121] D. Li, D. Danilov, Z. Zhang, H. Chen, Y. Yang, P.H.L. Notten, *J. Electrochem. Soc.* **162** (2015) A858-A869.
[122] H.J. Ploehn, P. Ramadass, R.E. White, *J. Electrochem. Soc.* **151** (2004) A456-A462.
[123] R. Deshpande, M. Verbrugge, Y.-T. Cheng, J. Wang, P. Liu, *J. Electrochem. Soc.* **159** (2012) A1730-A1738.
[124] I. Laresgoiti, S. Käbitz, M. Ecker, D.U. Sauer, *Journal of Power Sources* **300** (2015) 112.

[125] R. Deshpande, D.M. Bernardi, *J. Electrochem. Soc.* **164** (2017) A461-A474.
[126] M. Tang, S. Lu, J. Newman, *J. Electrochem. Soc.* **159** (2012) A1775-A1785.
[127] G.G. Eshetu, T. Diemant, S. Grugeon, R.J. Behm, S. Laruelle, M. Armand, S. Passerini, *ACS applied materials & interfaces* **8** (2016) 16087.
[128] M. Hess, *Electrochimica Acta* **244** (2017) 69.
[129] E. Peled, S. Menkin, *J. Electrochem. Soc.* **164** (2017) A1703-A1719.
[130] M. Broussely, S. Herreyre, P. Biensan, P. Kasztejna, K. Nechev, R. Staniewicz, *Journal of Power Sources* **97-98** (2001) 13.
[131] T. Waldmann, N. Ghanbari, M. Kasper, M. Wohlfahrt-Mehrens, *Journal of the Electrochemical Society* **162** (2015) A1500-A1505.
[132] R. Bernhard, M. Metzger, H.A. Gasteiger, *J. Electrochem. Soc.* **162** (2015) A1984-A1989.
[133] L. El Ouatani, R. Dedryvère, C. Siret, P. Biensan, S. Reynaud, P. Iratçabal, D. Gonbeau, *J. Electrochem. Soc.* **156** (2009) A103.
[134] F. Joho, P. Novák, *Electrochimica Acta* **45** (2000) 3589.
[135] M. Metzger, B. Strehle, S. Solchenbach, H.A. Gasteiger, *J. Electrochem. Soc.* **163** (2016) A798-A809.
[136] R. Jung, M. Metzger, F. Maglia, C. Stinner, H.A. Gasteiger, *The journal of physical chemistry letters* **8** (2017) 4820.
[137] R. Jung, M. Metzger, F. Maglia, C. Stinner, H.A. Gasteiger, *J. Electrochem. Soc.* **164** (2017) A1361-A1377.
[138] P. Peljo, H.H. Girault, *Energy Environ. Sci.* **11** (2018) 2306.
[139] M. Holzapfel, A. Würsig, W. Scheifele, J. Vetter, P. Novák, *Journal of Power Sources* **174** (2007) 1156.
[140] K. Wu, J. Yang, Y. Liu, Y. Zhang, C. Wang, J. Xu, F. Ning, D. Wang, *Journal of Power Sources* **237** (2013) 285.
[141] I. Belharouak, G.M. Koenig, T. Tan, H. Yumoto, N. Ota, K. Amine, *J. Electrochem. Soc.* **159** (2012) A1165-A1170.
[142] L.J. Krause, W. Lamanna, J. Summerfield, M. Engle, G. Korba, R. Loch, R. Atanasoski, *Journal of Power Sources* **68** (1997) 320.
[143] K.H. Lee, E.H. Song, J.Y. Lee, B.H. Jung, H.S. Lim, *Journal of Power Sources* **132** (2004) 201.
[144] C.W. Walker JR., *Army Research Laboratory* **ARL-TR-434** (1995).
[145] S.E. Sloop, J.K. Pugh, S. Wang, J.B. Kerr, K. Kinoshita, *Electrochem. Solid-State Lett.* **4** (2001) A42.
[146] A. Guéguen, D. Streich, M. He, M. Mendez, F.F. Chesneau, P. Novák, E.J. Berg, *J. Electrochem. Soc.* **163** (2016) A1095-A1100.
[147] C.L. Campion, W. Li, B.L. Lucht, *J. Electrochem. Soc.* **152** (2005) A2327.
[148] U. Heider, R. Oesten, M. Jungnitz, Challenge in manufacturing electrolyte solutions for lithium and lithium ion batteries quality control and minimizing contamination level, 1999.
[149] H. Liu, M. Wolf, K. Karki, Y.-S. Yu, E.A. Stach, J. Cabana, K.W. Chapman, P.J. Chupas, *Nano letters* **17** (2017) 3452.
[150] G. Sun, T. Sui, B. Song, H. Zheng, L. Lu, A.M. Korsunsky, *Extreme Mechanics Letters* **9** (2016) 449.
[151] B. Bitzer, A. Gruhle, *Journal of Power Sources* **262** (2014) 297.
[152] J.-M. Lim, T. Hwang, D. Kim, M.-S. Park, K. Cho, M. Cho, *Scientific reports* **7** (2017) 39669.
[153] D. Juarez-Robles, J.A. Jeevarajan, P.P. Mukherjee, *J. Electrochem. Soc.* **167** (2020) 160510.
[154] X. Zhang, W.J. Jiang, A. Mauger, Qilu, F. Gendron, C.M. Julien, *Journal of Power Sources* **195** (2010) 1292.
[155] T. Li, X.-Z. Yuan, L. Zhang, D. Song, K. Shi, C. Bock (2019).

[156] Y. Qian, P. Niehoff, M. Börner, M. Grützke, X. Mönnighoff, P. Behrends, S. Nowak, M. Winter, F.M. Schappacher, *Journal of Power Sources* **329** (2016) 31.
[157] S. Liu, L. Wang, C. Zhang, B. Chu, C. Wang, T. Huang, A. Yu, *Journal of Power Sources* **438** (2019) 226979.
[158] Z. Zhang, J. Yang, W. Huang, H. Wang, W. Zhou, Y. Li, Y. Li, J. Xu, W. Huang, W. Chiu, Y. Cui, *Matter* **4** (2021) 302.
[159] D. Chen, M.A. Mahmoud, J.-H. Wang, G.H. Waller, B. Zhao, C. Qu, M.A. El-Sayed, M. Liu, *Nano letters* **19** (2019) 2037.
[160] C. Zhan, T. Wu, J. Lu, K. Amine, *Energy Environ. Sci.* **11** (2018) 243.
[161] D.P. Abraham, T. Spila, M.M. Furczon, E. Sammann, *Journal of Power Sources* **11** (2008) A226.
[162] J.A. Gilbert, I.A. Shkrob, D.P. Abraham, *J. Electrochem. Soc.* **164** (2016) A389-A399.
[163] H. Shin, J. Park, A.M. Sastry, W. Lu, *Journal of Power Sources* **284** (2015) 416.
[164] S.R. Gowda, K.G. Gallagher, J.R. Croy, M. Bettge, M.M. Thackeray, M. Balasubramanian, *Physical chemistry chemical physics PCCP* **16** (2014) 6898.
[165] S. Kosch, A. Rheinfeld, S.V. Erhard, A. Jossen, *Journal of Power Sources* **342** (2017) 666.
[166] S. Du, M. Jia, Y. Cheng, Y. Tang, H. Zhang, L. Ai, K. Zhang, Y. Lai, *International Journal of Thermal Sciences* **89** (2015) 327.
[167] X. Zhang, X. Chang, Y. Shen, Y. Xiang, *Journal of Energy Storage* **11** (2017) 249.
[168] A. Hales, L.B. Diaz, M.W. Marzook, Y. Zhao, Y. Patel, G. Offer, *J. Electrochem. Soc.* **166** (2019) A2383-A2395.
[169] J. Sieg, M. Storch, J.P. Fath, A. Nuhic, J. Bandlow, B. Spier, D.U. Sauer, *Journal of Energy Storage* **30** (2020) 101582.
[170] B. Gyenes, D.A. Stevens, V.L. Chevrier, J.R. Dahn, *Journal of the Electrochemical Society* **162** (2015) A278-A283.
[171] J. Wilhelm, S. Seidlmayer, P. Keil, J. Schuster, A. Kriele, R. Gilles, A. Jossen, *Journal of Power Sources* **365** (2017) 327.
[172] T. Hüfner, M. Oldenburger, B. Bedürftig, A. Gruhle, *Journal of Energy Storage* **24** (2019) 100790.
[173] H.-G. Schweiger, O. Obeidi, O. Komesker, A. Raschke, M. Schiemann, C. Zehner, M. Gehnen, M. Keller, P. Birke, *Sensors (Basel, Switzerland)* **10** (2010) 5604.
[174] I. Bloom, A.N. Jansen, D.P. Abraham, J. Knuth, S.A. Jones, V.S. Battaglia, G.L. Henriksen, *Journal of Power Sources* **139** (2005) 295.
[175] M. Lewerenz, G. Fuchs, L. Becker, D.U. Sauer, *Journal of Energy Storage* **18** (2018) 149.
[176] J.P. Fath, D. Dragicevic, L. Bittel, A. Nuhic, J. Sieg, S. Hahn, L. Alsheimer, B. Spier, T. Wetzel, *Journal of Energy Storage* **25** (2019) 100813.
[177] H.M. Dahn, A.J. Smith, J.C. Burns, D.A. Stevens, J.R. Dahn, *J. Electrochem. Soc.* **159** (2012) A1405-A1409.
[178] I. Bloom, J. Christophersen, D.P. Abraham, K.L. Gering, *Journal of Power Sources* **157** (2006) 537.
[179] M. Lewerenz, A. Marongiu, A. Warnecke, D.U. Sauer, *Journal of Power Sources* **368** (2017) 57.
[180] M. Lewerenz, D.U. Sauer, *Journal of Energy Storage* **18** (2018) 421.
[181] M. Lewerenz, P. Dechent, D.U. Sauer, *Journal of Energy Storage* **21** (2019) 680.
[182] C.P. Aiken, J. Xia, D.Y. Wang, D.A. Stevens, S. Trussler, J.R. Dahn, *Journal of the Electrochemical Society* **161** (2014) A1548-A1554.
[183] T. Waldmann, A. Iturrondobeitia, M. Kasper, N. Ghanbari, F. Aguesse, E. Bekaert, L. Daniel, S. Genies, I.J. Gordon, M.W. Löble, E. de Vito, M. Wohlfahrt-Mehrens, *J. Electrochem. Soc.* **163** (2016) A2149-A2164.
[184] Carl Roth GmbH + Co KG, 2019, accessed 15 May 2020.
[185] P. Lenard, *Ann. Phys.* **313** (1902) 149.

[186] P. van der Heide, X-ray photoelectron spectroscopy: An introduction to principles and practices, Wiley, Hoboken, NJ, 2012.
[187] NobelPrize.org, 1922, https://www.nobelprize.org/prizes/physics/1921/ceremony-speech/, accessed 25 May 2020.
[188] NobelPrize.org, 1981, https://www.nobelprize.org/prizes/physics/1981/summary/, accessed 25 May 2020.
[189] R. Hausbrand, G. Cherkashinin, H. Ehrenberg, M. Gröting, K. Albe, C. Hess, W. Jaegermann, *Materials Science and Engineering: B* **192** (2015) 3.
[190] Thermo Fisher Scientific Inc., https://xpssimplified.com/angle_resolve_xps.php, accessed 2 February 2021.
[191] A.M. Andersson, D.P. Abraham, R. Haasch, S. MacLaren, J. Liu, K. Amine, *J. Electrochem. Soc.* **149** (2002) A1358.
[192] K. Araki, N. Sato, *Journal of Power Sources* **124** (2003) 124.
[193] M. Klett, R. Eriksson, J. Groot, P. Svens, K. Ciosek Högström, R.W. Lindström, H. Berg, T. Gustafson, G. Lindbergh, K. Edström, *Journal of Power Sources* **257** (2014) 126.
[194] J.P. Fath, Modellierung von Lithium-Ionen-Batterien zur Lebensdauerprädiktion unter besonderer Berücksichtigung des Anodenüberhangeffekts: Dissertation, KIT Scientific Publishing, Karlsruhe, 2022.

List of Figures

Copyright Acknowledgements:

[1]
"Reprinted from Royal Society of Chemistry, Islam, MS & Fisher, CAJ 2014, 'Lithium and sodium battery cathode materials: Computational insights intovoltage, diffusion and nanostructural properties', Chemical Society Reviews, vol. 43, no. 1, pp. 185-204, Copyright 2014, with permission from Royal Society of Chemistry https://doi.org/10.1039/c3cs60199d

[2]
"Reprinted from Journal of Power Sources, 245 (2014), N. Legrand, B. Knosp, P. Desprez, F. Lapicque, S. Raël, *Physical characterization of the charging process of a Li-ion battery and prediction of Li plating by electrochemical modelling*, 208-216, Copyright 2014, with permission from Elsevier" http://dx.doi.org/10.1016/j.jpowsour.2013.06.130

[3]
"Reprinted from Journal of Power Sources, 307 (2016), D. Burow, K. Sergeeva, S. Calles, K. Schorb, A. Börger, C. Roth, P. Heitjans, *Inhomogeneous degradation of graphite anodes in automotive lithium ion batteries under low-temperature pulse cycling conditions*, 806-814, Copyright 2016, with permission from Elsevier" http://dx.doi.org/10.1016/j.jpowsour.2016.01.033

[4]
"Reprinted from Journal of The Electrochemical Society, 163 (10) (2016), T. Waldmann, A. Iturrondobeitia, M. Kasper, N. Ghanbari, F. Aguesse, E. Bekaert, L. Daniel, S. Genies, I.J. Gordon, M.W. Löble, E. de Vito, M. Wohlfahrt-Mehrens, *Review—Post-Mortem Analysis of Aged Lithium-Ion Batteries: Disassembly Methodology and Physico-Chemical Analysis Techniques*, A2149-A2164, Copyright 2016, with permission from The Electrochemical Society" https://doi.org/10.1149/2.1211609jes

[5]
"Reprinted from Journal of Power Sources 443 (2019), M. Storch, S.L. Hahn, J. Stadler, R. Swaminathan, D. Vrankovic, C. Krupp, R. Riedel, *Post-mortem analysis of calendar aged large-format lithium-ion cells: Investigation of the solid electrolyte interphase*, 227243, Copyright 2019, with permission from Elsevier" https://doi.org/10.1016/j.jpowsour.2019.227243

[6]
"Reprinted from Journal of Power Sources 506 (2021) M. Storch, J.P. Fath, J. Sieg, D. Vrankovic, A. Mullaliu, C. Krupp, B. Spier, S. Passerini, R. Riedel, *Cycle parameter dependent degradation analysis in automotive lithium-ion cells*, 230227, Copyright 2021, with permission from Elsevier" https://doi.org/10.1016/j.jpowsour.2021.230227

[7]
"Reprinted from Journal of Energy Storage 41 (2021), M. Storch, J.P. Fath, J. Sieg, D. Vrankovic, C. Krupp, B. Spier, R. Riedel, *Temperature and Lithium Concentration Gradient Caused Inhomogeneous Plating in Large-format Lithium-ion Cells*, 102887, Copyright 2021, with permission from Elsevier" https://doi.org/10.1016/j.est.2021.102887

[8]

"Reprinted from Journal of Power Sources 400 (2018), S.L. Hahn, M. Storch, R. Swaminathan, B. Obry, J. Bandlow, K.P. Birke, *Quantitative validation of calendar aging models for lithium-ion batteries*, 402-414, Copyright 2018, with permission from Elsevier" https://doi.org/10.1016/j.jpowsour.2018.08.019

[9]

"Reprinted from Journal of Energy Storage 29 (2020), J.P. Fath, L. Alsheimer, M. Storch, J. Stadler, J. Bandlow, S. Hahn, R. Riedel, T. Wetzel, *The influence of the anode overhang effect on the capacity of lithium-ion cells – a 0D-modeling approach,* 101344, Copyright 2020, with permission from Elsevier" https://doi.org/10.1016/j.est.2020.101344

List of Tables

"Reprinted from Journal of Power Sources 443 (2019), M. Storch, S.L. Hahn, J. Stadler, R. Swaminathan, D. Vrankovic, C. Krupp, R. Riedel, *Post-mortem analysis of calendar aged large-format lithium-ion cells: Investigation of the solid electrolyte interphase*, 227243, Copyright 2019, with permission from Elsevier"

Journal of Power Sources 443 (2019) 227243

Contents lists available at ScienceDirect

Journal of Power Sources

journal homepage: www.elsevier.com/locate/jpowsour

Post-mortem analysis of calendar aged large-format lithium-ion cells: Investigation of the solid electrolyte interphase

Mathias Storch [a,b,*], Severin Lukas Hahn [a], Jochen Stadler [a], Ramanathan Swaminathan [a], Dragoljub Vrankovic [b], Carsten Krupp [a], Ralf Riedel [b]

[a] Daimler AG, Neue Strasse 95, 73230, Kirchheim u.T., Germany
[b] Fachgebiet Disperse Feststoffe, Fachbereich Material- und Geowissenschaften, Technische Universität Darmstadt, Otto-Berndt-Str. 3, 64287, Darmstadt, Germany

HIGHLIGHTS

- Investigation of solid electrolyte interphase growth due to calendar aging.
- A novel graphite-stage dependent solid electrolyte interphase growth is presented.
- Determination of inhomogeneous aging due to gas-assisted lithium plating.

GRAPHICAL ABSTRACT

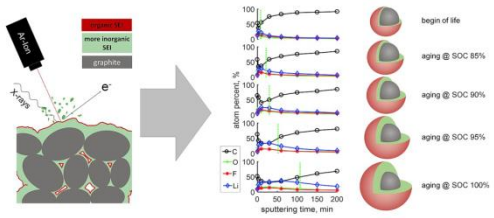

ARTICLE INFO

Keywords:
Lithium-ion battery
Calendar aging
Post-mortem analysis
X-ray photoelectron spectroscopy
Solid electrolyte interphase

ABSTRACT

Although the growth of the solid electrolyte interphase is considered one of the most important degradation phenomena of lithium-ion cells, the mechanism is not yet fully understood. In this work, we present a detailed post-mortem analysis of calendar aged large-format graphite/Li($Ni_{1/3}Mn_{1/3}Co_{1/3}$)O_2-based lithium-ion cells. X-ray photoelectron spectroscopy depth profiling reveals a distinct coherence of the growth of the solid electrolyte interphase with the phases of the lithiated graphite. Since the graphite phases are in direct correlation with the state of charge and the anode potential, the thickness of the SEI resulting from calendar aging is determined by the storage state of charge. The composition of the SEI has been analyzed as mainly organic near to the electrolyte and more inorganic towards the carbon active material. The same dependency as of the state of charge on the SEI thickness is found for the capacity retention and for the amount of irreversibly lost lithium. Additionally, gas is formed during the aging period and trapped in between the electrodes, leading to associated inhomogeneous lithium plating.

1. Introduction

Lithium-ion batteries are being used in portable electronics for more than 25 years, due to their benefit of high power and high energy densities. These advantages and the continuously decreasing price make Li-ion batteries viable for the application in individual transportation. For automotive applications, a long lifetime and indispensable safety have to be ensured. It is thus imperative to identify critical operation

* Corresponding author. Daimler AG, Neue Strasse 95, 73230, Kirchheim u.T., Germany.
E-mail address: mathias.storch@daimler.com (M. Storch).

https://doi.org/10.1016/j.jpowsour.2019.227243
Received 4 April 2019; Received in revised form 5 September 2019; Accepted 1 October 2019
Available online 11 October 2019
0378-7753/

conditions and to understand how they degrade the cell. Therefore, lifetime tests have to be performed and investigation of the cells by post-mortem analysis is required. Degradation of battery cells is commonly divided into cyclic and calendar modes, in which the capacity of the cell decreases and its resistance increases. The cyclic aging appears during the operation of the cell (charging or discharging) and the calendar aging during the resting periods, when the cell is stored without electric load. Especially calendar aging, which occurs over a period of years, has to be accelerated for testing and model development. Since it is known that calendar aging intensifies by applying high storage voltages and/or high temperatures, both parameters are most prominently varied [1–3].

There are many studies [4–8] dealing with degradation mechanisms in lithium-ion batteries. In calendar aging, the most important is the growth of the solid electrolyte interphase (SEI) in combination with electrolyte decomposition. However, the numerous studies are mainly performed on lab scale cells and most often for a few formation cycles only [5,6,9]. The main reason for SEI formation and growth is the electrochemical instability of typically used carbonate solvents in the operating potential window of a lithium-ion battery. When anode potentials reach below 0.8 V vs. Li/Li^+, the carbonate solvents decompose into several gaseous and solid components, which form the SEI [10]. However, not only the electrolyte solvents are important, also the additives, intended to improve lifetime and safety, influence the composition and stability of the SEI. In an ideal system the formation of SEI is a self-passivating process. Nevertheless, complete passivation is inhibited by tunneling electrons [11] through the SEI leading to formation of new SEI on top of the existing SEI and the electrolyte might diffuse through the existing SEI, forming new SEI at the graphite surface [12]. Additionally, the SEI may break open due to graphite volume changes and excavates the graphite surface [13–15]. These processes enable further SEI growth which leads to continuous losses of electrolyte and lithium [16]. Thereby the cell performance in terms of resistance and capacity deteriorates [17–20].

Understanding how the composition and thickness of the SEI evolves during aging requires detailed physical-chemical analysis of the electrodes and deposited material, commonly known as post-mortem analysis [21]. Waldmann et al. [21] demonstrated the variety of possible, destructive and non-destructive methods. However, literature suggests surface sensitive X-ray photoelectron spectroscopy (XPS) with its operation depth of 3–10 nm as most suitable method to analyze the SEI which is a few nanometer thick [22–28]. Most often, the composition of the initial SEI was examined after formation in small-sized, lab/-hand-built cells without any long-term aging.

Studies using carbonate based electrolytes with $LiPF_6$ as electrolyte, revealed that the main SEI components are lithium ethylene dicarbonate ($(CH_2OCO_2Li)_2$), lithium alkyl carbonates ($ROCO_2Li$), lithium alkoxide (ROLi), lithium carbonate (Li_2CO_3) and lithium fluoride (LiF) [24, 29–32]. Furthermore, these components are found to be arranged in a multilayer system whereat a dense inorganic inner layer of up to 10 nm in thickness, arranges in the vicinity of the graphite particles. In contact with the electrolyte solution a porous organic outer layer is formed which is up to 100 nm thick [13,25,33]. Tang and Newman [33] assume that the named inner layer is formed immediately and does not vary in thickness after once formed. Aurbach [13] describes the growth of the SEI as a breakdown and repair mechanism due to volume changes in which fresh graphite surface is exposed to electrolyte. Additional possible formation routes of the SEI are proposed by Smith et al. [34], where new SEI forms in the porous part of the existing SEI or impurity enhanced SEI growth takes place.

SEI formation and growth in commercial lithium-ion cells have been investigated by Lu et al. [35] and German et al. [19]. Lu et al. [35] investigated calendar aging for 6 months at 60% state of charge (SOC) and 100% SOC with and without subsequent cycling, observing enhanced SEI thickening due to high SOC aging and additional cycling. At the current state, many studies of the SEI have been performed, but still a long-term aging experiment of automotive-grade lithium-ion cells and a fine SOC resolution is missing.

Hence, a comprehensive study on calendar aging of 50.8 Ah large-format automotive pouch bag cells has been carried out in advance, followed by extensive post-mortem analysis presented in this work. The electrode materials, harvested from the pouch cells were analyzed using scanning electron microscopy (SEM), inductively coupled plasma optical emission spectrometry (ICP-OES) for compositional investigations and XPS depth profiling of the SEI deposits on the anode surfaces.

2. Experimental

The results in this work are based on a calendar aging matrix carried out with 54 commercial large-format automotive Li-ion pouch bag cells with a nominal capacity of 50.8 Ah produced by Litec Battery GmbH. Subsequently, volume measurements and post-mortem analysis were performed.

2.1. Calendar aging experiment

Investigated cells consist of graphite as anode and $Li(Ni_{1/3}Mn_{1/3}Co_{1/3})O_2$ (NMC111) as cathode material, separated by an Al_2O_3 coated poly ethylene membrane soaked in carbonate based electrolyte with $LiPF_6$ as conducting salt. Each cell comprises 34 double-side coated anodes, 33 double-side coated cathodes and 68 separator sheets. The test procedure evaluates the calendar aging characteristics during storage at constant conditions with daily recharge to keep the voltage constant. Test points were covering 0%–100% SOC at constant temperature of 50 °C with two cells at each point. More detailed description of the aging test is reported elsewhere [36]. Labelling of the samples follows the rule prefix "S" and the corresponding storage SOC from the aging experiment in % is attached, e. g. S100 for the cell stored at 100% SOC.

Calendar aging periods were interrupted by check-up tests monitoring the capacity as well as the resistivity trends. The test setup was comprised of climate chambers "UF110" (Memmert GmbH + Co. KG, Germany) and testing devices "Cell Test System CTS" (BaSyTec GmbH, Germany) for voltage control and daily recharge as well as "Multiple Cell Tester MCT" (Digatron Power Electronics GmbH, Germany) for regular check-ups. Total calendar aging time was about ~280 days. After the aging experiment, the cells were discharged to 3 V and kept at room temperature. Shortly before carrying out the post-mortem analysis a final check-up was performed comprising of a C/10 followed by a C/24 capacity measurement at 25 °C (C being 50.8 A). All cells were then discharged to 3 V in constant current-constant voltage mode with 1C discharge current and C/20 cut-off current.

2.2. Cell volume measurement

The cell volume was measured to determine the amount of gas evolved during the aging test. The measurement itself is adapted from Aiken et al. and optimized to the larger battery dimensions [37]. The setup consists of a water basin filled with deionized water (conductivity < 10 µS), a force gauge "Sauter FH10" (Sauter, Germany) and a lab balance "Series 321 LX" (Precisa Gravimetrics AG, Switzerland). After measuring the weight of the cells, they were hung on the force gauge and completely immersed in water. The cell volumes were calculated according to Archimedes principle and referenced to the volume of a cell at begin-of-life (BOL) [36].

2.3. Post-mortem analysis

Cell opening was carried out in an argon-filled glove box "MB200MOD" (MBraun Inert-Gas Systeme, Germany). To prevent any short cuts the pouch foil and the tabs were cut using a ceramic knife. One by one the stacked electrode/separator sheets were taken off. To remove crystallized residues of the conducting salt, the sheets were soaked in dimethyl carbonate (Sigma-Aldrich, Germany) for a total of 6 min.

Subsequently the sheets were dried and prepared for further investigations.

Appearance of the electrodes' surface was evaluated by image processing analysis using the open source software ImageJ [38]. Photographs of five double-side coated electrodes from layer 5 to 25 in steps of 5 were taken for the processing. The images were normalized in terms of brightness and coloration before separating distinct colored areas with several thresholding steps in HSB color space and on greyscale. Binary images were obtained, allowing the calculation of a mean areal percentage covered by the distinct colored surface.

For the ICP-OES analysis, a total area of 9.42 cm^2 double-side coated and representative electrode sheet including the current collector foil was used. The sample materials were always cut from the same position of the cell out of electrode layer number 20. The electrodes were separately dissolved in aqua regia and the solutions were analyzed using an OPTIMA 4300 DV (PerkinElmer Inc., US) optical emission spectrometer. Since the sample area was always the same, but the mass was differing, the measurement output in mg kg^{-1} was recalculated by the weight and area of the samples using the molar mass of lithium 6.941 g mol^{-1}, resulting in comparable values of lithium per area in µmol cm^{-2}.

A Sigma 300 VP scanning electron microscope (Carl Zeiss AG, Germany) was used to image the sample surfaces and possible surface deposits. SEM-micrographs were recorded by secondary electrons with an acceleration voltage of 5 kV and a magnification of 5000x. SEM-EDX parameters were 20 kV acceleration voltage and a measurement time of 50 s. Focused ion beam scanning electron microscopy (FIB-SEM) was performed on a Crossbeam 540 (Carl Zeiss AG, Germany) with acceleration voltage of 30 kV and last preparation current of 1.5 nA.

X-ray photoelectron spectroscopy was performed on a PHI 5800 ESCA System (Physical Electronics GmbH, Germany) using parameters adopted and adjusted from literature [19]. The XPS was equipped with monochromatic Al-Kα radiation, an angle of 45° between the sample and the analyzer and an analyzer pass energy of 93.9 eV for survey spectra and 29.35 eV for detail spectra. The lateral sample area was 800 × 800 $µm^2$. Sample preparation was performed in a nitrogen-filled glovebox (MBraun Inert-Gas Systeme, Germany) and to avoid contamination of the samples a gas-tight transfer container was used. The measurement is composed of eight measurement points, one before sputter etching and one each after sputter times of 3, 10, 30, 60, 100, 150 and 200 min. The etching rate on SiO_2 is calibrated to 1 nm min^{-1}. At every step a survey spectra and a detail spectra was recorded to generate depth profiles in atom percent versus sputter time. For further evaluation the spectra have been calibrated to the binding energy of LiF. A core level deconvolution procedure from Malmgren et al. [39] using line shapes of 70% gaussian and 30% lorentzian and an intensity normalization by the corresponding total peak area were applied.

Micro-Raman spectra of the electrode samples were recorded by using a micro-Raman spectrometer HR800 (Horiba Jobin Yvon, Japan) equipped with a solid state laser of wavelength 488 nm and a Raman shift range of 550 cm^{-1} to 4000 cm^{-1}. The samples were packed in gas-tight containers with laser transmittive glass windows. For all samples, the filters and measuring parameters were kept constant.

3. Results and discussion

As a starting point for further investigations, the capacity retention of the cells aged at various SOC set-points at a constant temperature of 50 °C are shown in Fig. 1a. The capacity retention is calculated by dividing the 1C discharge capacity of the last check-up test by the corresponding initial 1C discharge capacity of the first check-up test for each cell. The development of the cell capacities measured in the regular check-ups during the aging experiment can be reviewed elsewhere [36]. It is assumed, that the results found in this work are valid for room temperature aging as well, following Arrhenius law [40]. A storage SOC of 0%–15% leads to a high capacity retention of 94%–99% (sector A). A capacity retention of around 90% results from storage SOC between

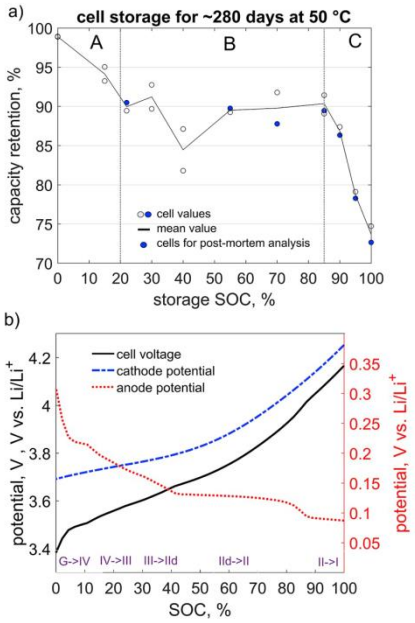

Fig. 1. a.) 1C discharge end-of-test capacity retention vs. the storage SOC of the aging experiment. Each dot represents a single cell and the line represents the calculated mean value. High capacity retention can be observed in the low storage SOC region, followed by a plateau between 22.5% SOC and 85% SOC followed by a strong decrease when exceeding 85% SOC. b.) cell voltage vs. SOC and the corresponding cathode and anode halfcell potentials vs. Li/Li^+, measured with 3-electrode test cells with a current rate of C/24. These potential curves are measured and valid for begin-of-life cell and might shift during the aging. On the bottom of the graph the graphite stages are listed for the comparison with the XPS measurements [41].

22.5% and 85% (sector B) with the only exception at SOC 40%. At a storage SOC higher than 85% (sector C) the capacity retention decreases strongly reaching 74% at SOC 100%. These sectors correlate to the lithiation stages of the graphite electrode shown in Fig. 1b related to the anode potential, which was measured with begin-of-life material in 3-electrode lab scale cells [36]. Section B correlates with the transition of stage III to stage II and section C correlates with the transition of stage II to stage I [41]. A comparable capacity retention trend was observed by Keil et al. [20] explaining the steps in the retention values by the influence of the graphite stages during intercalation. Since the balancing of the electrodes is specially designed for each cell the SOC positions of the steps can vary by using different cells.

However, to study the driving force and the mechanisms resulting in the observed capacity loss, a detailed post-mortem study is performed on one cell of each set-point. For the purpose of clarity, the results are shown for selected set-points, representing the general trends.

3.1. Post-mortem analysis

Prior to post-mortem analysis the cells were discharged uniformly to 3 V, thereby the effect of active lithium remaining in the anodes in the following measurements is minimized. Additionally the remaining conducting salt was washed out in a DMC bath. However, traces of $LiPF_6$ might rest in the samples.

3.1.1. Inductively coupled plasma optical emission spectrometry

The areal amount of lithium in the electrodes was determined using ICP-OES. Since the cells were discharged to 3 V it can be assumed, that the lithium content at the anode reveals the amount of irreversibly lost lithium. Possible contamination by traces of the conducting salt is assumed not to influence the comparability of the lithium contents [36, 40]. The lithium loss of the aged electrodes is calculated in comparison to begin-of-life ($Li_{loss2BOL}$), which is the state after formation process, by using equation (1). The initial areal amount of active lithium $Li_{Cathode,\ initial}$ is determined by the sum of the measured areal amount of lithium in the begin-of-life anode and cathode. The delithiation factor is 54% for NMC111 at a cathode potential of ~4.3 V vs. Li/Li^+ [42]. It is limited by the amount of lithium in the cathode that can be delithiated without causing the crystal structure to collapse and to irreversibly release oxygen [43].

$$Li_{\mathrm{loss2BOL}} = \frac{Li_{\mathrm{Anode}} - Li_{\mathrm{BOL,Anode}}}{(Li_{\mathrm{Cathode,\ initial}} * delithiation\ \ factor) - Li_{\mathrm{BOL,Anode}}} \quad (1)$$

ICP-OES shows that the amount of lithium in the anodes Li_{Anode} of the aged cells is higher than in the initial begin-of-life state. The opposite is found for the amount of lithium in the cathodes $Li_{Cathode}$ of the same cells. Sample S22.5 shows the least $Li_{loss2BOL}$. In analogy to the capacity retention, the lithium concentration can be clustered, as the samples S55 to S70 exhibit similar distributions resulting in $Li_{loss2BOL}$ of around 8%. S85 to S100 show an increase in the lithium loss from 11.2% for S85 up to 17.2% for S100 which directly correlate to the different graphite stages shown in Fig. 1b. The differences in the values between lithium and capacity loss will be discussed in detail together with the phenomena in section 3.2. For both, $Li_{loss2BOL}$ and $C_{loss2BOL}$, a similar trend for the dependency on storage SOC can be observed. The development of the lithium concentration can be explained by loss of active lithium which is irreversibly lost to the anode. In the following the anodes including the lithium are analyzed to identify the precise location and the chemical compounds containing lithium.

3.1.2. Scanning electron microscopy

Since ICP-OES has shown that the lithium amount at the anode increases with aging at increased SOC, SEM is used to investigate the surface morphology of the anode (see Fig. 2). The pristine anode material, having had no contact with electrolyte exhibits a smooth surface morphology. The begin-of-life anode after formation has some deposits on top of the particle indicating that the SEI starts to form during the formation process of the cell. The electrodes harvested from the cells S22.5 and S85 show slightly more deposits while the amount of these deposits appear to increase when increasing the aging SOC beyond 90% [40]. The morphology of the surface deposits is rather rough and porous than dense and continuous which indicates breaking and chipping off of the SEI even during the limited operation while performing the regular check-ups, as it is assumed in the SEI fracture model found in literature [13–15]. Since SEM cannot give quantitative results, these surface deposits have been analyzed in detail by XPS depth profiling.

3.1.3. X-ray photoelectron spectroscopy

Fig. 3 reveals depths profiles of the chemical composition of anode surfaces of samples BOL, S22.5, S85, S90, S95 and S100 measured by XPS combined with Ar^+-ion sputtering. Fractions of carbon, oxygen, fluorine and lithium are evaluated from the surface to a depth of up to 200 min, being main constituents of the SEI. The depth is calculated from the sputtering time and the Ar^+-ion etching rate calibrated on SiO_2 of 1 nm min^{-1}.

The depth profiles show that the surfaces of all samples are dominated by carbon ~50–70% and oxygen ~20% and show low amount of lithium and fluorine ~10%. Together with the Li/C ratio shown in Fig. 4 and the deconvoluted C1s, O1s and F1s core levels shown in Fig. 5, the surface can be identified as a mixture of mainly organic compounds, carbonates (CO_3, 291 eV and 533.5 eV), polyethers and polymers (C–O, 286.5 eV and 533 eV) and lithium hydroxide (LiOH, 531.5 eV). The present fluorine is bound as $LiPF_6$ residues (688 eV) [26], which could not be completely washed out and reaction products of the conducting salt with different species of carbonates (e.g. F_2PO_2Li, CH_3OCH_3, LiF) as discussed by Parimalam et al. [44].

Sputtering into the electrode's surface first leads to a decrease of carbon and oxygen and an increase of lithium and fluorine concentrations representing the transition from the organic surface SEI to a more inorganic, LiF and LiOR dominated inner SEI [39,45]. Proceeding to 10 min sputter time mainly the LiF, LiOR and LiOH are present. The BOL's carbon content increases steep and steadily, stabilizing around a carbon concentration of 90–95% after 200 min sputter time, which

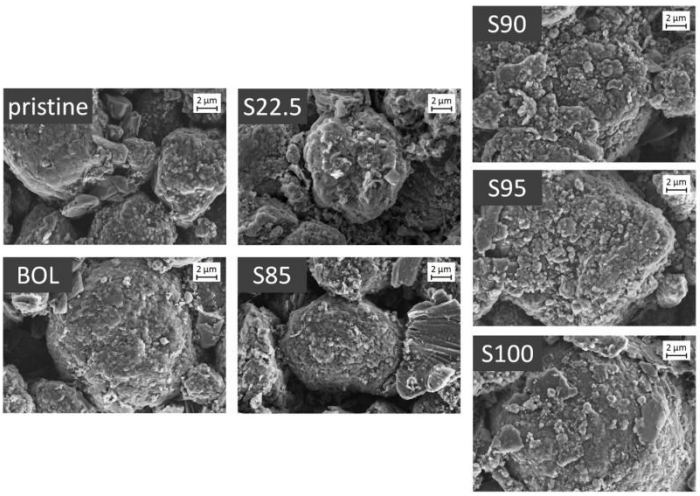

Fig. 2. SEM-micrographs of the anode materials pristine, begin-of-life and increase in storage SOC. The higher the storage SOC the more deposits on the graphite particle are found.

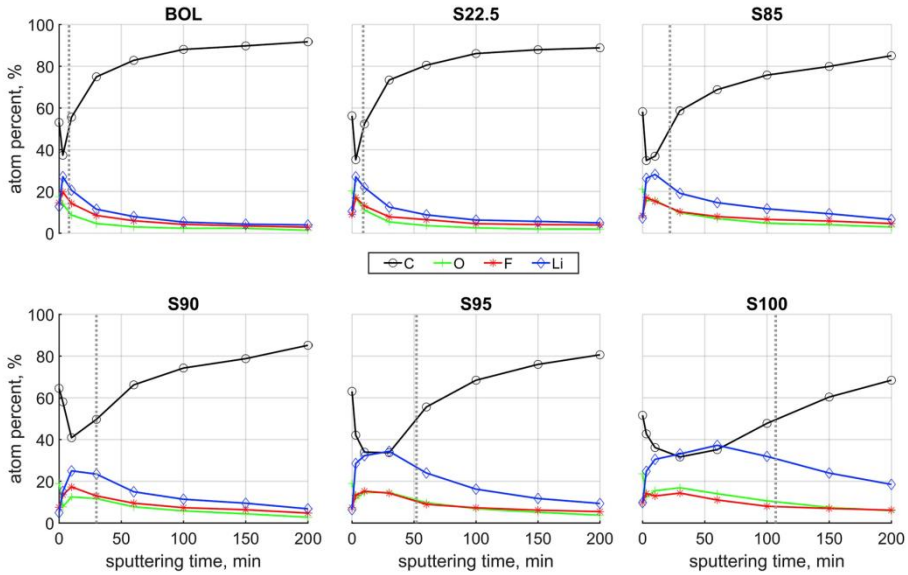

Fig. 3. Depth profiles of the carbon, oxygen, fluorine and lithium concentrations versus sputtering time for anodes at begin-of-life and S22.5, S85, S90, S95 and S100. Sputtering depth can be calculated from sputtering time and an etching rate of 1 nm min^{-1} on SiO_2. The depth profiles indicate a SOC dependent growth of the SEI during calendar aging to thicknesses of up to 100 nm (dotted line).

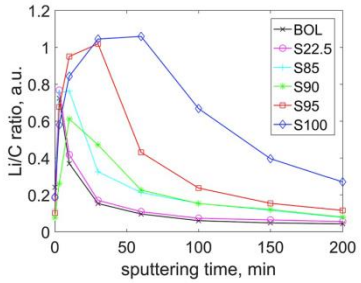

Fig. 4. Lithium/carbon ratio depth profiles of the anode samples BOL, S22.5, S85, S90, S95 and S100. After the low Li/C ratio in the beginning shows the organic SEI part, a more inorganic SEI follows represented by the ratio of ~1.

relates to the electrodes base material of carbon with C–C at 284.4 eV and C–H 285 eV [45]. At the same time the oxygen (C–O, LiOH, Li_2O), lithium (LiOR, LiOH, LiF) and fluorine (LiF) concentrations decrease to only a few percent. In case of Li_2O it remains unclear whether it is a SEI compound or an artefact of the sputter process [27,39].

Sample S22.5 exhibits similar depth profile, C1s, O1s and F1s core level spectra compared to BOL. A small, but for the SEI characteristic plateau in the four depth profiles and in the depth profile of the Li/C ratio can be identified at a sputter time range between 3 min and 10 min in S85. Further increase of the storage SOC to 100% leads to both, an increase of the length of this plateau and to a rise in the total amount of O, F, and Li. The plateau shows up because of and according to the thickness of the predominantly inorganic SEI composed of LiF, LiOH, Li_2O and LiOR.

The characteristic plateau in the depth profiles was already observed in the literature, however, due to a lack of comparable electrode materials with varying aging states and therefore SEI thicknesses the plateau was not considered to represent the SEI thickness up to now [26,45,46]. To get a better hold on comparing the thicknesses, the crossing point of the carbon depth profile with the 50% concentration line is defined as criteria for the SEI thickness. Due to the heterogeneous surface morphology of the samples, the thickness of the SEI obviously cannot be determined absolutely on a lateral range of hundredth of μm^2 and should rather be understood as an indication on how the SEI growth is related to the aging conditions.

The SEI thicknesses estimated accordingly are listed in Table 2 and show an exponential increase with storage SOC, suggesting a strong dependency between the SEI growth and the cell's state of charge during calendar aging. The trend of SEI thickness matches well with the results from ICP-OES and the graphite stages shown in Fig. 1b and Table 1. The strongest increase in thickness is observed at S100 with a thickness of more than 100 nm. Regarding the anode potentials during calendar aging for the individual cells (see Fig. 1b), the anode potential lays on the plateau of stage II- > I transition for a storage SOC above 85%. On each plateau of the graphite potential curve the two phases coexist e.g. in section C, Fig. 1a, both phases II and I are present [41,47]. We suggest that the SEI growth depends on the stage of the graphite. An additional influence on the SEI growth can be the difference of the graphite potential of the two plateaus (III- > II and II- > I) of approx. 40 mV as a driving force [41,48]. Combining the higher SEI growth rate at high SOC with the models of breakdown and repair by Aurbach et al. [13] an increased SEI thickness at high SOC seems reasonable. Complementary the continuous conversation of the newly formed SEI due to high temperature as explained by Parimalam et al. [44] might accelerate the SEI thickness growth. The suggested growth of SEI is in good accordance with the findings of Keil et al. [20] on the correlation of the capacity retention with the anode potential during storage.

The determined BOL SEI thickness is in the range of previously measured SEI thickness on the similar cell by German et al. [19] with an estimated SEI thickness of ~5–10 nm and ~10–15 nm estimated by

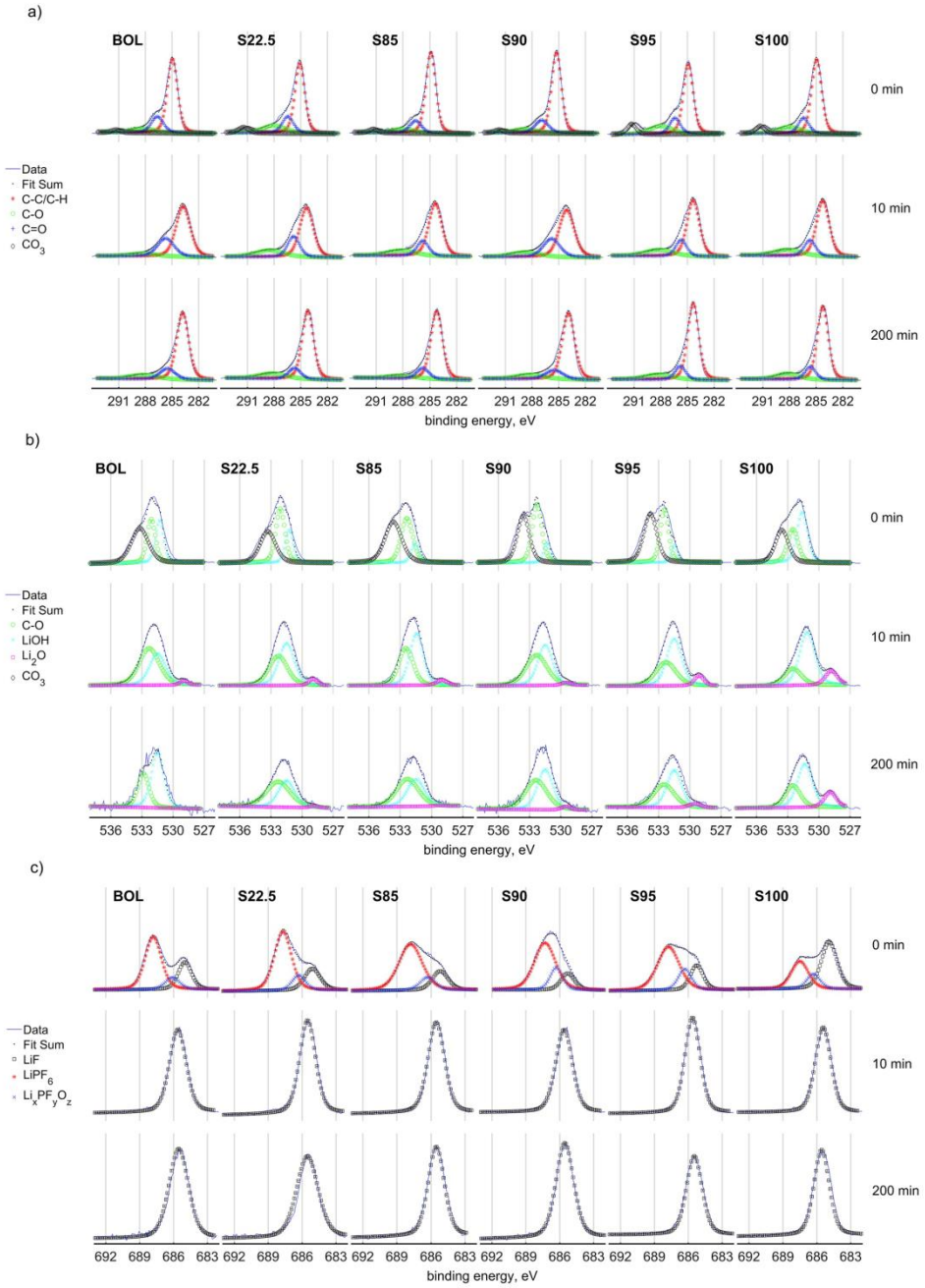

Fig. 5. Core level spectra of a) C1s, b) O1s and c) F1s of the samples BOL, S22.5, S85, S90, S95 and S100. The measured data is deconvoluted using peak positions of [24–26,39,44]. Sputter times are given on the right side of each row.

Table 1
Amount of lithium in the electrodes, anode and cathode, measured via ICP-OES. Including the calculated Li loss compared to BOL available lithium. For comparison, the mean end of test capacity loss is listed.

Cell conditions	Li_{Anode} [a] [µmol cm^{-2}]	$Li_{Cathode}$ [a] [µmol cm^{-2}]	$Li_{loss2BOL}$ [b] [%]	$C_{loss2BOL}$ [c] [%]
begin-of-life	11.80	131.98	-	-
S22.5	15.31	121.15	5.3	9.52
S55	17.05	121.52	8.0	10.03
S70	17.51	121.16	8.7	10.22
S85	19.15	118.59	11.2	9.65
S90	19.90	114.79	12.3	13.14
S95	20.82	111.65	13.7	21.30
S100	23.11	110.15	17.2	26.35

[a] Measured by ICP-OES, error ±0.1%.
[b] Calculated by equation (1).
[c] Measured prior to post-mortem analysis.

Table 2
Estimated SEI thickness measured by XPS depth profiling. 50% carbon concentration is set as thickness criteria. Increasing the storage SOC leads to an increase in SEI thickness.

Sample-ID	Estimated SEI thickness [nm]
BOL	8
S22.5	9
S85	22
S90	30
S95	52
S100	107

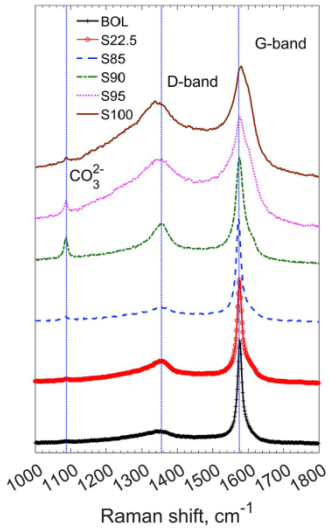

Fig. 6. Raman spectra in the shift range of 1000 cm^{-1} to 1800 cm^{-1}. CO_3^{2-} is verified to be present on the aged electrodes. The graphite order of S90, S95 and S100 is decreased and the number of defects is increased.

Eshkenazi et al. [26] for the SEI grown on self-made soft carbon electrodes. In comparison to SEI thickness determined after long-term aging, Lu et al. [35] measured SEI thicknesses of 6 month calendar aged anodes to be > 70 nm and Lee et al. [49] estimated SEI thicknesses between 100 nm and 315 nm for cyclic aging. Since these studies some parameters are different than in the present one, our estimated SEI thicknesses of 10 nm–107 nm for long-term calendar aged cells with varying storage SOC are reasonable. The method can easily be adopted to evaluate the SEI growth dependencies of varying cell types, compositions and aging conditions.

3.1.4. Raman spectroscopy

The Raman spectra of the samples are depicted in Fig. 6, a band at 1088 cm^{-1} verifies the presence of CO_3^{2-} on the aged anodes [50]. The characteristic G- and D-band of carbonaceous materials can also be identified [51]. In samples with high SOC (S90, S95 and S100) a shoulder at approx. 1600 cm^{-1} appears, corresponding to the D′ band. Presence of the D (1320 cm^{-1}) and D′ bands in the Raman spectra of graphite indicate presence of disorder in carbon phase [52]. Additionally, increase in their intensity, compared to intensity of G-band, on higher SOCs indicates enhanced degradation of graphite surface caused by enhanced aging. Li et al. [53] already observed enhanced structural degradation of graphite anodes cycled at high temperatures. Apart from the thermal stresses, the cycling SOC window prove to have strong influence on graphite degradation [54] However, a fitting of the Raman bands of the high SOC samples for quantitative evaluation is not feasible due to strong fluorescence background caused by increased amount of decomposition products on the electrodes surface.

3.2. Gas-assisted lithium plating

In addition to lithium loss due to SEI-growth, a second important mechanism contributes to loss of active lithium. Post-mortem analysis reveals an inhomogeneous distribution of brown-yellowish deposits on the graphite anodes for the cells aged at 50 °C and stored at high SOC (>85%). In Fig. 7a, anode electrodes of cells S85, S90, S95 and S100 are depicted. It is clearly visible that increase in SOC shows increased amount of deposits. A magnified image of S100 (Fig. 7b) shows the morphology of the surface deposit. The FIB-SEM micrograph and the SEM top view micrograph in Fig. 7c reveal that the surface deposits are several microns thick deposited on top of the graphite particles similar to the Li-Plating found by Petzl and Danzer [55].

Comparable patterns were found by Matadi et al. [3] in pouch cells that were calendar aged at elevated temperatures and 100% SOC. They showed metallic lithium being part of the deposits and suggested a pathway of formation: at high potentials and temperatures, electrolyte may decompose and thereby form gas bubbles between the electrode sheets leading to a local loss of contact between the electrodes and the electrolyte. In their following checkup tests, the current density increases at the edges of the bubbles, resulting in higher overpotentials that cause local lithium plating even at high temperatures [3]. Literature has shown that in lithium-ion cells gas species like H_2, C_2H_4 and CO_2 [56–58] can be formed due to the reaction of the solvents with the electrodes or during the decomposition of the conducting salt in presence of impurities e.g. trace water [59].

As the deposits are distributed inhomogeneously on the surface, it is not straightforward to quantify the amount of the lithium being lost due to plating. Complementary to the XPS-study of active lithium lost to SEI growth, we analyzed this second mechanism in terms of cell volume determination, visual evaluation of the electrodes (see Fig. 8), as well as ICP-OES and FIB-SEM. As an example for the procedure steps to analyze the surface coverage, the binary image of the photograph of an anode electrode is depicted in the inset in Fig. 8. Both, the gas volume evolved and the anode coverage, remain negligible up to sample S70. With increasing storage SOC above 70%, the gas volume raises exponentially, ending up at around 17% gain of the cells original volume for sample S100. From the trend of both properties, it is obvious that the increase of the cell volume and the anode area covered with deposits are linked to each other.

ICP-OES shows a two fold increase in lithium of electrode samples containing deposits compared to the inconspicuous anode material. This strong increase indicates that, similar to the findings of Matadi et al. [3],

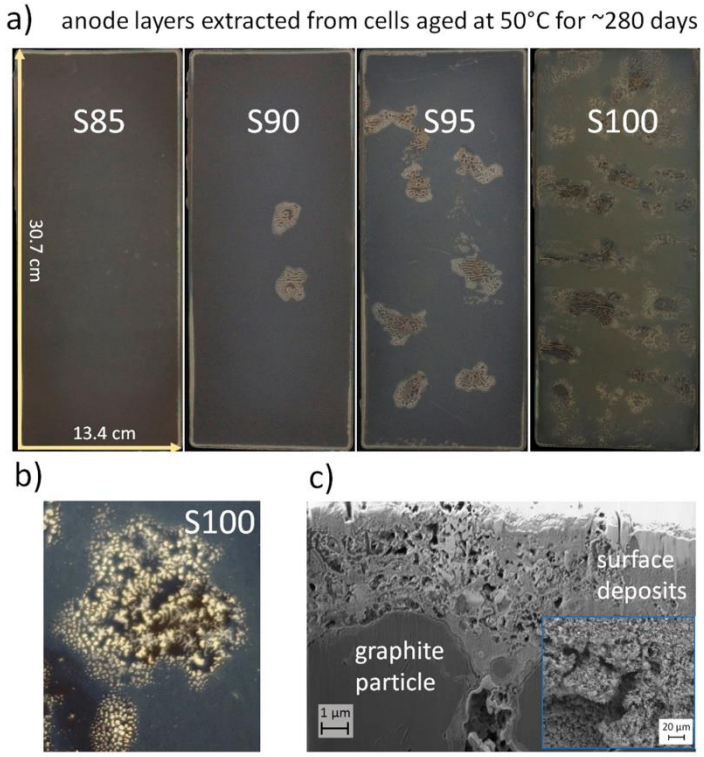

Fig. 7. a) Optical micrographs of surface deposits emerging on anode sheets of the samples S85, S90, S95 and S100, b) magnified optical micrograph of S100 surface deposit, c) FIB-SEM cross-section of surface deposits on graphite particles with 7500x magnification and the corresponding SEM top view micrograph. The surface deposits are several microns thick on top of the graphite particles and the surface deposits occur in increasing amount as storage SOC is increased.

the surface deposits are caused by heavy lithium plating. A similar effect leading to localized Li-plating was investigated experimentally and by simulation by Cannarella et al. [60], whereat the inactive regions were created by local pore closure of the separator. Additionally, Stiaszny et al. [1] found similar strong deposits randomly distributed on the anodes of cells calendar aged at 60 °C with high SOC, which could not be explained by conducting salt or solvent decomposition exclusively. EDX was measured on top of the thick deposited material as it can be seen in the inset in Fig. 7c and as comparison on a normally aged area comparing to Fig. 2. Despite lithium is not measurable in EDX, the elements stemming from the electrolyte reaction with plated lithium can be identified (Table 3). Thus, the deposits possess an oxygen concentration strongly increasing from 7.6 to 57.5 at%. In the same time, phosphor and sulfur concentrations increase from 0.6% and 0.4% to 6.3% and 2.3%, respectively. The increase of these three elements is explained by the reaction of lithium with the conducting salt $LiPF_6$ and electrolyte solvents/additives. Similar to graphite at low potentials vs. Li/Li^+ (stage I) the plated lithium forms an oxygen-rich SEI when reacting with the electrolyte.

As this gas-assisted lithium plating mainly occurs due to test conditions, which shall accelerate aging, effort is required to avoid this mechanism taking place. We assume that the additional loss of active lithium due to gas-assisted Li-plating can be avoided by firmly clamping the pouch cells between stiff plates in order to press the formed gas from the cell interior into the gas pockets.

The inhomogeneities found here are explaining the differences between the measured capacity retentions and the corresponding lithium concentrations, which have been measured on anode electrode material not having the lithium plated on top (Table 1). A possible explanation for the process leading to the found cell aging is that an increase in SOC leads to an increase in SEI formation and in the same time, as byproducts, gases form, while the high temperature of 50 °C causes additional gases due to thermal decomposition of the electrolyte. Then over the aging time the gas forms bubbles, which steadily grow and lead to gas-assisted lithium plating during the check-up tests. The plated lithium again reacts with the electrolyte and forms new gases.

Summarizing we can notice that in large-scale lithium-ion batteries inhomogeneities play an important role, and every present mechanism need to be examined separated from each other. Analysing these inhomogeneities on lab-scale experiments, maybe by gathering material from known commercial cells might be a big opportunity for further understanding of the fundamental aging mechanism. In our study different mechanism contributed to the overall loss of active lithium into inactive lithium as SEI component or thick deposited lithium. The amount of active lithium is one of the capacity determining parameters and in this study is responsible for the loss of cell capacity.

4. Conclusions

In this work, we performed post-mortem analysis of large-format automotive lithium-ion cells after a long-term temperature accelerated calendar aging period. The cells stored with high SOC (>85%) show

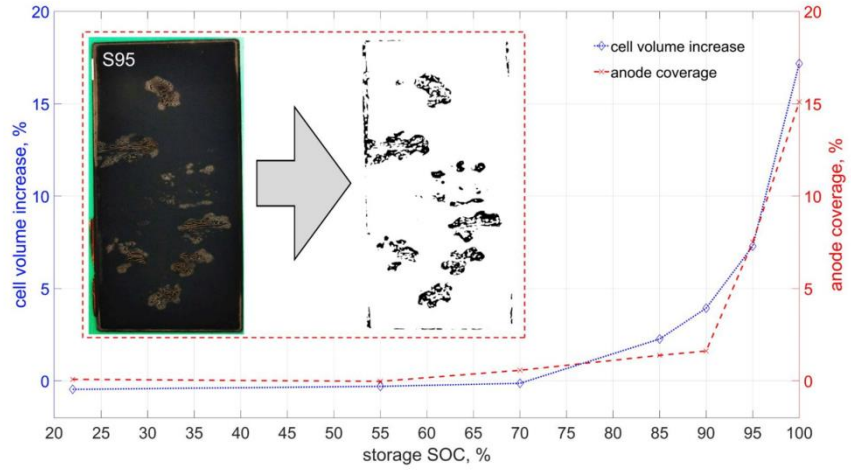

Fig. 8. Cell volume increase determined according to Archimedes principle and anode coverage determined via image analysis versus the storage SOC during aging experiment. The cell volume increase data has been previously published in Ref. [36]. Inset a) shows a binary image from image analysis separating the inconspicuous and the covered electrode area. A correlation between cell volume increase and fraction of anode surface covered with lithium plating deposits is shown.

Table 3
Element concentrations in the S100 anode and corresponding deposits determined via SEM-EDX analysis. The deposit possess strong increase of oxygen, phosphor and sulfur and decrease of carbon. It should be noted that lithium is not measureable in EDX due to low atomic mass.

sample	carbon at %	oxygen at %	fluorine at %	phosphor at %	sulfur at %
S100	87.4	7.6	4.0	0.6	0.4
S100-deposit	30.5	57.5	3.4	6.3	2.3

severe deterioration of performance, displaying up to 26% loss of capacity and strong SEI growth after 280 days operated at 50 °C. In contrary, cells with SOC lower than 85% prove to have less than half the capacity losses (~10%) independent of the adjusted SOC. The main reason for the capacity loss was assigned to the irreversible loss of lithium to the anode.

Detailed investigation of the SEI showed that it mainly contains lithium, fluorine, oxygen and carbon distributed within organic SEI near to the electrolyte and a more inorganic SEI near to the electrodes's surface. Once more, when aging the cell with the anode potential being on the plateau of transition stage II to stage I, which is the case for SOCs over 85% caused accelerated SEI growth leading to strong SEI thickening. Graphite seems to preferentially grow an organic layer on top of the more inorganic LiF, Li2O, LiOH and LIOR containing inner layer. Thus, in order to enhance battery lifetime, the present study suggests to avoid the upper SOC window (graphite plateau II- > I) and rather keep the SOC low during idle periods.

After careful investigation of the complete electrode surface of the cells stored at high SOCs (>85%), regions of strong, several microns thick, surface deposits differing from above mentioned SEI are found. The deposited material can be assigned to lithium plating occurring during the regularly carried out check-ups. These by deposits clogged areas of the anode surface are in direct correlation with the amount of gas build up and kept in between the electrode sheets of the cell emphasizing the importance of certain pressure applied on the large-format cells during their operation.

In this study we have shown that a post-mortem analysis with numerous and well selected investigation methods like XPS depth profiling, ICP-OES elemental quantification, SEM, Raman spectroscopy, gas-volume measurements and visual characterization is crucial to gain understanding of SEI formation and further aging processes. However, further investigation of the degradation mechanisms (e.g. SEI growth, Li plating, gassing, etc.) during long-term calendar and cyclic aging of large-format lithium-ion batteries is needed to completely understand and control their aging behavior.

Acknowledgements

Funding from the German Federal Ministry of Economic Affairs and Energy of the Project DriveBattery2015 (03ET6060F) is gratefully acknowledged. The responsibility for this publication rests with the authors. The authors acknowledge the Matworks GmbH, Aalen, SGS Fresenius Institut, Dresden and the Ulm university, Ulm for performing the physical-chemical analysis. The BatterieIngenieure GmbH, Aachen, is thanked for conducting the calendar aging experiment. Naqeeb Tahasildar is thanked for helping to harvest electrode materials and to measure cell volume.

References

[1] B. Stiaszny, J.C. Ziegler, E.E. Krauß, M. Zhang, J.P. Schmidt, E. Ivers-Tiffée, J. Power Sources 258 (2014) 61–75. https://doi.org/10.1016/j.jpowsour.2014.02.019.
[2] M. Ecker, N. Nieto, S. Käbitz, J. Schmalstieg, H. Blanke, A. Warnecke, D.U. Sauer, J. Power Sources 248 (2014) 839–851. https://doi.org/10.1016/j.jpowsour.2013.09.143.
[3] B.P. Matadi, S. Geniès, A. Delaille, T. Waldmann, M. Kasper, M. Wohlfahrt-Mehrens, F. Aguesse, E. Bekaert, I. Jiménez-Gordon, L. Daniel, X. Fleury, M. Bardet, J.-F. Martin, Y. Bultel, J. Electrochem. Soc. 164 (2017) A1089–A1097. https://doi.org/10.1149/2.0631706jes.
[4] M. Broussely, P. Biensan, F. Bonhomme, P. Blanchard, S. Herreyre, K. Nechev, R. J. Staniewicz, J. Power Sources 146 (2005) 90–96. https://doi.org/10.1016/j.jpowsour.2005.03.172.
[5] J. Vetter, P. Novák, M.R. Wagner, C. Veit, K.-C. Möller, J.O. Besenhard, M. Winter, M. Wohlfahrt-Mehrens, C. Vogler, A. Hammouche, J. Power Sources 147 (2005) 269–281. https://doi.org/10.1016/j.jpowsour.2005.01.006.
[6] P. Verma, P. Maire, P. Novák, Electrochim. Acta 55 (2010) 6332–6341. https://doi.org/10.1016/j.electacta.2010.05.072.
[7] V.A. Agubra, J.W. Fergus, J. Power Sources 268 (2014) 153–162. https://doi.org/10.1016/j.jpowsour.2014.06.024.

[8] C. Schlasza, P. Ostertag, D. Chrenko, R. Kriesten, D. Bouquain, in: 2014 IEEE Transportation Electrification Conference and Expo (ITEC), 2014, pp. 1–6. https://doi.org/10.1109/ITEC.2014.6861811.
[9] V. Agubra, J. Fergus, Materials (Basel, Switzerland) 6 (2013) 1310–1325. https://doi.org/10.3390/ma6041310.
[10] R. Imhof, J. Electrochem. Soc. 145 (1998) 1081–1087. https://doi.org/10.1149/1.1838420.
[11] D. Li, D. Danilov, Z. Zhang, H. Chen, Y. Yang, P.H.L. Notten, J. Electrochem. Soc. 162 (2015) A858–A869. https://doi.org/10.1149/2.0161506jes.
[12] H.J. Ploehn, P. Ramadass, R.E. White, J. Electrochem. Soc. 151 (2004) A456–A462. https://doi.org/10.1149/1.1644601.
[13] D. Aurbach, J. Power Sources 89 (2000) 206–218. https://doi.org/10.1016/S0378-7753(00)00431-6.
[14] R. Deshpande, M. Verbrugge, Y.-T. Cheng, J. Wang, P. Liu, J. Electrochem. Soc. 159 (2012) A1730–A1738. https://doi.org/10.1149/2.049210jes.
[15] I. Laresgoiti, S. Käbitz, M. Ecker, D.U. Sauer, J. Power Sources 300 (2015) 112–122. https://doi.org/10.1016/j.jpowsour.2015.09.033.
[16] R.D. Deshpande, D.M. Bernardi, J. Electrochem. Soc. 164 (2017) A461–A474. https://doi.org/10.1149/2.0841702jes.
[17] R. Kostecki, J. Lei, F. McLarnon, J. Shim, K. Striebel, J. Electrochem. Soc. 153 (2006) A669–A672. https://doi.org/10.1149/1.2170551.
[18] A.J. Smith, J.C. Burns, D. Xiong, J.R. Dahn, J. Electrochem. Soc. 158 (2011) A1136–A1142.
[19] F. German, A. Hintennach, A. LaCroix, D. Thiemig, S. Oswald, F. Scheiba, M. J. Hoffmann, H. Ehrenberg, J. Power Sources 264 (2014) 100–107. https://doi.org/10.1016/j.jpowsour.2014.04.071.
[20] P. Keil, S.F. Schuster, J. Wilhelm, J. Travi, A. Hauser, R.C. Karl, A. Jossen, J. Electrochem. Soc. 163 (2016) A1872–A1880. https://doi.org/10.1149/2.0411609jes.
[21] T. Waldmann, A. Iturrondobeitia, M. Kasper, N. Ghanbari, F. Aguesse, E. Bekaert, L. Daniel, S. Genies, I.J. Gordon, M.W. Löble, E. de Vito, M. Wohlfahrt-Mehrens, J. Electrochem. Soc. 163 (2016) A2149–A2164. https://doi.org/10.1149/2.1211609jes.
[22] D. Aurbach, J. Electrochem. Soc. 143 (1996) 3809–3820. https://doi.org/10.1149/1.1837300.
[23] A. Schechter, D. Aurbach, H. Cohen, Langmuir 15 (1999) 3334–3342. https://doi.org/10.1021/la981048h.
[24] A.M. Andersson, K. Edström, J. Electrochem. Soc. 148 (2001) A1100–A1109. https://doi.org/10.1149/1.1397771.
[25] A.M. Andersson, A. Henningson, H. Siegbahn, U. Jansson, K. Edström, J. Power Sources 119–121 (2003) 522–527. https://doi.org/10.1016/S0378-7753(03)00277-5.
[26] V. Eshkenazi, E. Peled, L. Burstein, D. Golodnitsky, Solid State Ion. 170 (2004) 83–91. https://doi.org/10.1016/S0167-2738(03)00107-3.
[27] K. Edström, M. Herstedt, D.P. Abraham, J. Power Sources 153 (2006) 380–384. https://doi.org/10.1016/j.jpowsour.2005.05.062.
[28] L. El Ouatani, R. Dedryvère, J.-B. Ledeuil, C. Siret, P. Biensan, J. Desbrières, D. Gonbeau, J. Power Sources 189 (2009) 72–80. https://doi.org/10.1016/j.jpowsour.2008.11.031.
[29] C.R. Yang, Y.Y. Wang, C.C. Wan, J. Power Sources 72 (1998) 66–70. https://doi.org/10.1016/S0378-7753(97)02655-4.
[30] D. Aurbach, B. Markovsky, M.D. Levi, E. Levi, A. Schechter, M. Moshkovich, Y. Cohen, J. Power Sources 81–82 (1999) 95–111. https://doi.org/10.1016/S0378-7753(99)00187-1.
[31] D. Aurbach, J. Power Sources 119–121 (2003) 497–503. https://doi.org/10.1016/S0378-7753(03)00273-8.
[32] M. Nie, B.L. Lucht, J. Electrochem. Soc. 161 (2014) A1001–A1006. https://doi.org/10.1149/2.054406jes.
[33] M. Tang, J. Newman, J. Electrochem. Soc. 158 (2011) A530–A536. https://doi.org/10.1149/1.3567765.
[34] A.J. Smith, J.C. Burns, D. Xiong, J.R. Dahn, J. Electrochem. Soc. 158 (2011) A1136–A1142. https://doi.org/10.1149/1.3625232.
[35] M. Lu, H. Cheng, Y. Yang, Electrochim. Acta 53 (2008) 3539–3546. https://doi.org/10.1016/j.electacta.2007.09.062.
[36] S.L. Hahn, M. Storch, R. Swaminathan, B. Obry, J. Bandlow, K.P. Birke, J. Power Sources 400 (2018) 402–414. https://doi.org/10.1016/j.jpowsour.2018.08.019.
[37] C.P. Aiken, J. Xia, D.Y. Wang, D.A. Stevens, S. Trussler, J.R. Dahn, J. Electrochem. Soc. 161 (2014) A1548–A1554. https://doi.org/10.1149/2.0151410jes.
[38] J. Schindelin, I. Arganda-Carreras, E. Frise, V. Kaynig, M. Longair, T. Pietzsch, S. Preibisch, C. Rueden, S. Saalfeld, B. Schmid, J.-Y. Tinevez, D.J. White, V. Hartenstein, K. Eliceiri, P. Tomancak, A. Cardona, Nat. Methods 9 (2012) 676. EP. https://doi.org/10.1038/nmeth.2019.
[39] S. Malmgren, K. Ciosek, M. Hahlin, T. Gustafsson, M. Gorgoi, H. Rensmo, K. Edström, Electrochim. Acta 97 (2013) 23–32. https://doi.org/10.1016/j.electacta.2013.03.010.
[40] T. Waldmann, M. Wilka, M. Kasper, M. Fleischhammer, M. Wohlfahrt-Mehrens, J. Power Sources 262 (2014) 129–135. https://doi.org/10.1016/j.jpowsour.2014.03.112.
[41] D. Billaud, F.X. Henry, Solid State Commun. 124 (2002) 299–304.
[42] M.S. Whittingham, Chem. Rev. 104 (2004) 4271–4302. https://doi.org/10.1021/cr020731c.
[43] R. Jung, M. Metzger, F. Maglia, C. Stinner, H.A. Gasteiger, J. Electrochem. Soc. 164 (2017) A1361–A1377.
[44] B.S. Parimalam, A.D. MacIntosh, R. Kadam, B.L. Lucht, J. Phys. Chem. C 121 (2017) 22733–22738.
[45] D. Bar-Tow, J. Electrochem. Soc. 146 (1999) 824. https://doi.org/10.1149/1.1391688.
[46] K. Araki, N. Sato, J. Power Sources 124 (2003) 124–132. https://doi.org/10.1016/S0378-7753(03)00593-7.
[47] K.E. Thomas-Alyea, C. Jung, R.B. Smith, M.Z. Bazant, J. Electrochem. Soc. 164 (2017) E3063–E3072.
[48] P.M. Attia, S. Das, S.J. Harris, M.Z. Bazant, W.C. Chueh, J. Electrochem. Soc. 166 (2019) E97–E106. https://doi.org/10.1149/2.0231904jes.
[49] J.T. Lee, N. Nitta, J. Benson, A. Magasinski, T.F. Fuller, G. Yushin, Carbon 52 (2013) 388–397. https://doi.org/10.1016/j.carbon.2012.09.049.
[50] P. Pasierb, S. Komornicki, M. Rokita, M. Rękas, J. Mol. Struct. 596 (2001) 151–156. https://doi.org/10.1016/S0022-2860(01)00703-7.
[51] F. Tuinstra, J.L. Koenig, J. Chem. Phys. 53 (1970) 1126–1130. https://doi.org/10.1063/1.1674108.
[52] D. Li, D.L. Danilov, H.J. Bergveld, R.-A. Eichel, P.H.L. Notten, in: A. Eftekhari (Ed.), Future Lithium-Ion Batteries, Royal Society of Chemistry, London, 2019, pp. 220–250.
[53] D. Li, D.L. Danilov, L. Gao, Y. Yang, P.H.L. Notten, Electrochim. Acta 210 (2016) 445–455.
[54] V.A. Sethuraman, L.J. Hardwick, V. Srinivasan, R. Kostecki, J. Power Sources 195 (2010) 3655–3660.
[55] M. Petzl, M.A. Danzer, J. Power Sources 254 (2014) 80–87.
[56] M. Lanz, P. Novák, J. Power Sources 102 (2001) 277–282. https://doi.org/10.1016/S0378-7753(01)00826-6.
[57] D. Aurbach, J. Electrochem. Soc. 141 (1994) 603–611. https://doi.org/10.1149/1.2054777.
[58] M. Metzger, B. Strehle, S. Solchenbach, H.A. Gasteiger, J. Electrochem. Soc. 163 (2016) A798–A809. https://doi.org/10.1149/2.1151605jes.
[59] R. Bernhard, M. Metzger, H.A. Gasteiger, J. Electrochem. Soc. 162 (2015) A1984–A1989. https://doi.org/10.1149/2.0191510jes.
[60] J. Cannarella, C.B. Arnold, J. Electrochem. Soc. 162 (2015) A1365–A1373.

"Reprinted from Journal of Power Sources 506 (2021) M. Storch, J.P. Fath, J. Sieg, D. Vrankovic, A. Mullaliu, C. Krupp, B. Spier, S. Passerini, R. Riedel, *Cycle parameter dependent degradation analysis in automotive lithium-ion cells*, 230227, Copyright 2021, with permission from Elsevier"

Journal of Power Sources 506 (2021) 230227

Contents lists available at ScienceDirect

Journal of Power Sources

journal homepage: www.elsevier.com/locate/jpowsour

Cycle parameter dependent degradation analysis in automotive lithium-ion cells

Mathias Storch [a,b,*], Johannes Philipp Fath [a], Johannes Sieg [a], Dragoljub Vrankovic [a,b], Angelo Mullaliu [c,d], Carsten Krupp [a], Bernd Spier [a], Stefano Passerini [c,d], Ralf Riedel [b]

[a] Mercedes-Benz AG, Neue Strasse 95, 73230, Kirchheim u.T., Germany
[b] Fachgebiet Disperse Feststoffe, Fachbereich Material- und Geowissenschaften, Technische Universität Darmstadt, Otto-Berndt-Str. 3, 64287, Darmstadt, Germany
[c] Helmholtz Institute Ulm (HIU), Helmholtzstrasse 11, 89081, Ulm, Germany
[d] Karlsruhe Institute of Technology (KIT), P.O. Box 3640, 76021, Karlsruhe, Germany

HIGHLIGHTS

- Cyclic aging investigation of large-format automotive lithium-ion cells.
- Correlation between operational parameter and degradation mechanism.
- SEI growth accelerated by temperature and cell voltage.
- Loss of electric contact as major cathode degradation mechanism.
- Manganese dissolution at high SOC range.

GRAPHICAL ABSTRACT

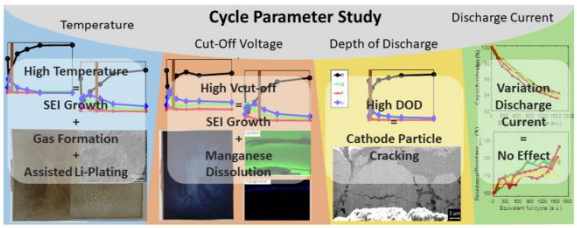

ARTICLE INFO

Keywords:
Lithium-ion battery
Cycle aging
Post-mortem analysis
Solid electrolyte interphase
Transition metal dissolution
Cathode degradation

ABSTRACT

In this study, we report on the operational parameter dependent degradation mechanisms occurring in cycled large-format automotive lithium-ion cells. The comprehension of these mechanisms is a prerequisite for design and operation of long-life lithium-ion cells. The degradation mechanisms are evaluated in dependence of cycle temperature, cut-off voltage, depth of discharge and discharge current, performing an extensive post-mortem analysis on cells subjected to a one-year-long cycle test. The main degradation mechanisms in the cells cycled at 60 °C are the large formation of gas, gas-assisted lithium plating, and, additionally, temperature-accelerated growth of the solid electrolyte interphase (SEI), as revealed by XPS depth-profiling. The growth of the SEI is intensified by using higher cut-off voltages, while transition metal dissolution is observed via STEM. The manganese ions incorporate into the SEI, causing a strong blue coloration of the anodes' surface. The major effect in the cells cycled at high depth of discharge is the loss of cathode active material, as revealed by ICP-OES, XRD, and FIB-SEM measurements. The variation of the discharge current has no effect on the type of degradation mechanism occurring in the cells cycled at 20% depth of discharge.

* Corresponding author. Mercedes-Benz AG, Neue Strasse 95, 73230, Kirchheim u.T., Germany.
E-mail address: mathias.storch@daimler.com (M. Storch).

https://doi.org/10.1016/j.jpowsour.2021.230227
Received 9 February 2021; Received in revised form 8 May 2021; Accepted 27 June 2021
Available online 16 July 2021

1. Introduction

One of the most important requirements for lithium-ion batteries (LIB) in long-life application is the resistance to cyclic degradation. However, up to now, only a few long-term studies on commercial lithium-ion cells with subsequent extensive post-mortem analysis for the operation correlated degradation analysis are issued [1–3]. Typically, the characterization of the aging behavior of LIB is done, performing accelerated aging tests at intense operational conditions, which may favor certain degradation mechanism. For example, lithium plating due to excessive charge currents [4], and gassing due to high temperature [5], may not occur in the same extent when moderate, but more realistic, operational conditions are applied. To avoid harsh operational conditions and optimize battery lifetime, a more profound understanding of the correlation of the degradation mechanisms with the operational parameter is essential.

Many studies, dealing with the cycle degradation behavior of LIB, observe accelerated aging at high charge currents in combination with low temperatures, where the well-known deposition of metallic lithium is the main degradation mechanism [4,6–8]. Lithium plating might as well occur at ambient and raised temperature. When the specified charge current is too high or the battery conditions get inhomogeneous, e.g., through partial inactivation, temperature gradients, or current density gradients, etc. [9–13], the local deposition of metallic lithium is promoted. Often the observation of lithium plating and its correlated loss of active lithium superposes the further known degradation mechanism [14–16] like the growth of the solid electrolyte interphase (SEI) [17,18], the dissolution of transition metals from the positive electrode [19–22], the degradation of anode [23] and cathode active materials [24–27] and the formation of gases [28–31]. However, with today's knowledge it is feasible to prevent the cells from lithium plating during aging test, by control of the charge current below a critical limit [6,32] and homogeneous operational conditions [12,13,33].

Therefore, when analyzing the correlation of operational conditions and degradation modes, it is required that all possible influences beside the one investigated parameter have to be kept minimal and constant, e.g., pressure, thermal conditions, rest periods, charge current, discharge current, state of charge (SOC), and depth of discharge (DOD).

The unique feature of this study is the careful selection of the experimental conditions and cycling parameters in order to separate the influence of single operational conditions and provoke degradation by only one operational parameter. Therefore, for each cell in the test only one parameter was changed at a time compared to the center point of the test. All other operational and boundary conditions (e.g., pressure, thermal conditions, rest periods, charge current, discharge current, SOC, and DOD) were kept constant. Thus, operational parameters and the corresponding main degradation mechanism in large-format automotive lithium-ion cells could be investigated separately. The characteristic aging data, namely capacity retention, cell resistance course during the aging test and differential voltage (DV) analysis are presented. This data is complemented by an extensive post-mortem analysis comprising cell volume measurement, visual inspection, scanning electron microscopy (SEM), inductively coupled plasma optical emission spectroscopy (ICP-OES), x-ray photoelectron spectroscopy (XPS) depth-profiling, x-ray diffraction (XRD), scanning transmission electron spectroscopy (STEM), and three-electrode test cell measurements.

2. Experimental

In this study, large-format, pouch-bag, lithium-ion cells with a measured capacity of 39 Ah (discharge current = 3.7 A) were subjected to long-term cycling aging tests. The cells used were composed of graphite negative electrodes (anodes), $LiNi_{0.6}Mn_{0.2}Co_{0.2}O_2$:$LiNi_{1/3}Mn_{1/3}Co_{1/3}O_2$ (NMC622:NMC111) in ratio of 0.9:0.1 positive electrodes (cathodes) and an Al_2O_3-coated PE-membrane soaked the 1 M $LiPF_6$ solution in ethylene carbonate (EC), ethyl methyl carbonate (EMC), and diethyl carbonate (DEC) mixture as the electrolyte. The cell formation process was already performed by the supplier. The received cells are referred to as beginning of life (BOL) state. Each cell comprises 33 double-side coated anodes and 32 double-side coated cathodes z-folded into the separator. Dimensions of the anodes are 174·140 mm^2 and for the cathodes 172·136 mm^2 with an electrode thickness of ~160 µm and ~138 µm (current collector thickness Cu ~10 µm, Al ~13 µm), respectively. The above-mentioned electrode thicknesses, measured with a micrometer-screw, refer to complete double-side coated electrodes including the current collector foil.

For minimization of the pressure effect, a custom-made clamping system was developed comprising six cylindric screws M6x110 (Würth GmbH, Germany), springs 0D12370 (Febrotec GmbH, Germany), and two 30 mm thick anodized aluminum plates (~120 N/spring, ~29 kPa on the cell). The cycle experiment was performed using a fully automatic cycler with a maximum of ± 50 A and ± 200 A (Digatron Power Electronics GmbH, Germany) depending on the maximum required current. Temperature control was provided by using climatic chambers (MK240 and MK720, BINDER GmbH, Germany).

For reproducibility check, two cells were used at each point of the test matrix. The aging test comprises regularly performed check-up tests at 30 °C for each cell, monitoring the cell capacity, cell resistance and discharge data set for DV analysis. The check-up test is composed of a first resting period to provide a uniform cell temperature of 30 °C, followed by three cycles at 18.5 A, and then one cycle with a current of 3.7 A is performed for low current capacity and to provide a data set for DV analysis. Finally, a 50 A discharge pulse is applied at 100% SOC to determine cell resistance in analogy to Schweiger et al. [34].

The parameter sets for each test point are listed in Table 1. The operational parameters of interest are the temperature, the upper cut-off voltage (V_C), the DOD and the discharge current. The designation of the samples follows the rule prefix according to the varied parameter and value. An exception is the cell cycled up to 3.7 V at 30 °C with a DOD of 20% and a discharge current of 37 A, which is kind of a reference point to all other matrix points. As the degradation in real-life usage is expected to be low, operating parameters were selected to be representative of the target application. In order to investigate a DOD of 80%, V_C had to be raised to 3.95 V. As comparable boundary condition, the averaged charge throughput per time is kept constant for all tests, realized by adjusting the rest periods. The maximum charge current without causing lithium plating was determined by a method of Sieg et al. [32] and is set to 18.5 A for all cells. Owing to technical issues of the setup, all cycling experiments had an interruption of ~60 days after the cycling phase one and before check-up two, however no effect on the degradation behavior of the cells results.

The cell volume of each cell was measured prior and after the aging test by a method adapted from Aiken et al. [35], but optimized to the larger battery dimensions. The setup consists of a water basin filled with deionized water (conductivity < 10 µS), a force gauge "Sauter FH10" (Sauter, Germany) and a lab balance "Series 321 LX" (Precisa Gravimetrics AG, Switzerland). After measuring the weight of the cells, they were hung on the force gauge and completely covered with water (no air

Table 1
Parameter sets and naming convention of the investigated samples.

V_C (V)	DOD (%)	Temperature (°C)	I_{DCH} (A)	Designation rule
3.7	20	30	37	TVDC
3.7	20	15	37	T15
3.7	20	45	37	T45
3.7	20	60	37	T60
3.55	20	30	37	V3.55
3.85	20	30	37	V3.85
4.2	20	30	37	V4.2
3.95	80	30	37	DOD80
3.7	20	30	111	C3
3.7	20	30	185	C5

bubbles attached to the cell case). According to Archimedes principle, the cell volume was calculated, and the volume change was determined. Additionally, the changes in thickness of the cells, after extraction from the clamping system, were measured using a thickness gauge.

Prior to the cell opening, all cells where equally discharged to 3 V in CC-CV mode with a current of 5 A and 0.74 A cut-off current, this step was repeated three times with 24 h rest in between. Post-mortem analysis was performed in an argon-filled glovebox "MB200MOD" (MBraun Inertgas-Systeme GmbH, Germany) with residual $O_2 < 0.1$ ppm and $H_2O < 0.1$ ppm. After cutting the cells open, the electrodes were washed in dimethyl carbonate (Merck KGaA, Germany) bath for 10 min, subsequently dried, photographed, and stored for further analysis. More detailed information on cell opening procedure is presented elsewhere [36].

SEM micrographs were recorded using an "EVO 25" (Carl Zeiss AG, Germany) in secondary electron mode, an acceleration voltage of 3 kV, magnification of 5000x and a working distance of approximately 6 mm. ICP-OES was performed by dissolving 10.18 cm^2 of double-side coated electrode in aqua regia. The analysis of the SEI was performed using XPS depth-profiling with the identical equipment as presented elsewhere [36] (monochromatic Al-Kα, 45° sample to analyzer, $E_{pass,survey} = 93.9$ eV, $E_{pass,detail} = 29.35$ eV). For detailed spectra, 0, 3, 10, 30, 60, 100, and 200 min of sputter time were chosen. SEI thickness is estimated by referencing to a calibrated etching rate on SiO_2 of 1 nm min^{-1}, even though we are aware that it can be higher for porous organic SEI.

XRD patterns were recorded by means of a Bruker D8 diffractometer equipped with a Cu-Kα source ($\lambda = 0.15406$ nm) in the $10° < 2\theta < 90°$ range with a step size of 0.02° and a 5 s/point acquisition time. Sequential Rietveld refinement was performed using GSAS software [37] in the $16° < 2\theta < 90°$ range, considering a biphasic system consisting of NMC622 and NMC111 phases. Phase fractions were refined only for BOL sample and kept constant while sequentially refining the dataset (NMC622/NMC111 = 85/15). A trigonal structure (s.g.: $R\bar{3}m$, 166) was assumed for both phases as model, and manually edited to consider the different atomic ratios in each phase. Atomic parameters were refined only for the NMC622 phase by considering a fixed elemental composition ratio, i.e., Ni:Mn:Co = 6:2:2. Two different Wyckoff sites were considered for the Ni species, i.e., the *3a* and *3b* sites, corresponding to the typical intraplanar layer and the octahedral lithium sites, respectively, to account for the transition metal migration to the Li site. The total fraction of Ni species (*3a*+*3b*) was constrained to 0.6. In case of the NMC622 phase, an additional site for the Ni species was added to account for the transition metal migration to the Li site. The background was fitted with a Chebyshev polynomial function consisting of nine coefficients. Instrumental parameters were retrieved by means of a LaB_6 standard, hence, instrumental broadening parameters, i.e., U, V, W, X, and Y, were kept fixed to 11.143 $cdeg^2$, -14.31 $cdeg^2$, 5.542 $cdeg^2$, 2.023 cdeg, and 4.052 cdeg, respectively. Peak shape was refined only by optimizing the microstrain broadening parameter (calculated as unitless fraction of $\Delta d/d \cdot 10^6$, d being the interplanar distance) and by fixing the Lorentzian-Gaussian mixing to 0.5 for all samples. Scale, background, sample displacement, unit cell parameters, peak shape, and atomic parameters were refined in this order.

STEM imaging was performed on an "ARM 200" (JEOL Ltd., Japan) equipped with a "Quantum EELS- Gatan" (Nanolab Technologies Inc., USA) for electron energy loss spectroscopy (EELS). Sample handling and preparation was constantly performed in argon. Prior to the liftout, a carbon protective layer was deposited on the particle of interest. A "XB550" (Carl Zeiss AG, Germany) focused ion beam scanning electron microscope (FIB-SEM) applying gallium ions was used for FIB-liftout.

Three-electrode tests were performed using the "PAT-Cell" set-up (El-Cell GmbH, Germany) and corresponding single use consumables. Two types of PAT-Cells were assembled, half-cells (cathode vs. metallic lithium) and full-cells (anode vs. cathode vs. metallic lithium ring). The coating on one side of the electrodes extracted from the cells was removed using a sponge and 2-propanol. After drying, electrode disks with 18 mm in diameter were punched out and used to assemble full-cells and half-cells versus metallic lithium foil (thickness 0.38 mm, Merck KGaA, Germany). A formation procedure was performed (2x ±0.7 mA, 2x ±1.4 mA, 2x ±3.5 mA, 1x ±0.7 mA). The evaluation of the full-cells was done in the same voltage window as the original cell: the cells were discharged from 4.2 V to 2.5 V with a current of approximately C/24 compared to BOL capacity. The evaluation of cathode capacity was done in the potential range from 3.3 V to 4.3 V vs. Li/Li^+ with the same current as for the full-cells. For evaluation of the lithium content in a delithiated cathode electrode, similar cells were assembled, i.e., 8 cells for BOL, T15, T60, V3.55, V4.2, and DOD80. These cells were delithiated to a potential of 4.2 V vs. Li/Li^+ using three steps of CC-CV charging with 0.7 mA and 0.07 mA cut-off each, with resting periods of 15 min for relaxation. The cells were disassembled; the cathodes were washed in dimethyl carbonate, dried, and packed for ICP-OES analysis.

3. Results and discussion

3.1. Capacity, resistance, and differential voltage analysis

The capacity retention, the resistance versus equivalent full cycle (EFC), and the differential voltage versus charge are shown in Fig. 1. A summary of the electric and post-mortem characteristics is given in Table 2. In general, the data of each two cells per test point are well reproducible and only a few spikes occur. The capacity of all the cycled cells decreases and the resistance increases with increasing test time. The observed end-of-test capacity retention ranges between 85.7% and 98.4% while the resistance ranges from 108% to 439%. The lowest capacity degradation is analyzed for V3.55 while the highest capacity degradation is found for T60 followed by DOD80. The lowest and strongest resistance changes are measured for C3 and T60, respectively.

The end-of-test capacity retention in dependence of the cycle temperature (Fig. 1a) decreases with increasing temperature from 94.7% (15 °C) to 93.7% (30 °C) to 91.4% (45 °C) reaching only 85.7% by cycling at 60 °C. At the same time, the end-of-test pulse-resistance heavily increases for the cells cycled at 60 °C to more than 400%, and to ~157% for the cells cycled at 45 °C, while moderate resistance increases by ~18% and ~14% for the cells cycled at 30 °C and 15 °C, respectively. The resistance course (Fig. 1b) shows a sudden increase around cycle number 650 and 1200 for the cells cycled at 60 °C and 45 °C, respectively, resulting in a kink in the resistance trend. The reason for this finding is most likely the formation of gases inside the cells, since the cell volume also increased versus BOL state as listed in Table 2. This feature indicates a temperature-dependent formation of gas. When a critical amount of gas is formed, it cannot be pushed out of the electrode stack into the gas pockets at the edge area of the cell. The remaining gas bubbles inside the electrode stack inactivate ion paths, resulting in lithium plating in the following cycles. The lithium plating, together with the lowered active area, causes a strong increase in resistance [11,36]. However, these bubbles weakly affect the measured capacity, since the resistance effect on the capacity measurement at C/10 is low. The source of the formed gas can be the formation and growth of the SEI and, in parallel, the decomposition of the conducting salt $LiPF_6$. When catalyzed by traces of impurities, i.e., HF and H_2O, the decomposition can occur at temperatures <60 °C [38,39]. Additionally, according to equation (1) [40], dissolved $LiPF_6$ is in equilibrium with LiF and PF_5. Campion et al. [41] presented the reactions of PF_5 with different solvents and formation of CO_2. Thus, the equilibrium in equation (1) is shifted to the right [40,42].

$$LiPF_6(sol) \rightleftharpoons LiF(s) + PF_5(sol) \quad (1)$$

The generated gas bubbles also influence the differential voltage shown in Fig. 1c. The graph of T60 confirms inhomogeneity, by graphite peak broadening [43], and lithium loss by the shortened distance from the graphite peak to the end of discharge on the right. The slight

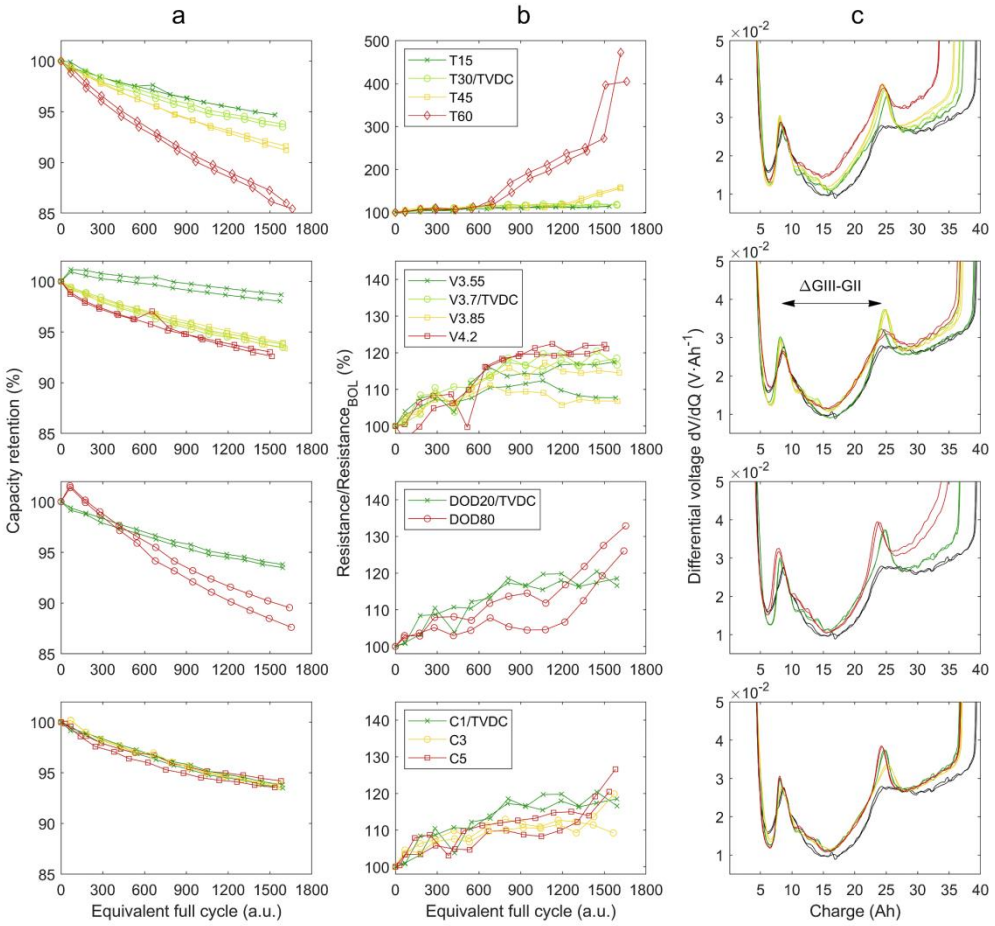

Fig. 1. a) C/10 discharge capacity retention versus equivalent full cycle, b) 50 A discharge pulse resistance at 100% SOC versus equivalent full cycle and c) differential voltage graphs versus charge of the beginning of life cells (black) and the aged cells. From top to bottom the temperature, the cut-off voltage, the depth of discharge, and the discharge current series are shown.

Table 2
End-of-test electric data and summarized results of post-mortem analysis.

sample	capacity ($\%_{BOL}$)	resistance ($\%_{BOL}$)	Δcell volume (%)	Δcell thickness (%)	SEI estimation (nm)	Mn_{anode} (mg/cm^2)	$capacity_{cathode}$ ($\%_{BOL}$)	ΔGIII-GII (Ah)	$Li_{cathode,delithiated}$ ($\%_{BOL}$)
BOL	100	100	0	0	7	0.003	100	16.91	100
T15	94.7	114	0.7	2.3	14	0.018	99.1	17.03	98.02
TVDC	93.7	118	1.5	3.3	24	0.017	93.4	16.72	–
T45	91.4	157	2.7	4.5	22	0.016	92.7	16.42	–
T60	85.7	439	12.8	8.2	51	0.011	86.8	16.30	110.93
V3.55	98.4	113	1.5	3.7	20	0.012	98.8	16.15	99.53
V3.85	93.7	111	1.2	2.7	24	0.024	95.5	16.82	–
V4.2	92.8	121	2.8	3.1	45	0.027	94.1	16.64	100.69
DOD80	87.6	129	2.2	4.3	6	0.015	78.8	15.95	113.84
C3	93.8	108	1.7	4.0	–	–	–	16.90	–
C5	93.9	111	1.9	4.1	–	–	–	16.28	–

- not measured

decrease in graphite peak distance (ΔGIII-GII), with increasing cycling temperature, represents a slight loss of anode active material (<2%). The parallel upwards shift of the DV curves indicates a shift of anode vs. cathode [44] while the increasing slope of the DV curves at higher SOC, indicates a decrease of cathode capacity [13].

For the cut-off voltage variation, the end-of-test C/10-capacity decreases to 98.4% for V3.55, to 93.7% for V3.85, and 92.8% for the cells cycled up to 4.2 V. For the cells cycled up to 3.55 V, the so-called overhang effect is clearly present [45–47]. The cell capacities increase between the first and second check-up tests by approximately 1%. Prior to the test, all cells were preconditioned at 100% SOC, resulting in reversible capacity increase when cycled at lower SOC. However, the overhang is expected to be reversible and does not affect the cell degradation mechanisms. The cell resistance compared to BOL for V3.55 and V3.85 differ slightly (113% and 111%, respectively). In contrast, the cells cycled up to 4.2 V exhibit a higher resistance increase (121%). The DV graph of sample V3.55 is remarkably similar to the BOL DV. Solely, the graphite peaks are more pronounced, which is known as homogenization effect of the lithium distribution between overhang and active area. This effect is more pronounced at low mean SOC during the cycling phase [47,48]. The DV graphs of the samples TVDC and V3.85 show the same lithium homogenization effect. Additionally, the slope of the DV curves increases similar to that of T60, indicating for cathode degradation. Even more, the slope increases for V4.2. The high SOC during the cycling phase and the associated cycling on an anode potential plateau inhibits the equalization of the overhang and the outer active areas, hence the graphite peak is broadened and inhomogeneous lithium distribution is promoted [44].

The high DOD (80%, cut-off voltage increased to 3.95 V) leads to stronger degradation of the cells compared to a DOD of 20%, resulting in an end of test capacity retention of 86.6% compared to 93.7%, which is comparable to the behavior reported in literature [49–51]. The effect is much higher than for an increased cut-off voltage and is thus assumed to be based on the depth of discharge. Again, the overhang effect [45–47] is present between the first and second check-up test. During the above-mentioned test interruption, the DOD80 cells were kept at 0% SOC which emptied the anode overhang mostly. The interruption had less effect on the rest of the cycled cells, since their SOC during rest remained close to the mean SOC of the measurement. The resistance of DOD80 exhibits an increase to 129% versus 118% for the cells cycled at 20% DOD. The corresponding DV graphs indicate a stronger loss of active cathode material in combination with a shift of anode potential versus cathode potential. A slightly more pronounced loss of anode active material is indicated by the decrease in the graphite peak distance (ΔGIII-GII).

The results for discharge currents 37 A, 111 A and 185 A show that the capacity retention and resistance increase are weakly affected by the discharge current variation. The capacity retention ranges from 93.7% to 93.9% and the end of test resistance ranges from 108% to 118%. Additionally, the differential voltages of the cells cycled with varying discharge current are similar with a slight broadening and less shift of the graphite peak GII of sample C3. However, these deviations are rather small and none of the further measurement data of the six cells cycled with varying discharge current show significant differences. The degradation of the used cell is assumed to be independent from the discharge current [52] with the applied complementing operational parameters. Especially, the low DOD compared to literature and the corresponding lower heating and occurrence of temperature gradients are critical factors [51,53]. Therefore, further results of the cells C3 and C5 are attached in the supplementary part S2.

To summarize, the electrical measurements show an intensified aging of the cells cycled at higher temperatures, upper cut-off voltages, and higher depth of discharge, while the influence of the discharge current seems insignificant.

3.2. Post-mortem analysis – anode degradation

To identify the degradation mechanisms leading to the observed capacity and resistance course, an extensive post-mortem study followed. The photographs of the negative electrodes, subsequent to cell opening, are depicted in Fig. 2. Compared to the BOL anode, most of the cycled anodes show a yellow-brownish coloring with an irregular wave-like pattern, comparable to those reported in literature [1]. In sample T60, anomalous light grey dots are found in the magnified optical image (Fig. 2b). These dots are not observed in the cell center and intensify towards the cell edge. The corresponding SEM micrograph (Fig. 2c) indicates that these light-grey dots are surfaces deposits. Analysis of the cell volume prior to post-mortem analysis shows an increase in cell volume with cycling temperature (see Table 2). A total cell volume increase of 12.8% for T60 results from substantial electrolyte decomposition (SEI growth + $LiPF_6$ decomposition) under the formation of gases like H_2, CO, CO_2, CH_4, and C_2H_4 [30,54]. Together with the large lithium loss observed in the DV and the similarity to lithium plating deposits reported in the literature [11,36,55], the superficial degradation mechanism of T60 can be identified as electrolyte dry-out in combination with gas-assisted lithium plating. Cycle aging at lower temperatures (45 °C, 30 °C and 15 °C) does not evoke such a high amount of gases, and, thus, no such lithium plating occurs. However, these cells still degrade caused by SEI growth, i.e., the second main degradation mechanism [3,55]. The SEM micrographs of the anodes shown in Fig. 3 indicate no visible surface changes of T15 compared to the BOL electrode. For TVDC, T45 and T60 the thin surface-covering layer appears thicker.

Regarding the cells from the cut-off voltage series, Fig. 2 reveals no significant optical differences between the samples V3.55, TVDC and V3.85. Sample V4.2 instead appears in a shining blue color, the first guess of not completely delithiated graphite [9,56,57] is proven to be wrong. During washing in DMC (wetting the electrode with solvent) the graphite grey color of the BOL cell appears in the same grey as the BOL anode. Thus, the blue coloring is assumed to be a surface layer effect as discussed at the end of this section. The SEM images of the cut-off voltage series show a slight increase of the amount of the surface layer with increase in cut-off voltage, especially for V4.2. The anode of the cell cycled at 80% DOD, instead, seems unaltered compared to that of the cell cycled at 20% DOD.

Thus, a detailed analysis using XPS depth-profiling was performed (Fig. 4, Table 2) in analogy to Ref. [36]. The depth profiles of the four most important elements, carbon (as active material and SEI constituent) as well as lithium, oxygen, and fluorine, i.e., the main constituents of the SEI, are depicted in Fig. 4. The first measuring point on the top most surface, i.e., without any sputtering, shows a high amount of carbon (~50–70 at%), which steeply decrease up to 10 min sputter time, displaying the transition from the mainly organic outer SEI to the inorganic inner SEI [58,59]. Additionally, the low Li/C ratio (Fig. 5a) in the beginning of the depth profile identifies the organic SEI part while, the more inorganic SEI is well represented by a Li/C ratio > 1. The corresponding detailed XPS spectra of the C1s, O1s and F1s binding energy regions are shown in Fig. S3 (Supplementary information). Higher sputter times evidence an increase of carbon, but a decrease of the other three elements, indicating the transition from the SEI to the anode active material. In analogy to Ref. [36] and Yoshida et al. [60], the increase above 50 at% of carbon is chosen as an estimation for the SEI thickness. An increase in the estimated SEI thickness from ~14 nm for T15, to ~24 nm for sample TVDC, ~22 nm for T45 and ~51 nm for T60 is found. Furthermore, the XPS depth-profiles of the cut-off voltage series reveal an increased SEI thickness of V4.2 (~45 nm), i.e., thicker than SEIs of V3.85 (~24 nm), TVDC (~23.5 nm) and V3.55 (~20 nm).

In contrast to the growth of the SEI in the cells cycled at high temperature and with high V_C, the optical and the SEM images of the anode gathered from the cell cycled with high DOD exhibits no characteristic visible degradation patterns (cf. Figs. 2 and 3). This first impression is

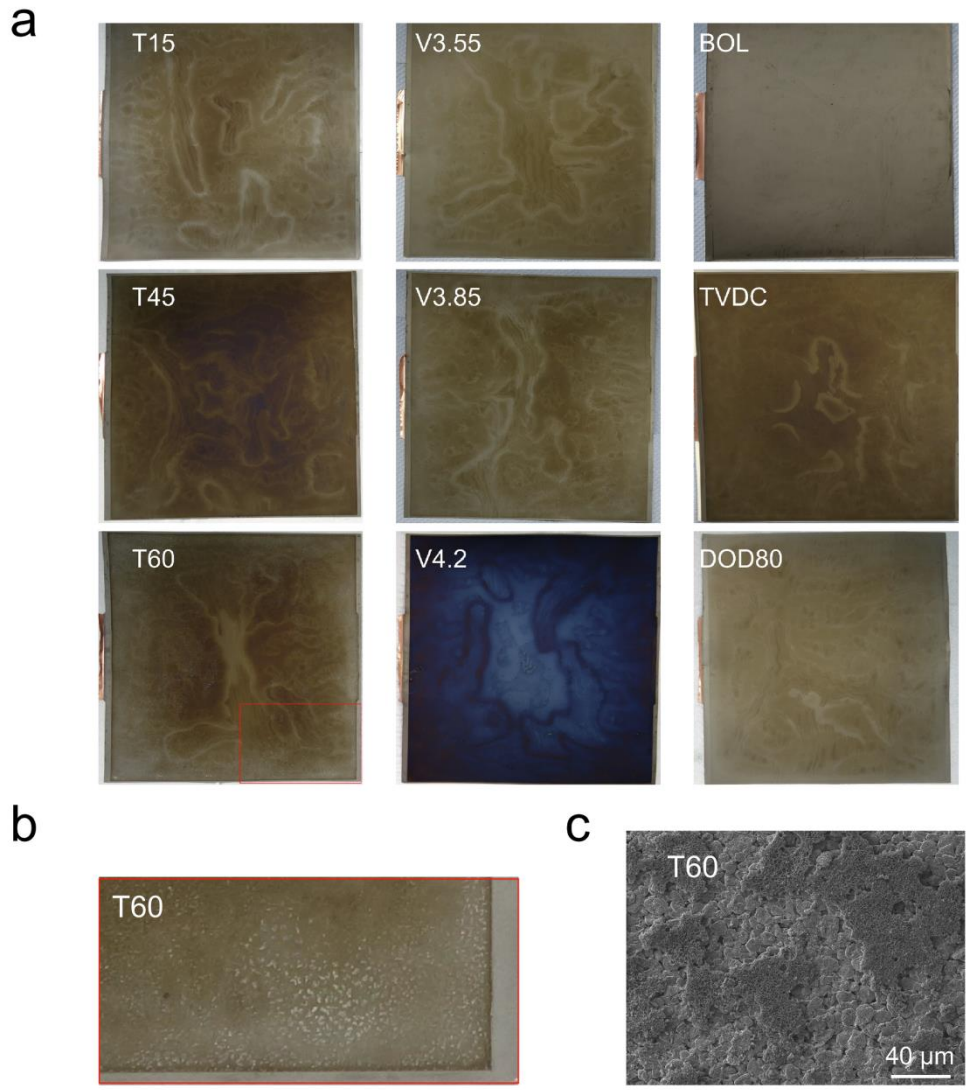

Fig. 2. a) Photographs of the gathered anode electrodes from the center of one cell per test point including a beginning of life anode, b) magnified photograph of the T60 anode showing the light grey dots in detail and c) SEM micrograph of surface deposits with magnification of 500x. The optical inspection shows a coloring of the aged electrodes towards yellow-brown, light grey dots for the cell cycled at 60 °C, and a strong blue coloring of the electrode gathered from the cell cycled up to 4.2 V. (For interpretation of the references to color in this figure legend, the reader is referred to the Web version of this article.)

validated by the XPS depth-profiling estimating SEI thickness of ~6 nm, which is less than from the cell aged with 20% DOD and in the range of a BOL anode. This small growth of the SEI contradicts our expectations as the graphite volume expansion and contraction during the high DOD cycling should intensify the SEI growth via the cracking and repair mechanism as presented in the literature [18,61,62]. However, the overall cell degradation with 13.4% capacity loss and 29% resistance increase is large.

A still open question is the origin of the blue coloring of the anode in V4.2. The SEI thickness is not considered to be the reason for the coloring since sample T60 has a comparable thickness of the surface layer (~50 nm compared to ~45 nm for sample V4.2) without blue coloring. A closer inspection of the manganese depth profiles (Fig. 6a) instead points towards an additional degradation mechanism, the so-called transition metal dissolution [19,21,22,63]. The manganese dissolves from the cathode and diffuses to the anode where it incorporates into the SEI layer and catalyzes further electrolyte decomposition reactions [20, 22]. The manganese atomic concentration increases with increased V_C

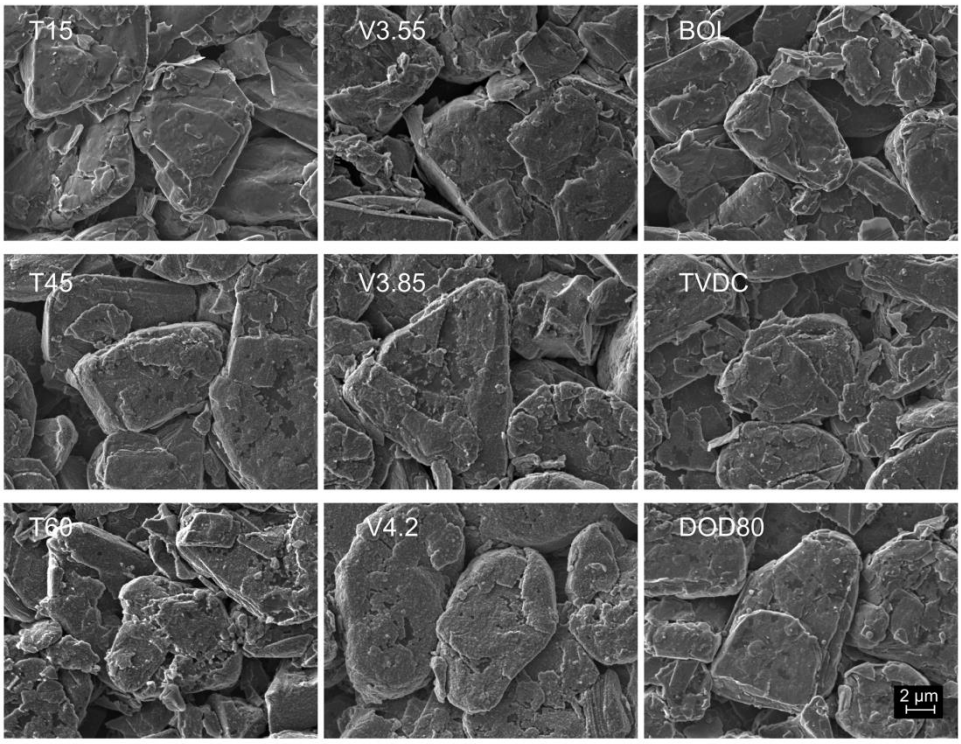

Fig. 3. Representative SEM micrographs of the anodes gathered from the cells cycled at different conditions and the begin of life cell. Compared to begin of life the T15 and DOD80 appear similar, the rest of the electrodes exhibit a surface cover layer in varying strength. However, no quantitative information can be gathered from these SEM micrographs.

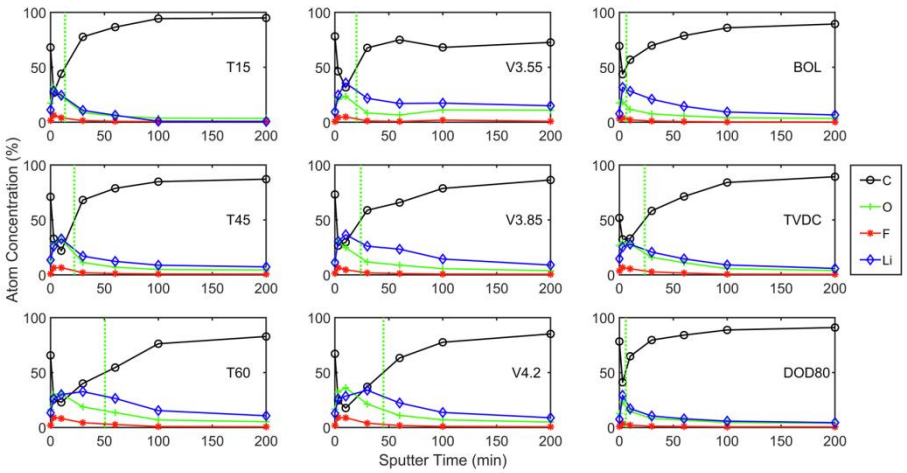

Fig. 4. XPS depth-profiles of carbon (C), oxygen (O), lithium (Li), and fluor (F), versus sputter time. The estimated thickness of the SEI is located at the carbon atomic concentration of 50%.

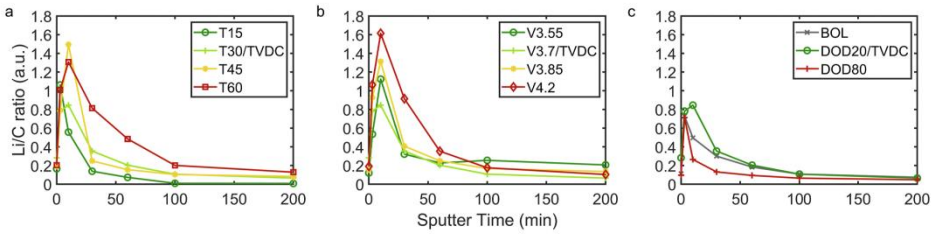

Fig. 5. Lithium to carbon ratio of a) the temperature, b) the cut-off voltage, and c) the DOD series. As the low Li/C ratio in the beginning shows the organic SEI part, a more inorganic SEI follows which is represented by the ratio of >1. For the temperature and the cut-off voltage series, higher cycle conditions result in higher and broader Li/C ratio.

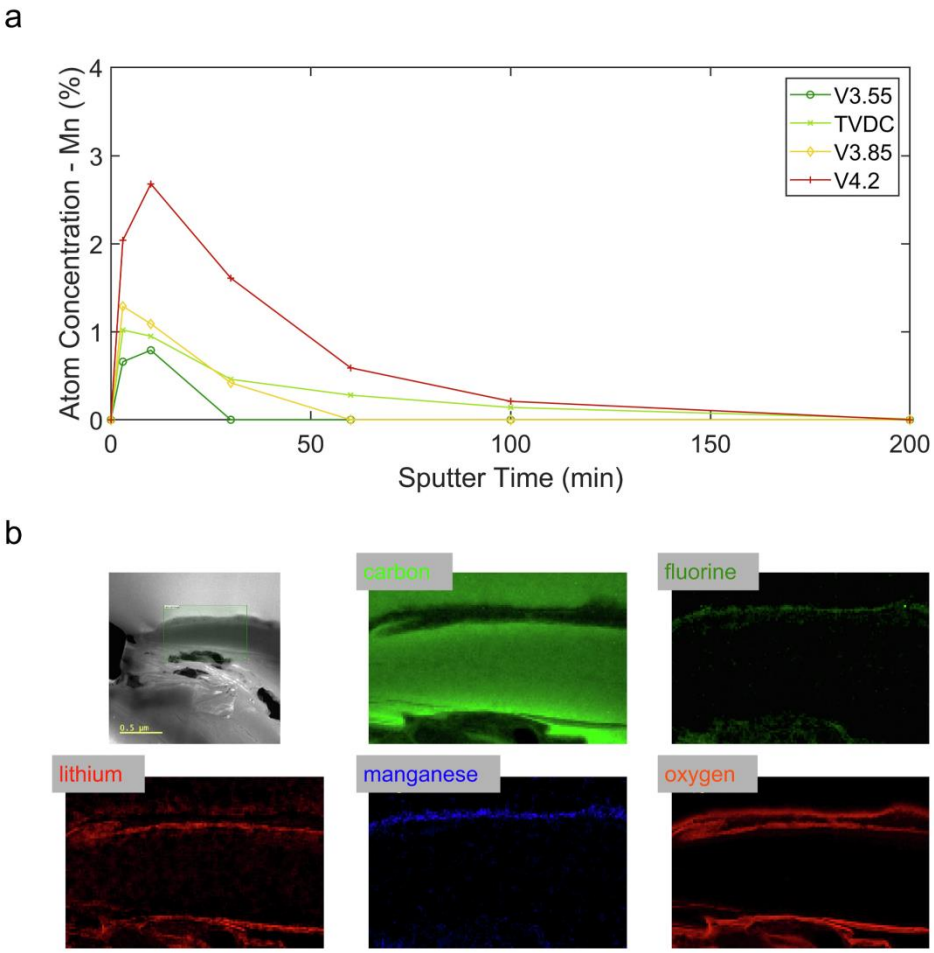

Fig. 6. a) Manganese XPS depth-profile of the cut-off voltage series and b) STEM/EELS micrographs showing elemental mapping of a top graphite particle in cross section. The images show, from top to bottom, the measurement artifact of a carbon cover layer for surface protection followed by the SEI represented by mainly F, Li, Mn, and O atoms. Then the graphite particle follows and again SEI in the porous system of the electrode.

from ~0.8% in V3.55 to ~2.8% in V4.2. The location of the deposited manganese is shown in the STEM/EELS images in Fig. 6b where a thin layer of accumulated manganese on the surface of the carbon particles is found. Besides the higher manganese content also the SEI representing elements fluorine and oxygen are found in the same position. The upper carbon-rich region is a protective layer deposited to protect the sample from destruction during preparation. Hence, the blue color on the anode of sample V4.2 is considered to originate from the Mn-ion containing SEI.

The post-mortem analysis of the cells' anodes reveals different aging mechanisms depending on the aging conditions. An increase in cycling temperature leads to intensified SEI growth accompanied with an intensified gas evolution, gas evolution from $LiPF_6$ decomposition and side effects as gas-assisted lithium plating. On the other hand, the increase in cut-off voltage leads to intensified SEI growth and manganese dissolution from the cathode, resulting in the Mn-ion incorporation into the top-most SEI. However, comparing this study with literature [2,16,52,56,64], it is important to mention that besides the gas-assisted lithium plating no further lithium plating is observed. Therefore, the choice of the charge current rates for electrochemical testing of lithium-ion batteries is crucial when degradation mechanisms different from lithium plating should be analyzed.

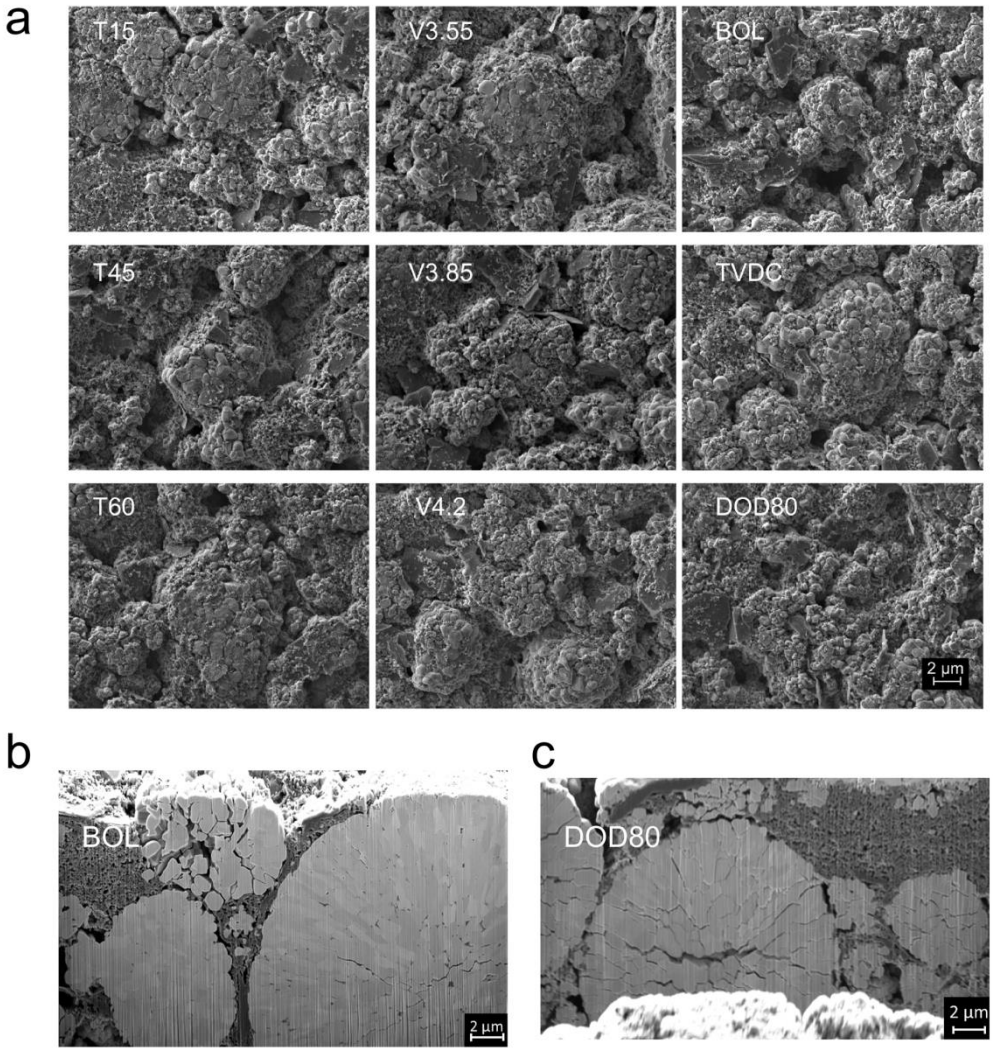

Fig. 7. a) Representative SEM micrographs of the cathode gathered from the cells cycled at different conditions and the beginning of life cell. b) FIB-SEM micrograph of the BOL cathode sample and c) FIB-SEM micrograph of the DOD80 cathode. Compared to beginning of life the DOD80 appears crushed without large secondary particles stemming from inter-granular cracking.

3.3. Post-mortem analysis – cathode degradation

The DV analysis predicts cathode loss as the main degradation mechanism. Therefore, several physical/chemical analyses were carried out to evaluate the loss of cathode active material and the respective mechanism. Optical images of the cathode are inconspicuous and thus are presented in Fig. S1 (Supplementary Information). The electrochemical analysis in half cell configuration with metallic lithium as the reference electrode confirms the loss in cathode capacity as listed in Table 2, which is, e.g., ~22% versus the BOL cathode capacity for DOD80. In general, the SEM micrographs of the cathode electrodes show small primary particles (less than a micrometer in diameter) are arranged in larger secondary particles up to 10 μm in diameter. However, in the positive electrode of DOD80, mainly small particles are observed while the large secondary particles seem to be teared apart. This finding indicates the occurrence of mechanical degradation of the DOD80 cathode, known as inter-granular cracking [21,24,25,27,49], resulting in the loss of electric contact and, therefore, in the partial insulation of the cathode active material. As a result, the insulated particles do not further contribute to the cell electrochemical cycling, and the incorporated lithium is lost, too. This is validated by measuring the lithium content in the partially delithiated cathode, i.e., held at 4.2 V versus lithium (see Table 2). The remaining lithium increases in the heavily degraded cathodes in the delithiated state. The FIB-SEM micrograph of the DOD80 cathode (Fig. 7c) again reveals inter-granular cracks present in the secondary cathode particles. These cracks appear intensified in the DOD80 cathode compared to the BOL cathode shown in Fig. 7b.

Further analysis of the degradation of the NMC electrodes is performed with X-ray diffraction and Rietveld refinement of the present crystalline phases (see Table 3). As example, the Rietveld refinement for the BOL sample is shown in Fig. S4b (Supplementary Information). Distinctive differences are seen between the lattice parameters of the BOL cathode and those of all aged cathodes. The higher signal to noise (S/N) ratio of the NMC622 phase enhances the reliability of the related parameters compared to the NMC111 phase and,thus, allows for the refinement of the atomic positions.

An increase of the cycling temperature results in a larger lattice parameter *a* and a smaller lattice parameter *c*. This corresponds to a higher occupation of the Ni^{3b} (Li-interslab layer) sites versus the Ni^{3a} (NMC-intraplanar layer) sites, which is an evidence for stronger cation mixing [65]. Moreover, the I_{003}/I_{104} intensities ratio for NMC622 decreases (cf. Supplementary Information S4a) as a result of the Ni/Li mixing. The trend of the lattice parameters of the cut-off voltage series is not very clear, however, the lattice parameter *a* decreases and *c* increases with increasing cut-off voltage. The analysis of the nickel occupation instead is clearer, higher cut-off voltages lead to less occupation of Ni^{3a} sites and more occupation of Ni^{3b} sites (see Fig. 8). The occurrence of cation mixing explains the lower cathode capacity of the cells cycled at elevated temperatures and cut-off voltages listed in Table 2.

The DOD80 sample again seems to be a special case, the lattice parameters *a* and *c* as well as the Ni^{3a} and Ni^{3b} occupation are close to the values of the BOL cathode. The crystal structure of the DOD80 cathode seems unaltered and no significant changes in the Ni sites occupation are identified. This again points towards a mechanical degradation of the DOD80 cathode, while the crystal structure remains unchanged.

The post-mortem analysis of the cells' cathodes reveals different aging mechanisms depending on the aging conditions. With an increase in cycling temperature the remaining cathode capacity decreases, which originates from mechanical degradation and cation mixing. Comparably, the findings for the cut-off voltage series suggest mechanical degradation and cation mixing as the main degradation mechanism. The cathode degradation due to an increase in depth of discharge is remarkable, here, the cathode mainly ages due to the mechanical degradation of the secondary cathode particles as shown by FIB-SEM analysis and ICP-OES.

4. Conclusion

In this study, the correlation between the operational conditions of large-format automotive lithium-ion cells and their resulting main degradation mechanisms is evaluated by performing a long-term cycle aging test, followed by an extensive post-mortem analysis. The presented results of our study are intended to provide a comprehensive set of electrochemical data with experimental prove of operation-dependent occurrence of the major degradation mechanisms. This knowledge is essential for the design of durable and sustainable lithium-ion battery systems.

The temperature series evidenced that elevated temperatures lead to an acceleration of degradation mainly due to the growth of the SEI and to strong gas formation, especially at 60 °C. The pressure on the cells was kept low and constant, and too low to displace the complete gas from the electrode stack into the gas pockets resulting in gas-assisted lithium plating. Additionally, the temperature dependence of the cation mixing is validated.

The cut-off voltage series revealed the growth of the solid electrolyte interphase in combination with transition metal dissolution for high voltage values, especially manganese ions, as the main reason for loss of cell capacity. However, the effect is less than expected and superposes with the overhang effect, which was not considered initially when the cycle aging test was planned and performed.

While the high loss of capacity of the cells cycled with large DOD of 80% was expected, the reason for this phenomenon found during post-mortem analysis is rather unexpected. Contrary to the literature, neither the growth of the SEI or the mechanical degradation of the anode nor crystal structure variations of the cathode were identified. The

Table 3
Results from the Rietveld refinement on cycled samples. The error related to each value for the last digit is inserted in brackets.

	BOL	T15	TVDC	T45	T60	V3.55	V3.85	V4.2	DOD80
R_{wp}/%	9.32	9.32	9.74	9.63	10.40	9.54	9.28	10.99	9.71
NMC 622 phase									
a/Å	2.8591(1)	2.8535(1)	2.8543(1)	2.8543(1)	2.8551(1)	2.8564(1)	2.8540(1)	2.8549(1)	2.8573(1)
c/Å	14.2724(6)	14.3135(7)	14.3027(8)	14.3029(7)	14.2987(8)	14.2932(9)	14.3069(10)	14.2998(9)	14.2856(7)
Volume/Å^3	101.038(7)	100.935(8)	100.910(9)	100.918(8)	100.941(9)	100.995(10)	100.921(11)	100.938(10)	101.007(8)
μstrain	1702(45)	1823(52)	1785(60)	1799(54)	1989(65)	1701(69)	2107(74)	1626(68)	1826(52)
Ni^{3a}	0.566(2)	0.566(3)	0.562(3)	0.557(3)	0.547(3)	0.560(3)	0.550(3)	0.548(3)	0.565(3)
Ni^{3b} (Li)	0.034(2)	0.034(3)	0.038(3)	0.043(3)	0.053(3)	0.040(3)	0.050(3)	0.052(3)	0.035(3)
z(O)	0.2559(3)	0.2547(3)	0.25308(4)	0.2538(4)	0.2528(4)	0.2516(5)	0.2511(4)	0.2522(5)	0.2549(3)
NMC 111 phase									
a/Å	2.8535(3)	2.8498(4)	2.8499(4)	2.8500(4)	2.8502(4)	2.8507(5)	2.8499(4)	2.8503(5)	2.8511(4)
c/Å	14.259(2)	14.288(2)	14.283(2)	14.285(2)	14.287(2)	14.283(3)	14.287(3)	14.282(3)	14.278(2)
Volume/Å^3	100.55(1)	100.49(2)	100.47(2)	100.49(2)	100.51(2)	100.52(2)	100.49(2)	100.48(2)	100.51(2)

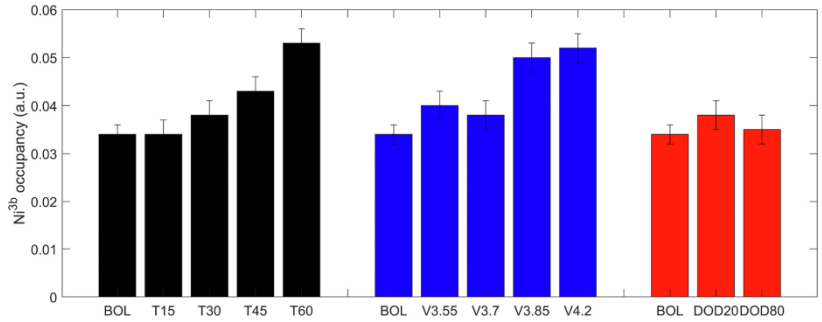

Fig. 8. Ni^{3b} occupancy of the temperature, the cut-off voltage, and the DOD series. An increase of the Ni^{3b} occupancy with temperature and cut-off voltage is present, while for the increased DOD no Ni^{3b} occupancy changes evolve.

reason for the loss of capacity found in our study was the heavy mechanical degradation of the cathode active material, leading to partial electric insulation of the particles.

Furthermore, this cycle aging study revealed no negative effect of an increased discharge current at the given cycle conditions for this cell in combination with relatively mild operational parameters, e.g., low DOD and low charge current at a medium state of charge.

CRediT authorship contribution statement

Mathias Storch: Conceptualization, Methodology, Investigation, Resources, Writing – original draft, Writing – review & editing, Visualization. **Johannes Philipp Fath:** Conceptualization, Methodology, Investigation, Writing – review & editing. **Johannes Sieg:** Conceptualization, Methodology, Investigation, Writing – review & editing. **Dragoljub Vrankovic:** Conceptualization, Methodology, Writing – review & editing. **Angelo Mullaliu:** Conceptualization, Methodology, Writing – original draft, Writing – review & editing. **Carsten Krupp:** Conceptualization, Methodology, Writing – review & editing. **Bernd Spier:** Conceptualization, Writing – review & editing, Supervision. **Stefano Passerini:** Conceptualization, Writing – review & editing, Supervision. **Ralf Riedel:** Conceptualization, Writing – review & editing, Supervision.

Declaration of competing interest

The authors declare that they have no known competing financial interests or personal relationships that could have appeared to influence the work reported in this paper.

Acknowledgment

The authors acknowledge the financial support of Mercedes-Benz AG, (Stuttgart, Germany) and Deutsche Accumotive GmbH & Co. KG (Kamenz, Germany). We would like to express our gratitude to the BatterieIngenieure GmbH, (Aachen, Germany) for conducting the cycle aging experiment. The NMI Naturwissenschaftliches und Medizinisches Institut an der Universität Tübingen (Reutlingen, Germany) is thanked for performing SEM-FIB and (S)TEM measurements with special sample handling in argon atmosphere. The SGS Fresenius Institut (Dresden, Germany) is thanked for performing ICP-OES and the Ulm university (Ulm, Germany) for performing the XPS measurements. We would also like to thank our colleagues from Mercedes-Benz AG for the support during analysis and for sharing their knowledge with us. The KIT authors acknowledge the basic funding of the Helmholtz Association.

Appendix A. Supplementary data

Supplementary data to this article can be found online at https://doi.org/10.1016/j.jpowsour.2021.230227.

References

[1] M. Ecker, P. Shafiei Sabet, D.U. Sauer, Influence of operational condition on lithium plating for commercial lithium-ion batteries – electrochemical experiments and post-mortem-analysis, Appl. Energy 206 (2017) 934–946, https://doi.org/10.1016/j.apenergy.2017.08.034.

[2] B. Stiaszny, J.C. Ziegler, E.E. Krauß, J.P. Schmidt, E. Ivers-Tiffée, Electrochemical characterization and post-mortem analysis of aged LiMn2O4–Li(Ni0.5Mn0.3Co0.2)O2/graphite lithium ion batteries. Part I, J. Power Sources 251 (2014) 439–450, https://doi.org/10.1016/j.jpowsour.2013.11.080.

[3] T. Waldmann, M. Wilka, M. Kasper, M. Fleischhammer, M. Wohlfahrt-Mehrens, Temperature dependent ageing mechanisms in Lithium-ion batteries – a Post-Mortem study, J. Power Sources 262 (2014) 129–135, https://doi.org/10.1016/j.jpowsour.2014.03.112.

[4] J.C. Burns, D.A. Stevens, J.R. Dahn, In-situ detection of lithium plating using high precision coulometry, J. Electrochem. Soc. 162 (2015) A959–A964, https://doi.org/10.1149/2.0621506jes.

[5] K.H. Lee, E.H. Song, J.Y. Lee, B.H. Jung, H.S. Lim, Mechanism of gas build-up in a Li-ion cell at elevated temperature, J. Power Sources 132 (2004) 201–205, https://doi.org/10.1016/j.jpowsour.2004.01.042.

[6] T. Waldmann, B.-I. Hogg, M. Kasper, S. Grolleau, C.G. Couceiro, K. Trad, B. P. Matadi, M. Wohlfahrt-Mehrens, Interplay of operational parameters on lithium deposition in lithium-ion cells, J. Electrochem. Soc. 163 (2016) A1232–A1238, https://doi.org/10.1149/2.0591607jes.

[7] M. Petzl, M. Kasper, M.A. Danzer, Lithium plating in a commercial lithium-ion battery – a low-temperature aging study, J. Power Sources 275 (2015) 799–807, https://doi.org/10.1016/j.jpowsour.2014.11.065.

[8] R.V. Bugga, M.C. Smart, Lithium plating behavior in lithium-ion cells, ECS Trans. 25 (2009) 241–252, https://doi.org/10.1149/1.3393860.

[9] D. Burow, K. Sergeeva, S. Calles, K. Schorb, A. Börger, C. Roth, P. Heitjans, Inhomogeneous degradation of graphite anodes in automotive lithium ion batteries under low-temperature pulse cycling conditions, J. Power Sources 307 (2016) 806–814, https://doi.org/10.1016/j.jpowsour.2016.01.033.

[10] N. Ghanbari, T. Waldmann, M. Kasper, P. Axmann, M. Wohlfahrt-Mehrens, Inhomogeneous degradation of graphite anodes in Li-ion cells: a postmortem study using glow discharge optical emission spectroscopy (GD-OES), J. Phys. Chem. C 120 (2016) 22225–22234, https://doi.org/10.1021/acs.jpcc.6b07117.

[11] B.P. Matadi, S. Geniès, A. Delaille, T. Waldmann, M. Kasper, M. Wohlfahrt-Mehrens, F. Aguesse, E. Bekaert, I. Jiménez-Gordon, L. Daniel, X. Fleury, M. Bardet, J.-F. Martin, Y. Bultel, Effects of biphenyl polymerization on lithium deposition in commercial graphite/NMC lithium-ion pouch-cells during calendar aging at high temperature, J. Electrochem. Soc. 164 (2017) A1089–A1097, https://doi.org/10.1149/2.0631706jes.

[12] V. Müller, R.-G. Scurtu, M. Memm, M.A. Danzer, M. Wohlfahrt-Mehrens, Study of the influence of mechanical pressure on the performance and aging of Lithium-ion battery cells, J. Power Sources 440 (2019), 227148, https://doi.org/10.1016/j.jpowsour.2019.227148.

[13] J. Sieg, M. Storch, J.P. Fath, A. Nuhic, J. Bandlow, B. Spier, D.U. Sauer, Local degradation and differential voltage analysis of aged lithium-ion pouch cells, J. Energy Storage 30 (2020), 101582, https://doi.org/10.1016/j.est.2020.101582.

[14] J. Vetter, P. Novák, M.R. Wagner, C. Veit, K.-C. Möller, J.O. Besenhard, M. Winter, M. Wohlfahrt-Mehrens, C. Vogler, A. Hammouche, Ageing mechanisms in lithium-ion batteries, J. Power Sources 147 (2005) 269–281, https://doi.org/10.1016/j.jpowsour.2005.01.006.

[15] C. Schlasza, P. Ostertag, D. Chrenko, R. Kriesten, D. Bouquain, Review on the aging mechanisms in Li-ion batteries for electric vehicles based on the FMEA method, in: 2014 IEEE Transportation Electrification Conference and Expo (ITEC), 2014, pp. 1–6, https://doi.org/10.1109/ITEC.2014.6861811.
[16] T. Waldmann, B.-I. Hogg, M. Wohlfahrt-Mehrens, Li plating as unwanted side reaction in commercial Li-ion cells – a review, J. Power Sources 384 (2018) 107–124, https://doi.org/10.1016/j.jpowsour.2018.02.063.
[17] R. Imhof, In situ investigation of the electrochemical reduction of carbonate electrolyte solutions at graphite electrodes, J. Electrochem. Soc. 145 (1998) 1081–1087, https://doi.org/10.1149/1.1838420.
[18] D. Aurbach, Review of selected electrode–solution interactions which determine the performance of Li and Li ion batteries, J. Power Sources 89 (2000) 206–218, https://doi.org/10.1016/S0378-7753(00)00431-6.
[19] D.P. Abraham, T. Spila, M.M. Furczon, E. Sammann, Evidence of transition-metal accumulation on aged graphite anodes by SIMS, J. Power Sources 11 (2008) A226, https://doi.org/10.1149/1.2987680.
[20] H. Shin, J. Park, A.M. Sastry, W. Lu, Degradation of the solid electrolyte interphase induced by the deposition of manganese ions, J. Power Sources 284 (2015) 416–427, https://doi.org/10.1016/j.jpowsour.2015.03.039.
[21] J.A. Gilbert, I.A. Shkrob, D.P. Abraham, Transition metal dissolution, ion migration, electrocatalytic reduction and capacity loss in lithium-ion full cells, J. Electrochem. Soc. 164 (2016) A389–A399, https://doi.org/10.1149/2.1111702jes.
[22] S.R. Gowda, K.G. Gallagher, J.R. Croy, M. Bettge, M.M. Thackeray, M. Balasubramanian, Oxidation state of cross-over manganese species on the graphite electrode of lithium-ion cells, Phys. Chem. Chem. Phys. PCCP 16 (2014) 6898–6902, https://doi.org/10.1039/c4cp00764f.
[23] C.R. Birkl, M.R. Roberts, E. McTurk, P.G. Bruce, D.A. Howey, Degradation diagnostics for lithium ion cells, J. Power Sources 341 (2017) 373–386, https://doi.org/10.1016/j.jpowsour.2016.12.011.
[24] G. Sun, T. Sui, B. Song, H. Zheng, L. Lu, A.M. Korsunsky, On the fragmentation of active material secondary particles in lithium ion battery cathodes induced by charge cycling, Extreme Mech. Lett. 9 (2016) 449–458, https://doi.org/10.1016/j.eml.2016.03.018.
[25] J.-M. Lim, T. Hwang, D. Kim, M.-S. Park, K. Cho, M. Cho, Intrinsic origins of crack generation in Ni-rich LiNi0.8Co0.1Mn0.1O2 layered oxide cathode material, Sci. Rep. 7 (2017), 39669, https://doi.org/10.1038/srep39669.
[26] H. Liu, M. Wolf, K. Karki, Y.-S. Yu, E.A. Stach, J. Cabana, K.W. Chapman, P. J. Chupas, Intergranular cracking as a major cause of long-term capacity fading of layered cathodes, Nano Lett. 17 (2017) 3452–3457, https://doi.org/10.1021/acs.nanolett.7b00379.
[27] P. Yan, J. Zheng, M. Gu, J. Xiao, J.-G. Zhang, C.-M. Wang, Intragranular cracking as a critical barrier for high-voltage usage of layer-structured cathode for lithium-ion batteries, Nat. Commun. 8 (2017), 14101, https://doi.org/10.1038/ncomms14101.
[28] M. Holzapfel, A. Würsig, W. Scheifele, J. Vetter, P. Novák, Oxygen, hydrogen, ethylene and CO2 development in lithium-ion batteries, J. Power Sources 174 (2007) 1156–1160, https://doi.org/10.1016/j.jpowsour.2007.06.182.
[29] J. Self, C.P. Aiken, R. Petibon, J.R. Dahn, Survey of gas expansion in Li-ion NMC pouch cells, J. Electrochem. Soc. 162 (2015) A796–A802, https://doi.org/10.1149/2.0081506jes.
[30] R. Bernhard, M. Metzger, H.A. Gasteiger, Gas evolution at graphite anodes depending on electrolyte water content and SEI quality studied by on-line electrochemical mass spectrometry, J. Electrochem. Soc. 162 (2015) A1984–A1989, https://doi.org/10.1149/2.0191510jes.
[31] R. Jung, M. Metzger, F. Maglia, C. Stinner, H.A. Gasteiger, Chemical versus electrochemical electrolyte oxidation on NMC111, NMC622, NMC811, LNMO, and conductive carbon, J. Phys. Chem. Lett. 8 (2017) 4820–4825, https://doi.org/10.1021/acs.jpclett.7b01927.
[32] J. Sieg, J. Bandlow, T. Mitsch, D. Dragicevic, T. Materna, B. Spier, H. Witzenhausen, M. Ecker, D.U. Sauer, Fast charging of an electric vehicle lithium-ion battery at the limit of the lithium deposition process, J. Power Sources 427 (2019) 260–270, https://doi.org/10.1016/j.jpowsour.2019.04.047.
[33] A. Hales, L.B. Diaz, M.W. Marzook, Y. Zhao, Y. Patel, G. Offer, The cell cooling coefficient: a standard to define heat rejection from lithium-ion batteries, J. Electrochem. Soc. 166 (2019) A2383–A2395, https://doi.org/10.1149/2.0191912jes.
[34] H.-G. Schweiger, O. Obeidi, O. Komesker, A. Raschke, M. Schiemann, C. Zehner, M. Gehnen, M. Keller, P. Birke, Comparison of several methods for determining the internal resistance of lithium ion cells, Sensors 10 (2010) 5604–5625, https://doi.org/10.3390/s100605604.
[35] C.P. Aiken, J. Xia, D.Y. Wang, D.A. Stevens, S. Trussler, J.R. Dahn, An apparatus for the study of in situ gas evolution in Li-ion pouch cells, J. Electrochem. Soc. 161 (2014) A1548–A1554, https://doi.org/10.1149/2.0151410jes.
[36] M. Storch, S.L. Hahn, J. Stadler, R. Swaminathan, D. Vrankovic, C. Krupp, R. Riedel, Post-mortem analysis of calendar aged large-format lithium-ion cells: investigation of the solid electrolyte interphase, J. Power Sources 443 (2019), 227243, https://doi.org/10.1016/j.jpowsour.2019.227243.
[37] B.H. Toby, R.B. von Dreele, GSAS-II the Genesis of a Modern Open-Source All Purpose Crystallography Software Package, 2013, https://doi.org/10.1107/S0021889813003531.
[38] C.W. Walker JR., Improved Electrolytes for Lithium Rechargeable Batteries, vol. 434, Army Research Laboratory ARL-TR, 1995. https://ntrl.ntis.gov/NTRL/dashboard/searchResults/titleDetail/ADA301953.xhtml.
[39] L.J. Krause, W. Lamanna, J. Summerfield, M. Engle, G. Korba, R. Loch, R. Atanasoski, Corrosion of aluminum at high voltages in non-aqueous electrolytes containing perfluoroalkylsulfonyl imides; new lithium salts for lithium-ion cells, J. Power Sources 68 (1997) 320–325, https://doi.org/10.1016/S0378-7753(97)02517-2.
[40] S.E. Sloop, J.K. Pugh, S. Wang, J.B. Kerr, K. Kinoshita, Chemical reactivity of PF5 and LiPF6 in ethylene carbonate/dimethyl carbonate solutions, Electrochem. Solid State Lett. 4 (2001) A42, https://doi.org/10.1149/1.1353158.
[41] C.L. Campion, W. Li, B.L. Lucht, Thermal decomposition of LiPF[sub 6]-based electrolytes for lithium-ion batteries, J. Electrochem. Soc. 152 (2005), A2327, https://doi.org/10.1149/1.2083267.
[42] A. Guéguen, D. Streich, M. He, M. Mendez, F.F. Chesneau, P. Novák, E.J. Berg, Decomposition of LiPF 6 in high energy lithium-ion batteries studied with online electrochemical mass spectrometry, J. Electrochem. Soc. 163 (2016) A1095–A1100, https://doi.org/10.1149/2.0981606jes.
[43] M. Lewerenz, A. Marongiu, A. Warnecke, D.U. Sauer, Differential voltage analysis as a tool for analyzing inhomogeneous aging, J. Power Sources 368 (2017) 57–67, https://doi.org/10.1016/j.jpowsour.2017.09.059.
[44] M. Lewerenz, G. Fuchs, L. Becker, D.U. Sauer, Irreversible calendar aging and quantification of the reversible capacity loss caused by anode overhang, J. Energy Storage 18 (2018) 149–159, https://doi.org/10.1016/j.est.2018.04.029.
[45] B. Gyenes, D.A. Stevens, V.L. Chevrier, J.R. Dahn, Understanding anomalous behavior in coulombic efficiency measurements on Li-ion batteries, J. Electrochem. Soc. 162 (2015) A278–A283, https://doi.org/10.1149/2.0191503jes.
[46] M. Lewerenz, P. Dechent, D.U. Sauer, Investigation of capacity recovery during rest period at different states-of-charge after cycle life test for prismatic Li(Ni1/3Mn1/3Co1/3)O2-graphite cells, J. Energy Storage 21 (2019) 680–690, https://doi.org/10.1016/j.est.2019.01.004.
[47] J.P. Fath, L. Alsheimer, M. Storch, J. Stadler, J. Bandlow, S. Hahn, R. Riedel, T. Wetzel, The influence of the anode overhang effect on the capacity of lithium-ion cells – a 0D-modeling approach, J. Energy Storage 29 (2020), 101344, https://doi.org/10.1016/j.est.2020.101344.
[48] T. Hüfner, M. Oldenburger, B. Bedürftig, A. Gruhle, Lithium flow between active area and overhang of graphite anodes as a function of temperature and overhang geometry, J. Energy Storage 24 (2019), 100790, https://doi.org/10.1016/j.est.2019.100790.
[49] D. Juarez-Robles, J.A. Jeevarajan, P.P. Mukherjee, Degradation-safety analytics in lithium-ion cells: Part I. Aging under charge/discharge cycling, J. Electrochem. Soc. 167 (2020), 160510, https://doi.org/10.1149/1945-7111/abc8c0.
[50] M. Ecker, N. Nieto, S. Käbitz, J. Schmalstieg, H. Blanke, A. Warnecke, D.U. Sauer, Calendar and cycle life study of Li(NiMnCo)O2-based 18650 lithium-ion batteries, J. Power Sources 248 (2014) 839–851, https://doi.org/10.1016/j.jpowsour.2013.09.143.
[51] Y. Preger, H.M. Barkholtz, A. Fresquez, D.L. Campbell, B.W. Juba, J. Romàn-Kustas, S.R. Ferreira, B. Chalamala, Degradation of commercial lithium-ion cells as a function of chemistry and cycling conditions, J. Electrochem. Soc. 167 (2020), 120532, https://doi.org/10.1149/1945-7111/abae37.
[52] S.F. Schuster, T. Bach, E. Fleder, J. Müller, M. Brand, G. Sextl, A. Jossen, Nonlinear aging characteristics of lithium-ion cells under different operational conditions, J. Energy Storage 1 (2015) 44–53, https://doi.org/10.1016/j.est.2015.05.003.
[53] T.S. Bryden, A. Holland, G. Hilton, B. Dimitrov, C.P. de León Albarrán, A. Cruden, Lithium-ion degradation at varying discharge rates, Energy Procedia 151 (2018) 194–198, https://doi.org/10.1016/j.egypro.2018.09.047.
[54] I. Belharouak, G.M. Koenig, T. Tan, H. Yumoto, N. Ota, K. Amine, Performance degradation and gassing of Li 4 Ti 5 O 12/LiMn 2 O 4 lithium-ion cells, J. Electrochem. Soc. 159 (2012) A1165–A1170, https://doi.org/10.1149/2.013208jes.
[55] K. Jalkanen, J. Karppinen, L. Skogström, T. Laurila, M. Nisula, K. Vuorilehto, Cycle aging of commercial NMC/graphite pouch cells at different temperatures, Appl. Energy 154 (2015) 160–172, https://doi.org/10.1016/j.apenergy.2015.04.110.
[56] M. Klett, R. Eriksson, J. Groot, P. Svens, K. Ciosek Högström, R.W. Lindström, H. Berg, T. Gustafson, G. Lindbergh, K. Edström, Non-uniform aging of cycled commercial LiFePO4//graphite cylindrical cells revealed by post-mortem analysis, J. Power Sources 257 (2014) 126–137, https://doi.org/10.1016/j.jpowsour.2014.01.105.
[57] M. Kassem, C. Delacourt, Postmortem analysis of calendar-aged graphite/LiFePO4 cells, J. Power Sources 235 (2013) 159–171, https://doi.org/10.1016/j.jpowsour.2013.01.147.
[58] S. Malmgren, K. Ciosek, M. Hahlin, T. Gustafsson, M. Gorgoi, H. Rensmo, K. Edström, Comparing anode and cathode electrode/electrolyte interface composition and morphology using soft and hard X-ray photoelectron spectroscopy, Electrochim. Acta 97 (2013) 23–32, https://doi.org/10.1016/j.electacta.2013.03.010.
[59] D. Bar-Tow, A study of highly oriented pyrolytic graphite as a model for the graphite anode in Li-ion batteries, J. Electrochem. Soc. 146 (1999) 824, https://doi.org/10.1149/1.1391688.
[60] T. Yoshida, M. Takahashi, S. Morikawa, C. Ihara, H. Katsukawa, T. Shiratsuchi, J. Yamaki, Degradation mechanism and life prediction of lithium-ion batteries, J. Electrochem. Soc. 153 (2006) A576, https://doi.org/10.1149/1.2162467.
[61] I. Laresgoiti, S. Käbitz, M. Ecker, D.U. Sauer, Modeling mechanical degradation in lithium ion batteries during cycling, J. Power Sources 300 (2015) 112–122, https://doi.org/10.1016/j.jpowsour.2015.09.033.
[62] R. Deshpande, D.M. Bernardi, Modeling solid-electrolyte interphase (SEI) fracture, J. Electrochem. Soc. 164 (2017) A461–A474, https://doi.org/10.1149/2.0841702jes.
[63] C. Zhan, T. Wu, J. Lu, K. Amine, Dissolution, migration, and deposition of transition metal ions in Li-ion batteries exemplified by Mn-based cathodes – a

critical review, Energy Environ. Sci. 11 (2018) 243–257, https://doi.org/10.1039/C7EE03122J.
[64] M. Lewerenz, A. Warnecke, D.U. Sauer, Post-mortem analysis on LiFePO 4 | Graphite cells describing the evolution & composition of covering layer on anode and their impact on cell performance, J. Power Sources 369 (2017) 122–132, https://doi.org/10.1016/j.jpowsour.2017.10.003.
[65] T. Li, X.-Z. Yuan, L. Zhang, D. Song, K. Shi, C. Bock, Degradation Mechanisms and Mitigation Strategies of Nickel-Rich NMC-Based Lithium-Ion Batteries, 2019, https://doi.org/10.1007/s41918-019-00053-3.

Journal of Energy Storage 41 (2021) 102887

Contents lists available at ScienceDirect

Journal of Energy Storage

journal homepage: www.elsevier.com/locate/est

Temperature and Lithium Concentration Gradient Caused Inhomogeneous Plating in Large-format Lithium-ion Cells

Mathias Storch [a,b,*], Johannes Philipp Fath [a], Johannes Sieg [a], Dragoljub Vrankovic [a], Carsten Krupp [a], Bernd Spier [a], Ralf Riedel [b]

[a] Mercedes-Benz AG, Neue Straße 95, 73230 Kirchheim u.T., Germany
[b] Fachgebiet Disperse Feststoffe, Fachbereich Material- und Geowissenschaften, Technische Universität Darmstadt, Otto-Berndt-Str. 3, 64287 Darmstadt, Germany

ARTICLE INFO

Keywords:
Lithium-ion battery
Lithium plating
Post-mortem analysis
Inhomogeneous degradation
Lithium-ion flow
Differential voltage analysis

ABSTRACT

Although lithium plating is one of the most-investigated degradation mechanisms occurring in lithium-ion batteries, many degradation studies still view inhomogeneous lithium plating as an artifact. It is often caused by mechanical stress, gas formation and encapsulation, or temperature and current gradients on account of the cell size. In this work, large-format lithium-ion cells are cycled at conditions harmless on the material level, but cause heavy lithium plating in the center of the commercial cell. Failure analysis requires visual inspection and further material evaluation to identify the reason for malfunction. A combination of temperature gradient and current density gradient evoke a lithium concentration gradient, which equalizes by a lateral lithium-ion flow. The inhomogeneous distribution of lithium again distorts the operating potential window, resulting in local violation of the critical lithium plating condition. Thus, our study shows that inhomogeneity in a large-format lithium-ion cell has to be taken into account when designing the operating window. In addition, accelerated testing of large-format lithium-ion cells raises degradation mechanisms, which do not appear during regular usage.

1. Introduction

The transformation of the mobility sector from gasoline to electric-powered transportation has raised the demand for extremely durable lithium-ion batteries under intense operation. Excellent performance in terms of energy density and available power on a wide range of operating conditions for a long period is mandatory. The majority of research studies on the degradation behavior of large-format lithium-ion cells use accelerated testing under intense conditions e.g. T~0 °C or T~40 °C, combined with the application of high currents [1–5]. In order to perform realistic lifetime tests, the operating conditions have to be carefully selected. The material characteristics, the applied pressure, and the temperature control have to be properly managed. However, in many studies, the operating conditions evoke the generation of temperature and current density gradients, resulting in non-uniform degradation [3,6–9]. Therefore, a deeper understanding of the appearance and the effects of these gradients is necessary to find the ideal operating conditions.

Among others, lithium plating is a frequently-observed aging phenomenon in lithium-ion cells. In many cases, it is provoked by cycling tests at low temperature and rapid charging at a high state of charge (SOC) [4,10–12]. However, lithium plating can also be a result of non-uniform pressure [6,13], temperature and current density [7,14], or electrolyte dry-out and gas inclusions [3,8,15]. Lithium plating occurs when the anode potential drops below 0 V vs. Li/Li^+. This is caused by an excessive number of lithium-ions arriving at the anode surface without the possibility to either enter the anode particle or diffuse inside the electrode fast enough [16]. Plated lithium can be partly reused in the following cycle as lithium strips during the discharge process. However, the irreversible reaction of lithium with the electrolyte and formation of electrically insulated islands [17] results in the phenomenon that a considerable amount of lithium is excluded from further cycling, resulting in cell capacity loss. Sieg et al. [18] recently established a method using a three-electrode cell assembly, which enables the identification of the cell- and electrode-specific limiting currents for fast-charging procedures at a wide range of temperatures. Even though, small-scale three-electrode cells do not take all boundary conditions of the large-format cells into account, Sieg et al. [18] demonstrated that the

* Corresponding author.
E-mail address: mathias.storch@daimler.com (M. Storch).

https://doi.org/10.1016/j.est.2021.102887
Received 25 November 2020; Received in revised form 23 March 2021; Accepted 24 June 2021
Available online 14 July 2021

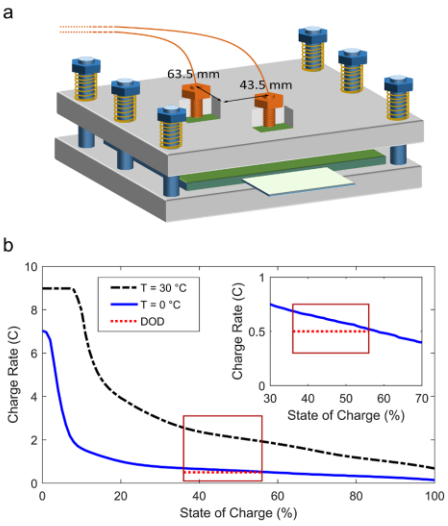

Fig. 1. a.) Schematic test setup consisting of the custom-made cell clamping system, two temperature sensors (orange) and lithium-ion cell (green). Springs are chosen to ensure pressure on the cell of 29 ±3 kPa. One temperature sensor is placed in the center; the other one is shifted by 43.5 mm in x-direction and 63.5 mm in y-direction. b.) Charging current map (charge rate versus the state of charge) of the used automotive-grade cell, inset of the applied charge rate for the used depth of discharge (DOD, red dotted) in the aging experiment.

results are valid on the pouch and battery-pack levels.

In this study, a long-term aging test with 39 Ah pouch cells is performed to identify the critical influence of a high discharge rate at low and medium temperatures. According to the experimental design, no enhanced degradation at low-temperature cycling is expected. The applied current profiles are tuned in such a way that low-temperature lithium plating is suppressed. Nevertheless, the results indicate that inhomogeneous degradation of the cells still occurred, which is consistent with the literature [14,19]. The underlying mechanism of local lithium plating is analyzed in detail and the mechanism is illustrated. The degradation behavior is first analyzed on the basis of electrochemical data, namely the capacity retention, the electrical resistance, and differential voltage (DV) analysis [19–23]. Subsequently, post-mortem analysis and additional three-electrode cell testing were performed to contribute to the scientific discussion on inhomogeneous aging in large-scale lithium-ion cells.

2. Experimental

2.1. Pouch cell cycle test

Large-format pouch bag lithium-ion cells with a measured capacity of $C = 39$ Ah were subjected to a long-term cyclic aging experiment. The cells used were composed of graphite anodes, $LiNi_{0.6}Mn_{0.2}Co_{0.2}O_2$: $LiNi_{1/3}Mn_{1/3}Co_{1/3}O_2$ (NMC622:NMC111) in ratio of 0.9:0.1 cathodes and an Al_2O_3-coated PE-membrane soaked in an ethylene carbonate (EC), ethyl methyl carbonate (EMC), and diethyl carbonate (DEC) -based $LiPF_6$ electrolyte solution. A formation process was performed by the supplier and the cell, as received, is referred to as the beginning of life (BOL) state. Each cell comprises 33 double-side coated anodes and 32 double-side coated cathodes z-folded into the separator. The dimensions of the anodes are 174·140 mm^2 and for the cathodes 172·136 mm^2, with electrode thicknesses of ~160 µm and ~138 µm (current collector thickness Cu ~10 µm, Al ~13 µm) respectively. The electrode thicknesses were measured with a micrometer screw, each double-side coating including the current collector foil.

The aging experiment comprises two cells and a customized test setup (see Fig. 1a), which is designed to keep the pressure on the cells nearly constant during each cycle and over the whole period of aging. In total, six cylinder screws M6 × 110 (Würth GmbH, Germany) - assembled with springs 0D12370 (Febrotec GmbH, Germany) - were used to clamp the cell between two 30 mm thick anodized aluminum plates (~120 N/spring, ~29 kPa on the cell). The expected irreversible cell thickness increase of 1 mm leads to a maximum pressure rise of 3 kPa over the period of testing. Inserting-resistance-thermometer with Pt-100 (JUMO GmbH & Co. KG, Germany) temperature sensors were implemented to survey the cell temperature at the cell center and the cell edge, directly on the pouch-bag. The temperature sensors were in contact with the clamping plates, and, so, do not represent the cell inner temperature. Tests were performed on a fully-automatic cycler with a maximum of ±200 A (Digatron Power Electronics GmbH, Germany) and a MK240 (BINDER GmbH, Germany) climate chamber was used. The test comprises two sequences: Regular check-up tests to monitor the cell characteristics and a total of 13 aging sequences, which equals a total number of ~1200 – 1400 equivalent full cycles (EFC). The check-up tests were performed at 30 °C, three cycles with 18.5 A charge and discharge current, followed by one cycle 3.7 A charge and discharge current. At the end of each check-up test, a 50 A discharge pulse for 30 s at 100% state of charge - to determine the cell resistance in analogy with Schweiger et al. [24] - was performed. During the aging sequences, the ambient temperature was set to 0 °C for two cells and to 30 °C for two more cells. The electric profile for each cell was identical. A maximum charging voltage of $U_{CH,max}$ of 3.7 V, which is equal to an SOC of 57%, and a depth of discharge (DOD) of 20% of the actual capacity, measured in the previous check-up test, was set during the aging period. The charge current was set to 18.5 A (~0.5C) and the discharge current was set to 111 A (~3C).

Prior to the aging experiment, the charging current map of the used cell was analyzed using three-electrode cells "PAT-Cell" (EL-Cell GmbH, Germany) and a preparation procedure of the original cell materials in accordance with the method presented by Sieg et al. [18]. The resultant charging current rates at 0 °C and 30 °C, including the charge current applied in our aging test, are depicted in Fig. 1b. A charge current of 18.5 A and a cutoff current of 3.7 A in constant current–constant voltage mode (CC-CV) was chosen to prevent the cells from lithium plating, as the red dotted line lies lower than the blue and the black lines.

After the one-year lasting cycle test, the cells were characterized geometrically, and, finally, post-mortem analysis was performed. Cell thickness was measured using a thickness gauge and 10 points distributed over the complete cell.

2.2. Post-mortem analysis

Post-mortem analysis was carried out in an argon-filled glovebox "MB200MOD" (MBraun Inertgas-Systeme GmbH, Germany) with O_2<0.1 ppm and H_2O<0.1 ppm. Prior to the opening, the cells were discharged to 3 V in CC-CV mode, with a constant current of 5 A and a cut-off current of 0.74 A (~C/50). This discharge step was repeated three times, with breaks of 24 h for relaxation. The cells were cut open next to the seam of the pouch bag to tear through the current collector. The z-folded electrode stack was then expanded to separate the anode and the cathode foils. The electrodes were washed in four separated dimethyl carbonate baths, two for anode and two for cathode, two times for five minutes in each bath. After drying, the samples were extracted for further analysis.

Scanning electron microscope (SEM) micrographs were recorded with an "EVO 25" (Carl Zeiss AG, Germany) in secondary electron mode, with an acceleration voltage of 3 kV and a magnification of 1000x. Inductively coupled plasma optical emission spectroscopy (ICP-OES)

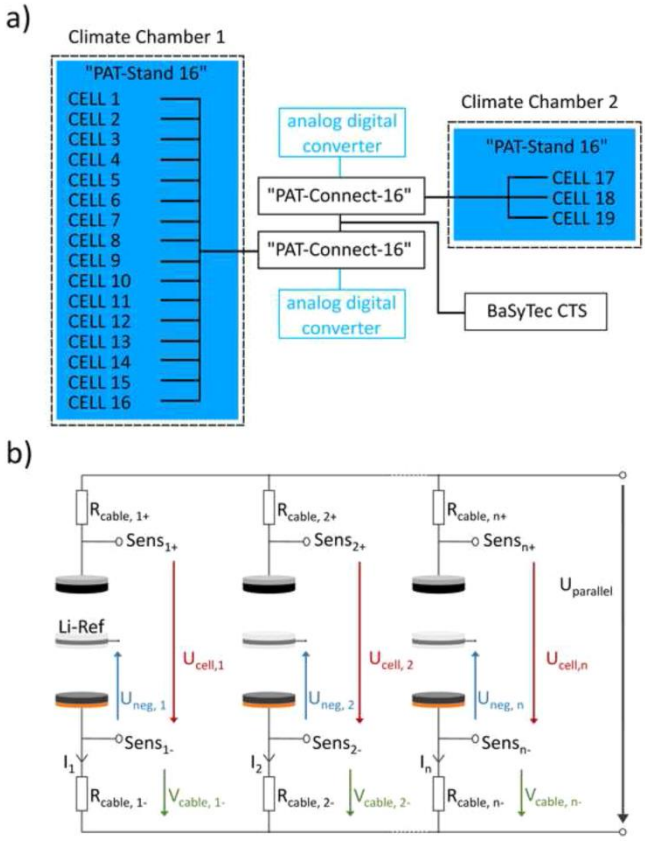

Fig. 2. a.) Three-electrode cell setup using equipment from EL-CELL GmbH to realize a parallel connection of 19 three-electrode cells, b.) three-electrode cell measurement setup.

was performed using double-side coated and representative electrode sheet, including the current collector foil. The sample materials were cut from the center and the edge position of electrode layer number 17. The electrodes are separately dissolved in aqua regia and the solutions were analyzed in an optical emission spectrometer.

2.3. *Three-electrode cell testing*

Three-electrode test cells "PAT-Cell" (EL-CELL GmbH, Germany) were used for reproduction of temperature gradients in lateral orientation of the electrode stack and locally resolved analysis of the degradation in the cell tested at 0 °C. The used electrodes were gathered from the middle of the disassembled pouch cells. For temperature gradient analysis, BOL material was prepared; for the degradation analysis, the electrodes from the respective cells. The electrode coating was removed from one side with n-methyl-2-pyrrolidon (NMP, Merck KGaA, Germany) on the cathode and with 2-Propanol on the anode. Full cells consisting of an anode and the opposed cathode coin of 18 mm in diameter were assembled with 85 µl of the original pouch cell electrolyte without additives. For the half cell measurements, the cathode coins were cycled versus a metallic lithium coin using 115 µl of electrolyte, a current of 0.29 mA in the potential limits 3.3 V to 4.3 V.

Temperature gradient reproduction was realized using a test setup (see Fig. 2a), comprising two separately controllable climate chambers, each containing a "PAT-Stand 16″ (EL-CELL GmbH, Germany) in parallel connection. In total, 19 three-electrode cells were distributed 16 versus 3 in the two chambers, according to the findings from post-mortem analysis representing the two separated areas of different aging (84.2% vs. 15.8% of the complete electrode area). A CTS cycler (Basytec GmbH, Germany) was used to apply a current profile onto the parallel connection in analogy to the current profile of the pouch cell cycle test. An analog digital converter was introduced to record the potentials and effective currents at each experimental cell (see Fig. 2). The test procedure comprised a constant temperature of 0 °C for the 16 cells and the temperature of the three cells was increased from 0 °C to 15 °C in steps of 5 °C. At each temperature step, 10 cycles were performed. The effective current on each of the three-electrode cells is measured in accordance with the plan shown in Fig. 2b, using the resistance - measured prior to the experiment for each temperature and channel - and the voltage [25,26]. The current was determined using Ohm's law.

Local degradation analysis was carried out in a 4 × 4 pattern, regularly arranged on the complete electrode area of the pouch cell cycled at 0 °C. A short cycle protocol of 1·C/10, 1·C/5, and 2·C/2 followed by a C/2 discharge was applied to the three-electrode cells prior to the actual recording of a C/10 and a final C/100 charge-discharge

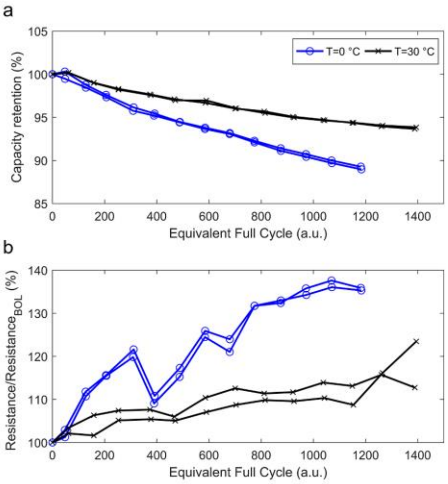

Fig. 3. a) C/10 capacity retention and b) resistance increase of in total ~1200 – 1400 equivalent full cycle, measured in the check-up tests.

cycle in order to determine the local electrode balancing.

3. Results and discussion

3.1. Capacity and resistance trends

During the cycle test, the capacity retention (Fig. 3a) and the resistance normalized to the BOL resistance (Fig. 3b) versus equivalent full cycles are recorded for two cells at each condition. The capacity of the cells cycled at 0 °C decrease to 89.1% of the capacity obtained at BOL state, whereas the cells cycled at 30 °C manage to keep 93.8%. It is remarkable that for each cycling condition, the results for both cells show low deviation in capacity retention, and an end-of-test difference of maximum 0.31% is found. Another important observation is that the degradation rate slows down during the test period from ~0.015%/cycle (5.9 mAh/cycle) in the first 200 equivalent full cycle (EFC) to ~0.007%/cycle (2.6 mAh/cycle) in the last 200 EFC for the cells cycled at 0 °C. For the cells cycled at 30 °C, the capacity loss is even smaller, being ~0.006%/cycle (2.5 mAh/cycle) in the first 200 EFC and decrease to ~0.002%/cycle (0.6 mAh/cycle) in the last 200 EFC. The measurements show continuous resistance increase for both measurement points over the testing period, amounting to approximately 15% for high temperature cycling and about 35% for low temperature cycling. The observed drop in resistance between check-up points 5 and 6 is a measurement artifact; it is caused by the test temperature in cycle sequence 5 being set to 40 °C for 12 days. Nevertheless, this temperature increase had only a minor influence on the capacity retention (compare Fig. 3a) and is expected to have a rather minor effect on the overall cell degradation modes. According to the experiment design, no lithium plating is expected. Nevertheless, the overall higher capacity loss and resistance increase in the cells cycled at 0 °C indicate irreversible changes in the cells and possible lithium plating. Differential voltage and post-mortem analysis are, therefore, inevitable to identify the degradation mechanisms.

3.2. Post-mortem analysis

After the cycle test, the cells were photographed and the cell thickness was measured. The photographs of the cells gathered before the post-mortem analysis, including the cell thickness data, are presented in Fig. 4a and Fig. 4b. The cells cycled at 30 °C exhibit homogenous cell thickness increase from 11.60 mm in BOL state to 11.90 mm after cycling. In contrast, the cells cycled at 0 °C show two separated areas, an inconspicuous outer area with a thickness of 11.85 mm, and an elliptical-like bump at the center of the cell. The long side of the observed bump is parallel to the current collector and amounts to 0.7 mm in height. This results in a total cell thickness of 12.55 mm. The photographs of a representative anode from each cell with SEM micrographs as insets (see Fig. 4c and Fig. 4d) allow further identification of the underlying mechanism. An anode thickness difference of 22 µm between the outer area and the inner elliptical bump, together with visible surface deposits, can be clearly distinguished from the original anode material (SEM micrographs in Fig. 4d). Fig. 4 further shows 3 µm difference in thickness for the outer anode region between cells cycled at 30 °C and 0 °C. The reason for this finding might be an accelerated SEI growth at higher temperature [27,28]. The edge layers No. 1 and No. 33 did not show the observed elliptical-like bump on account of homogeneous cooling from the 30 mm thick aluminum plates; the image is shown in the appendix (see Fig. A1). The cathode photographs (see Fig. 4e and Fig. 4f) show weaker patterns and no obvious surface deposits. The cell cycled at 30 °C has an increased homogeneous cathode thickness at 147 µm compared to a BOL thickness (138 µm). For the cell cycled at 0 °C, the cathode thickness increase is inhomogeneous, reaching 150 µm in the center and 140 µm in the outer area.

In order to identify the underlying reason for the deposition and the chemical composition of the observed cover layer in the center of the 0 °C cycled anode, samples from different electrode areas are extracted and ICP-OES is performed (see Table 1). In analogy to our publication [15], sample extracted from the center of the electrode cycled at 0 °C with cover layer contains a significantly higher amount of lithium compared to BOL and to the outer area samples. In respect of the SEM micrographs (see Fig. 4), this clearly indicates the deposition of metallic lithium during cycling, known as lithium plating. With regard to the charge current map (see Fig. 1b) and the applied charge current during the cycle test of only 18.5 A together with the homogeneous force and thermal environment of the cell, such a strong emergence of lithium plating is surprising. On the material level, lithium plating is expected to be suppressed.

3.3. Local degradation analysis

Further information about the degradation mechanism is obtained from differential voltage analysis. The dV/dQ graphs for both testing points at the beginning of life and the end of testing are compared in Fig. 5a. At BOL, the measurements obtained at 0 °C and 30 °C display the same features; therefore, any difference obtained at the end of testing will be solely caused by the temperature induced aging. A clear peak at 8.7 Ah (SOC 22%) indicates stage III graphite and the weak peaks at 22.6 Ah and 24.6 Ah (SOC 58% and 63%) indicate stage II graphite [29]. According to Bloom et al. [20], the splitting of the peak may be linked to non-uniformity of the anode production. Lewerenz et al. [21] and Fath et al. [19,30] assign this feature to the presence of anode overhang causing inhomogeneity in the cell, which we find more likely. At the end of tests, the DV graphs show significant differences for cells tested at different temperatures. The peaks of the cell cycled at 30 °C are more pronounced and slightly shift to lower SOC value. This indicates a more homogeneous lithium distribution compared to the BOL state and homogeneous degradation throughout the cell [14,22,23]. In contrast, the peaks obtained for the cell cycled at 0 °C appear less pronounced and broadened, indicating an electrode deactivation and a loss of anode active material [31]. Furthermore, the higher dV/dQ values between 10 Ah and 35 Ah represent the displacement of the anode and cathode potentials versus each other [21]. In order to investigate the degradation mechanisms catalyzed by temperature, a more detailed and localized analysis is required. DV analysis of the 16 three-electrode cells gathered

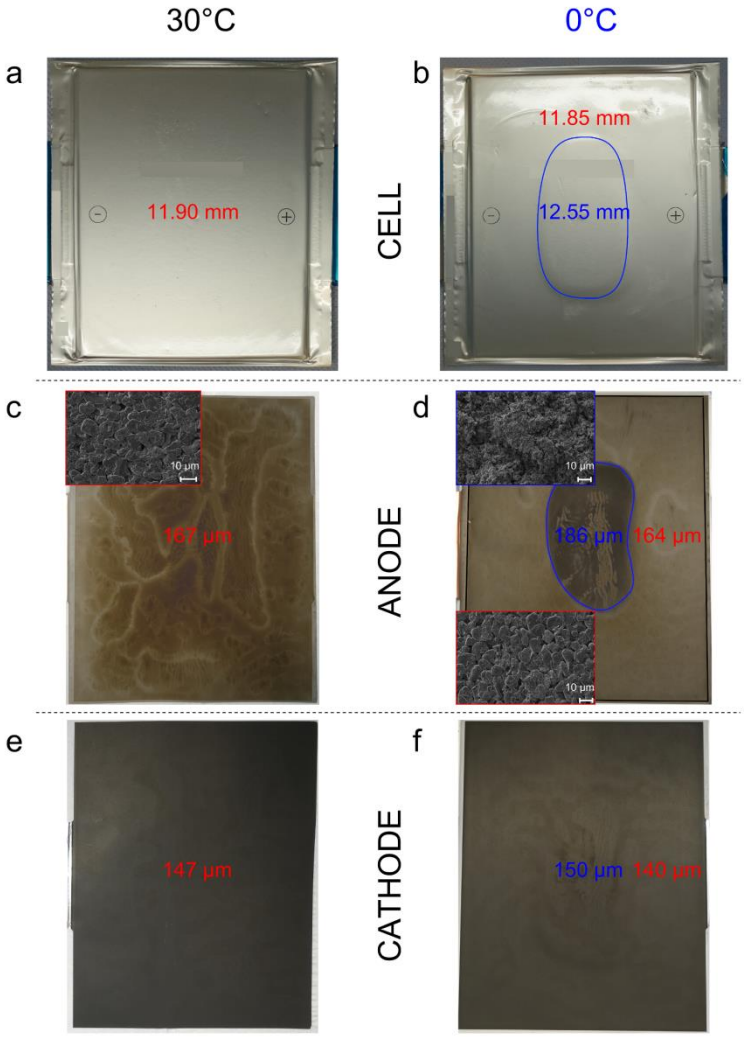

Fig. 4. Images of the pouch cells (a and b), the extracted anodes, including SEM micrographs as insets (c and d) and the corresponding cathode images (e and f). Left column represents the images taken from the cell cycled at 30 °C and the cell cycled at 0 °C is shown in the right column. An elliptical-like bump in the center of the 0 °C cell is observed (blue), stemming from a cover layer formed on the anode. The 30 °C cell instead has a homogeneous thickness distribution and appearance (red).

Table 1
Lithium content in the double-side coated electrodes, including possible surface deposits measured via ICP-OES.

Electrode location	Lithium in anode vs. BOL	Lithium in cathode vs. BOL
0 °C outer	129.4 ± 0.5%	90 ± 0.7%
0 °C center	191.4 ± 3%	100 ± 3.6%

from the cell cycled at 0 °C (following 4 × 4 pattern) are shown in Fig. 5b and compared to the results obtained for BOL state. As shown in 3.2, the electrode is inhomogeneous; a thick layer of plated lithium covers the center area, which is surrounded by an uncovered area. DV results also show a clear separation between the center and the outer area of the electrode. The peaks characteristic for graphite staging are distinctive in the dV/dQ graphs of the electrode outer area and slightly shifted toward lower Q values compared to BOL. Furthermore, the 12 cells obtained from the electrode outer area show differences in lithium loss, dependent on their sampling position. Namely, four cells (Positions 1, 4, 13, 16) obtained from the corner of the electrodes show a shorter distance between the graphite peak at $Q = 4$ mAh and the end of the graph, thereby indicating higher lithium loss compared to the other outer area cells (2, 3, 5, 8, 9, 12, 14, 15). In addition, the locally resolved C/10-capacity retention in reference to BOL was measured using these three-electrode cells. Fig. 5c shows the lowest capacity retention in the electrode center, followed by the electrode corners and the rest of the

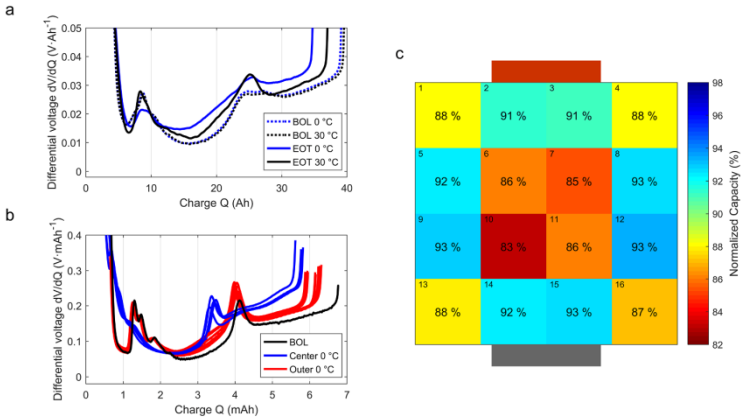

Fig. 5. Differential voltage analysis: a) pouch cell dV/dQ graphs in BOL state before cycle test and in the aged state after cycling at 0 °C and 30 °C, b) graphs of the three-electrode cells obtained from the cell cycled at 0 °C, BOL three-electrode cell DV is added for comparison. c) Local C/10-capacity retention of the cell cycled at 0 °C compared to BOL, measured with 16 three-electrode cells using electrodes harvested from the original pouch cell.

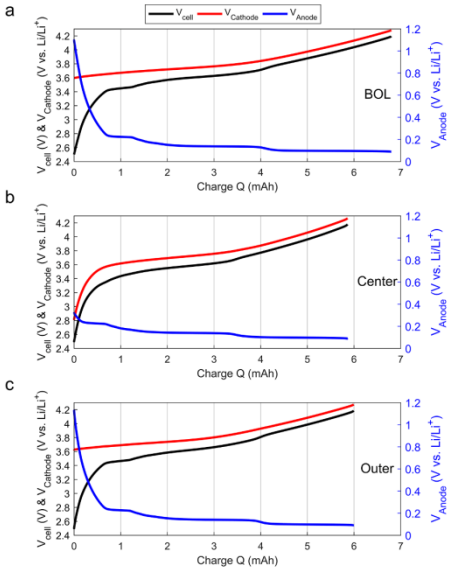

Fig. 6. Discharge potential graphs measured in three-electrode cells using electrodes from the a) beginning of life cell, b) the center of the pouch cell cycled at 0 °C and c) the outer area of the same cell. The data for b) and c) was obtained from the same three-electrode cells as used for the local analysis of the DV and the capacity retention in Fig. 5b and Fig. 5c.

electrode area. The reason for these three different areas can be explained with the temperature and lithium concentration deltas, as presented in section 3.4.

The higher dV/dQ between $Q = 2$ mAh and $Q = 6.3$ mAh result from a shift of the cathode potential versus the anode potential, as can be seen in Fig. 6. The DV results obtained on samples collected from the center of electrode strongly differ from the outer ones and BOL. The graphite peak positions are strongly shifted to lower Q values (lower SOCs), and the change in dV/dQ resulting from cathode-anode balancing is more intense. The strong degradation of the cathode sampled from the center of electrode leads to a shift in the cycling window. The corresponding lower cut-off potential drops from 3.6 V to 2.9 V vs. Li/Li^+ and the upper one drops from 4.27 V to 4.26 V vs. Li/Li^+. Strong cathode degradation causes a shift in the cut-off potential of the anode from ~1.1 V to ~0.3 V vs. Li/Li^+ and for the lower potential from ~0.089 V to ~0.087 V vs. Li/Li^+. Simultaneously, the phase transition points of the graphite shown in Fig. 5b and Fig. 6 shift to lower SOC and anode potentials > 0.3 V vs. Li/Li^+ are not reached anymore.

3.4. Validation of the degradation mechanism

The main finding of the degradation analysis is the inhomogeneous rise of plated lithium in the center of the pouch cell cycled at 0 °C, while the cell cycled at 30 °C appears homogeneously degraded. In the following, the reason for this difference in degradation is analyzed, and two thoughts are further presented. The single difference between the cycled cells is the ambient temperature set for the two measurement points. Hence, the temperature of 0 °C is assumed to play a crucial role for the appearance of inhomogeneous aging. Our first thought was that thermal gradients emerge inside the cell because of applied charge/discharge currents in combination with resistance and current density gradients. For the used cell geometry, thermal gradients - matching well with the observed degradation pattern of the 0 °C cell - were simulated by Zhang et al. [32], Du et al. [33], and Kosch et al. [34], with temperature gradient of up to ~10 K. In the cycling test, a high discharge current of 111 A was applied repeatedly; hence, a relatively strong heating is assumed. Owing to the increase in temperature, the resistance drops, and an even higher effective current affects the hot center area in the following cycles. During the charge process, the lithium plating limit might be violated locally, resulting in metallic lithium deposition.

In order to further validate this assumption, an experimental setup depicting the influence of a lateral thermal gradient on the electrodes representing (possible) thermal situations inside the cell is developed (see 2.4). As a parameter for the three-electrode cell setup, the area share of lithium plating on the anode of the cell cycled at 0 °C is calculated from image analysis; it amounts to 15.5%. Hence, the setup comprises a parallel connection of a total of 19 experimental cells, 16 cells in one climate chamber (cold outer cell area) and 3 cells in a second climate chamber (warm inner cell area), which results in 84.2% vs.

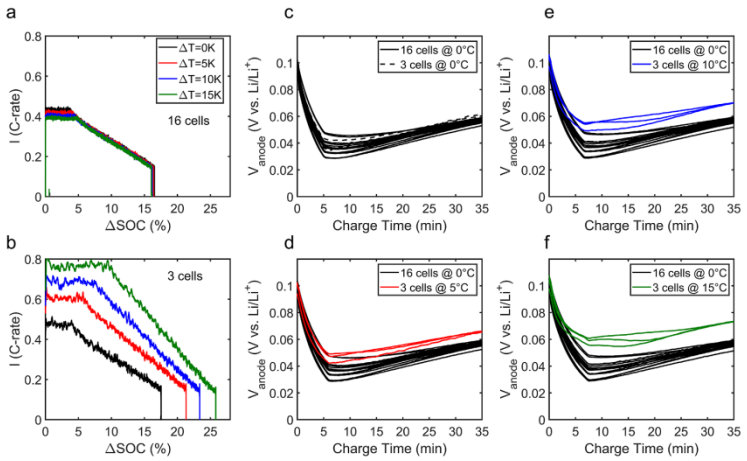

Fig. 7. Results of the three-electrode cell experiment: a.) current development for the 16 cells at constant 0 °C, b.) current development for the three cells at 0 °C, 5 °C, 10 °C, and 15 °C. c-f) Anode potential graphs in charge direction, the 16 cells were kept at 0 °C, while the three cells experienced a temperature of c) 0 °C, d) 5 °C, e) 10 °C, and f) 15 °C.

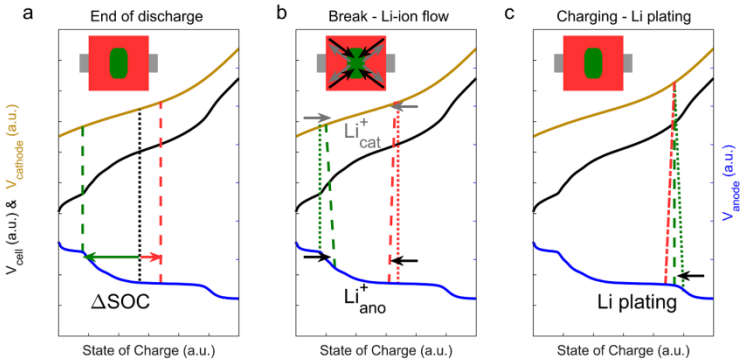

Fig. 8. Schematic evolution of the potentials of the cell during the aging test. The solid lines represent the electrode potentials and the cell voltage (black=cell voltage, blue=anode potential, and yellow=cathode potential). The dotted lines represent the expected potentials caused by operation, while the potentials caused by inhomogeneity effects are dashed lines. Electrode center area and corresponding potential changes are colored green and electrode outer area and corresponding potential changes are colored red. a) A delta in state of charge between the outer and the center area results from thermal gradient. b) During the rest period, the lithium-ion flow from outer to center area of the anode takes place due to potential gradient. The flow of lithium in the cathode in opposite direction is weaker due to the lower potential gradient. c) The shift in the center anode potential enables lithium plating in the following charging process.

15.8% of test area. The effective current rate on the 16 experimental cells at 0 °C and the three cells at temperatures between 0 °C and 15 °C versus corresponding ΔSOC are depicted in Fig. 7a and Fig. 7b respectively. The cycle profile starts at 3.62 V with a 0.5 C CC phase, followed by a CV phase at 3.92 V until the cut-off criteria of t>35 min is reached. After a rest period of 6 min, a 3C discharge follows. The testing profile is set to reproduce the testing profile of the original pouch cells. When both climate chambers are set to 0 °C, the current rates measured for both sets of experimental cells match well (cf. Fig. 7a and Fig. 7b). However, when a temperature difference is applied to the two sets of cells (16 cells at 0 °C and 3 cells stepwise increasing by 5 K between 0 °C and 15 °C), the current rate measured at the warmer cells strongly increases in both charge and discharge direction. At the same time, the current rate at the colder cells slightly diminishes. Accordingly, the ΔSOC changes to higher values for the warmer cells. In the rest period between charge and discharge, a small balancing discharge current in the warmer cells occurs because of different SOC. These findings are in good accordance with the studies of Fill et al. [26,35], which focuses on the theory and measurement of current distribution in parallel connected cells.

In a manner contradictory to our expectations, the anode potential graphs (see Fig. 7c-f) show that the anode potentials of the warmer cells (5 °C red, 10 °C blue, 15 °C green) are higher than the anode potentials of the colder cells (0 °C black) during charging. The reason might be the enhanced diffusion of lithium into the graphite particles at increased temperatures and, so, a faster transport of lithium from the particle surface into the bulk [16]. Our three-electrode cell experiment shows that a thermal gradient of up to 15 K does not solely cause lithium plating. Hence, an additional effect - which is not captured with the three-electrode cells - has to be superposed on that of the thermal gradient.

In order to explain these results, the ionic coupling of the cold and warm electrode areas is considered. We propose a lithium pumping effect inside the pouch cell comparable to the effect of filling and emptying of the so-called anode overhang [36,37], which is schematically demonstrated in Fig. 8. The center area of the pouch cell experiences a higher current density than the outer area (cf. Fig. 7b), which results in stronger discharge of the center area. Hence, the local cell voltage in the center area (green) is lower than that of the outer area

(red) respectively; the anode potential is higher and the cathode potential is lower (see Fig. 8a). In the following rest period (see Fig. 8b), the potential gradient starts to equal out by a lithium-ion flow from lower to higher potential in the anode and from higher to lower potential in the cathode, as indicated by the black and gray arrows in the inset of the cell. Since the potential gradient in the anode is higher than in the cathode, the lithium-ion flow in the anode is again higher than in the cathode. A shift in the electrode balancing is the result. In the following cycles, this effect accumulates lithium in the cell center and the operating potential window is distorted more and more. During the charge periods (see Fig. 8c), the center anode potential can drop to the lower plateau and the critical lithium plating condition are fulfilled. The lithium plating irreversibly captures active lithium, which cannot intercalate into the graphite anymore; hence, the anode potential shifts to a higher value (shift from dotted to dashed line in Fig 8c (green)). This lowers the actual local SOC of the anode center area; however, it is still higher than that of the anode outer area. Therefore, the lithium plating and the lateral lithium-ion flow are acting in a contrary manner. When the lifetime test further progresses, the plated lithium in the center drastically increases in resistance; it is not taking part in charge or discharge as before. The amount of new lithium plating is reduced. The presented pumping effect agrees well with the pumping mechanism presented by Spingler et al. [9], who observed inhomogeneous lithium plating in the center of cylindrical LFP/C cells together with a non-uniform charge distribution. The deviations in local SOC in combination with the ionic coupling of the inner and outer electrode areas result in a stronger degradation than expected for homogeneous conditions.

In parallel to the lithium plating effect, the abovementioned higher DOD in the warmer center of the pouch cell causes a stronger degradation of the cathode (cf. Fig. 6b and Fig. 6c), leading to a misbalancing of the anode and cathode [38]. The cathode capacity of the cell tested at 30 °C is ~2.75 mAh·cm^{-2} homogeneous on the whole layer, while for the cell tested at 0 °C, the outer cathodes have a capacity of ~2.71 mAh·cm^{-2} and the center electrodes have a capacity of 2.47 mAh·cm^{-2}. However, Sieg et al. [14] observed a similar lithium plating in the cell center without the degradation of the respective cathode areas in terms of capacity. The results of the three-electrode cells in lateral resolution and the ICP-OES lithium content measurement listed in Table 1 verify the lateral lithium flow. Nevertheless, the in-situ detection of the flow of lithium is not realizable by standard measurements; hence, a simulative verification of the lithium flow would be helpful.

4. Conclusion

In this work, large-format lithium-ion cells are cycled at two constant temperatures of 0 °C and 30 °C, with high discharge current applied. The degradation in terms of capacity fading and resistance increase amplifies for the cells in the low temperature cycle. This stronger fading is found to be caused by inhomogeneous lithium plating in the lateral center of the cell and throughout all layers. Since lithium plating occurs preferentially at lower temperatures and high charge currents, the test is designed to prevent the cells from plating. Tests using three-electrode cells do not show anode potentials below 0 V vs. Li/Li$^+$. Lithium plating, therefore, should not occur with the applied current profile. In the absence of lithium plating, the cells cycled at 30 °C should show stronger degradation on account of accelerated SEI formation and electrolyte consumption. Nevertheless, strong local lithium plating occurred at 0 °C cycle test; it is verified by SEM, ICP-OES, DV analysis, and three-electrode cell measurements.

We found that temperature gradients inside the cell, which build up as a result of the high discharge current and local current density gradient, cannot be solely responsible for the lithium plating in the center of the cell. The essential points enabling the inhomogeneous cell aging and lithium plating are the generation of electrode potential gradients and the ionic coupling. The transport of lithium to the cell center distorts the electrode balancing, leading to local violation of the critical lithium plating condition. In addition, higher SOCs and DODs in the center of the cell lead to accelerated degradation of the cathode.

Our study shows that for a long lifetime of large-format lithium-ion cells, it is extremely important to suppress the formation of gradients. Possible solutions for this challenge can be the extension of rest periods in order to enable the relaxation of the gradient. Also, alternative cooling concepts e.g. tab cooling, which reduce thermal gradients inside the cell, might help avoid potential gradients. Nevertheless, it is important to note that this study refers to borderline conditions where temperature is low and currents are elevated, and one has to be aware that these conditions cause stronger aging effects, which may not occur in later battery applications.

Fig. A1. Edge anode layer without the elliptical-like lithium plating bump of the cell tested at 0 °C. This indicates the good cooling of the outer electrode layers due to the contact to the aluminum plates. However, solely layer 1 and 33 show this behavior, pointing out the difficulty of measuring the temperature gradient inside the lithium-ion cell from the outside.

Credit author statement

Mathias Storch: Conceptualization, Methodology, Investigation, Resources, Writing - Original Draft, Writing - Review & Editing, Visualization

Johannes Fath: Conceptualization, Methodology, Investigation, Writing - Review & Editing

Johannes Sieg: Conceptualization, Methodology, Investigation, Writing - Review & Editing, Visualization

Dragoljub Vrankovic: Conceptualization, Methodology, Writing - Review & Editing, Visualization

Carsten Krupp: Conceptualization, Methodology, Writing - Review & Editing,

Bernd Spier: Conceptualization, Writing - Review & Editing, Supervision

Ralf Riedel: Conceptualization, Writing - Review & Editing, Supervision

Declaration of Competing Interest

The authors declare that they have no known competing financial interests or personal relationships that could have appeared to influence the work reported in this paper.

Acknowledgements

The authors acknowledge the financial support of Daimler AG, Germany and Deutsche Accumotive GmbH & Co. KG, Germany. We would like to express our gratitude to BatterieIngenieure GmbH, Aachen

for performing the cycle test. We would also like to thank our colleagues from Daimler AG for the support during analysis and for sharing their knowledge with us. We thank Alexander Fill and Tim Herdt for proof-reading the article.

Appendix

Fig. A1

References

[1] T. Waldmann, M. Wilka, M. Kasper, M. Fleischhammer, M. Wohlfahrt-Mehrens, Temperature dependent ageing mechanisms in Lithium-ion batteries – A Post-Mortem study, J. Power Sources 262 (2014) 129–135, https://doi.org/10.1016/j.jpowsour.2014.03.112.

[2] J.C. Burns, D.A. Stevens, J.R. Dahn, In-Situ Detection of Lithium Plating Using High Precision Coulometry, J. Electrochem. Soc. 162 (2015) A959–A964, https://doi.org/10.1149/2.0621506jes.

[3] N. Ghanbari, T. Waldmann, M. Kasper, P. Axmann, M. Wohlfahrt-Mehrens, Inhomogeneous Degradation of Graphite Anodes in Li-Ion Cells: a Postmortem Study Using Glow Discharge Optical Emission Spectroscopy (GD-OES), The J. Phys. Chem. C 120 (2016) 22225–22234, https://doi.org/10.1021/acs.jpcc.6b07117.

[4] M. Ecker, P. Shafiei Sabet, D.U. Sauer, Influence of operational condition on lithium plating for commercial lithium-ion batteries – Electrochemical experiments and post-mortem-analysis, Appl. Energy 206 (2017) 934–946, https://doi.org/10.1016/j.apenergy.2017.08.034.

[5] A.S. Mussa, A. Liivat, F. Marzano, M. Klett, B. Philippe, C. Tengstedt, G. Lindbergh, K. Edström, R.W. Lindström, P. Svens, Fast-charging effects on ageing for energy-optimized automotive LiNi1/3Mn1/3Co1/3O2/graphite prismatic lithium-ion cells, J. Power Sources 422 (2019) 175–184, https://doi.org/10.1016/j.jpowsour.2019.02.095.

[6] J. Cannarella, C.B. Arnold, The Effects of Defects on Localized Plating in Lithium-Ion Batteries, J. Electrochem. Soc. 162 (2015) A1365–A1373, https://doi.org/10.1149/2.1051507jes.

[7] D. Burow, K. Sergeeva, S. Calles, K. Schorb, A. Börger, C. Roth, P. Heitjans, Inhomogeneous degradation of graphite anodes in automotive lithium ion batteries under low-temperature pulse cycling conditions, J. Power Sources 307 (2016) 806–814, https://doi.org/10.1016/j.jpowsour.2016.01.033.

[8] B.P. Matadi, S. Geniès, A. Delaille, T. Waldmann, M. Kasper, M. Wohlfahrt-Mehrens, F. Aguesse, E. Bekaert, I. Jiménez-Gordon, L. Daniel, X. Fleury, M. Bardet, J.-F. Martin, Y. Bultel, Effects of Biphenyl Polymerization on Lithium Deposition in Commercial Graphite/NMC Lithium-Ion Pouch-Cells during Calendar Aging at High Temperature, J. Electrochem. Soc. 164 (2017) A1089–A1097, https://doi.org/10.1149/2.0631706jes.

[9] F.B. Spingler, M. Naumann, A. Jossen, Capacity Recovery Effect in Commercial LiFePO4 /Graphite Cells, J. Electrochem. Soc. 167 (2020) 40526, https://doi.org/10.1149/1945-7111/ab7900.

[10] M. Petzl, M.A. Danzer, Nondestructive detection, characterization, and quantification of lithium plating in commercial lithium-ion batteries, J. Power Sources 254 (2014) 80–87, https://doi.org/10.1016/j.jpowsour.2013.12.060.

[11] A. Matasso, D. Wong, D. Wetz, F. Liu, Effects of High-Rate Cycling on the Bulk Internal Pressure Rise and Capacity Degradation of Commercial LiCoO 2 Cells, J. Electrochem. Soc. 162 (2015) A885–A891, https://doi.org/10.1149/2.0461506jes.

[12] T. Waldmann, M. Kasper, M. Wohlfahrt-Mehrens, Optimization of Charging Strategy by Prevention of Lithium Deposition on Anodes in high-energy Lithium-ion Batteries – Electrochemical Experiments, Electrochim. Acta 178 (2015) 525–532, https://doi.org/10.1016/j.electacta.2015.08.056.

[13] V. Müller, R.-G. Scurtu, M. Memm, M.A. Danzer, M. Wohlfahrt-Mehrens, Study of the influence of mechanical pressure on the performance and aging of Lithium-ion battery cells, J. Power Sources 440 (2019), 227148, https://doi.org/10.1016/j.jpowsour.2019.227148.

[14] J. Sieg, M. Storch, J.P. Fath, A. Nuhic, J. Bandlow, B. Spier, D.U. Sauer, Local degradation and differential voltage analysis of aged lithium-ion pouch cells, J. Energy Storage 30 (2020), 101582, https://doi.org/10.1016/j.est.2020.101582.

[15] M. Storch, S.L. Hahn, J. Stadler, R. Swaminathan, D. Vrankovic, C. Krupp, R. Riedel, Post-mortem analysis of calendar aged large-format lithium-ion cells: investigation of the solid electrolyte interphase, J. Power Sources 443 (2019), 227243, https://doi.org/10.1016/j.jpowsour.2019.227243.

[16] N. Legrand, B. Knosp, P. Desprez, F. Lapicque, S. Raël, Physical characterization of the charging process of a Li-ion battery and prediction of Li plating by electrochemical modelling, J. Power Sources 245 (2014) 208–216, https://doi.org/10.1016/j.jpowsour.2013.06.130.

[17] J. Vetter, P. Novák, M.R. Wagner, C. Veit, K.-C. Möller, J.O. Besenhard, M. Winter, M. Wohlfahrt-Mehrens, C. Vogler, A. Hammouche, Ageing mechanisms in lithium-ion batteries, J. Power Sources 147 (2005) 269–281, https://doi.org/10.1016/j.jpowsour.2005.01.006.

[18] J. Sieg, J. Bandlow, T. Mitsch, D. Dragicevic, T. Materna, B. Spier, H. Witzenhausen, M. Ecker, D.U. Sauer, Fast charging of an electric vehicle lithium-ion battery at the limit of the lithium deposition process, J. Power Sources 427 (2019) 260–270, https://doi.org/10.1016/j.jpowsour.2019.04.047.

[19] J.P. Fath, D. Dragicevic, L. Bittel, A. Nuhic, J. Sieg, S. Hahn, L. Alsheimer, B. Spier, T. Wetzel, Quantification of aging mechanisms and inhomogeneity in cycled lithium-ion cells by differential voltage analysis, J. Energy Storage 25 (2019), 100813, https://doi.org/10.1016/j.est.2019.100813.

[20] I. Bloom, J. Christophersen, K. Gering, Differential voltage analyses of high-power lithium-ion cells, J. Power Sources 139 (2005) 304–313, https://doi.org/10.1016/j.jpowsour.2004.07.022.

[21] M. Lewerenz, D.U. Sauer, Evaluation of cyclic aging tests of prismatic automotive LiNiMnCoO2-Graphite cells considering influence of homogeneity and anode overhang, J. Energy Storage 18 (2018) 421–434, https://doi.org/10.1016/j.est.2018.06.003.

[22] M. Lewerenz, G. Fuchs, L. Becker, D.U. Sauer, Irreversible calendar aging and quantification of the reversible capacity loss caused by anode overhang, J. Energy Storage 18 (2018) 149–159, https://doi.org/10.1016/j.est.2018.04.029.

[23] M. Lewerenz, P. Dechent, D.U. Sauer, Investigation of capacity recovery during rest period at different states-of-charge after cycle life test for prismatic Li(Ni1/3Mn1/3Co1/3)O2-graphite cells, J. Energy Storage 21 (2019) 680–690, https://doi.org/10.1016/j.est.2019.01.004.

[24] H.-G. Schweiger, O. Obeidi, O. Komesker, A. Raschke, M. Schiemann, C. Zehner, M. Gehnen, M. Keller, P. Birke, Comparison of several methods for determining the internal resistance of lithium ion cells, Sensors (Basel) 10 (2010) 5604–5625, https://doi.org/10.3390/s100605604.

[25] A. Fill, K.P. Birke, Impacts of cell topology, parameter distributions and current profile on the usable power and energy of lithium-ion batteries, in: International Conference on Smart Energy Systems and Technologies (SEST), 2019, pp. 1–6, https://doi.org/10.1109/SEST.2019.8849092.

[26] A. Fill, T. Mader, T. Schmidt, R. Llorente, K.P. Birke, Measuring Test Bench with Adjustable Thermal Connection of Cells to Their Neighbors and a New Model Approach for Parallel-Connected Cells, Batteries 6 (2020) 2, https://doi.org/10.3390/batteries6010002.

[27] M. Broussely, S. Herreyre, P. Biensan, P. Kasztejna, K. Nechev, R. Staniewicz, Aging mechanism in Li ion cells and calendar life predictions, J. Power Sources 97-98 (2001) 13–21, https://doi.org/10.1016/S0378-7753(01)00722-4.

[28] T. Waldmann, N. Ghanbari, M. Kasper, M. Wohlfahrt-Mehrens, Correlations between Electrochemical Data and Results from Post-Mortem Analysis of Aged Lithium-Ion Batteries, J. Electrochem. Soc. 162 (2015) A1500–A1505, https://doi.org/10.1149/2.0411508jes.

[29] D. Billaud, F. Henry, Structural studies of the stage III lithium–graphite intercalation compound, Solid State Commun. 124 (2002) 299–304, https://doi.org/10.1016/S0038-1098(02)00469-6.

[30] J.P. Fath, L. Alsheimer, M. Storch, J. Stadler, J. Bandlow, S. Hahn, R. Riedel, T. Wetzel, The influence of the anode overhang effect on the capacity of lithium-ion cells – a 0D-modeling approach, J. Energy Storage 29 (2020), 101344, https://doi.org/10.1016/j.est.2020.101344.

[31] M. Lewerenz, A. Marongiu, A. Warnecke, D.U. Sauer, Differential voltage analysis as a tool for analyzing inhomogeneous aging: a case study for LiFePO 4 |Graphite cylindrical cells, J. Power Sources 368 (2017) 57–67, https://doi.org/10.1016/j.jpowsour.2017.09.059.

[32] X. Zhang, X. Chang, Y. Shen, Y. Xiang, Electrochemical-electrical-thermal modeling of a pouch-type lithium ion battery: an application to optimize temperature distribution, J. Energy Storage 11 (2017) 249–257, https://doi.org/10.1016/j.est.2017.03.008.

[33] S. Du, M. Jia, Y. Cheng, Y. Tang, H. Zhang, L. Ai, K. Zhang, Y. Lai, Study on the thermal behaviors of power lithium iron phosphate (LFP) aluminum-laminated battery with different tab configurations, Int. J. Thermal Sci. 89 (2015) 327–336, https://doi.org/10.1016/j.ijthermalsci.2014.11.018.

[34] S. Kosch, A. Rheinfeld, S.V. Erhard, A. Jossen, An extended polarization model to study the influence of current collector geometry of large-format lithium-ion pouch cells, J. Power Sources 342 (2017) 666–676, https://doi.org/10.1016/j.jpowsour.2016.12.110.

[35] A. Fill, S. Koch, K.P. Birke, Analytical model of the current distribution of parallel-connected battery cells and strings, J. Energy Storage 23 (2019) 37–43, https://doi.org/10.1016/j.est.2019.02.031.

[36] B. Gyenes, D.A. Stevens, V.L. Chevrier, J.R. Dahn, Understanding Anomalous Behavior in Coulombic Efficiency Measurements on Li-Ion Batteries, J. Electrochem. Soc. 162 (2015) A278–A283, https://doi.org/10.1149/2.0191503jes.

[37] T. Hüfner, M. Oldenburger, B. Bedürftig, A. Gruhle, Lithium flow between active area and overhang of graphite anodes as a function of temperature and overhang geometry, J. Energy Storage 24 (2019), 100790, https://doi.org/10.1016/j.est.2019.100790.

[38] M. Börner, F. Horsthemke, F. Kollmer, S. Haseloff, A. Friesen, P. Niehoff, S. Nowak, M. Winter, F.M. Schappacher, Degradation effects on the surface of commercial LiNi 0.5 Co 0.2 Mn 0.3 O 2 electrodes, J. Power Sources 335 (2016) 45–55, https://doi.org/10.1016/j.jpowsour.2016.09.071.

Journal of Power Sources 400 (2018) 402–414

Contents lists available at ScienceDirect

Journal of Power Sources

journal homepage: www.elsevier.com/locate/jpowsour

Quantitative validation of calendar aging models for lithium-ion batteries

Severin Lukas Hahn[a,*], Mathias Storch[a], Ramanathan Swaminathan[a], Björn Obry[a], Jochen Bandlow[a], Kai Peter Birke[b]

[a] Daimler AG, Research & Development, Neue Strasse 95, 73230 Kirchheim u.T., Germany
[b] Chair for Electrical Energy Storage Systems, Institute for Photovoltaics, University of Stuttgart, Pfaffenwaldring 47, 70569 Stuttgart, Germany

EDITOR HIGHLIGHTS

- Extensive calendar aging study of automotive grade commercial pouch cells.
- Novel aging model considering an initial surface layer due to cell formation.
- Initial lithium loss due to formation is quantified by two matching methods.
- A quantitative validation technique splitting data into training and validation data.
- The derived model shows higher predictive capability than literature models.

GRAPHICAL ABSTRACT

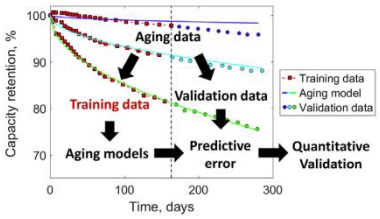

ARTICLE INFO

Keywords:
Lithium-ion battery
Calendar aging model
Lifetime prediction
Solid electrolyte interface
Loss of active lithium
Model validation

ABSTRACT

Calendar aging prediction is a key technique to develop durable and robust electric vehicles. Automotive grade pouch cells based on $LiNi_{1/3}Mn_{1/3}Co_{1/3}O_2$ and graphite are tested in an extensive accelerated calendar aging matrix and analyzed for capacity loss and evolved gas volume. This study derives an extended semi-empirical calendar aging model considering an initial solid electrolyte interface layer grown during the formation process. The extent of the thus lost active lithium is derived by open circuit voltage curve fitting as well as by inductive coupled plasma experiments. For this analysis the $LiNi_{1/3}Mn_{1/3}Co_{1/3}O_2$ first cycle inefficiency is considered. Additionally, a validation technique based on the split of aging data into training and validation data is introduced with which it is possible to quantify the predictive capability of aging models. Using this technique the developed calendar aging model of this study is compared with competing aging models in literature. The derived global aging model is quantitatively shown to exceed other models in terms of their predictive ability, especially when little data is provided to the model.

1. Introduction

Lithium-ion batteries have been widely employed in portable consumer electronics requiring only a few years of lifetime. Electric vehicles, however, are expected to retain a large part of the initial battery capacity for up to 200–300'000 km and 10–15 years operating in various climatic conditions. Despite being exhaustive it is possible to test the entire estimated energy throughput and the corresponding cyclic aging. Testing for calendar aging over lifetime, however, is infeasible. Thus, various calendar aging models [1–8] have been developed to predict battery lifetime. Their accuracy is highly important to the automotive and other industries due to quality assurance, warranty

* Corresponding author.
E-mail address: severin.hahn@daimler.com (S.L. Hahn).

https://doi.org/10.1016/j.jpowsour.2018.08.019
Received 14 June 2018; Received in revised form 23 July 2018; Accepted 7 August 2018
Available online 22 August 2018
0378-7753/

considerations and even regulatory requirements.

Cells degrade during storage because commonly used solvents such as ethylene carbonate are reduced at anode potentials below 0.8–1.2 V vs. Li/Li^+ which is inevitable when using graphite [9,10]. The solvent reduction products react with abundant Li^+ to form solid electrolyte interface (SEI) on the surface of anode particles [11,12]. These electrochemical side reactions consume both one lithium ion and a corresponding electron. Thus, the anode is delithiated while the cathode remains unaffected which is generally referred to as a purely *anodic side reaction* [12,13]. In fact, SEI growth takes place in absence of a cathode [14]. This anodic shift in relation to the cathode is equivalent to *loss of active lithium* [12,15]. In consequence the cycling window narrows which is the main cause for calendaric capacity loss in most lithium-ion batteries [3,12,13,16].

Observed capacity losses are passivated over time and strongly depend on temperature and charging state of the cell. The charging state may be defined by either cell voltage or empirically by state of charge (SOC). Several calendar aging models based on physical considerations have been presented in literature aiming to explain the observed behavior. Broussely et al. [1] assume a limiting electrical conductivity of the growing SEI attenuating further reduction which results in the well-known $t^{0.5}$ relationship for capacity loss where t is the aging time. However, inorganic SEI components such as LiF, Li_2CO_3 and Li_2O are known to be electrically insulating [17] indicating the model to be non-physical despite good results [1]. Further, the model assumes the immediate reaction upon electron transfer through the SEI. Consequently, (electro-)chemical kinetic effects such as an Arrhenius and exponential voltage dependency should not be observed. Still, corresponding temperature and voltage dependencies are found [7]. Ploehn et al. [2] then showed that a model considering limited solvent diffusion through the existing SEI with reduction on the anode surface yields the same $t^{0.5}$ relationship. Similar to Broussely et al. [1], an immediate reaction is assumed on the surface of the graphite denying a kinetic explanation for temperature and voltage dependence. It is important to realize that an Arrhenius dependency may be introduced assuming solid state diffusion of solvent molecules in SEI. The solid state diffusion coefficient D can be expressed as

$$D(T) = D_0 \cdot e^{\left(\frac{-E_a}{R \cdot T}\right)} \tag{1}$$

where D_0 is a frequency factor, E_a is the activation energy, R is the gas constant and T is the temperature. This expands the model of Ploehn et al. [2].

$$Q_{loss}(t) \propto \sqrt{D_0 \cdot t} \tag{2}$$

where Q_{loss} is the lithium lost due to solvent reduction and t is the aging time to a result

$$Q_{loss}(t, T) \propto \sqrt{D_0 \cdot e^{\left(\frac{-E_a}{R \cdot T}\right)} \cdot t} \propto e^{\left(\frac{-E_a}{2 \cdot R \cdot T}\right)} \cdot \sqrt{t} \propto e^{\left(\frac{C}{T}\right)} \cdot \sqrt{t} \tag{3}$$

where C is constant. A voltage dependency is not predicted. This model, however, is also disputed as the SEI has been shown to consist of a compact inner inorganic layer and a porous organic outer layer [2,18]. It is argued that solvent may not diffuse through this dense inner SEI layer composed of LiF, Li_2CO_3 and Li_2O [3,17]. Instead, Li et al. [3] suggest that electrons pass the inner SEI by tunneling. This results in a temporal behavior according to

$$Q_{loss}(t, x) = C_1(x) \cdot \ln(1 + C_2(x) \cdot t) \tag{4}$$

where C_1 and C_2 are factors that depend on the degree of lithiation x of the graphite anode [3]. While these parameters might be temperature dependent a clear exponential temperature dependency is not shown. Furthermore, Tang et al. [19] reject a tunneling effect based on their experimental results. In summary, theoretical considerations reveal strong modeling approaches but cannot encompass all aspects yet.

Due to the lack of a consistent theoretical model, many studies in literature successfully employ semi-empirical models to predict calendar aging [4–7,20–22]. These are often based on the discussed theoretical models. Even by the theorists [1,3] themselves the models are extended, adjusted or altered in order to describe the observed aging behavior lacking a clear physical explanation. Variable parameters are defined which are then fitted to the experimental data. In the following, fit parameters are denominated *pi* with the index i numerating parameters of a respective model. Ecker et al. [7] use the following exemplary aging model for the capacity retention $Q(t)/Q_0$ with both an Arrhenius term and a term similar to the Tafel equation

$$\frac{Q(t)}{Q_0} = 1 - \underbrace{p_1 \cdot e^{\frac{-p_2}{T}}}_{\substack{\text{Arrhenius} \\ \text{dependency}}} \cdot \underbrace{p_3^{p_4 \cdot (U_{cell} - U_0)}}_{\substack{\text{Voltage} \\ \text{dependency}}} \cdot \underbrace{t^{0.5}}_{\substack{\text{Time} \\ \text{dependency}}} \tag{5}$$

where T, U_{cell} and U_0 are the storage temperature, the cell voltage and a chosen equilibrium potential, respectively. Over the last years, researchers fitted different time dependencies than $p_1 \cdot t^{0.5}$ such as $p_1 \cdot t^{0.75}$ [5], the aforementioned $p_1 \cdot \ln(1 + p_2 \cdot t)$ [3], the superposition $p_1 \cdot t + p_2 \cdot t^{0.5}$ [5–7] or even fitted the time exponent itself with $p_1 \cdot t^{p_2}$ [4]. Also, different charging state dependencies such as the linear $p_3 \cdot U_{cell} + p_4$ [5], SOC^{p_3} [20,21] or $e^{p_3 \cdot SOC}$ [23] were investigated. These so-called *global* aging models like Eq. (5) may then be fitted in one step [22] to all aging conditions from an accelerated aging matrix. This is in contrast to models where parameters are fitted separately in a multi-step procedure or where only single aging conditions are fitted. When fit parameters p_i are thus determined by a global fit they may predict capacity loss due to storage for any timeframe at any charging state and temperature [7]. This paper will derive a novel semi-empirical global aging model based on theoretical considerations about the initial SEI layer grown during formation. For this, the extent of the initial SEI is investigated experimentally and used as a parameter of the aging model.

As the preceding discussion of various aging models suggests, it would be highly desirable to quantitatively rank lifetime prediction models in terms of their accuracy. In literature such aging models have been compared by their coefficient of determination R^2 to accelerated aging data [4–8,20,22]. This method, however, may critically favor overfitting models with many degrees of freedom. Overfitting describes the behavior of models which leads to a good fit to the given data but poor results compared with validation data. In fact, the predictive capability of aging models is not at all considered by R^2 analysis. Also, time dependencies are sometimes validated by R^2 analysis for select single curves [5,24] and not entire aging sets [7]. Only rarely, separate aging conditions are experimentally produced to validate the predictive capability, but only at select aging points [23]. Quantitative validation techniques for the predictive properties of lithium-ion battery aging models using the entire data set have not been discussed in literature to the best of our knowledge.

In response this paper aims to I) present a novel extended global aging model incorporating measured initial SEI growth due to formation, II) introduce a quantitative validation technique inspired by machine learning for aging models and III) compare the predictive capability of the extended model to existing models in literature. The comparison of these models is performed with data from an extensive calendar aging matrix of 54 automotive grade high-energy pouch cells which is discussed in detail. The derived aging model is parametrized with an experimentally determined initial lithium loss due to formation. After choosing common temperature and voltage dependencies for all considered aging models they are characterized for overfitting behavior and quantitatively ranked in terms of their predictive capability.

2. Experimental

The cell used for the aging experiment was the HEA50 pouch cell by Litec Battery GmbH with a nominal capacity of 50.8 Ah. These cells

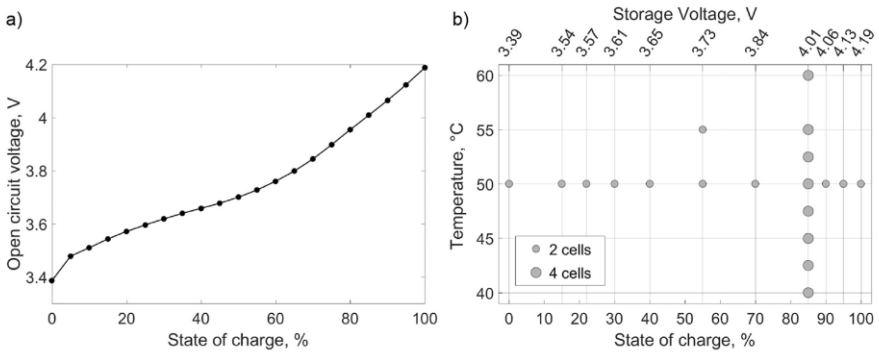

Fig. 1. a) OCV of the investigated cell at begin of life. b) Design of experiment matrix for accelerated calendar aging tests with corresponding number of cells investigated at specified storage conditions.

were commercially fitted in the electric vehicle Smart Electric Drive by Daimler. The cathode active material is $Li_yNi_{1/3}Mn_{1/3}Co_{1/3}O_2$ (NMC111) and the anode consists of graphite (Li_xC_6). The cell consists of 34 double coated anodes and 33 double coated cathodes for a total active area defined by the cathode surface of 26′785 cm^2. More cell parameters used in calculations are reported in the Supporting Information. The operating window of the cell is specified between U_{min} of 3.0 V and U_{max} of 4.2 V. According to nominal charge protocol the cell reaches a cell voltage of 4.19 V after relaxation which is defined as 100% SOC. After a nominal discharge protocol of 50.8 Ah the cell reaches 3.39 V after relaxation which is defined as 0% SOC. An open circuit voltage (OCV) curve by the manufacturer is presented in Fig. 1a).

2.1. Calendar aging matrix

The calendar aging was performed at different aging conditions ranging from 40 °C to 60 °C in temperature and from 0% to 100% in SOC for an effective storage time of about 280 days. The design of experiment matrix is shown in Fig. 1b). Storage cell voltages are also reported based on the OCV in Fig. 1a). Different temperatures at 85% SOC were tested with 4 cells each whereas different SOC were tested at 50 °C with 2 cells each. The different temperatures were prioritized to investigate the onset of differing aging mechanisms at high temperature statistically. Additionally, two cells were aged at 55 °C and 55% SOC. These were added to screen for a SOC dependency of the onset of other aging mechanisms. During aging cells were set in climate chambers (monitored to be $\pm$ 1 K of the target temperature) and mounted in a cell holder attached to the cell seam which meant possible cell expansion was unconstrained. Cells were held in open circuit condition during aging, but recharged daily to their storage voltage by applying a constant current (CC phase) of 3 A with a subsequent constant voltage (CV) phase (cut-off current was 0.2 A). In the first 75 days of calendar aging, periodical check-ups were performed every 5 days. Subsequently, check-ups were performed every 14 days.

2.2. Check-ups

The check-ups were performed in a climate chamber at 25 °C with the cells in the cell holder mount. Nominal charging was defined as CC-CV with 1C (1C = 50 A) and C/20 cutoff whereas nominal discharging was defined as a CC discharge with 1C. Before check-ups, the cell was charged or discharged nominally to 3.7 V followed by a pause of 3 h to achieve a homogeneous cell temperature. The cell was then nominally charged to 4.2 V. In order to equilibrate the cell, it was nominally discharged to 3.0 V and nominally recharged to 4.2 V three times with a pause of 5 min in between and followed by a 1 h pause for relaxation. Then, the 1C discharge capacity down to 3.0 V was measured by nominal discharge followed by another pause of 1 h after which the cell was nominally recharged to 4.2 V. After 5 min of pause, three resistance measurements at 80%, 50% and 30% SOC were performed. This was achieved by nominally discharging to respective SOC followed by a 1 h pause. A discharge pulse of 200 A was maintained for 30 s followed by a 5 min pause. Resistance measurements are not discussed in this publication due to its limited scope. Then, the cell is nominally discharged and recharged again to 3.0 and 4.2 V, respectively. After another 1 h of relaxation, a capacity measurement is performed using a C/10 CC discharge down to 3.0 V followed by 1 h of relaxation. The cell was then recharged to 4.2 V by CC-CV with C/10 with a C/20 cutoff. C/10 charging was inserted for charging characteristic analysis which will not be discussed here. The storage SOC was initially set by a nominal discharge to 3.0 V and a nominal charge to the desired storage voltage, cf. Fig. 1a) and b). The storage SOC was set before exposing the cells to the higher storage temperature. Results of multiple cells were averaged before analysis and model fitting in order to equalize the influence of aging conditions on fitting. Similarly, capacity retention is calculated for each cell separately before averaging.

2.3. Pouch, half-cell and full-cell measurements

A pouch cell that was not exposed to calendar aging, which will be referred to as the BOL (begin of life) cell, was nominally charged to 4.2 V. Then, discharge and charge curves were recorded for C/10 and C/24 each at 25 °C using a BaSyTec cycling system (BaSyTec GmbH). The cell was then nominally discharged to 3.0 V and cut open with a ceramic knife in an argon filled glovebox (O_2 < 0.1 ppm, H_20 < 0.1 ppm). The welded current collector tabs were carefully cut off. Central layers were extracted and washed in two repeated baths in dimethyl carbonate (DMC, Sigma Aldrich) for 3 min to remove residual electrolyte from the electrodes. Subsequently, the electrodes were dried of excess DMC at room temperature. The coating on one side of the double-coated electrodes was soaked with N-Methyl-2-pyrrolidone (NMP, Sigma Aldrich) and carefully removed and polished of residue with tissue paper before cutting Ø18 mm electrode coins from a central part of layers. This is a common procedure to extract coin electrodes [25,26]. Additionally, electrode coins were similarly extracted from pristine cathode layers which have neither been in contact with electrolyte nor been delithiated. These layers were not bathed in DMC prior to removal of one side of the double coated electrode with NMP. Half-cells and full-cells were assembled in ECC PAT Core cells (EL-CELL GmbH) with a Li-reference ring for the electrode potential measurement. BOL full-cells were built with the extracted cathodes and anodes

as the positive and negative electrodes, respectively. BOL half-cells with the positive electrode being either the extracted anode or cathode were built versus a 0.38 mm thick Li metal slab as working negative electrode (Sigma Aldrich). Pristine cathode half-cells were built similarly with the pristine cathodes as positive electrodes. All half-cells and full-cells were soaked with 158 µL 1 M LiPF6 in EC/DMC = 50/50 (v/v) electrolyte (LP30, BASF).

For the testing of all half- and full-cells the 1C rate was defined as 6.35 mA and experiments were conducted in a climate chamber at 25 °C using a BaSyTec cycling system (BaSyTec GmbH). BOL full-cells underwent a formation protocol consisting of 3x C/10, 2x C/5, 1x C/24 constant current charge-discharge cycles between voltage limits. Similarly, anode and cathode half-cells were formed with 3x C/10, 2x C/5, 2x C/2, 2x C, 1x C/24 constant current charge-discharge cycles. Cathode half-cells were cycled between 3.3 V and 4.3 V vs. Li/Li^+, anodes between 0.03 V and 1.0 V vs. Li/Li^+ and full-cells between 3.0 V and 4.2 V. Then, C/24 quasi OCV discharge and charge curves were recorded between the voltage limits. Two pristine cathodes were charged and discharged with C/24, but without formation cycles. All other 3-electrode cell experiments were performed with at least three cells for statistical significance.

2.4. ICP-OES measurements

For the inductive coupled plasma optical emission spectroscopy (ICP-OES) experiments double-coated BOL anode samples were cut from the DMC washed electrodes. Microwave digestion using aqua regia was carried out with three samples. The resulting solutions were analyzed separately twice via (ICP-OES) using an OPTIMA 4300 DV device (Perkin Elmer). Reported values are the average of these three experiments.

2.5. Volume analysis

Gas evolution at the end of calendar aging was determined by the Archimedes principle in a measurement setup described in detail by Aiken et al. [27]. Nominally discharged (to 3 V) cells were hung into deionized water with only the cell taps reaching above the water surface. The force holding up the cell was measured with a FH10 digital force gauge (Sauter GmbH). The volume of evolved gas during the calendar aging is determined by subtracting the volume of the BOL cell. Before averaging cell results, at least four force measurements were repeated and averaged for each cell.

3. Model development

In order to parametrize the model directly after introduction and introduce the validation technique, experimental results are preempted in this section.

3.1. Extended calendar aging model

Both theoretical models by Ploehn et al. [2] and Broussely et al. [1] intrinsically assume an immediate reaction upon the transfer of reaction components solvent molecules and electrons, respectively - which is limited by the SEI layer. It follows that with no passivation present, the corresponding SEI growth rate is large [28]. Interestingly, the early single-cell model fits by Broussely et al. [1] and Wright et al. [24] still allowed for an initial SEI at $t = 0$ (c.f. A.2). Some models employed in literature for commercial cells [4,5,7,21], however, are simply based on square root of time, $t^{0.5}$ as in Eq. (5). Asymptotically, their predicted capacity loss rate - $\partial Q_{loss}/\partial t$ - is infinite [18] at $t = 0$ as no SEI layer is assumed. In fact, this is true for any power law dependency used in literature [5,7,22] when $p_4 < 1$ in $Q_{loss} \propto t^{p_4}$ as

$$\lim_{t\to 0^+} \frac{\partial(Q_{loss} \propto t^{p_4})}{\partial t} = \infty \tag{6}$$

This is not in agreement with data for commercial cells.

We would like to point out before addressing the issue that for analysis in this regard, experiments of commercial cells in literature should be reviewed critically as recently anode overhang effects have been shown to cause steep initial losses and gains in capacity depending how cells were stored before $t = 0$ [29]. The overhang effect does not cause aging because it is reversible. As the present aging experiment was started well before publication by Lewerenz et al. [29] no countermeasure was taken. In fact, cells were stored for months at 75% SOC and room temperature before the aging experiment. The extent of this effect is discussed in Section 4.1.

It is proposed that the influence of an initial SEI growth during formation may be considered as an existing aging period upon which a second period is added. In this first period, i.e. during the formation process and consequent storage before use, capacity is lost. Theory suggests the lost capacity to be proportional to the grown SEI thickness as all reduced electrolyte species are assumed to react with abundant Li^+ [12]. The charge of the thus lost lithium directly equals the lost capacity [12,30] and will be abbreviated as lithium loss. Considering this initial SEI may be realized in a calendar aging model very similarly to the consideration of different temperature and SOC distributions superimposed over lifetime. A detailed discussion for a superimposed aging model of Eq. (5) and its calendaric commutativity is presented in Appendix A. Nothing similar was found in literature. Eq. (A.4) states that the degradation deg_2 during time Δt_2 after a preceding aging period with capacity loss deg_2 is

$$deg_2(\Delta t_2) = p_1 \cdot A(T_2, SOC_2) \cdot \left(\left(\frac{deg_1}{p_1 \cdot A(T_2, SOC_2)} \right)^{\frac{1}{p_4}} + \Delta t_2 \right)^{p_4} \tag{7}$$

where A is the combined Arrhenius and Tafel dependency of Eq. (5) for the temperature T_2 and SOC_2, respectively, which include the fit parameters p_2 and p_3. As the initial degradation equals the lithium lost during formation, $Liloss_{form.}$, the global extended aging model for the capacity retention Q/Q_0 follows as

$$\frac{Q(t, T, SOC)}{Q_0} = 1 - p_1 \cdot A(T, SOC) \cdot \left(\left(\frac{Liloss_{form.}}{p_1 \cdot A(T, SOC)} \right)^{\frac{1}{p_4}} + t \right)^{p_4} + Liloss_{form.} \tag{8}$$

when the capacity is reset to 100% at beginning of aging at $t = 0$ by adding $Liloss_{form.}$, the relative capacity equivalent to the lithium lost during formation. This effectively is a starting point shift on the existing t^{p_4} curve. Importantly, no additional fit parameter is added. Also, the only other unknown is the lithium lost during formation, a term proportional to the SEI thickness at $t = 0$ which may be determined experimentally. This parametrization will be discussed in the following. It should be pointed out that the above result can also be derived from the differential equation results of Broussely et al. [1] and Ploehn et al. [2] which is shown for the former in Appendix B. As a consequence of this theoretical consideration moderate aging conditions appear almost linear, while strong aging conditions show a more significant passivating behavior in the same objective timeframe.

Several authors have determined the lithium loss due to SEI formation by fitting combined half-cell potential curves to corresponding quasi open circuit voltage (OCV), differential voltage analysis (DVA) and incremental capacity analysis (ICA) curves [26,30,31]. In order to obtain the lithium loss in the present work an adapted technique by Schindler and Danzer [26] is applied which is only shortly described. Open circuit half-cell potentials (OCP) of anode and cathode half-cells are fitted to measured full cell cycling windows. Best fits to OCV curves are found when considering the deviation of the OCV and DVA curve as well as the error of the peak position in the DVA curve. The following

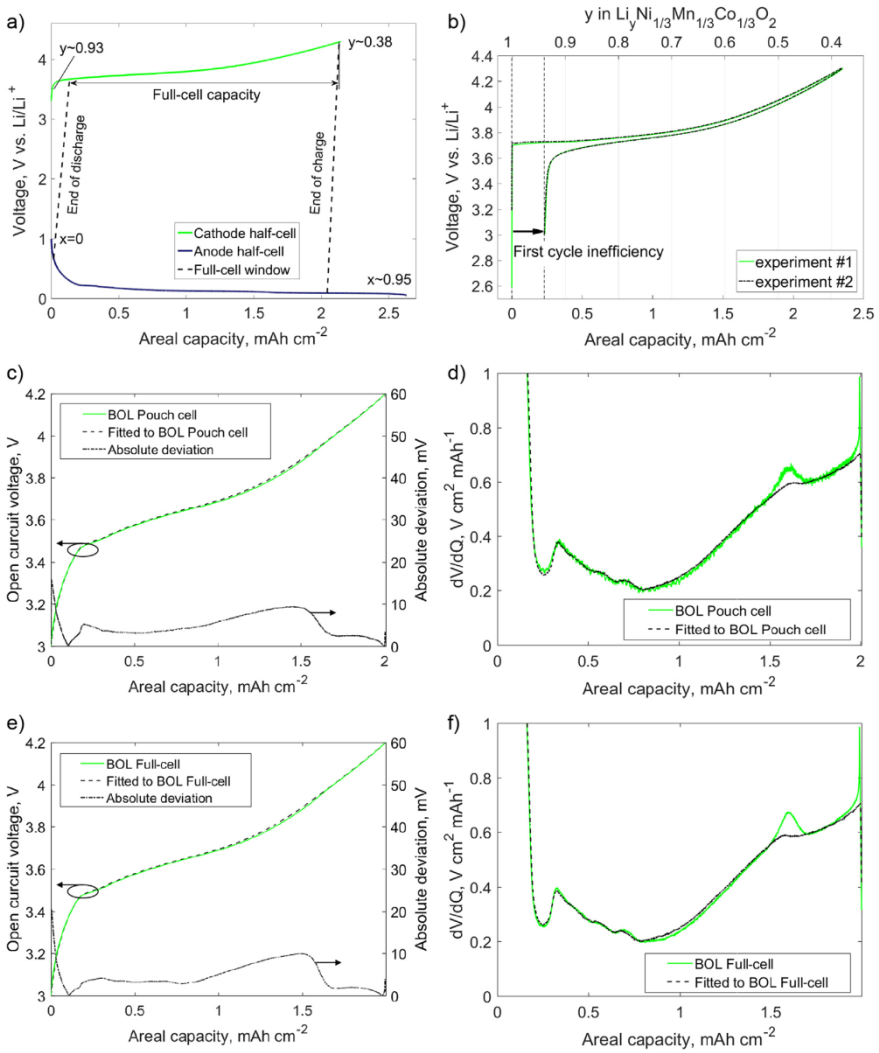

Fig. 2. a) Half-cell potential curves for Li_xC_6 and $Li_yNi_{1/3}Mn_{1/3}Co_{1/3}O_2$ electrodes of the BOL cell after formation with corresponding assumed lithiation states and a fitted full-cell cycling window. b) First cycle inefficiency of two pristine $Li_yNi_{1/3}Mn_{1/3}Co_{1/3}O_2$ electrode half-cells where y is the lithiation degree. c) Pouch cell OCV curve exemplary fitting result with the absolute deviation of the fit. d) Corresponding fitted DVA curve. e) An exemplary fitted full-cell OCV curve and f) corresponding DVA curve.

fitness function is equivalently used as Eq. (3.3) in Ref. [26]. The cycling window of full-cells and pouch cells is found by minimizing the fitness function

$$\boldsymbol{S} = \sum_{j}^{N} \left(\left(\left. \frac{\Delta U_j}{\Delta Q_j} \right|_{meas}^{i} - \left. \frac{\Delta U_j}{\Delta Q_j} \right|_{sim}^{i} \right)^2 + 4(U_j|_{meas}^{i} - U_j|_{sim}^{i})^2 \right) + 1.5 \cdot 10^5 ((\Delta Peak_1^i)^2 + (\Delta Peak_2^i)^2) \quad (9)$$

where $\Delta Peak_1^i$ and $\Delta Peak_2^i$ describe the distance of the first and second prominent peaks of the graphite DVA, respectively, between the simulated cell and i where $i \in \{\text{full-cell, pouch cell}\}$. N is the discretization of the OCV and DVA curves which was chosen as 10'000. The first and second peak in DVA can be assigned to the of stage IV→III transition and the stage II→I transition of graphite, respectively, as defined in Ref. [32]. The additional consideration of the mismatched peak distance improved the quality of the automated fit. The fitting calculations use one anode, one cathode and one full-cell (or pouch cell) curve. The standard deviation and mean of the fitting calculations reported were calculated from all possible permutations of measured cells in order to improve statistical significance.

Fig. 2a) shows one resulting electrode state diagram [30] with two

Table 1
Summary of measurement and fitting results for the initial lithium lost due to formation for model parametrization with calculated standard deviations.

Measured and fitted quantities	Full-cell fitting	Pouch cell fitting	ICP-OES measurement
NMC111 first cycle inefficiency measured	233.9 ± 2.9 µAh cm^{-2}	233.9 ± 2.9 µAh cm^{-2}	–
Electrode shift fitting of BOL cell	96.1 ± 19.8 µAh cm^{-2}	93.9 ± 14.2 µAh cm^{-2}	–
Number of fitted permutations	45	15	–
Lithium in discharged double coated BOL anode foil	–	–	5553.3 ± 5.8 mg kg^{-1}
Derived cumulative lithium lost due to formation	329.9 ± 19.8 µAh cm^{-2}	327.7 ± 14.2 µAh cm^{-2}	318.3 ± 0.3 µAh cm^{-2}
In terms of the BOL cell capacity	16.5 ± 1.0%	16.4 ± 0.7%	15.92 ± 0.02%

used half-cell potential curves from both the $Li_yNi_{1/3}Mn_{1/3}Co_{1/3}O_2$ cathode and the Li_xC_6 anode together with a fitted full cell window. Lithium loss causes the end of charge and end of discharge lines to be slanted [30]. Comparisons of simulated OCV curves to the respective measured full-cell and pouch cell are shown in Fig. 2c) and e). The corresponding DVA comparisons are presented in Fig. 2d) and f). Both the OCV and DVA curves are in good agreement. The absolute deviations of the OCV curves also shown in Fig. 2c) and e) are comparable to those achieved in literature [26].

The method [26] of fitting two half-cell OCP curves shifted relative to each other to simulate OCV curves may only determine the lithium loss of the anode relative to the measured cathode, c. f. Fig. 2a). Thus, equaling the fitted loss to $Liloss_{form.}$ is only valid when the discharged cathode is equal to the pristine, usually fully lithiated ($y = 1$), cathode. However, in contrast to Li_zFePO_4 as used in literature [26,31] using $Li_yNi_{1/3}Mn_{1/3}Co_{1/3}O_2$ leads to the cathode half-cell curve not returning to its initial lithiation state $y = 1$ upon discharge due to its well-known first cycle inefficiency [33]. Thus, half-cells with pristine cathodes were built and their first cycle inefficiency was determined in Fig. 2b). After the first delithiation, the cathode may only be discharged by CC to a lithiation state $y = 0.93$. This is in line with what was already investigated in detail by Seidlmayer et al. [33]. When observing a shift of the anode relative to a cathode which already lost lithium as it may not be fully relithiated, lithium equaling to the missing cathode lithiation $\Delta y = 0.07$ or 233.9 µAh cm^{-2} must have also been lost to the SEI during formation Consequently, the entire $Liloss_{form.}$ is the sum of the first cycle inefficiency of NMC111 and the fitted lithium loss between measured BOL anodes and cathodes as reported in Table 1. When fitting full-cell curves $Liloss_{form.}$ equals 16.5% or 329.9 µAh cm^{-2} of capacity with respect to the BOL full-cell capacity on average. Similarly, 16.4% or 327.7 µAh cm^{-2} is found for the BOL pouch cell.

This is comparable to values reported by Schindler and Danzer [26] and Dubarry et al. [31] with 26.5% and about 13.4% for $Liloss_{form.}$ in their respective $LiFePO_4$/graphite system. Similarly, Bloom et al. fitted 6% for a $LiNi_{0.85}Co_{0.05}Al_{015}.O_2$/graphite cell [30]. Obviously, the SEI growth heavily depends on the graphite BET (Brunauer-Emmet-Teller) surface area [34], graphite morphology [9], formation cycles [11] and electrolyte composition [10]. Hence, differing values are expected.

Lithium lost to the SEI remains in the anode when discharging a cell. The Li weight content in the BOL double coated anode from a cell discharged to 3.0 V was found to be 5555.3 mg kg^{-1} by ICP-OES as shown in Table 1. Based on cell parameters given in the Supplementary Information this corresponds to a $Liloss_{form.}$ of 318.3 µAh cm^{-2} or 15.92% of the initial capacity which is in very good agreement with the results of the fitting. As the ICP-OES results display lower standard deviations in Table 1 the extended aging model is considered in this work with the experimental value of 15.92% for $Liloss_{form.}$.

3.2. Quantitative validation technique

Machine learning employs the variable division of datasets into training and validation data [35,36]. In order to evaluate the predictive capabilities of calendar aging models the so-called out-of-sample evaluation [36] of the aging data is performed. This simple method is used for evaluation of time series predictors [36]. We suggest that lithium-ion battery aging models are special case of this category. Fig. 3a) shows three select mean capacity retention curves from the aging experiment fitted with Eq. (5) as an example. Aging model fitting in this paper is always based on least squares fitting of mean values. Instead of fitting the entire aging curve, the measurement data may also be divided into training data for $t < t_{cutoff}$ and validation data for $t < t_{cutoff}$ as illustrated in Fig. 3b) [36]. Now, an aging model is only fitted by providing the training data as input. The resulting aging model is also shown in Fig. 3b). Similar to literature the error of the fit to the training data is evaluated here by a locally normalized root mean square error (RMSE) of all n measurement points of all aging points

$$RMSE_{Training} = \sqrt{\frac{1}{n}\sum_{i}^{n}\left(\frac{y_{i,Model} - y_{i,Training}}{y_{i,Training}}\right)^2} \quad (10)$$

where $y_{i,Training}$ and $y_{i,Model}$ are the measured and predicted capacity retention values of the i-th measurement point, respectively. The aging model may naturally extrapolate further in time where it will predict the further aging behavior of the cells. This prediction is then compared to the measured values of the prepared validation data by again forming the $RMSE_{Validation}$ after Eq. (10). As shown in Fig. 3b) the model

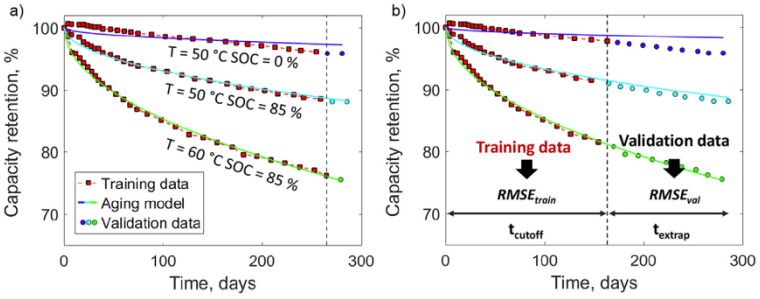

Fig. 3. a) Global aging model fitted to three selected aging data curves. b) Separation of data in time into a training and a validation data set. A global aging model is fitted to the training data in order to predict the further time evolution which is then compared to the measured data. The capacity retention in a) and b) is the average of the C/10 capacity measurements of cells aged at the specified aging points.

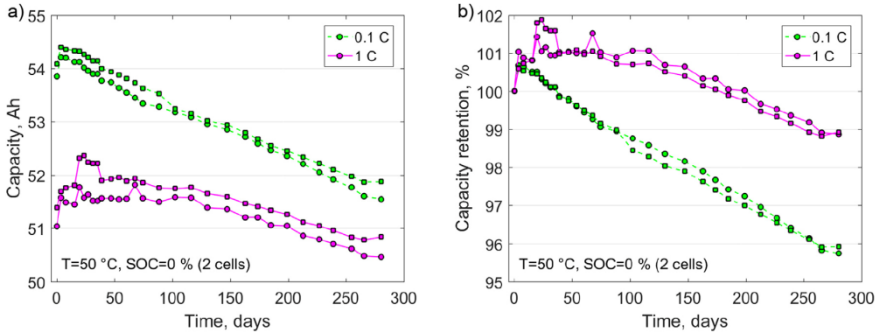

Fig. 4. A) Capacity evolution measured by both the 1C and C/10 discharge capacity for calendar aged cells at 50 °C and 0% SOC. b) Corresponding capacity retention curves with overshoot attributed to overhang effects [29].

may not exactly predict the validation data which is captured in the $RMSE_{Validation}$. Thus, this method can characterize the predictive capability of an aging model. The shorter the chosen t_{cutoff}, the longer is the extrapolated timeframe

$$t_{extrap} = t_{total} - t_{cutoff} \quad (11)$$

which will be varied later.

4. Results

4.1. Overhang effects

The capacity evolution was measured both by a 1C and C/10 discharge phase which is presented in Fig. 4a) for two cells aged at 50 °C and 0% SOC. The C/10 measurement was more stable and continuous than the 1C capacity. This is attributed to the smaller influence of resistance buildup for the C/10 measurement. Furthermore, C/10 capacity retention shown in Fig. 4b) displays less capacity overshoot, i.e. values above 100%, caused by anode overhang effects [29]. In the first capacity measurement, the anode overhang is filled to 75% SOC with unavailable lithium due to long storage at this state before use. Qualitatively, fast 1C measurements take capacity snapshots in time as they do not allow for significant equilibration of inhomogeneous lithiation of the anode. Thus, the measurement is taken with a highly lithiated overlap. In contrast, before the end of the C/10 discharge measurement more time is spent at lower SOC compared to the overlap lithiation regaining some of the unavailable lithium. This changes when the cells undergo days of calendaric storage at low SOC and high temperature as the overhang is delithiated. Subsequent fast 1C measurements get vastly higher capacities than the first capacity 1C measurement. Also, before the end of the C/10 discharge measurement more time is passed at higher SOC compared to the low storage SOC, relithiating some of the close overlap areas and thereby reducing additionally measured capacity, ie. overshoot.

In fact, C/10 measurements from aging points above 30% SOC did not show any measurable overshoot. Such effects are undesirable for model fitting as they mask the actual aging behavior at a certain aging point. As its overhang effects are minimal, the averaged C/10 capacity measurements was chosen for all aging model fitting and the 1C measurement is not discussed further.

4.2. Temperature dependency

In order to ensure a fair comparison between different time dependencies it is important to choose a good common basis for the temperature and voltage dependencies for all considered aging models. The temperature and voltage dependencies are discussed and chosen separately in the following.

Fig. 5a) shows the C/10 capacity retention evolution due to calendar aging at different temperatures and 85% SOC. Their exponential temperature dependency is observed by the straight slopes in the derived Arrhenius plot [7] in Fig. 6a). Clearly, above 52.5 °C the aging seems to exceed the exponential behavior. Before discussing the consequences for fitting, it is noted that this may be explained by the onset of $LiPF_6$ decomposition generating HF which impacts the SEI growth and generates gas. Gueguen et al. [37] concluded that even at room temperature, carbonate solvent oxidation species present in NMC111 cells above 4.2 V vs. Li/Li^+ may hydrolyze $LiPF_6$ generating HF and gas even in short term experiments. The cathode potential in this study at 85% storage SOC is expected to be 4.1 V vs. Li/Li^+ from the BOL full-cell measurements shown in Fig. 2a). Further, while $LiPF_6$ is thermally stable in carbonate solvents up to 85 °C [38], it may be hydrolyzed by trace water in the electrolyte by thermal activation already at lower temperatures [39,40]. Finally, HF attack is proposed to promote new SEI growth on the anode [41]. Despite an extensive study on the high temperature points at 55 and 60 °C and high cathode potential is beyond the scope of this paper, it is safe to assume that an additional aging mechanism is present. Thus, the aging conditions at 55 and 60 °C and 85% SOC are excluded from all further evaluation and fitting. Usually, exposure times of EVs to such high temperatures are very short and the resulting errors in calendar aging models are negligible. The additional point at 55 °C and 55% SOC is not discarded as it only had slightly more aging than the point at 50 °C and 55% SOC which suggests a SOC dependence of the onset of the discussed aging mechanism.

By least-squares fitting the Arrhenius term in Eq. (5) to the observed capacity loss between 40 and 52.5 °C, activation energies, E_a, between 27.7 and 28.7 kJ mol^{-1} are calculated [7] as presented in Fig. 6a). The found values are stable over lifetime and have the same order of magnitude as those found in literature for another NMC111/graphite cell at temperatures below 50 °C [7]. All global aging models presented later are fitted with an Arrhenius term. The measured gas evolution for cells aged at 85% SOC is shown in Fig. 5c). Cells at 55 and 60 °C and 85% SOC also show significant gas evolution, which either may be the effect of or induce the observed super-exponential aging at these conditions.

4.3. Voltage/SOC dependency

Fig. 5b) shows the C/10 capacity retention for the cells aged at 50 °C for the different storage SOC. Recently, Keil and Jossen [13] demonstrated that the capacity fade depends on the anode potential during

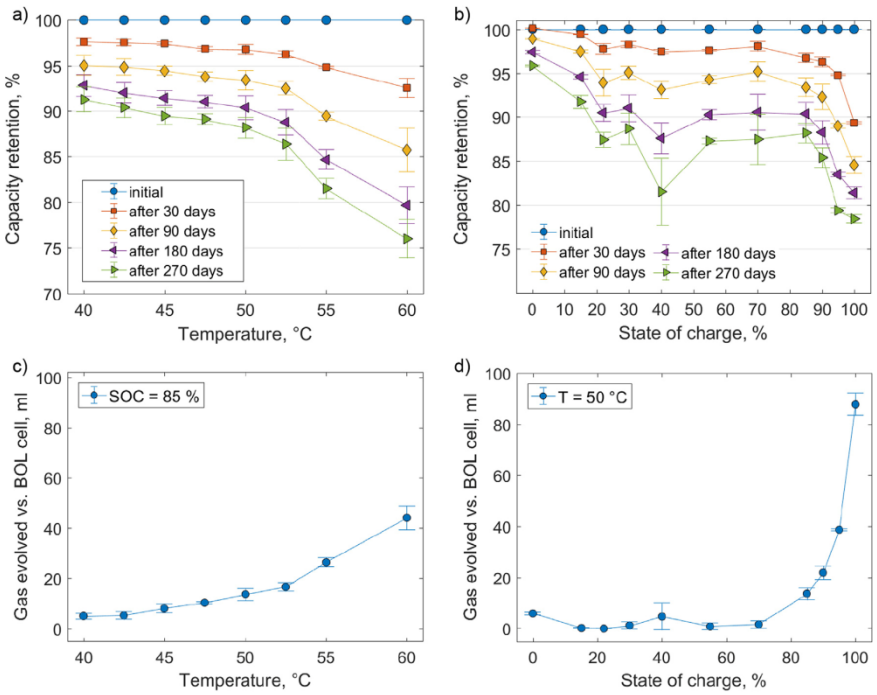

Fig. 5. a) + b) Capacity retention evolution for cells aged at a) 85% SOC and varied temperature as well as b) at 50 °C and varied SOC. c) + d) Gas evolution vs. BOL cell for cells aged at c) 85% SOC and varied temperature as well as d) at 50 °C and varied SOC.

storage. In their publication all cells on the first anode plateau displayed similar aging. The fade increased when the storage happened at the second anode plateau at higher anode lithiation and thus lower potential vs. Li/Li^+. As shown in Fig. 2a) the investigated cell in the present study is conservatively designed and displays this drop to the second anode plateau in the BOL cell at 78% SOC which can also be seen from the peaks in the DVA curves in Fig. 2d) and 2.f). Cells aged at slightly higher SOC are expected to shift [12,13,30,42] to lower lithiation degrees and thus to the higher anode potential plateau over lifetime due to loss of active lithium. The cells aged at 100% SOC and 40% SOC displays a different aging characteristic to the rest of the cells as shown in Fig. S1 in the Supplementary Information. Fig. 5d) shows

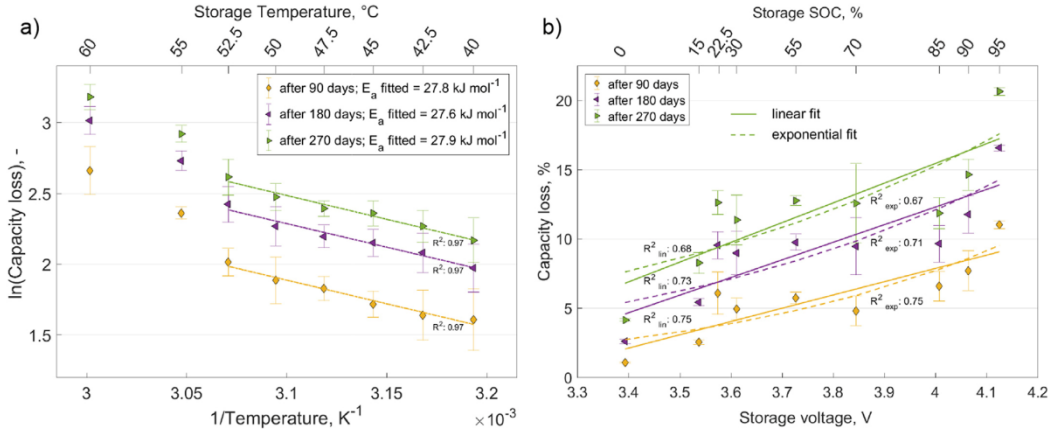

Fig. 6. a) Arrhenius plot of capacity loss with fitted dependency for aging points at 85% SOC with calculated activation energies E_a. b) Linear $p_1 + p_2 \cdot U_{cell}$ and exponential $p_1 \cdot e^{p_2 \cdot (U_{cell} - U_0)}$ voltage dependencies fitted to aging points at a temperature of 50 °C. Corresponding R^2 values are reported for all fits.

Table 2
Considered global calendar aging models with fit parameters pi with literature sources where they apply.

Abbreviation	Formula for capacity retention	Source and comments	Number of fit parameters,-
t^1	$1 - p_1 \cdot A_1 \cdot t^1$	Exemplary model	3
$t^{0.75}$	$1 - p_1 \cdot A_1 \cdot t^{0.75}$	Schmalstieg et al. [5]	3
$t^{0.5}$	$1 - p_1 \cdot A_1 \cdot \sqrt{t}$	Ecker et al. [7] among others	3
t^{p4}	$1 - p_1 \cdot A_1 \cdot t^{p_4}$	Belt et al. [4]	4
Extended t^{p4}	$1 - p_1 \cdot A_1 \cdot \left(\left(\frac{Liloss_{form.}}{p_1 \cdot A_1} \right)^{\frac{1}{p_4}} + t \right)^{p_4} + Liloss_{form.}$	This work, extended from Broussely et al. [1]	4
Extended $t^{0.5}$	$1 - p_1 \cdot A_1 \cdot \left(\left(\frac{Liloss_{form.}}{p_1 \cdot A_1} \right)^{\frac{1}{0.5}} + t \right)^{0.5} + Liloss_{form.}$	This work, extended from Broussely et al. [1]	3
Extended $t^{0.27}$	$1 - p_1 \cdot A_1 \cdot \left(\left(\frac{Liloss_{form.}}{p_1 \cdot A_1} \right)^{\frac{1}{0.27}} + t \right)^{0.27} + Liloss_{form.}$	This work, extended from Broussely et al. [1]	3
ln (1 + t)	$1 - p_1 \cdot A_1 \cdot \ln(1 + p_2 \cdot t)$	Simplified from Li et al. [3]	4
$t + t^{0.5}$	$1 - p_1 \cdot A_1(p_2, p_3) \cdot t^1 - p_4 \cdot A_2(p_5, p_6) \cdot t^{0.5}$	Schmalstieg et al. [5], Kbitz et al. [6]	6
Arrhenius and Tafel dependency	where $A_1 = e^{(p_2 \cdot U_{cell})} \cdot e^{\left(\frac{p_3}{T}\right)} A_2 = e^{(p_5 \cdot U_{cell})} \cdot e^{\left(\frac{p_6}{T}\right)}$	This work, voltage dependency simplified from Ecker et al. [7]	2 per aging term

the gas evolution for cells stored at 50 °C. The cell at 100% SOC experienced strong gassing. As the cells were unconstrained during storage such extreme gassing may induce inactivation of sites, conduction paths or even delamination of layers. This could again be caused by the onset of cathodic $LiPF_6$ degradation even at 50 °C at the higher cathode potentials of 4.28 V vs. Li/Li^+, c.f. Fig. 2a). At least, this gives a strong indication that different aging mechanisms apart from SEI-growth play a role here. Additionally, the 40% SOC storage point at 3.65 V shows unexpectedly high aging which is not in agreement with expectation nor literature [13]. Further investigation by post-mortem analysis is necessary. Consequently, the 40% and 100% aging points are not considered for the aging models. To the best of our knowledge the complex anode potential dependencies [13] discussed above are not realized in theoretical nor semi-empirical aging models in literature as of yet. The $p_1 \cdot e^{p_2 \cdot SOC}$ [21] and SOC^{p_1} dependencies are rejected due to the arbitrary definition of SOC. Furthermore, the former predicts no aging at 0% SOC which is clearly wrong. Thus, for the voltage dependency only two empirical models are considered here: The linear voltage term $p_1 + p_2 \cdot U_{cell}$ by Schmalstieg et al. [5] and a simplified Tafel dependency $p_1 \cdot e^{p_2 \cdot (U_{cell} - U_0)}$ which is derived from Ecker et al. [7], c.f. Eq. (5), by reducing one additional fit parameter. The fitting of the base is neglected as fitting for it with the entire dataset produces values very close to Eulers number, namely 2.727 instead of $e \approx 2.718$. Also, this reduces the overfitting potential. For U_0 2.5 V is chosen. Note that in the case of global aging fitting, the U_0 term is not needed and encompassed in pre-exponential fitting parameters, i.e. p_1, in Eq. (5). The subtractive exponential term $e^{-p_2 \cdot U_0}$ may be factored out. Then, the term collapses into another fit parameter $p_{1,new} = p_1 \cdot e^{-p_2 \cdot U_0}$ as U_0 is constant. Fig. 6b) shows the fits for the two voltage dependencies with their corresponding R^2 values for different aging times similar to Fig. 6a). Both the fits are very similar and have negligible difference in terms of goodness of fit. Similar fits are also reported in literature [5]. A detailed discussion of overfitting model detection using the validation technique is presented in Section 4.6. With this later presented technique it is possible to understand from Fig. S2 that the linear $p_1 + p_2 \cdot U_{cell}$ dependency strongly overfits and shows slightly worse predictive capability compared to the exponential $p_1 \cdot e^{p_2 \cdot (U_{cell} - U_0)}$ dependency. Thus, the exponential $p_1 \cdot e^{p_2 \cdot (U_{cell} - U_0)}$ dependency is chosen for all considered models.

4.4. Considered aging models

All investigated and compared aging models are listed and named in Table 2. Every model is fitted with the same temperature and voltage dependency abbreviated with $A_1(T, U, p_2, p_3)$ also written out in Table 2. Most models are employed in literature. The $t + t^{0.5}$ model [5] is considered here with two separate voltage and temperature dependencies (A_1,A_2) with separate fit parameters for the two additive terms. Further, the complex tunneling model by Li et al. [3] is simplified to $p_1 \cdot A_1 \cdot \ln(1 + p_4 \cdot t)$. It should be noted that this model considers an initial SEI thickness which is included in the fitting parameters p_1 and p_4 in the simplified version considered here.

4.5. Validation results and detection of overfitting aging models

The characteristics and potential of the validation method is shown for the linear t^1, $t^{0.5}$ and the $t + t^{0.5}$ model. The RMSE to the training data of these models is shown for variable cutoff times t_{cutoff} in Fig. 7a). At low t_{cutoff}, even the simple linear model fits well to the training data while the $t^{0.5}$ model does not. This is attributed to the requirement of the infinitely negative slope at $t = 0$ given in the $t^{0.5}$ model. Consequently, the $t + t^{0.5}$ model shows values similar to the linear model as the linear term is preferentially fitted at low t_{cutoff}. This may be visually observed in the corresponding aging fits in Fig. S3.a) and S3.b) for t_{cutoff} at 41 days. At higher t_{cutoff} the $t + t^{0.5}$ model shows very good fit to data. This is expected as the model is highly variable with six free parameters and two separate time dependencies. Also at larger t_{cutoff}, the $t^{0.5}$ model expectedly recovers in comparison to the simple linear model, but does not surpass the $t + t^{0.5}$ model. This is also expected as the adaptive $t + t^{0.5}$ model may simply fit a pure $t^{0.5}$ dependency. The general trend is an increasing RMSE to training data with larger t_{cutoff} mostly due to larger losses after aging which may not be fitted well. It is thus more useful to compare the relative errors of different models.

When comparing the models in terms of their capability to extrapolate, however, the picture changes drastically. Fig. 7b) shows the RMSE to the validation data of the discussed models for different extrapolation timeframes t_{extrap}. Clearly, the simple linear model does not extrapolate well displaying a large discrepancy to the validation data. In contrast and despite its arguably bad fit to training data, the $t^{0.5}$ model predicts the validation data well. When fitting little data, i.e. for large t_{extrap}, the $t + t^{0.5}$ model shows erratic behavior in the quality of extrapolation. In general, however, the $t + t^{0.5}$ model cannot predict the validation data when little data is provided, c.f. Fig. S3.a). The preferential fitting to the linear term of the $t + t^{0.5}$ model is thus a clear example of overfitting to the given data. For smaller t_{extrap} the prediction clearly becomes easier as both more data is available and less validation

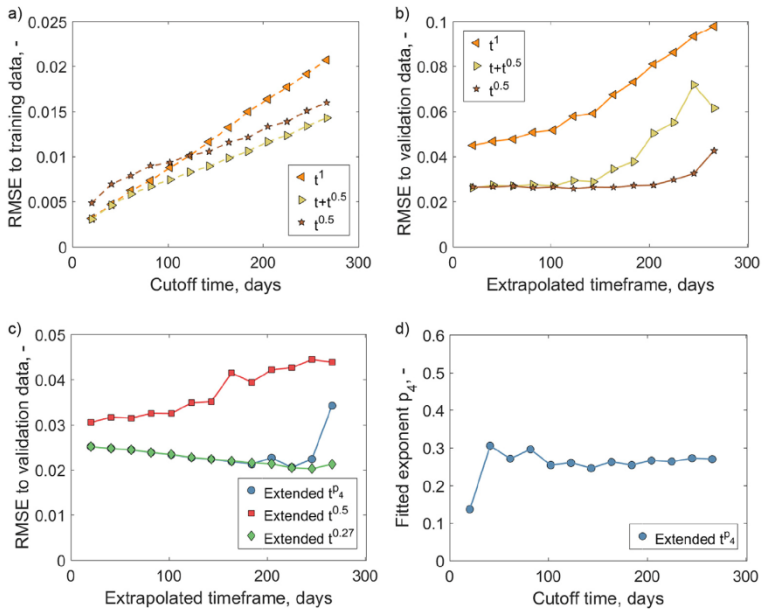

Fig. 7. a) RMSE of the linear, $t^{0.5}$ and combined $t + t^{0.5}$ aging model fits to training data b) RMSE to validation data of the linear, $t^{0.5}$ and combined $t + t^{0.5}$ aging model. c) RMSE to validation data for extended aging models with differing exponents d) Fitted parameter p_4 for the extended t^{p4} model.

data needs to be predicted. Thus, the $t + t^{0.5}$ model is increasingly better when extrapolations are shorter than 80 days achieving similar results to the $t^{0.5}$ model. Even the simple linear model improves its prediction with lower t_{extrap}. This is generally the case for models which may fit the training data well as short extrapolations in time are very easy.

In combination, Fig. 7a) and 7.b) clearly illustrate that a good fit to data does not make for a good aging model. The $t^{0.5}$ model with continuously worse fit to data may predict further aging better than the adaptive $t + t^{0.5}$ model.

4.6. Extended model results

In model development the exponent p_4 of the extended t^{p4} model was not necessarily fixed. When assuming pure theory by Ploehn et al. [2] and Broussely et al. [1], however, p_4 is set to 0.5. This is compared to the aging model where the exponent p_4 is fitted as an additional fit parameter. The RMSE to validation data is shown in Fig. 7c) for both models. Clearly, the extended $t^{0.5}$ model performs worse than a model fitting the exponent. Interestingly, the extended t^{p4} settles to a low extrapolation error early, i.e. at low t_{cutoff}. After an initial period the fitted exponent p_4 converges to a nearly constant value close to 0.27 at higher t_{cutoff} as shown in Fig. 7d). In fact, when an aging model is fitted with the exponent 0.27 the results of the extended model even improve. The RMSE to validation data of the extended $t^{0.27}$ model is also shown in Fig. 7c) which has a similar behavior as when the exponent is fitted, but the model delivers constantly good extrapolations even when little data is provided. It is interesting that for the extended t^{p4} and $t^{0.27}$ models, the validation error actually increases when predicting less. This may be attributed to the makeup of the validation data as the RMSE is an absolute measure of errors. Validation data of smaller extrapolated timeframes contains mainly highly aged data where absolute errors of aging models tend to be larger. At least, this shows that the extended t^{p4} and especially the extended $t^{0.27}$ model do not tend to overfit, even at small t_{cutoff}.

4.7. Quantitative comparison of aging models

When comparing the RMSE to training data as shown in Fig. 8a) it underlines the difficulty to compare models by just their fit to data. While the fit to data is clearly worse for the linear and $t^{0.5}$ models, other models - mostly with more free parameters - all fit relatively well to training data. Indeed, differences between aging models are hardly distinguishable. With the exception of very low t_{cutoff} the best fit is achieved by the extended models. Note that for most points the extended t^{p4} model converged to nearly the same fit as the extended $t^{0.27}$ model. The third best fit was achieved by the ln (1 + t) model for t_{cutoff} larger than 50 days. For t_{cutoff} larger than 140 days this is followed by good fits of models in the order $t^{p4} > t + t^{0.5} > t^{0.75} > t^{0.5} > t^{1}>$.

Fig. 8b) shows the RMSE to validation data of the considered aging models. Clearly, several models cannot extrapolate well in an initial period which is attributed to overfitting to training data. However, this overfitting tendency varies for the different models. Qualitatively, this overfitting tendency may be ranked in order of $t + t^{0.5} > t^{p4} > t^{0.5} > t^{0.75} >$ ln (1 + t) > extended t^{p4} > extended $t^{0.27}$ for the considered models. The models with more free parameters are not generally more prone to overfitting as one might expect. Both the ln (1 + t) and extended t^{p4} model tend to overfit less than the t^{p4} model despite also fitting four fit parameters. While the $t + t^{0.5}$ may be able to fit well when t_{extrap} is small, its general predictive ability is comparatively poor also impacted due to the large overfitting issues. The $t^{0.75}$ model is less prone to overfitting. Still, its predictive capability is also poor, even when extrapolating small timeframes. While both the t^{p4} and the $t^{0.5}$ model have a better predictive ability, the t^{p4} model suffers from its tendency to overfit as discussed earlier. After a short initial period of fitting difficulties at low t_{cutoff} the ln (1 + t) model shows good predictions. Finally, both extended $t^{0.27}$ and extended t^{p4} models display the most accurate extrapolations of the models considered here. They

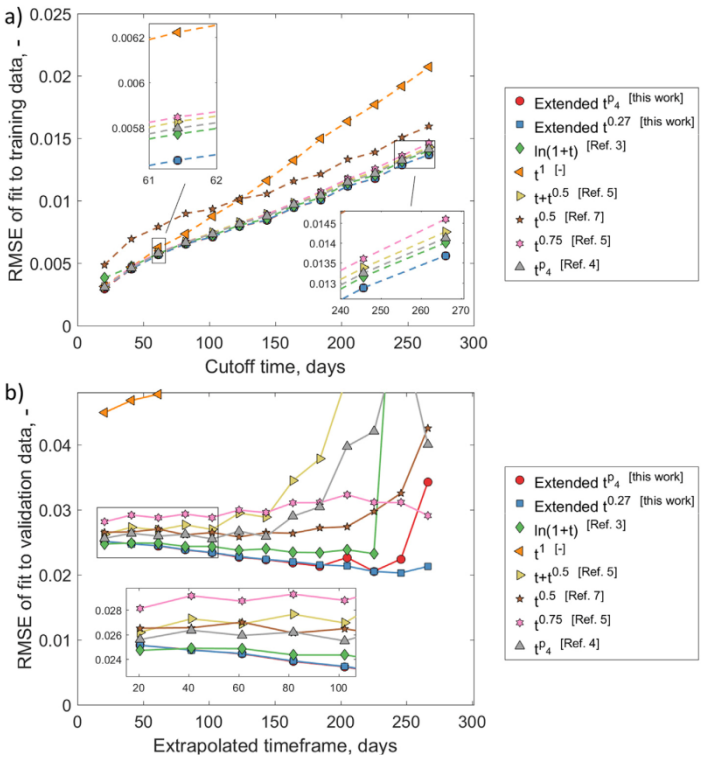

Fig. 8. a) RMSE to training data of several aging models from literature compared to the extended models developed in this work. The extended t^{p4} model is not visible as it converged to nearly the same points as the extended $t^{0.27}$ model b) RMSE to validation data of considered aging models.

are only surpassed for very small t_{extrap} by the ln (1 + t) model. Thus the models are ranked for their predictive ability in order extended $t^{0.27}$ > extended t^{p4} > ln (1 + t) > $t^{0.5}$ > t^{p4} > t + $t^{0.5}$> $t^{0.75}$>t^1.

5. Conclusion

In this work a quantitative aging model validation technique based on the split of measurement data into training and validation data was introduced. Furthermore, an extended global aging model was established which considers the initial lithium loss due to formation. Using the introduced validation technique, the derived model was compared to existing models.

Current aging models simply based on a square root time dependency are not able to describe the aging of cells after formation. Based on theoretical considerations an extended global aging model was derived considering the existence of an initial SEI due to formation. The loss of capacity due to the initial SEI growth as a physical parameter for the model was determined with both OCV/DVA fitting of BOL full- and pouch cells as well as Li detection in a discharged anode by ICP-OES. The fitting method required the additional consideration of the well-known $LiNi_{1/3}Mn_{1/3}Co_{1/3}O_2$ first cycle inefficiency. Both methods are in good agreement and a value of 318.3 µAh cm^{-2} was used in the extended aging models. Freeing the theoretical exponent of the time dependency to a fit parameter p_4 in the extended model semi-empirical model yielded excellent results and displayed stable results for an exponent of $p_4 = 0.27$.

In order to compare different time dependencies of aging models, a common voltage and temperature dependency was selected. The influence of temperature was modeled with the Arrhenius dependency showing a very good fit up to 52.5 °C. For the voltage dependency a state-of-the-art Tafel approach was chosen which showed reasonable results. Clearly, the shifting anode potential over lifetime should be considered in further research on calendar aging models.

The introduced validation technique is able to detect overfitting aging models and their consequent lack of ability to extrapolate. In fact, it was shown that a good fit to data does not necessarily make a good aging model. Some models with more fitting parameters overfit significantly. The number of fit parameters, however, is also not necessarily an indication of an overfitting aging model which emphasizes the need for this quantitative evaluation. The validation technique also allows for a quantitative comparison of aging models where the extended models derived in this work exceed previous models. The only other competitive model is the ln (1 + t) model based on the theoretical tunneling model by Li et al. [3]. The results suggest that the better predictive ability of the ln (1 + t) and the extended models may be enabled by their ability to consider an initial SEI thickness. Thus, the presented methods to evaluate the initial SEI in commercial cells may prove useful to source additional information for aging models.

The introduced validation technique and the derived extended aging model are powerful tools for further detailed development of aging models for lithium-ion batteries.

Detailed post-mortem analyses of cells from this calendar aging matrix are being conducted and will be published soon.

Acknowledgement

Funding from the German Federal Ministry of Economic Affairs and Energy of the project DriveBattery2015 (03ET6060F) is gratefully acknowledged. The responsibility for this publication rests with the authors. The authors acknowledge the SGS Institute Fresenius, Dresden, for conducting the ICP-OES measurements and BatterieIngenieure GmbH, Aachen, for conducting the calendar aging experiment. Naqeeb Tahasildar is thanked for helping to harvest electrodes and measure gas evolution.

Appendix A. Calendaric commutativity for t^{p4} aging models

For models based on free or fixed exponents p_4 and $A(T, SOC)$ describing the SOC and temperature dependence degradation deg_1 suffered from an aging step Δt_1 equals

$$deg_1 = p_1 \cdot A(T_1, SOC_1) \cdot (\Delta t_1)^{p_4} \tag{A.1}$$

For an additional aging period with T_2 and SOC_2 a reference time $t_{Ref,2}$ needs to be found

$$t_{Ref,2} = \left(\frac{deg_1}{p_1 \cdot A(T_2, SOC_2)} \right)^{\frac{1}{p_4}} \tag{A.2}$$

Thus, aging for the new time interval may be calculated by

$$deg_2 = p_1 \cdot A(T_2, SOC_2) \cdot (t_{Ref,2} + \Delta t_2)^{p_4} \tag{A.3}$$

This seems to depend on succession order of aging steps. However, it reduces to

$$deg_2 = p_1 \cdot A(T_2, SOC_2) \cdot \left(\left(\frac{deg_1}{p_1 \cdot A(T_2, SOC_2)} \right)^{\frac{1}{p_4}} + \Delta t_2 \right)^{p_4} \tag{A.4}$$

$$deg_2 = p_1 \cdot A(T_2, SOC_2) \cdot \left(\left(\frac{p_1 \cdot A(T_1, SOC_1) \cdot (\Delta t_1)^{p_4}}{p_1 \cdot A(T_2, SOC_2)} \right)^{\frac{1}{p_4}} + \Delta t_2 \right)^{p_4} \tag{A.5}$$

$$deg_2 = p_1 \cdot A(T_2, SOC_2) \cdot \left(\left(\frac{A(T_1, SOC_1)}{A(T_2, SOC_2)} \right)^{\frac{1}{p_4}} \cdot \Delta t_1 + \Delta t_2 \right)^{p_4} \tag{A.6}$$

$$deg_2 = p_1 \left((A(T_1, SOC_1))^{\frac{1}{p_4}} \cdot \Delta t_1 + \cdot (A(T_2, SOC_2))^{\frac{1}{p_4}} \cdot \Delta t_2 \right)^{p_4} \tag{A.7}$$

Considering the summation, the succession order is irrelevant. q.e.d. This may be expanded to any i number of temperature and SOC aging setpoints at T_i and SOC_i for times Δt_i. Then, the total degradation deg_i of i aging steps equals

$$deg_i = p_1 \left(\sum_i [A(T_i, SOC_i)]^{\frac{1}{p_4}} \cdot \Delta t_i \right)^{p_4} \tag{A.8}$$

Appendix B. Derivation of the extended model based on Broussely et al.

The result by Broussely et al. [1] may be summarized as

$$e_o \cdot x + \frac{1}{2} \cdot A \cdot x^2 - B \cdot t = 0 \tag{B.1}$$

while

$$B = k \cdot \phi \cdot s \tag{B.2}$$

where x is the reacted lithium, e_0 is the SEI thickness after formation, A is a proportionality factor correlating the consumed lithium to a thickness of SEI, k is a proportionality factor for the reaction rate, ϕ is the limited conductivity of electrons in the SEI and s is the surface area. Often, aging models use the simple form with e_0 assumed to be 0 which results in the famous $\sqrt{t}$ relationship. Keeping e_0, however, yields

$$x_{1,2} = \frac{-e_0 \pm \sqrt{e_0^2 + 2 \cdot A \cdot B \cdot t}}{A} \tag{B.3}$$

where only positive corrosion results are physical. This reduces to

$$x = \frac{-e_0}{A} + \left(\left(\frac{e_0}{A} \right)^2 + 2 \cdot \frac{B}{A} \cdot t \right)^{0.5} \tag{B.4}$$

where we insert

$$Liloss_{form.} = \frac{e_0}{A} \quad \text{and} \quad p_1 = \sqrt{2 \cdot \frac{B}{A}} \tag{B.5}$$

Finally, the equation for corroded lithium

$$x = p_1 \cdot \left(\left(\frac{Liloss_{form.}}{p_1} \right)^2 + t \right)^{0.5} - Liloss_{form.} \quad \text{(B.6)}$$

arrives at the same result as the formula in Eq. (8) with $p_4 = 0.5$ and where p_1 may contain the Arrhenius and Tafel dependencies.

Appendix C. Supplementary data

Supplementary data related to this article can be found at https://doi.org/10.1016/j.jpowsour.2018.08.019

References

[1] M. Broussely, S. Herreyre, P. Biensan, P. Kasztejna, K. Nechev, R. Staniewicz, Aging mechanism in Li ion cells and calendar life predictions, J. Power Sources 97–98 (2001) 13–21, https://doi.org/10.1016/S0378-7753(01)00722-4.

[2] H.J. Ploehn, P. Ramadass, R.E. White, Solvent diffusion model for aging of lithium-ion battery cells, J. Electrochem. Soc. 151 (3) (2004) A456, https://doi.org/10.1149/1.1644601.

[3] D. Li, D. Danilov, Z. Zhang, H. Chen, Y. Yang, P.H.L. Notten, Modeling the SEI-formation on graphite electrodes in $LiFePO_4$ batteries, J. Electrochem. Soc. 162 (6) (2015) A858–A869, https://doi.org/10.1149/2.0161506jes.

[4] J. Belt, V. Utgikar, I. Bloom, Calendar and PHEV cycle life aging of high-energy, lithium-ion cells containing blended spinel and layered-oxide cathodes, J. Power Sources 196 (23) (2011) 10213–10221, https://doi.org/10.1016/j.jpowsour.2011.08.067.

[5] J. Schmalstieg, S. Käbitz, M. Ecker, D.U. Sauer, A holistic aging model for Li $(NiMnCo)O_2$ based 18650 lithium-ion batteries, J. Power Sources 257 (2014) 325–334, https://doi.org/10.1016/j.jpowsour.2014.02.012.

[6] S. Käbitz, J.B. Gerschler, M. Ecker, Y. Yurdagel, B. Emmermacher, D. André, T. Mitsch, D.U. Sauer, Cycle and calendar life study of a graphite—$LiNi_{1/3}Mn_{1/3}Co_{1/3}O_2$ Li-ion high energy system. Part A: full cell characterization, J. Power Sources 239 (2013) 572–583, https://doi.org/10.1016/j.jpowsour.2013.03.045.

[7] M. Ecker, J.B. Gerschler, J. Vogel, S. Käbitz, F. Hust, P. Dechent, D.U. Sauer, Development of a lifetime prediction model for lithium-ion batteries based on extended accelerated aging test data, J. Power Sources 215 (2012) 248–257, https://doi.org/10.1016/j.jpowsour.2012.05.012.

[8] I. Baghdadi, O. Briat, J.-Y. Delétage, P. Gyan, J.-M. Vinassa, Lithium battery aging model based on Dakin's degradation approach, J. Power Sources 325 (2016) 273–285, https://doi.org/10.1016/j.jpowsour.2016.06.036.

[9] P. Verma, P. Maire, P. Novák, A review of the features and analyses of the solid electrolyte interphase in Li-ion batteries, Electrochim. Acta 55 (22) (2010) 6332–6341, https://doi.org/10.1016/j.electacta.2010.05.072.

[10] D. Aurbach, Review of selected electrode–solution interactions which determine the performance of Li and Li ion batteries, J. Power Sources 89 (2) (2000) 206–218, https://doi.org/10.1016/S0378-7753(00)00431-6.

[11] F. German, A. Hintennach, A. LaCroix, D. Thiemig, S. Oswald, F. Scheiba, M.J. Hoffmann, H. Ehrenberg, Influence of temperature and upper cut-off voltage on the formation of lithium-ion cells, J. Power Sources 264 (2014) 100–107, https://doi.org/10.1016/j.jpowsour.2014.04.071.

[12] A.J. Smith, J.C. Burns, D. Xiong, J.R. Dahn, Interpreting high precision coulometry results on Li-ion cells, J. Electrochem. Soc. 158 (10) (2011) A1136, https://doi.org/10.1149/1.3625232.

[13] P. Keil, A. Jossen, Calendar aging of NCA lithium-ion batteries investigated by differential voltage analysis and coulomb tracking, J. Electrochem. Soc. 164 (1) (2016) A6066–A6074, https://doi.org/10.1149/2.0091701jes.

[14] C. Daniel, J.O. Besenhard, Handbook of Battery Materials, Wiley-VCH Verlag GmbH & Co. KGaA, Weinheim, Germany, 2011, https://doi.org/10.1002/9783527637188.

[15] I. Bloom, J. Christophersen, K. Gering, Differential voltage analyses of high-power lithium-ion cells, J. Power Sources 139 (1–2) (2005) 304–313, https://doi.org/10.1016/j.jpowsour.2004.07.022.

[16] M. Petzl, M. Kasper, M.A. Danzer, Lithium plating in a commercial lithium-ion battery - a low-temperature aging study, J. Power Sources 275 (2015) 799–807, https://doi.org/10.1016/j.jpowsour.2014.11.065.

[17] Y.-X. Lin, Z. Liu, K. Leung, L.-Q. Chen, P. Lu, Y. Qi, Connecting the irreversible capacity loss in Li-ion batteries with the electronic insulating properties of solid electrolyte interphase (SEI) components, J. Power Sources 309 (2016) 221–230, https://doi.org/10.1016/j.jpowsour.2016.01.078.

[18] E. Peled, S. Menkin, SEI: Past, present and future, J. Electrochem. Soc. 164 (7) (2017) A1703–A1719, https://doi.org/10.1149/2.1441707jes.

[19] M. Tang, S. Lu, J. Newman, Experimental and theoretical investigation of solid-electrolyte-interphase formation mechanisms on glassy carbon, J. Electrochem. Soc. 159 (11) (2012) A1775–A1785, https://doi.org/10.1149/2.025211jes.

[20] J. de Hoog, J.-M. Timmermans, D. Ioan-Stroe, M. Swierczynski, J. Jaguemont, S. Goutam, N. Omar, J. van Mierlo, P. van den Bossche, Combined cycling and calendar capacity fade modeling of a Nickel-Manganese-Cobalt Oxide Cell with real-life profile validation, Appl. Energy 200 (2017) 47–61, https://doi.org/10.1016/j.apenergy.2017.05.018.

[21] S. Paul, C. Diegelmann, H. Kabza, W. Tillmetz, Analysis of ageing inhomogeneities in lithium-ion battery systems, J. Power Sources 239 (2013) 642–650, https://doi.org/10.1016/j.jpowsour.2013.01.068.

[22] E. Redondo-Iglesias, P. Venet, S. Pelissier, Eyring acceleration model for predicting calendar ageing of lithium-ion batteries, J. Energy Storage 13 (2017) 176–183, https://doi.org/10.1016/j.est.2017.06.009.

[23] E. Sarasketa-Zabala, I. Gandiaga, L.M. Rodriguez-Martinez, I. Villarreal, Calendar ageing analysis of a $LiFePO_4$/graphite cell with dynamic model validations: towards realistic lifetime predictions, J. Power Sources 272 (2014) 45–57, https://doi.org/10.1016/j.jpowsour.2014.08.051.

[24] R.B. Wright, CG. Motloch, J.R. Belt, J.P. Christophersen, C.D. Ho, R.A. Richardson, I. Bloom, S.A. Jones, V.S. Battaglia, G.L. Henriksen, T. Unkelhaeuser, D. Ingersoll, H.L. Case, S.A. Rogers, R.A. Sutula, Calendar- and cycle-life studies of advanced technology development program generation 1 lithium-ion batteries, J. Power Sources 110 (2) (2002) 445–470, https://doi.org/10.1016/S0378-7753(02)00210-0.

[25] B. Stiaszny, J.C. Ziegler, E.E. Krauß, J.P. Schmidt, E. Ivers-Tiffée, Electrochemical characterization and post-mortem analysis of aged $LiMn_2O_4$-$Li(Ni_{0.5}Mn_{0.3}Co_{0.2})O_2$/graphite lithium ion batteries. Part I: cycle aging, J. Power Sources 251 (2014) 439–450, https://doi.org/10.1016/j.jpowsour.2013.11.080.

[26] S. Schindler, M.A. Danzer, A novel mechanistic modeling framework for analysis of electrode balancing and degradation modes in commercial lithium-ion cells, J. Power Sources 343 (2017) 226–236, https://doi.org/10.1016/j.jpowsour.2017.01.026.

[27] C.P. Aiken, J. Xia, D.Y. Wang, D.A. Stevens, S. Trussler, J.R. Dahn, An apparatus for the study of in situ gas evolution in Li-Ion pouch cells, J. Electrochem. Soc. 161 (10) (2014) A1548–A1554, https://doi.org/10.1149/2.0151410jes.

[28] M.B. Pinson, M.Z. Bazant, Theory of SEI formation in rechargeable batteries: capacity fade, accelerated aging and lifetime prediction, J. Electrochem. Soc. 160 (2) (2012) A243–A250, https://doi.org/10.1149/2.044302jes.

[29] M. Lewerenz, J. Münnix, J. Schmalstieg, S. Käbitz, M. Knips, D.U. Sauer, Systematic aging of commercial $LiFePO_4$—graphite cylindrical cells including a theory explaining rise of capacity during aging, J. Power Sources 345 (2017) 254–263, https://doi.org/10.1016/j.jpowsour.2017.01.133.

[30] I. Bloom, A.N. Jansen, D.P. Abraham, J. Knuth, S.A. Jones, V.S. Battaglia, G.L. Henriksen, Differential voltage analyses of high-power, lithium-ion cells, J. Power Sources 139 (1–2) (2005) 295–303, https://doi.org/10.1016/j.jpowsour.2004.07.021.

[31] M. Dubarry, C. Truchot, B.Y. Liaw, K. Gering, S. Sazhin, D. Jamison, C. Michelbacher, Evaluation of commercial lithium-ion cells based on composite positive electrode for plug-in hybrid electric vehicle applications. Part II. Degradation mechanism under 2C cycle aging, J. Power Sources 196 (23) (2011) 10336–10343, https://doi.org/10.1016/j.jpowsour.2011.08.078.

[32] N.A. Cañas, P. Einsiedel, O.T. Freitag, C. Heim, M. Steinhauer, D.-W. Park, K.A. Friedrich, Operando X-ray diffraction during battery cycling at elevated temperatures: a quantitative analysis of lithium-graphite intercalation compounds, Carbon 116 (2017) 255–263, https://doi.org/10.1016/j.carbon.2017.02.002.

[33] S. Seidlmayer, I. Buchberger, M. Reiner, T. Gigl, R. Gilles, H.A. Gasteiger, C. Hugenschmidt, First-cycle defect evolution of $Li_{1-x}Ni_{1/3}Mn_{1/3}Co_{1/3}O_2$ lithium ion battery electrodes investigated by positron annihilation spectroscopy, J. Power Sources 336 (2016) 224–230, https://doi.org/10.1016/j.jpowsour.2016.10.050.

[34] M. Winter, Graphites for lithium-ion cells: the correlation of the first-cycle charge loss with the brunauer-emmett-teller surface area, J. Electrochem. Soc. 145 (2) (1998) 428, https://doi.org/10.1149/1.1838281.

[35] C. Bergmeir, J.M. Benítez, On the use of cross-validation for time series predictor evaluation, Inf. Sci. 191 (2012) 192–213, https://doi.org/10.1016/j.ins.2011.12.028.

[36] C. Bergmeir, R.J. Hyndman, B. Koo, A note on the validity of cross-validation for evaluating autoregressive time series prediction, Comput. Stat. Data Anal. 120 (2018) 70–83, https://doi.org/10.1016/j.csda.2017.11.003.

[37] A. Guéguen, D. Streich, M. He, M. Mendez, F.F. Chesneau, P. Novák, E.J. Berg, Decomposition of $LiPF_6$ in high energy lithium-ion batteries studied with online electrochemical mass spectrometry, J. Electrochem. Soc. 163 (6) (2016), https://doi.org/10.1149/2.0981606jes A1095–A1100.

[38] H. Yang, G.V. Zhuang, P.N. Ross, Thermal stability of $LiPF_6$ salt and Li-ion battery electrolytes containing $LiPF_6$, J. Power Sources 161 (1) (2006) 573–579, https://doi.org/10.1016/j.jpowsour.2006.03.058.

[39] S.F. Lux, I.T. Lucas, E. Pollak, S. Passerini, M. Winter, R. Kostecki, The mechanism of HF formation in $LiPF_6$ based organic carbonate electrolytes, Electrochem. Commun. 14 (1) (2012) 47–50, https://doi.org/10.1016/j.elecom.2011.10.026.

[40] T. Kawamura, S. Okada, J.-i. Yamaki, Decomposition reaction of $LiPF_6$-based electrolytes for lithium ion cells, J. Power Sources 156 (2) (2006) 547–554, https://doi.org/10.1016/j.jpowsour.2005.05.084.

[41] K. Kim, I. Park, S.-Y. Ha, Y. Kim, M.-H. Woo, M.-H. Jeong, W.C. Shin, M. Ue, S.Y. Hong, N.-S. Choi, Understanding the thermal instability of fluoroethylene carbonate in $LiPF_6$ -based electrolytes for lithium ion batteries, Electrochim. Acta 225 (2017) 358–368, https://doi.org/10.1016/j.electacta.2016.12.126.

[42] R. Fu, S.-Y. Choe, V. Agubra, J. Fergus, Development of a physics-based degradation model for lithium ion polymer batteries considering side reactions, J. Power Sources 278 (2015) 506–521, https://doi.org/10.1016/j.jpowsour.2014.12.059.

Journal of Energy Storage 29 (2020) 101344

Contents lists available at ScienceDirect

Journal of Energy Storage

journal homepage: www.elsevier.com/locate/est

The influence of the anode overhang effect on the capacity of lithium-ion cells – a 0D-modeling approach

Johannes Philipp Fath[a,*], Lennart Alsheimer[a], Mathias Storch[a,b], Jochen Stadler[a], Jochen Bandlow[a], Severin Hahn[a], Ralf Riedel[b], Thomas Wetzel[c]

[a] Mercedes-Benz AG, Neue Straße 95, 73230 Kirchheim unter Teck, Germany
[b] Fachgebiet Disperse Feststoffe, Fachbereich Material- und Geowissenschaften, Technische Universität Darmstadt, Otto-Berndt-Str. 3, 64287, Darmstadt, Germany
[c] Institute of Thermal Process Engineering, KIT, Kaiserstraße 12, 76131 Karlsruhe, Germany

ARTICLE INFO

Keywords:
Anode overhang
Lithium distribution
Reversible capacity modeling
Capacity measurement
Differential voltage analysis
Lithium-ion battery

ABSTRACT

In this work, the behavior of the anode overhang effect in lithium-ion cells is experimentally investigated and simulated for experimental three electrode cells. An empirical method is presented to transfer the simple 0D-model from the experimental cell level to pouch cells. An anode overhang model will help to correctly interpret cyclic and calendaric aging experiments e.g. in terms of a more reliable and detailed separation of reversible and irreversible capacity losses as well as evaluating the actual state of health of a lithium-ion battery. For the three electrode cells different cathode diameters are used to modulate different sized anode overhang areas. Moreover, the influence of different state of charges on the reversible capacity effect is investigated. To examine the influence of the separator on the evolution of usable cell capacity different separator thicknesses are applied. It is found that the properties of the separator significantly influence the rate at which balancing processes between overhang and active region take place. The results show good accordance of the experimental results to the simulation.

1. Introduction

The demand for electric vehicles (EV) and plug-in hybrid electric vehicles (PHEV) rapidly increases which is recognizable by increasing stock development and sales figures of EV and PHEV in the last years [1–3]. Especially long range and battery life time are important issues for the customer and the implementation of electro mobility in the existing infrastructure [4]. Thus, a reliable life time prediction is crucial for both the manufacturer and the end consumer. In this regard, the prediction of reversible and irreversible capacity losses in the cell has to be taken into account. Gyenes et al. [5] identified the migration of active lithium into the inactive area of the oversized anode as one of the main reversible capacity losses - the anode overhang effect. They showed that inter-and deintercalation of lithium in the overhang has a large effect on measurements of the coulombic efficiency (CE). CE among others is used for quantifying aging effects. Interference of the overhang with CE measurements can result in values greater than unity and may lead to a wrong interpretation of the results [5]. Wilhelm et al. [6] observed the overhang effect as well, using CE measurements and additional post-mortem analysis. They concluded that determining the state of health (SOH) through capacity tests performed directly after an aging experiment is prone to deliver values that are not directly comparable to each other.

In this work, the anode area which has an opposite cathode is further referred to as the active region whereas the rest of the anode without an opposite cathode is called the overhang area. This overhang area contributes to observable capacity increase or loss during calendric and cyclic aging and depends on state of charge (SOC), temperature and the size of the anode overhang in a cell as for example observed by Lewerenz et al. [7–9]. For a calendar aging experiment with prismatic 25 Ah cells Lewerenz et al. [7] corrected the measured capacities by taking a reversible overhang capacity into account. Being able to subtract reversible capacity recovery effects caused by the overhang effect will result in better lifetime prediction methods and estimation of the actual SOH. Lewerenz et al. [9] presented two methods to identify the irreversible aging in cyclic aged cells, namely the slope method and relaxation method. Additionally the influence of homogeneity of lithium distribution (HLD) and its effect on determining the aging rates was examined. The slope method assumes linear aging after the overhang is in equilibrium with the active region which may not be applicable to different cells with varying cell chemistries. It requires long enough testing times to evaluate the linear aging rate, too. The

* Corresponding author.
E-mail address: johannes_philipp.fath@daimler.com (J.P. Fath).

https://doi.org/10.1016/j.est.2020.101344
Received 3 December 2019; Received in revised form 4 February 2020; Accepted 3 March 2020

relaxation method additionally prolongs the required testing time, causing higher costs and occupying testing capacities in the laboratory. If the overhang effect is evaluated simulatively, no additional assumptions about a possible linear aging behavior have to be made and testing times are kept as short as possible.

The reversible capacity effect was also experimentally examined by Dagger et al. [10]. They built pouch cells with different overhang sizes and confirmed the reversible nature of the lithium losses due to the overhang including methods like inductively coupled plasma-optical emission spectroscopy (ICP-OES). Grimsmann et al. [11] performed post-mortem analyses on pouch cells and found that lithium plating in the region of the anode edges is strongly related to the overhang. They proposed reducing the size of the overhang to improve quick-charge behavior of the cell. Additional information about the lithiation state in the anode overhang region can improve the lifetime of a cell e.g. by adjusting charging currents dependent on lithium concentrations in the relevant cell areas. David et al. [12] observed a reversible capacity as well in their experiments using cells with artificial coating defects on the cathode. These coating defects effectively result in an opposite and partly inactive anode within the cell stack. They compared the cycle life of cells with differently sized and shaped cathode coating defects and found that the inactive anode region forms a thinner solid electrolyte interface (SEI) whereas active areas near the defects are likely to show more severe degradation, especially the cathode next to the defect. A 2D-model for a cross-section was presented and solved for the normalized lithium concentrations in the electrodes using a finite elements formulation [12]. A drawback of such detailed models is the need for generating a suitable mesh and generally the higher numerical complexity. If e.g. stacking tolerances and differently sized overhangs are included, each electrode layer with its individual overhang areas would have to be modeled in 2D or even 3D. Different overhang sizes on an experimental cell scale were realized by Son et al. [13]. Besides a decreasing coulombic efficiency, they also mentioned that the anode overhang area can negatively contribute to the overall aging process due to higher SEI formation rates in case of larger anode areas.

Kennell et al. [14] presented a two-dimensional model and simulated the current density and potential distribution in the overhang region. Their model predicts lithium concentration gradients in the graphite anode which form more likely in late charging phases because of the potential plateaus that are found for the graphite open circuit potential. The equalization of lithium concentrations in the anode bulk material is slow when the potential gradient is small. It is also shown that the current density decreases in the overhang the longer the distance is to the active cell region [14]. For time scales from several minutes up to hours, only a fraction of the overhang takes part in the charge transfer reactions and therefore contributes actively to the effective anode capacity that is experienced. The rest of the overhang is regarded as inactive on short time scales but instead essentially contributes to reversible capacity effects on time scales of several days or months.

To summarize, the capacity influencing effect of the overhang is superimposed on other reversible effects, e.g. the stripping process after lithium plating occurred [15], as well as irreversible degradation effects. Being able to distinguish reversible capacity loss from the losses caused by irreversible aging processes improves the interpretation and evaluation of lifetime experiments. This publication focuses on the prediction of the time depending capacity change caused by the anode overhang effect by developing a 0D-model that is able to predict the reversible capacity of a lithium-ion cell while being kept simple to parameterize. For validation and optimization of the model the overhang effect is realized in three electrode cells with different cathode sizes and separator thicknesses. The lithium gradient is equalized at different time scales, depending on the size of the overhang, the SOC and the separator thickness.

2. Experimental

The investigation of the anode overhang effect was done with 3-electrode PAT-cells (EL-Cell, Germany) with lithium-reference ring using a double-layered separator composed of 180 µm thick non-woven polypropylene cloth and a 38 µm thick polyethylene layer [16]. The cells were assembled in an argon-filled glove box. As electrolyte a mixture of ethylene carbonate (EC), ethyl methyl carbonate (EMC), diethyl carbonate (DEC) and lithium hexafluorophosphate $LiPF_6$ was used. Before opening, the new, unaged pouch cell was discharged to a cell voltage of 3.0 V. The double-sided electrode sheets were then prepared the same way as described in more detail by Sieg et al. [17] and Hahn et al. [18]. The sheets were first washed in dimethyl carbonate (DMC), then one side of the coating was removed using N-Methyl-2-pyrrolidone (NMP). Electrodes for the experimental cells with a radius of 9 mm were stamped out of the prepared lithium nickel manganese cobalt oxide cathode with the respective stoichiometry of approximately 6:2:2 (NMC-622) as well as the graphite anode sheets. To simulate the anode overhang, the cathode radius r_{cat} was further reduced to 7 mm, 7.5 mm and 8 mm and placed central toward the anode. The placement of the electrode coin was done manually and without any additionally added spacers. This may result in some variations of the characteristic overhang lengths. The characteristic length of the anode overhang is the difference of anode and cathode radius $\Delta r_{oh} = r_{an} - r_{cat}$. To investigate the effect of the separator thickness d_{sep} for the 7.5 mm radius cathodes the original double-layered separator was removed and replaced by a 28 µm thick ceramic coated polymer separator (CCPS) SEPARION S240P30 (Evonik Litarion GmbH, Germany) as also used by Schadeck et al. [19]. The thin separator was used in the experimental cells to test a setup that is comparable to industrially manufactured cells, although the original and unaltered double layered separators are likely to give more stable results. An overview of the different configurations is given in Table 1. Fig. 2 shows exemplarily two different separator configurations with dimensions.

The check-up tests and storage phases were conducted in a climate chamber at 25 °C. During the cell assembly small SEI cracks might have emerged. Nevertheless, since the electrode sheets were obtained from a commercially manufactured state of the art cell, the electrodes are assumed to be already homogenously formatted by the cell manufacturer and will not show extensive degradation. The initial SEI covering of the graphite particles may have smaller defects after the preparation steps but to recover the SEI and to guarantee a homogeneous electrolyte distribution, several charge/discharge formation steps were applied before starting the regular storage experiment. The formation started with three full C/10 cycles followed by two full C/5-cycles and a C/24 cycle. For the formation and capacity measurements the lower cut-off voltage was set to 2.5 V which corresponds to a SOC of 0% and the upper cut-off voltage was set to 4.2 V corresponding to a SOC of 100%. A cell with SOC of 50% is later defined by a voltage of 3.68 V. Fig. 1 shows the anode potential respectively as a function of the normalized lithium concentration in the graphite and the corresponding SOC-points are marked for 0%, 50% and 100% SOC.

After this formation, the cells were immediately discharged again to the desired initial SOC_{init} = 0% using low C-rates of C/24 followed by a pause of at least 24 h. This is done to restore the state of a completely discharged anode. After an initial 1C-capacity test consisting of a 1C charge step with constant current–constant voltage (CC—CV) followed by a 1C discharge step with constant current (CC), the cells were charged to the intended storage-SOC, the SOC_{relax}. The initial and relaxation SOCs were chosen that way to cover both the complete SOC range (SOC: 0% → 100% and 100% → 5%) and its behavior in passing only half of the SOC-range (SOC: 0% → 50% and SOC: 50% → 5%). Every 36 h after a storage phase a new capacity test was performed. The capacity test procedures and storage phases were repeated ten times. Each measurement was conducted with four cells. If a cell showed unreasonable behavior and defects, it was later sorted out and left

Table 1
Overview of performed measurements and different configurations of the experimental cells.

Configuration	r_{cat} /mm	Δr_{oh} /mm	d_{sep} /µm	Separator	No. Cells & experiments
1	8	1	218	Double-Layered (EL-Cell)	3 experimental cells*: SOC_{init} 0% → SOC_{relax} 100%
2	7.5	1.5	218	Double-Layered (EL-Cell)	4 experimental cells: 1. SOC_{init} 0% → SOC_{relax} 100% 2. SOC_{init} 100% → SOC_{relax} 5%
					3 experimental cells*: 1. SOC_{init} 0% → SOC_{relax} 50% 2. SOC_{init} 50% → SOC_{relax} 5%
3	7	2	218	Double-Layered (EL-Cell)	4 experimental cells: SOC_{init} 0% → SOC_{relax} 100%
4	7.5	1.5	28	CCPS (SEPARION)	4 experimental cells: SOC_{init} 0% → SOC_{relax} 100%

Annotation: * - outlier cell sorted out.

unregarded in the results. A minimum of three working cells per experiment was ensured. The affected experiments are marked in Table 1.

For the empirical upscaling of the model from experimental cell scale to a pouch cell with 40 Ah, data from a CC−CV measurement of the pouch cell is later used for validation. This cell type was also used to get the electrode coins for the previously explained experimental cells. This ensures transferability since the exact same graphite anode and NMC-622 cathode materials were used. Possible differences can arise from electrolyte additives that may not be contained in the experimental cell electrolyte, separator properties that differ from the commercial CCPS used in the experimental cells and deviations in the overhang lengths due to unevenly stapled electrode layers caused by manufacturing process tolerances. It is assumed that the charge throughput during the CV-discharge phase directly correlates to the reversible capacity that is recovered at low SOC. The cell was therefore kept at 3 V in a CV-phase for more than eight days. The equipment used was a CTS from BasyTec GmbH with dynamic current range switching from 1 mA to 5 A and a current precision ranging from 0.2 µA to 1 mA respectively [20].

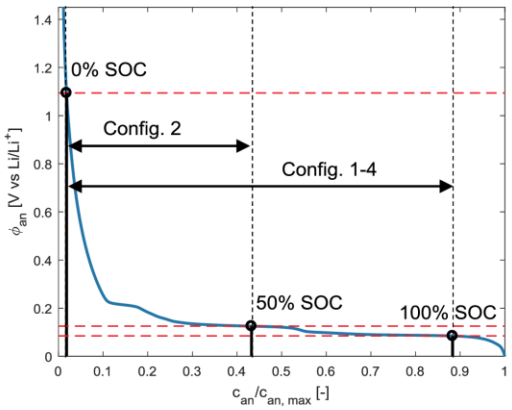

Fig. 1. The anode potential used in the model as a function of the normalized lithium concentration in the solid active material. Additionally, the SOC-range and the configurations used in the experiments is shown.

3. Modeling

3.1. Basic equations

For the 0D-modeling approach, mass balances for the cyclable lithium in the cathode, the active anode region and the overhang region are set up as shown in Eqs. (7)–(9). To keep the number of parameters and variables low, no charge transfer reactions or diffusion in solid and liquid materials are included. Instead, it is assumed that the molar flux j_{oh} of cyclable lithium between the overhang region and the active anode is a function of temperature as well as the anode potentials $\varphi_{an,\,oh}$ and $\varphi_{an,\,act}$ in the overhang (index: oh) and active region (index: act) that is described using a first order approximation

$$j_{oh} = f(T,\ \varphi_{an,oh} - \varphi_{an,act}) \approx \frac{k_0(T)}{l_{char}} \cdot (\varphi_{an,oh} - \varphi_{an,act}) \quad (1)$$

with a proportionality factor k_0 and a characteristic length l_{char} which is later used as a statistic variable to describe differently sized overhang areas with equalization effects on different time scales. To start with, this simplified approach is used for the experimental cell setup and is

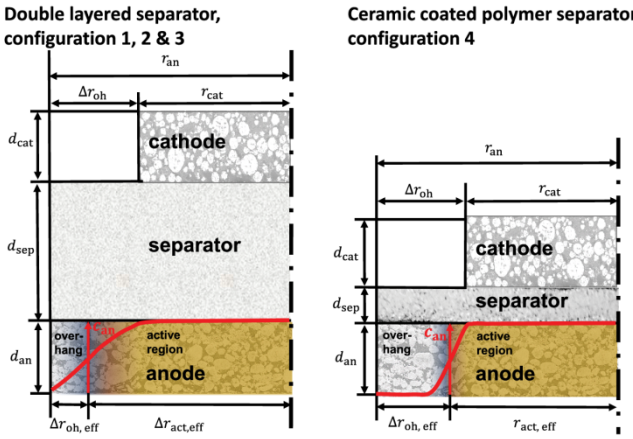

Fig. 2. Schematic representation of different separator thicknesses and its assumed effect on the lithiation states in the active anode area. The red line shows possible lithium concentrations in the graphite to illustrate the reason for a geometric correction of the effective overhang capacity that contributes to capacity recovery effects. With a thin separator the effective active anode area becomes smaller compared to the setup with a thick separator. The border region between overhang and active area becomes more defined with sharp edges concerning the lithiation state of the graphite particles.

valid for symmetrical cell configurations. Following this, the molar amount per time $\frac{dN_{an,\,oh}}{dt}$ of lithium migrating into the overhang is the flux multiplied with the area A_b of the overhang boundary, which is perpendicular to the lateral flux of lithium:

$$\frac{dN_{an,\,oh}}{dt} = j_{oh} \cdot A_b \tag{2}$$

$$A_b = d_{an} \cdot b \tag{3}$$

The thickness of the electrodes is defined as d_{an} and d_{cat} and b is the boundary length separating the overhang region and the active region, which is equal to the boundary length of the cathode sheet. Since the potential in the electrodes is expressed as a function of the lithium concentration in the active material, Eq. (2) combined with (3) is extended with the inverse of the overhang active material volume $V_{an,\,oh}$, which is equal to the product of the overhang electrode volume V_{oh} and the active material volume fraction $\varepsilon_{s,\,an}$:

$$\frac{dN_{an,oh}}{dt} \cdot \frac{1}{\varepsilon_{s,an} V_{oh}} = j_{oh} d_{an} b \cdot \frac{1}{\varepsilon_{s,an} V_{oh}} \tag{4}$$

Substituting the expression $\frac{dN_{an,\,oh}}{\varepsilon_{s,an} V_{oh}}$ with $dc_{an,\,oh}$ and using Eq. (1) gives

$$\frac{dc_{an,oh}}{dt} = \frac{k_0}{l_{char}} (\varphi_{an,oh} - \varphi_{an,act}) \cdot \frac{d_{an} b}{\varepsilon_{s,an} V_{oh}} \tag{5}$$

Eq. (5) is then simplified to Eq. (7) using

$$V_{oh} = d_{an} \cdot A_{oh}^{eff} \tag{6}$$

The concentration of lithium in the active material is defined as c_{an} for the anode and c_{cat} for the cathode. Applied currents I_{cell} to the cell are considered by adding the term j_i, $\{i = an,\ cat\}$ in Eq. (10) to the mass balances which describes the exchange of lithium between the cathode and the active anode area. The different electrode areas are named A_{oh}^{eff} and A_{act}. The overhang area described by Eq. (7) is directly coupled to the active anode resulting in Eq. (8).

$$\frac{dc_{an,\,oh}}{dt} = \frac{k_0}{l_{char}} \cdot \frac{b}{\varepsilon_{s,an} A_{oh}^{eff}} (\varphi_{an}(c_{an,\,oh}) - \varphi_{an}(c_{an,\,act})) \tag{7}$$

$$\frac{dc_{an,act}}{dt} = -\frac{dc_{an,oh}}{dt} \cdot \frac{V_{oh}}{V_{act}} + \frac{j_{an}}{d_{an}} \tag{8}$$

$$\frac{dc_{cat,act}}{dt} = -\frac{j_{cat}}{d_{cat}} \tag{9}$$

with

$$j_i = \frac{I_{cell}}{F \cdot A_{act} \cdot \varepsilon_{s,i}} \tag{10}$$

where $F = 96,485$ As mol^{-1} is the Faraday constant and $\varepsilon_{s,\,i}$ the volume fraction of the active material

The half-cell potentials φ_i are a function of the lithium-ion concentration in the active material. The experimental cell data for φ_i is from a C/100 quasi-open circuit potential measurement of the active material vs. a lithium metal counter electrode and is implemented as a lookup table.

With the concentrations of intercalated lithium in the active material it is possible to calculate the total molar amount of lithium N_{tot} of the cell that is theoretically available for cycling using Eq. (14) with Eq. (11)-(13):

$$N_{an,oh} = c_{an,oh} \cdot \varepsilon_{s,an} \cdot A_{oh} \cdot d_{an} \tag{11}$$

$$N_{an,act} = c_{an,act} \cdot \varepsilon_{s,an} \cdot A_{act} \cdot d_{an} \tag{12}$$

$$N_{cat,act} = c_{cat,act} \cdot \varepsilon_{s,cat} \cdot A_{act} \cdot d_{cat} \tag{13}$$

$$N_{tot} = N_{an,oh} + N_{an,act} + N_{cat,act} \tag{14}$$

Finally, a reversible loss of lithium LL_{rev} is defined with Eq. (15). The loss is relative to a reference state (*) with total lithium amount N_{tot}, a known electrode balancing for the active region and an anode overhang, containing $N_{an,oh}^{*}$ mole of intercalated lithium, that is in equilibrium with the active anode:

$$LL_{rev} = \frac{(N_{tot} - N_{an,oh}^{*}) - (N_{tot} - N_{an,oh})}{(N_{tot} - N_{an,oh}^{*})} \tag{15}$$

The reversible lithium loss LL_{rev} is used to derive the new half-cell balancing and get an updated SOC–OCV curve. According to the voltage boundaries U_{min} and U_{max} that define the SOC start and end points, the theoretical available intrinsic capacity C_{int} is calculated using the procedure as explained in [21].

Since in the check-up test the 1C-capacity C_{1C} is measured, the intrinsic capacity C_{int} of the model is corrected by subtracting a capacity offset ΔC_R that is caused by ohmic resistances and polarization overpotentials:

$$C_{1C} = C_{int} - \Delta C_R \tag{16}$$

The value for ΔC_R is the difference between the first 1C discharge capacity and the capacity of a C/24 discharge at the end of the initial formation cycle of the experimental cell:

$$\Delta C_R = C_{1C,1} - C_{C/24} \tag{17}$$

3.2. Superpositioning of differently sized overhang areas

For upscaling the 0D-model to a large scale rectangular pouch cell, starting from measurements on circular experimental cells, it is necessary to deal with differently sized overhang areas as well as unsymmetrical overhang configurations. Since the electrode sheets are ususally coated on both sides, the upper most and lowest anode layer of the electrode stack result in an additional overhang region. Since the characteristic length of multiple centimeters is much larger compared to the small overhang caused by small sized cathodes within the stack, this overhang region has a slower time constant and therefore it is necessary to consider it in life time experiments. Additionally, the overhang sizes can differ in height and width. The contribution of differently sized overhang regions was previously shown by Hüfner et al. [22]. In the following the basic modeling concept derived in 3.1 is further extended for application on large scale pouch cells using the idea of modeling differently sized overhang areas as presented in [22]. As an additional improvement, also variations of the characteristic overhang length caused by tolerances in the stacking process will be included using simple distribution functions for multiple overhang regions and combining them in the 0D-modeling approach via superpositioning.

Assuming that k_0 is in the same range of values for experimental cells as well as the pouch cell, Eqs. (7) and (8) are extended by summing up the amount of lithium that each of the P overhang elements with index p is exchanging with the active anode region:

$$\frac{dc_{\mathrm{p,\,oh}}}{dt} = \frac{k_0}{l_{p,\,char}}(\varphi_{p,\mathrm{oh}} - \varphi_{\mathrm{an,\,act}})\cdot\frac{b_p}{\varepsilon_{s,an}A^{eff}_{p,oh}} \tag{18}$$

$$\frac{dN_{\mathrm{tot,oh}}}{dt} = \sum_{p=1}^{p=P}\frac{dc_{\mathrm{p,oh}}}{dt}\cdot\varepsilon_{s,an}V_{p,oh} \tag{19}$$

$$\frac{dc_{\mathrm{an,act}}}{dt} = -\frac{dN_{\mathrm{tot,oh}}}{dt}\cdot\frac{1}{\varepsilon_{s,an}V_{act}} + \frac{j_{\mathrm{an}}}{d_{\mathrm{an}}} \tag{20}$$

The distribution function for the overhang elements later used in the simulation of the reversible capacity in the pouch cell is plotted in Fig. 3a). The distribution is directly derived from the electrode sheet geometry, including an assumption for the stacking tolerances, as described in the following procedure by Eq. (21) to Eq. (23).

To start with, in the case of ideal stacking without any lateral displacement, there are four different overhang regions: two small regions in the stack and two large regions in the outer anode sheets, each with an individual boundary of the length b_p since the pouch is rectangular and not ideally square. The width w_{cat} and heigth h_{cat} of a cathode sheet is used to derive the boundary lengths in the short overhang. The characteristic length $l_{p,\,char}$ is the length of the migration path for the lithium from the overhang into the active region. For the two small rectangular regions as illustrated in Fig. 3b), the total overhang area is given by Eq. (21):

$$A_{p,oh} = 2n_{layer}\cdot b_p\cdot l_{p,\,char} \tag{21}$$

With $b_p = 2n_{layer}w_{cat}$, $l_{p,\,char} = l_{p,oh}$ for $p = 1$ and $b_p = 2n_{layer}h_{cat}$, $l_{p,\,char} = l_{p,oh}$ for $p = 2$.

For the large regions on the two outer anode sheets, the width and height of the respective anode layers are used as boundary lengths. The rectangular area is diagonally divided into four triangles, two triangles with the same size respectively as shown in Fig. 3b) as well. It gives the following total area of the corresponding “bin” in the distribution by Eq. (22):

$$A_{p,oh} = 2\cdot 2\cdot\frac{1}{2}l_{p,\,char}\,b_p \tag{22}$$

With $b_p = w_{an}$, $l_{p,\,char} = \frac{1}{2}h_{an}$ for $p = 3$ and $b_p = h_{an}$, $l_{p,\,char} = \frac{1}{2}w_{an}$ for $p = 4$.

In the next step, the small overhang areas ($p = 1, 2$) is further divided into areas with fractional size ρ, that represent unevenly stacked layers with a certain tolerance for the lateral displacement $\pm\ \sigma_p$ and their own characteristic length $l_{p+,char}/l_{p-,char}$:

$$A_{p,oh} = \rho\cdot b_p\cdot l_{p,\,char} + \frac{1-\rho}{2}\cdot b_p\cdot l_{p-,char} + \frac{1-\rho}{2}\cdot b_p\cdot l_{p+,char} \tag{23}$$

with $l^{\pm}_{p,char} = l_{p,\,char} \pm \sigma_p$. For the simulation later on the fractional size was chosen to be $\rho = 0.5$ and the stacking tolerance was set to $\sigma_p = 0.5\ mm$ for $p = 1, 2$.

To include a temperature dependency for k_0 an Arrhenius relation is used that is also previously assumed by Lewerenz et al. [7]. They fitted an activation energy of $E_A = 6.45{\cdot}10^4\ J{\cdot}mol^{-1}$ to data points derived from calendaric aging experiments. This value is likely influenced by the temperature dependency of the aging experiments and is only valid, if the irreversible capacity losses follow a linear trend. Hüfner et al. [22] examined the temperature dependency as well and found an increasing lithium migration rate of factor 1.4 with a temperature increase of $\Delta T = 10$ K which results in an activation energy of approximately $E_A = 2.60{\cdot}10^4$ J mol^{-1}. Their experiments were designed to explicitly evaluate the overhang capacity and therefore the activation energy for the overhang processes is likely to be lower than the value given in [7].

In the model, the implemented temperature dependency takes the form

$$k_0(T) = k_0^*\cdot exp\left(-\frac{E_A}{R}\left(\frac{1}{T^*} - \frac{1}{T}\right)\right) \tag{24}$$

with an activation energy E_A, the ideal gas constant R and temperature T. $T^* = 298.15$ K is the reference temperature and k_0^* the corresponding proportionality factor fitted to the measured data at T^*.

As mentioned in the introduction and later shown in the results, one cannot use the same active cell area for the cathode and the anode region. This effect is caused by inhomogeneous current distributions which cause the effective, active anode area $A^{eff}_{act,an}$ to appear larger and the overhang accordingly smaller than in the ideal case with perfectly parallel ionic current flow perpendicular to the electrode layer. In other words, regions of the anode that do not have a direct cathode counterpart are still partly participating in the inter- and deintercalation reactions on short time scales during current phases. For a 0D-model that focuses on modeling large time scales up to several days, this effect is considered in a geometric correction. The geometry correction is done by introducing a utilization factor η_{oh}. The data structure of the electrode parameters used by the overhang model was originally inherited by the MATLAB-based pseudo-two-dimensional Newman model published by Torchio et al. [23]. To conserve the theoretical electrode capacity of the graphite anode while changing the effective electrode areas, the utilization factor has also to be considered e.g. in the volume fraction. To derive the effective values for the active material volume fraction and the corrected overhang area, first the following equations are set up:

$$c_{\mathrm{s,max,\,an}}\cdot\varepsilon^{eff}_{s,an}\cdot A^{eff}_{oh} = c_{\mathrm{s,max,\,an}}\cdot\varepsilon_{\mathrm{s,\,an}}\cdot A_{\mathrm{oh}}\cdot\eta_{\mathrm{oh}} \tag{25}$$

$$c_{\mathrm{s,max,\,an}}\cdot\varepsilon^{eff}_{s,an}\cdot A^{eff}_{act,an} = c_{\mathrm{s,max,\,an}}\cdot\varepsilon_{\mathrm{s,\,an}}\cdot A_{act,an} + c_{\mathrm{s,max,\,an}}\cdot\varepsilon_{\mathrm{s,\,an}}\cdot A_{\mathrm{oh}}\cdot(1-\eta_{\mathrm{oh}}) \tag{26}$$

In the model framework itself, the active area for the anode and the cathode is always considered to be identical. What is basically done in the geometric correction is the calculation of effective values for an anode that has a smaller effective overhang and respectively a higher capacity in its active region than the true cell setup, but is equal in its active area as stated in (27):

$$A^{eff}_{act,an} = A_{act,cat} = A_{act} \tag{27}$$

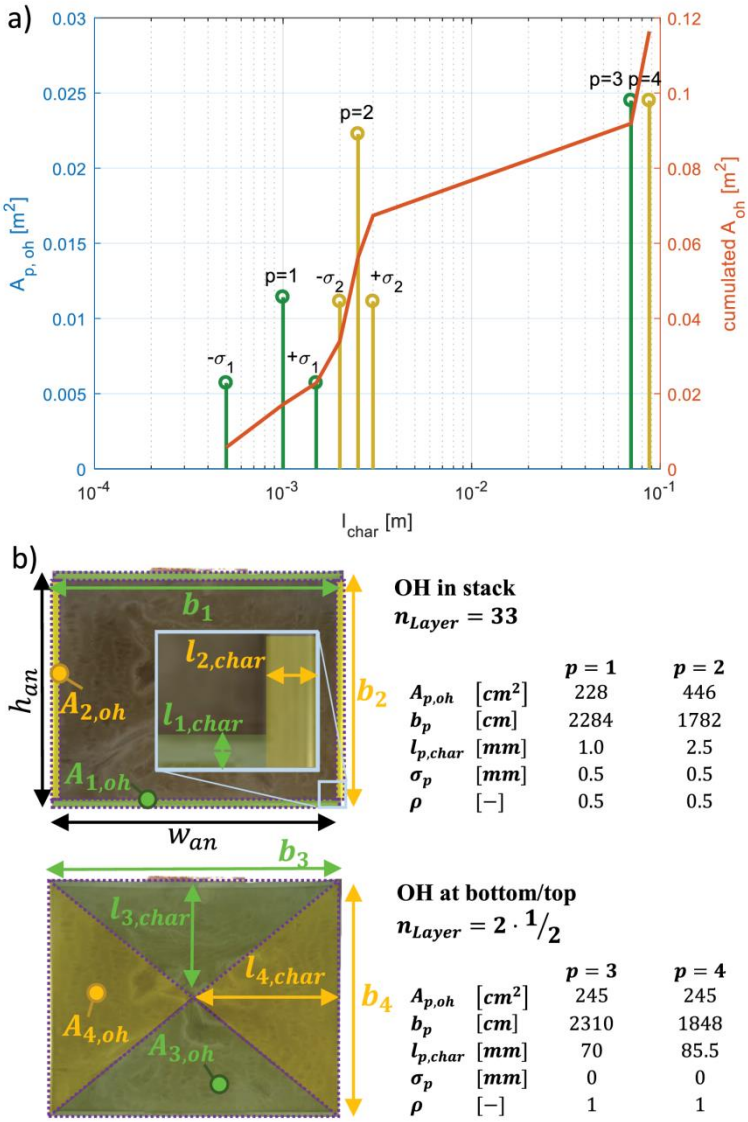

Fig. 3. a) The sizes of the superpositioned overhang elements (left y-axis) and their cumulative sum (right y-axis) plotted over their characteristic length. The characteristic length as well as their respective boundary length determine the timescale on which the overhang is equalized with the active cell region. b) Schematic illustration of the small overhang areas of an anode sheet in the stack as well as the derivation for the larger overhang caused by the bottom and upper layer in a stacked pouch cell.

Using (27) and substituting $A_{act,an}^{eff}$ with A_{act} in (26) and solving for $\varepsilon_{s,an}^{eff}$ delivers (28):

$$\varepsilon_{s,an}^{eff} = \varepsilon_{s,\,an} + \varepsilon_{s,\,an}(1-\eta_{oh})\cdot\frac{A_{oh}}{A_{act}} \tag{28}$$

Now that the new effective volume fraction is known, one can solve Eq. (25) for A_{oh}^{eff}:

$$A_{oh}^{eff} = \frac{\varepsilon_{s,\,an}}{\varepsilon_{s,an}^{eff}}\cdot A_{oh}\cdot\eta_{oh} \tag{29}$$

A utilization factor of $\eta_{oh} = 1$ for example represents the theoretical ideal case where $A_{oh}^{eff} = A_{oh}$ and the whole overhang contributes to the reversible capacity effect on large time scales.

The SOC–OCV curve used in the model is always set up and updated for the active region. It is therefore not a real OCV but a quasi-OCV

Table A 1
. Overview of cell configurations and model parameters.

Variable	Unit	Config. 1	Config. 2	Config. 3	Config. 4	Pouch
An. Material [3]	–	graphite				
Cat. Material [3]	–	NMC-622				
d_{sep} [3]	μm	218	218	218	28	20–30
d_{an} [3]	μm	70.5				
d_{cat} [3]	μm	60				
r_{cat} [2]	mm	8	7.5	7	7.5	–
r_{an} [2]	mm	9	9	9	9	–
h_{cat} [2]	mm	–				135
w_{cat} [2]	mm					173
h_{an} [2]	mm					140
w_{an} [2]	mm					175
$\varepsilon_{s,\ an}$ [3]	–	0.53				
$\varepsilon_{s,\ cat}$ [3]	–	0.51				
$\varepsilon_{s,an}^{eff}$ [4]		0.59	0.63	0.64	0.58	0.53
$c_{s,\ max,\ an}$ [3]	mol·m^{-3}	29,703				
$c_{s,\ max,\ cat}$ [3]	mol·m^{-3}	50,361				
A_{oh} [2]	m^2	5.34E-5	7.78E-5	1.01E-4	7.78E-4	1.16E-1
A_{oh}^{eff} [4]	m^2	2.36E-5	3.57E-5	5.43E-5	5.51E-5	1.16E-1
$A_{act,\ cat}$ [2]	m^2	2.01E-4	1.77E-4	1.54E-4	1.70E-4 [1]	1.54
η_{oh} [4]	–	0.5	0.55	0.66	0.78	1
k_{0*} [4]	mol·V^{-1}·d^{-1}·m^{-1}	4E-6	4E-6	4E-6	1.4E-6	2.2E-6
ΔC_R [2], [4]	mAh	0.2	0.2	0.2	0.2	–

Annotations:
[1] Decreased active area due to possible gas inclusions. Cells also showed higher standard-deviations.
[2] Constant measured/calculated parameter.
[3] Constant parameter from literature/manufacturer information [16,19,21,27].
[4] Adjustable overhang model fit parameter.

since the cell is not necessarily in an equilibrium state regarding different lithiation states in the active and overhang region. On short time scales that are relevant to describe the dynamic behavior e.g. in equivalent circuit models this quasi-OCV can be assumed to be stationary and doesn't have to be updated in every iteration. The model equations are solved and integrated over time using the MATLAB ode15s solver since it can deal with differential as well as algebraic equations. The parameters used for the simulations in the following section are listed in the appendix, Table A 1.

4. Results

4.1. Variation of the overhang size and the separator

Fig. 4a) shows the measured 1C capacities of the experimental cells (markers) as well as the simulated intrinsic capacities (dashed) and the equivalent corrected capacities (solid) using Eq. (17). With decreasing radius of the cathode coin the initial capacity decreases accordingly. At the start of the experiment the anode overhang is nearly empty at a SOC_{init} of 0%. Then all cells are stored at SOC_{relax} of 100% for 17 days and for all cells the usable 1C capacity decreases over time due to a loss of cyclable lithium in the active cell region and lithiation of the anode overhang. The capacity loss during storage increases with the size of the overhang as expected. The rate of capacity loss decreases with time since the potential gradient between the overhang and the active region becomes smaller and mass transport of the lithium-ions by diffusion and migration into the overhang slows down. After approximately ten days a continuous and almost linear decrease of the capacity is being observed that is likely to be influenced by calendric aging effects of the experimental three electrode cell. The corrected simulated capacities agree well with the measurement data. The 0D-model is able to describe the evolution of capacity over time.

In Fig. 4b) the data for cathodes with 7.5 mm radius and two different separator configurations are plotted. Although they have the same size of the cathode the capacity fade differs significantly due to flow of lithium into the overhang. The cells with a thin separator (blue, configuration 4) show higher losses compared to cells with a thick separator (red, configuration 2). This observation is most likely caused by the different geometric dimensions in the cell. With larger distances between anode and cathode the actual effective anode area increases. The flow of lithium-ions in the cell between the electrodes during charging or discharging is not ideally perpendicular to the electrodes. There is a lateral component that makes the effective anode area appear larger on short time scales than its cathode counterpart. Therefore in the model the effective lengths and areas of the overhang and active anode have to be adjusted by applying a geometric correction on the cell parameters as described in the previous section with Eqs. (25)–(29).

It can also be seen in Table A 1 that for configuration 2 the proportionality factor k for the equalization process is higher and the process takes less time to get into a steady state compared to the cells with configuration 4. For the lateral diffusion and migration processes of ions in the electrolyte the anisotropic material properties of the electrodes as well as the properties of the separator need to be considered. Zhao et al. [24] compared separator materials based on ceramic fiber (CF) to the commonly used separators based on stretched polyethylene (PE) as well as ceramic filled PE-separators (C-PE). The CF-based separator shows higher porosity and electrolyte uptake, resulting in higher ionic conductivities compared to PE and C-PE. The SEM-pictures in [24] clearly show the high pore volume and the highly interconnected 3D pore structures forming in fiber based separators, whereas the pores in PE-separator are smaller and not interconnected in the lateral direction, thus implying more anisotropic properties in PE-based separators. The cells with the thick separator have a polypropylene fiber layer of appr. 180 µm thickness [16] that is considered to be also well permeable for lithium-ions in lateral direction, comparable to the CF-separator in [24]. Whereas the thin separator consists of a porous ceramic filled polymer layer that is optimized to have a high permeability for ions that move perpendicular to the electrode layer. Therefore the flow of lithium in lateral direction is more limited to the porous anode domain that also has anisotropic properties due to calendering of the electrodes and the flake-like shape of graphite particles. Anisotropic anode properties e.g. were modeled by He et al. [25]

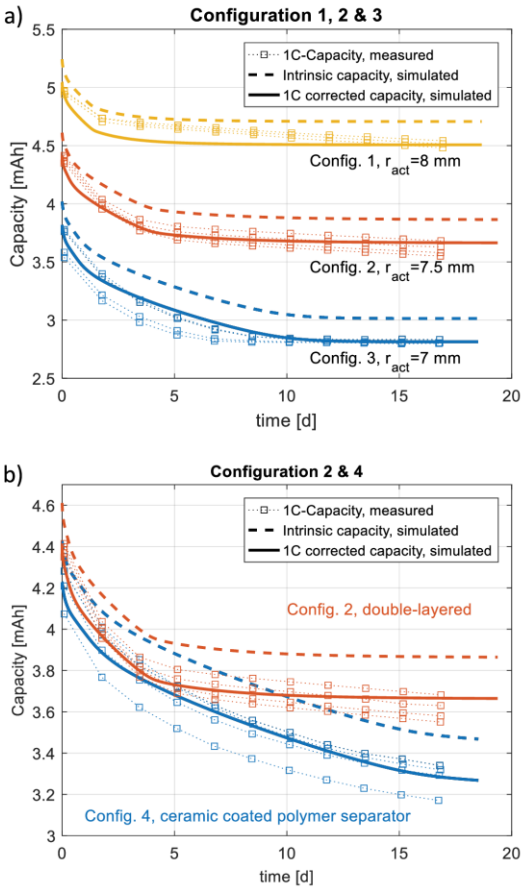

Fig. 4. a) Variation of the cathode radius using the double layered separator for configuration 1, 2 and 3. With smaller cathode radius the overhang capacity increases whereas the overall cell capacity decreases. b) Comparison between the ceramic coated polymer separator in configuration 4 (blue) and the double layered separator (red) for a cathode radius of 7.5 mm in configuration 2. The figure shows that the effective overhang area is larger for cells with a thin ceramic coated polymer separator because the capacity decreases more compared to the cells with double layered separator. The equalization process is slower for configuration 4 which might be caused by lower effective diffusivities in lateral direction.

who simulated the resulting microstructure based on ellipsoid graphite particles and derived anisotropic tortuosity values.

4.2. Variation of storage SOC

After the first experiments of the cells with configuration 2 with a thick separator and 7.5 mm cathode radius at high storage SOCs, the exact same cells are used to invert the experiment and store them at a low SOC_{relax}. In case of a fully reversible process, the same capacity as in the beginning is measured. But the polarization overpotentials during the 1C steps cause a relaxation after the lower cut-off voltage is reached, so the actual relaxed SOC_{relax} is always higher. Therefore, a final SOC_{relax} of approximately 5% for the active region in the model was chosen for the storage at low SOCs as shown in Fig. 5.

Fig. 5a) shows the capacity curves for the storage at SOC_{relax} = 50% and the following storage phase at SOC_{relax} = 5%. A lower final capacity is measured than in the beginning. The capacity keeps decreasing, too. The capacity loss is most likely caused by irreversible aging of the experimental cells. Possible reasons are missing additives in the electrolyte used for the experimental cells which otherwise prevent side reactions in the pouch cell and in general the long-term instability of the used experimental three electrode cells. The simulated values show a slightly higher reversible capacity. This is likely caused by the shape of the anode half-cell potential which forms a plateau in this voltage range. Therefore the speed of the equalization process is very sensitive to the potential gradient and also hysteresis effects are more likely to have an effect which so far are not considered in the model.

In Fig. 5b) the data for the maximum SOC difference of 100% is displayed. The reversible capacity is found to be approximately twice the value observed for the storage at 50% SOC which meets the expectations. When stored at low SOC, the reversible part of the capacity is regained faster than it took to lose the capacity when fully charged. The process is faster when the larger active area is kept at a low SOC. Higher gradients in the anode potential speed up the process as also seen in experiments performed by Hüfner et al. [22]. At the end of the test an irreversible capacity fade is also observed. For an experiment duration up to several weeks aging processes in the experimental cells have to be considered since they show much higher irreversible capacity loss rates compared to more stable, commercially produced cells.

At the beginning of the second storage experiment at t = 20 d just before storing at low SOC in Fig. 5b), a higher capacity was measured for all cells. This was caused by an intermediate C/10 measurement after 17 days of storage to perform a differential voltage analysis (DVA)

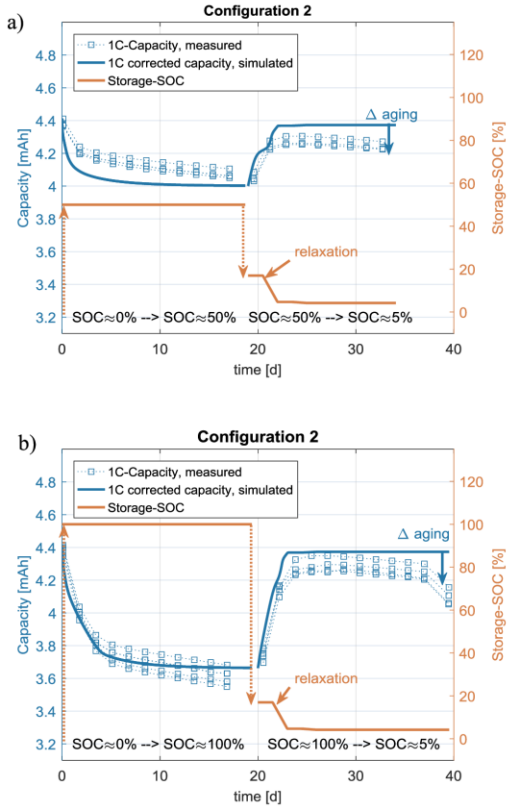

Fig. 5. a) 1C capacities of cells (blue) and corresponding storage-SOC-profiles (red) with 7.5 mm cathode radius first stored at 50% SOC and then after appr. 20 days discharged to a low SOC. b) 1C capacities of cells with 7.5 mm cathode radius first stored at 100% SOC) and then after 20 days discharged to a low SOC.

and incremental capacity analysis (ICA) as plotted in Fig. 6a) and b), respectively. During the C/10 discharge, obviously a significant amount of lithium was regained from the overhang. Large part of the lithium is regained at lower voltages during the C/10 discharge and therefore a highly charged overhang prolongs the discharge phase. An indicator for the large overhang is the shifted minimum in the DVA of Fig. 6a) when comparing the curves marked with "1" to the dotted curves marked with "2" or the following charge step "3". When the overhang is full, the first minimum in the voltage derivative curve appears at an x-value of approximately 1.6 mAh, compared to an x-value of 1–1.1 mAh at formation or during the following charge step. Looking at the related ICA-diagram in Fig. 6b) this circumstance becomes clearer: When the cells with full overhang ("2") are discharged, they show a lower charge alteration with decreasing voltage until a cell voltage of 3.55 V is reached. From this point on a large amount of lithium is regained from the overhang during discharge, resulting in higher values for $\frac{dQ}{dU}$. Although the aforementioned effect of shifting the minimum in DVA curves is overemphasized in the used experimental cells due to the extreme ratio of overhang area to active area, the overhang effect can have an influence on interpreting DVA data and may lead to over or underestimating certain kind of losses, especially the loss of cyclable lithium or loss of accessible graphite intercalation sites.

Because this effect of a single C/10 measurement is unneglectable in the following storage phase, it was not conducted between the storage phases in Fig. 5a) which showed no sudden jumps of the 1C-capacity. After the C/10 discharge and charge experiment the cells therefore are stored again at SOC = 100% to re-lithiate the overhang to have a defined initial state for the second storage phase at SOC = 5%. If several storage experiments are conducted serially one should have in mind that already a C/10 capacity measurement will cause a change of the usable 1C capacity due to equalization processes that take place during the experiment.

4.3. Upscaling to 40 Ah pouch cell

For the application of the 0D-model it is important to have a procedure for upscaling the results from experimental cell level to a large scale cell with several ampere hours of capacity as described in 3.2. Since per definition a 0D-model cannot resolve any mass transport effects in space and differently sized overhang regions in large scale cells are present, these multiple overhang areas and their contribution to the reversible capacity evolution over time are therefore superpositioned and included in the equations by summing up the terms respectively. The separator used in the pouch cell is likely different but assumed to be comparable to the CCPS used in configuration 4 and by Schadeck et al. [19]. The proportionality factor k_0 used for the pouch cell simulation lies in the range previously determined with the experimental cells and is chosen to be $k_0 = 2.2E-6\ mol\ V^{-1}\ d^{-1}\ m^{-1}$. It is therefore higher than the value determined for CCPS but lower compared to the value of the double-layered separator.

For validation of the upscaling procedure and the introduction of a characteristic overhang distribution, experimental data from a 40 Ah pouch cell is taken for validation. The cell is stored in a storage locker at an SOC of 70% for several months at room temperature in the laboratory as it was delivered by the cell manufacturer. Therefore it is assumed that the overhang is also charged to an SOC of approximately 70%. Then it is discharged to 3 V with a current of −3.7 A. After reaching a cell voltage of 3 V a constant voltage phase is initiated and the measured current during the CV-phase is integrated. This CV charge throughput which can be mainly attributed to lithium that is regained from the overhang according to Hüfner et al. [22] is a measure for the reversible capacity. It is then compared to the change of capacity that the 0D-model outputs as displayed in Fig. 7.

Fig. 7a) shows that a simple 0D-model is well capable of describing the charge that is transferred between overhang and active region when a distribution of different overhang areas and characteristic length scales is used which are derived directly from the cell geometry. The simulation matches well with the integrated charge throughput of the 40 Ah pouch cell. With a proper set of parameters the absolute error is less than a tenth of an ampere-hour. The small, constant slope that is still present after more than 7 days in Fig. 7a) is attributed to the large overhang which is consistent with the findings by Hüfner et al. [22].

The model is not only capable of describing the transient behavior of the overhang effect adequately but also the total change of the available reversible capacity. Especially for lifetime experiments that usually take up to several months the model produces promising results to apply on aging data. It is then possible to differentiate between reversible and irreversible capacity effects, since it converges to a constant reversible lithium loss as long as the boundary conditions do not change.

To illustrate the effect on aging experiments, a simulation study is conducted. Fig. 7b) shows the results obtained from the pouch cell parameters for two different hybrid electric vehicle SOC profiles. Depending on the SOC value at which the vehicle will start going into hybrid mode, it will result in differently charged anode overhang regions and therefore result in differently effective usable capacities. The exemplary User 1 is discharging down to a SOC of 5% and then the vehicle stays in hybrid mode whereas User 2 goes in hybrid mode as

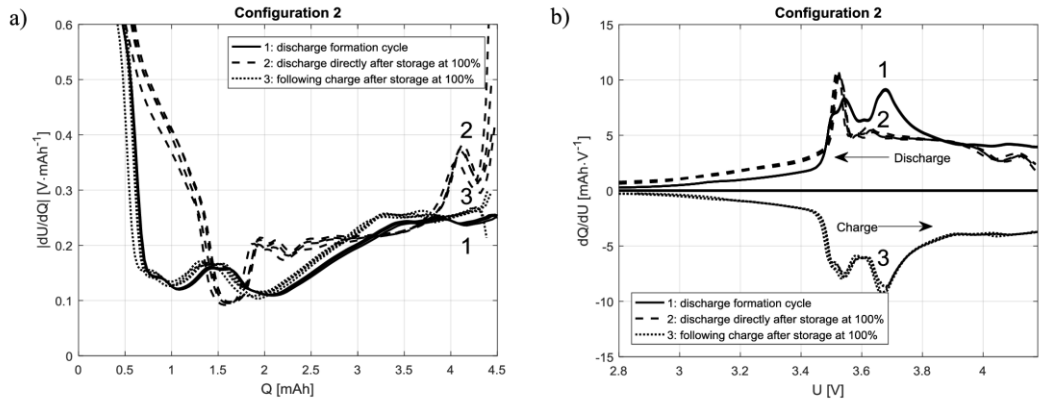

Fig. 6. a) C/10 DVA-curves of the four experimental cells with 7.5 mm cathode radius and 9 mm anode radius recorded during the initial cycles (1), the first discharge after 17 days of storage at 100% (2) and the following C/10 charging after the storage (3). The half-cell matching of the cell changes significantly during the discharge measurement directly after the storage phase. When charged again, the curves tend to align with the initial DVA before the experiment. b) ICA-curves derived from the same data. At low current rates, especially in the low cell voltage ranges below 3.55 V, the reversible capacity loss is nearly completely recovered in the experimental three electrode cells.

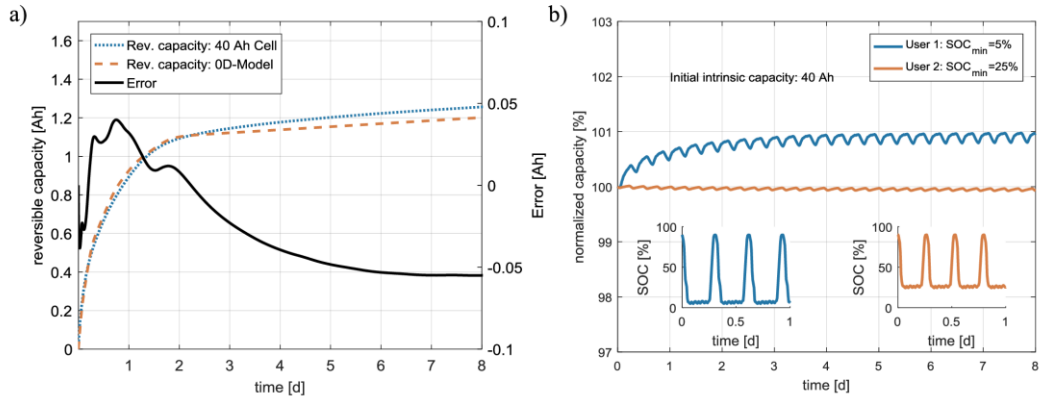

Fig. 7. a) Comparison of the scaled 0D-model (dashed) to measurement data obtained from a 40 Ah pouch cell (dotted). The reversible capacity is the charge throughput during a constant voltage phase of several days at 3 V after a storage phase at 3.87 V. The error (solid) shows the difference between modeled capacity and the integrated CV current of the pouch cell. b) Simulation study with two different SOC user profiles for the pouch-cell parameters. It shows the characteristic evolution of the normalized cell capacity and cut section of both SOC-profiles. The initial SOC was set to 30%.

soon as 25% SOC is reached. Both profiles are simulated without any irreversible aging effects. The results clearly show that, depending on the SOC profiles and the initial state of the cell, apparent capacity gains can be seen. This happens when the reference SOC at begin of the experiment is higher than the mean effective cycling SOC. If this effect is neglected in life time prediction methods, it will negatively influence the ability of a lifetime model to predict the end of life of the cell. Nevertheless, it could become necessary to adjust the proportionality factor over lifetime. Lewerenz et al. [26] found via capacity difference analysis (CDA), that the speed of lateral lithium-ion flow may decrease in aged cells that show extensive formation of a covering layer or electrolyte dry out which blocks pores in the anode and electrochemically deactivates parts of the anode. The formation of dense covering layers on the anode is likely caused by lithium plating. In future life time test therefore it should be prevented by proper adjustment of the charging currents as proposed by Sieg et al. [17] and the influence of the remaining aging effects on lateral lithium flow should be evaluated, whether it is caused by dry electrode areas or the like.

5. Conclusion

We have shown that the evolution of the cell capacity can be described dependent on the size of the anode overhang and the storage SOC using a 0D-modeling approach for small experimental cells as well as for large pouch cells. Being able to calculate the reversible capacity losses and gains is exceptional helpful for determining the actual state of health of a lithium-ion battery. As the model predicts and experiments in literature and this work confirm, operating a lithium-ion battery at a low SOC improves the usable capacity of the cell. The lithium recovery process at low SOC is faster than the loss process at high SOC due to the nonlinear shape of the graphite anode potential. Since the number of free parameters is small, the model is straightforward to

parameterize. The results show that the choice of the separator material and its dimensions has an effect on the reversible effects of lithium flow in and out of the anode overhang region. A thin separator decreases the effective usable anode area and slows down the balancing of lithiation states inside the anode. Furthermore, for upscaling the model on large pouch cells it is necessary to deal with the contribution of multiple overhang areas by superpositioning the effects but keeping it simple to set up and parameterize at the same time. An overhang model that is able to describe the cell capacity on large time scales of several days and up to months facilitates application to data recorded in aging experiments and allows for a better assessment of the actual state of health. The reversible effects can be subtracted from the measured capacities, yielding a corrected, irreversible capacity loss that is independent of storage conditions or mean cycling SOCs. This will likely improve the prediction of a lithium ion cell's lifetime.

CRediT authorship contribution statement

Johannes Philipp Fath: Conceptualization, Methodology, Software, Investigation, Writing - original draft, Writing - review & editing, Visualization. **Lennart Alsheimer:** Conceptualization, Methodology, Investigation, Writing - original draft, Visualization. **Mathias Storch:** Conceptualization, Validation, Investigation, Writing - original draft, Writing - review & editing. **Jochen Stadler:** Conceptualization, Methodology, Validation. **Jochen Bandlow:** Conceptualization, Methodology. **Severin Hahn:** Conceptualization, Methodology. **Ralf Riedel:** Supervision. **Thomas Wetzel:** Conceptualization, Supervision.

Declaration of Interests

The authors declare the following financial interests/personal relationships which may be considered as potential competing interests. **Employment:** Johannes Philipp Fath, Lennart Alsheimer, Mathias Storch, Jochen Stadler, Jochen Bandlow, Severin Hahn. **No known competing financial interests:** Ralf Riedel, Thomas Wetzel.

Acknowledgment

This research was supported by Mercedes-Benz AG. We would like to thank all colleagues from Mercedes-Benz AG who supported this work.

Appendix

Table A 1

References

[1] ZSW, Bestand Elektro-Pkw weltweit, 2018, https://www.zsw-bw.de/mediathek/datenservice.html#c6700, accessed 3 April 2019.
[2] "MeinAuto" as cited in Statista, Elektromobilität: Nachfrage erreicht neue Bestmarke: Anteil der Pkw mit Elektro- oder Hybridantrieb an den online nachgefragten Pkw in Deutschland im Zeitraum Januar 2016 bis Januar 2019, 2018, https://www.meinauto.de/presse/pressemitteilungen/202-elektromobilitaet-nachfrage-erreicht-neue-bestmarke, accessed 3 April 2019.
[3] D. Pelegov, J. Pontes, Main drivers of battery industry changes: electric vehicles—a market overview, Batteries 4 (2018) 65, https://doi.org/10.3390/batteries4040065.
[4] "Stern" as cited in Statista, Was sind nach Ihrer Ansicht die wichtigsten Gründe für die bislang noch schwache Nachfrage nach Elektroautos?, 2017, https://de.statista.com/statistik/daten/studie/725762/umfrage/moegliche-gruende-fuer-die-schwache-nachfrage-nach-elektroautos-in-deutschland/, accessed 3 April 2019.
[5] B. Gyenes, D.A. Stevens, V.L. Chevrier, J.R. Dahn, Understanding anomalous behavior in coulombic efficiency measurements on Li-ion batteries, J. Electrochem. Soc. 162 (2015) A278–A283, https://doi.org/10.1149/2.0191503jes.
[6] J. Wilhelm, S. Seidlmayer, P. Keil, J. Schuster, A. Kriele, R. Gilles, A. Jossen, Cycling capacity recovery effect: a coulombic efficiency and post-mortem study, J Power Sources 365 (2017) 327–338, https://doi.org/10.1016/j.jpowsour.2017.08.090.
[7] M. Lewerenz, G. Fuchs, L. Becker, D.U. Sauer, Irreversible calendar aging and quantification of the reversible capacity loss caused by anode overhang, J. Energy Storage 18 (2018) 149–159, https://doi.org/10.1016/j.est.2018.04.029.
[8] M. Lewerenz, D.U. Sauer, Evaluation of cyclic aging tests of prismatic automotive LiNiMnCoO$_2$-graphite cells considering influence of homogeneity and anode overhang, J. Energy Storage 18 (2018) 421–434, https://doi.org/10.1016/j.est.2018.06.003.
[9] M. Lewerenz, P. Dechent, D.U. Sauer, Investigation of capacity recovery during rest period at different states-of-charge after cycle life test for prismatic Li(Ni1/3Mn1/3Co1/3)O2-graphite cells, J. Energy Storage 21 (2019) 680–690, https://doi.org/10.1016/j.est.2019.01.004.
[10] T. Dagger, J. Kasnatscheew, B. Vortmann-Westhoven, T. Schwieters, S. Nowak, M. Winter, F.M. Schappacher, Performance tuning of lithium ion battery cells with area-oversized graphite based negative electrodes, J Power Sources 396 (2018) 519–526, https://doi.org/10.1016/j.jpowsour.2018.06.043.
[11] F. Grimsmann, T. Gerbert, F. Brauchle, A. Gruhle, J. Parisi, M. Knipper, Hysteresis and current dependence of the graphite anode color in a lithium-ion cell and analysis of lithium plating at the cell edge, J. Energy Storage 15 (2018) 17–22, https://doi.org/10.1016/j.est.2017.10.015.
[12] L. David, R.E. Ruther, D. Mohanty, H.M. Meyer, Y. Sheng, S. Kalnaus, C. Daniel, D.L. Wood, Identifying degradation mechanisms in lithium-ion batteries with coating defects at the cathode, Appl. Energy 231 (2018) 446–455, https://doi.org/10.1016/j.apenergy.2018.09.073.
[13] B. Son, M.-.H. Ryou, J. Choi, S.-.H. Kim, J.M. Ko, Y.M. Lee, Effect of cathode/anode area ratio on electrochemical performance of lithium-ion batteries, J. Power Sources 243 (2013) 641–647, https://doi.org/10.1016/j.jpowsour.2013.06.062.
[14] G.F. Kennell, R.W. Evitts, Two-dimensional lithium-ion battery modeling with electrolyte and cathode extensions, ACES 02 (2012) 423–434, https://doi.org/10.4236/aces.2012.24052.
[15] B. Epding, B. Rumberg, H. Jahnke, I. Stradtmann, A. Kwade, Investigation of significant capacity recovery effects due to long rest periods during high current cyclic aging tests in automotive lithium ion cells and their influence on lifetime, J. Energy Storage 22 (2019) 249–256, https://doi.org/10.1016/j.est.2019.02.015.
[16] EL-Cell GmbH, New separator for pat insulation sleeves, 2017, https://el-cell.com/new-separator-for-pat-insulation-sleeves, accessed 27 May 2019.
[17] J. Sieg, J. Bandlow, T. Mitsch, D. Dragicevic, T. Materna, B. Spier, H. Witzenhausen, M. Ecker, D.U. Sauer, Fast charging of an electric vehicle lithium-ion battery at the limit of the lithium deposition process, J. Power Sources 427 (2019) 260–270.
[18] S.L. Hahn, M. Storch, R. Swaminathan, B. Obry, J. Bandlow, K.P. Birke, Quantitative validation of calendar aging models for lithium-ion batteries, J. Power Sources 400 (2018) 402–414, https://doi.org/10.1016/j.jpowsour.2018.08.019.
[19] U. Schadeck, K. Kyrgyzbaev, H. Zettl, T. Gerdes, R. Moos, Flexible, heat-resistant, and flame-retardant glass fiber nonwoven/glass platelet composite separator for lithium-ion batteries, Energies 11 (2018) 999, https://doi.org/10.3390/en11040999.
[20] BasyTec GmbH, CTS technical specification, 2015, https://basytec.de/prospekte/CTS%202015_01.pdf, accessed 21 January 2020.
[21] J.P. Fath, D. Dragicevic, L. Bittel, A. Nuhic, J. Sieg, S. Hahn, L. Alsheimer, B. Spier, T. Wetzel, Quantification of aging mechanisms and inhomogeneity in cycled lithium-ion cells by differential voltage analysis, J. Energy Storage 25 (2019) 100813, , https://doi.org/10.1016/j.est.2019.100813.
[22] T. Hüfner, M. Oldenburger, B. Bedürftig, A. Gruhle, Lithium flow between active area and overhang of graphite anodes as a function of temperature and overhang geometry, J. Energy Storage 24 (2019) 100790, , https://doi.org/10.1016/j.est.2019.100790.
[23] M. Torchio, L. Magni, R.B. Gopaluni, R.D. Braatz, D.M. Raimondo, LIONSIMBA: a matlab framework based on a finite volume model suitable for Li-ion battery design, simulation, and control, J. Electrochem. Soc. 163 (2016) A1192–A1205, https://doi.org/10.1149/2.0291607jes.
[24] X. Zhao, Z. Zhang, S. Yang, G. Liang, Inorganic ceramic fiber separator for electrochemical and safety performance improvement of lithium-ion batteries, Ceram. Int. 43 (2017) 14775–14783, https://doi.org/10.1016/j.ceramint.2017.07.219.
[25] S. He, J. Zeng, B.T. Habte, F. Jiang, Numerical reconstruction of microstructure of graphite anode of lithium-ion battery, Sci. Bull. 61 (2016) 656–664, https://doi.org/10.1007/s11434-016-1048-4.
[26] M. Lewerenz, A. Warnecke, D.U. Sauer, Introduction of capacity difference analysis (CDA) for analyzing lateral lithium-ion flow to determine the state of covering layer evolution, J. Power Sources 354 (2017) 157–166.
[27] S. Tippmann, Modellierung Und Experimentelle Charakterisierung des Degradationsverhaltens durch Lithium-Plating an Lithium-Ionen-Zellen unter Automobilen Betriebsbedingungen, Universität Stuttgart, 2016 Dissertation, [1. Auflage],2015.

Acknowledgements

I wish to express my gratitude for Prof. Dr. Ralf Riedel, my supervisor. He gave me the possibility to carry out my research beginning with my bachelor thesis in 2013, my master thesis in 2016 and finally my PhD thesis. I thank him for constant support and constructive feedback during the entire time.

Prof. Dr. Kai-Peter Birke is acknowledged for the second survey of this thesis and providing me with knowledge on modeling of lithium-ion batteries.

I would like to thank Dr. Carsten Krupp for the unlimited time for supervision of my research at the Daimler AG, the regular meetings on my progress and aid with writing and publishing the articles.

Dr. Dragoljub Vrankovic I want to thank for the time he spent on discussions on scientific topics, our publications and of course private activities. Dr. Magdalena Graczyk-Zajac and Dragoljub teached me in faithful lab work and precise scientifc writing, thank you a lot for this.

The group of “Disperse Feststoffe” is thanked for scientific and personal interchange.

I would like to acknowledge my colleagues at Daimler AG:
Dr. Bernd Spier and Dr. Karin Hauff as managers of the team and for support on the decisions I made during my time at the Daimler AG.
Dr. Barbara Seling for the supervision and organization in the lab of Deutsche Accumotive.
Johannes Fath, Severin Hahn, Tobias Deich, Johannes Sieg, Alexander Fill for the collaboration on many scientific topics and especially Dok16-Reko.
Naqeeb Tahasildar, Florian Klein, Iris Dienwiebel and especially Jochen Stadler who help me with lab work and plenty of scientific discussions.

I gratefully acknowledge the financial support of the Daimler AG.

Curriculum Vitae

Personal details

First name/Surname Mathias Storch

Personal experience and education

2021 - present	Development engineer Mercedes-Benz AG, Kirchheim unter Teck
2016 - present	PhD candidate Technische Universität Darmstadt –Department of Material Science – FG Disperse Feststoffe Daimler AG, Kirchheim unter Teck
2014 - 2016	Research assistant Technische Universität Darmstadt – Department of Material Science – FG Disperse Feststoffe
2014 - 2016	Master in Material Science Technische Universität Darmstadt – Department of Material Science
2010 - 2014	Bachelor in Material Science Technische Universität Darmstadt – Department of Material Science
2010	Abitur Ernst-Göbel Schule, Höchst, Germany

Complete Publications List

Sieg J, Schmid AU, Rau L, Gesterkamp A, **Storch M**, Spier B, Birke KP, Sauer DU: Fast-charging capability of lithium-ion cells: Influence of electrode aging and electrolyte.
Applied Energy 305 (2022) 117747

Storch M, Fath JP, Sieg J, Vrankovic D, Krupp C, Mullaliu A, Spier B, Passerini S, Riedel R: Cycle parameter dependent degradation analysis in automotive lithium-ion cells.
Journal of Power Sources 506 (2021) 230227

Deich T, **Storch M**, Steiner K, Bund A: Effects of module stiffness and initial compression on lithium-ion cell aging.
Journal of Power Sources 506 (2021) 230163

Storch M, Fath JP, Sieg J, Vrankovic D, Krupp C, Spier B, Riedel R: Temperature and Lithium Concentration Gradient Caused Inhomogeneous Plating in Large-format Lithium-ion Cells.
Journal of Energy Storage 41 (2021) 102887

Sieg J, **Storch M**, Fath J, Nuhic A, Bandlow J, Spier B, Sauer D U: Local degradation and differential voltage analysis of aged lithium-ion pouch cells.
Journal of Energy Storage 30 (2020) 101582

Fath JP, Alsheimer L, **Storch M**, Stadler J, Bandlow J, Hahn, S, Riedel R, Wetzel T: The influence of the anode overhang effect on the capacity of lithium-ion cells – a 0D-modeling approach.
Journal of Energy Storage 29 (2020) 101344

Storch M, Hahn SL, Stadler J, Swaminathan R, Vrankovic D, Krupp C, Riedel R: Post-mortem analysis of calendar aged large-format lithium-ion cells: Investigation of the solid electrolyte interphase.
Journal of Power Sources 443 (2019) 227-243

Hahn SL, **Storch M**, Swaminathan R, Obry B, Bandlow J, Birke KP: Quantitative validation of calendar aging models for lithium-ion batteries.
Journal of Power Sources 400 (2018) 402–414

Storch M, Vrankovic D, Graczyk-Zajac M, Riedel R: The influence of pyrolysis temperature on the electrochemical behavior of porous carbon-rich SiCN polymer-derived ceramics.
Solid State Ionics 315 (2018) 59–64

Kaspar J, **Storch M**, Schitco C, Riedel R, Graczyk-Zajac M: SiOC(N)/Hard Carbon Composite Anodes for Na-Ion Batteries: Influence of Morphology on the Electrochemical Properties.
Journal of the Electrochemical Society 163 (2015) A156-A162

Patents:

Storch M, Krupp C, Bandlow J, Method for optimizing battery life and battery management system, German Patent registration DE 10 2018 009833 A1

Bandlow J, **Storch M**, Krupp C, Method for producing an electrical energy store with an arranging a sacrificial electrode and electrical energy storage device, German Patent Registration DE 10 2018 009099 A1

Storch M, Krupp C, Bandlow J, Method for adapting the capacity of an electrochemical energy store of a motor vehicle, German Patent Registration DE 10 2018 007151 A1

Bandlow J, **Storch M**, Electrical energy storage device, German Patent Registration DE 10 2018 009715 A1

Krupp C, Bandlow J, **Storch M**, Electrical energy storage device, in particular for a motor vehicle, German Patent Registration DE 102018008618 A1

Krupp C, Bandlow J, **Storch M**, Electrical energy storage device, in particular for a motor vehicle, German Patent Registration DE 10 2018 008900 A1

Krupp C, Bandlow J, **Storch M**, Cell stack for an energy storage device of a motor vehicle, in particular of a motor vehicle, German Patent Registration DE 10 2018 006424 A1

D. Vrankovic, **M. Storch**, C. Schitco, M. Graczyk-Zajac, R. Riedel, Solvent assisted synthesis of micro/mesoporous ceramics from preceramic polymers, German Patent registration DE 10 2016 116 732 A1.

Conference Contributions

16th Symposium on Modeling and Experimental Validation of Electrochemical Energy Technologies
12.-13. March 2019, Braunschweig, Germany
Investigation of SEI-growth in large-format lithium-ion cells via XPS depth-profiling

MSE - Materials Science and Engineering 2014
23.-25. September 2014, Darmstadt, Germany
Synthesis and characterization of polymer-derived SiOC-/SiCN-Hard-Carbon composites as potential Na-ion storage material